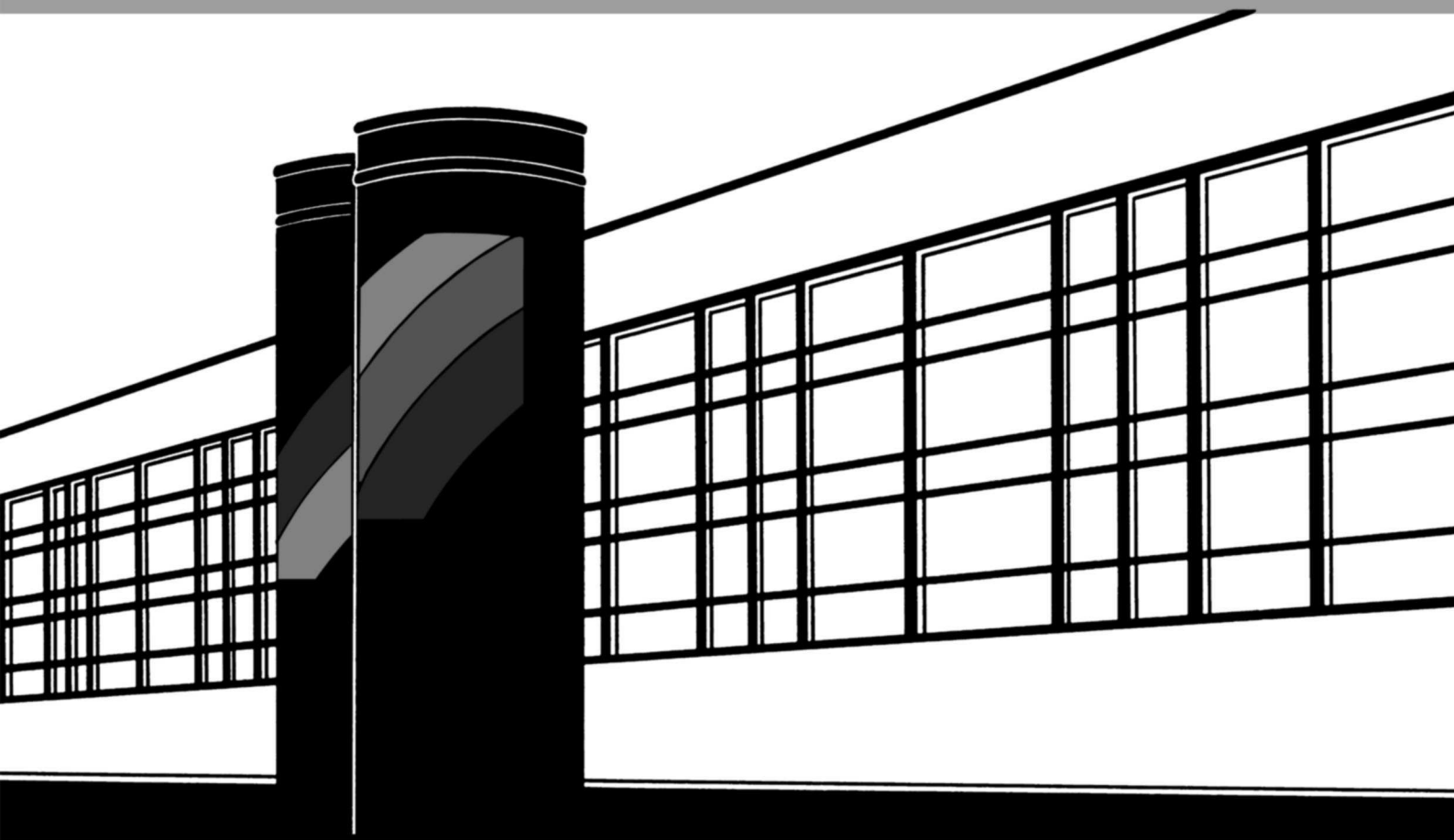


Institut für Wasserbau · Universität Stuttgart

# *Mitteilungen*





# **Multi-Scale Modeling of Multi-Phase–Multi-Component Processes in Heterogeneous Porous Media**

Von der Fakultät Bau- und Umweltingenieurwissenschaften der Universität  
Stuttgart  
zur Erlangung der Würde eines Doktors der  
Ingenieurwissenschaften (Dr.-Ing.) genehmigte Abhandlung

Vorgelegt von

**Jennifer Niessner**

aus Gerlingen

Hauptberichter:

Prof. Dr.-Ing. Rainer Helmig

Mitberichter:

Prof. Magne Espedal

Dr. Jean Roberts, Directeur de  
Recherche

Tag der mündlichen Prüfung:

27. Juli 2006

Institut für Wasserbau der Universität Stuttgart

2006







**D93 Multi-Scale Modeling of Multi-Phase–Multi-Component Processes  
in Heterogeneous Porous Media**

**Niessner, Jennifer:**

Multi-Scale Modeling of Multi-Phase–Multi-Component Processes in Heterogeneous Porous Media / von Jennifer Niessner. Institut für Wasserbau, Universität Stuttgart. - Stuttgart: Inst. für Wasserbau der Univ., 2006

(Mitteilungen / Institut für Wasserbau, Universität Stuttgart ; H. 151)

Zugel.: Stuttgart, Univ., Diss., 2006

ISBN 3-9337 61-54-9

NE: Institut für Wasserbau < Stuttgart >: Mitteilungen

Gegen Vervielfältigung und Übersetzung bestehen keine Einwände, es wird lediglich um Quellenangabe gebeten.

Herausgegeben 2006 vom Eigenverlag des Instituts für Wasserbau, Universität Stuttgart

Druck: Sprint-Digital-Druck GmbH, Stuttgart

# Acknowledgement

The dissertation at hand has emerged from my activity at the chair of Hydromechanics and Modeling of Hydrosystems at the Institute of Hydraulic Engineering at the University of Stuttgart. The work was partly done in the frame of a scholarship of the “Landesgraduiertenförderung Baden-Württemberg, and partly in the frame of the SFB 404 project “Mehrfeldprobleme in der Kontinuumsmechanik, Teilprojekt A3, Mehrphasenprozesse in porösen Medien ”.

I am especially grateful to Prof. Rainer Helmig for the confidence and for taking over the main supervision of the doctoral thesis. His motivation, engagement and enthusiasm as well as his readiness to discuss created a great atmosphere of scientific work in a very agreeable and relaxed environment.

Furthermore, I would like to thank Prof. Magne S. Espedal, and Dr. Jean E. Roberts for their interest in my work and for taking over the co-supervision. I would like to thank Prof. Espedal again as well as Prof. Helge Dahle from the University of Bergen, Norway, for giving me the possibility to spend two month of valuable and inspiring discussions at the University of Bergen. Lots of thanks to Håkon Hægland—also from the University of Bergen—and to Vegard Kippe from SINTEF technologies, Oslo, Norway, for their help on streamline tracing and simulation.

Besides, I am grateful to Prof. Yalchin Efendiev and Prof. Richard Ewing from Texas A & M University, Texas, USA, for very valuable discussions. I would like to thank the latter again for sharing his code on volume averaging and calculation of coarse-grid permeabilities by local pressure solutions.

The work at the Institute of Hydraulic Engineering has always been a pleasure for me—I deeply enjoyed the scientific as well as the non-scientific activities. Therefore—big thanks to the colleagues from IWS for providing this pleasant and nice atmosphere!

I would also like to thank Amir Aghakouchak for his help, who—as a student worker—did parts of the simulations presented in this work.

Finally, my warmest thanks appertain my parents who have always supported me. Thanks also to my very dear friends Daniela and Stephanie who always managed to make me laugh when work became a bit hard.

*"In all things of nature there is something of the marvelous."*

Aristotle (384 BC - 322 BC)

# Contents

<b>Abstract</b>	<b>i</b>
<b>Zusammenfassung</b>	<b>iii</b>
<b>1 Introduction</b>	<b>1</b>
1.1 Motivation . . . . .	1
1.2 Literature Overview . . . . .	9
1.3 Goal and Structure . . . . .	12
<b>2 Physical Background</b>	<b>15</b>
2.1 Scales and Processes . . . . .	15
2.2 Basic Definitions . . . . .	23
2.2.1 Phase . . . . .	23
2.2.2 Component . . . . .	24
2.3 Fluid Parameters . . . . .	24
2.3.1 Density . . . . .	24
2.3.2 Viscosity . . . . .	25
2.4 Matrix Parameters . . . . .	25
2.4.1 Porosity . . . . .	26
2.4.2 Absolute Permeability . . . . .	26
2.5 Parameters Describing Fluid–Matrix Interaction . . . . .	26
2.5.1 Saturation . . . . .	27
2.5.2 Capillary Pressure . . . . .	27
2.5.3 Relative Permeability . . . . .	30
2.5.4 Mass and Mole Fraction, Concentrations . . . . .	32
2.6 Diffusion and Dispersion . . . . .	33
2.6.1 Molecular Diffusion . . . . .	34
2.6.2 Capillary Diffusion . . . . .	34
2.6.3 Numerical Diffusion . . . . .	35
2.6.4 Dispersion . . . . .	36
2.7 Laws for Fluid Phase Equilibria . . . . .	39

<b>3</b>	<b>Mathematical Modeling</b>	<b>42</b>
3.1	Equations for Multi-Phase Processes . . . . .	42
3.2	Equations for Multi-Phase–Multi-Component Processes . . . . .	44
3.3	Fully Coupled vs. Fractional Flow Formulation . . . . .	45
3.3.1	Fully Coupled Formulation . . . . .	46
3.3.2	Fractional Flow Formulation . . . . .	48
3.4	Flash Calculations . . . . .	51
3.4.1	Flash for a Two-Phase–Two-Component System . . . . .	52
3.4.2	Flash for a Three-Phase–Three-Component System . . . . .	56
3.4.2.1	Flash for a 3p3c System—Mass Transfer Model A . . . . .	57
3.4.2.2	Flash for a 3p3c System—Mass Transfer Model B . . . . .	57
3.4.2.3	Flash for a 3p3c System—Mass Transfer Model C . . . . .	59
<b>4</b>	<b>Discretization</b>	<b>62</b>
4.1	Preliminary Remarks . . . . .	63
4.2	Time Discretization . . . . .	64
4.3	Space Discretization . . . . .	68
4.3.1	Discontinuous Galerkin Method . . . . .	68
4.3.1.1	DG for the Pressure Equation . . . . .	68
4.3.1.2	DG for the Saturation Equation . . . . .	73
4.3.1.3	DG for the Concentration Equations . . . . .	75
4.3.2	Streamline Methods . . . . .	76
4.3.2.1	Streamline Tracing . . . . .	78
4.3.2.2	Front Tracking . . . . .	80
<b>5</b>	<b>Multi-Scale Approach</b>	<b>82</b>
5.1	Preliminary Remarks . . . . .	82
5.2	General Remarks . . . . .	83
5.3	Overview of the Solution Concept . . . . .	85
5.4	Upscaling: the Concept of Volume Averaging . . . . .	86
5.4.1	Volume Averaging for a Linear Buckley-Leverett Problem . . . . .	87
5.4.2	Volume Averaging for a Nonlinear Buckley-Leverett Problem . . . . .	92
5.5	General Solution Strategy . . . . .	97
5.5.1	Solution Strategy for Local 2p2c Processes . . . . .	98
5.5.2	Solution Strategy for Local 3p3c Processes . . . . .	102
<b>6</b>	<b>Examples</b>	<b>107</b>
6.1	Testing of <i>DG fine</i> . . . . .	111
6.1.1	General Remarks and Algorithm . . . . .	111
6.1.2	Results . . . . .	112
6.2	Testing of <i>DG upscaled</i> . . . . .	117
6.2.1	The module <i>DG coarse I</i> . . . . .	119

6.2.2	The module <i>DG coarse II</i> . . . . .	120
6.2.3	The module <i>DG fine <math>\bar{v}</math></i> . . . . .	122
6.2.4	Results of the Comparisomal Studies . . . . .	123
6.3	Testing of <i>DG local 2p2c</i> . . . . .	132
6.3.1	General Remarks and Algorithm . . . . .	132
6.3.2	Results of the Comparisomal Studies . . . . .	133
6.4	Testing of <i>DG local 3p3c</i> . . . . .	139
6.4.1	General Remarks and Algorithm . . . . .	139
6.4.2	Results of the Comparisomal Studies . . . . .	140
6.5	Summary of the Results . . . . .	146
<b>7</b>	<b>Final Remarks</b>	<b>148</b>
7.1	Summary of the Thesis Work . . . . .	148
7.2	Fields of Future Research . . . . .	150
<b>A</b>	<b>Vapor Pressures, Molar Masses, and Henry Constants</b>	<b>153</b>
<b>B</b>	<b>Evaluations for a <math>\mathcal{K}_\alpha^\kappa</math> Flash for a 3p3c System</b>	<b>155</b>
B.1	Evaluations for a 3p3c System—Case B . . . . .	155
B.1.1	Derivation of the Mole Equilibrium Ratios $K_w^1$ , $K_w^3$ , $K_n^2$ , and $K_n^3$ . . . . .	155
B.1.2	Evaluation of the Mole Fractions $x_\alpha^\kappa$ . . . . .	157
B.1.3	Evaluation of the Saturations $S_n$ and $S_g$ . . . . .	158
B.2	Evaluations for a 3p3c System—Case C . . . . .	158
<b>C</b>	<b>Parameters for <math>P_2</math> Basis Functions for DG Schemes</b>	<b>160</b>

# List of Figures

1	Grundwassersystem, dessen ungesättigte Zone mit einem LNAPL verunreinigt ist. . . . .	iv
2	Betrachtung lokaler 3p3c-Prozesse (oben) bzw. lokaler 2p2c Prozesse (unten) in einem globalen Zweiphasenmodell. . . . .	v
3	Prinzipübersicht des entwickelten Mehrskalenalgorithmus. . . . .	viii
1.4	Processes in the hydrosystem subsurface. . . . .	2
1.5	Heterogeneities on different scales without taking into account the fluid phases. . . . .	3
1.6	Different processes on different scales in a homogeneous medium. . . . .	4
1.7	Three-phase–three-component setup considered in this work. . . . .	6
1.8	Two-phase–two-component setup considered in this work. . . . .	6
1.9	Block and intrinsic heterogeneities (photo taken from an experiment carried out at the VEGAS research facility, Universität Stuttgart). . . . .	8
1.10	Interface between wetting and non-wetting phase at 20°C (left hand side) and 70°C (right hand side) (taken from Hiester et al. [2003]). . . . .	8
2.11	Definition of scales. . . . .	16
2.12	Definition of the representative elementary volume (picture on the right hand side after Bear [1972]). . . . .	17
2.13	Heterogeneities and multi-phase–multi-component processes on fine and coarse scale. . . . .	17
2.14	Treatment of heterogeneities (left hand side) and of locally complex processes (right hand side) in the frame of this work. . . . .	18
2.15	Dispersion due to local-scale (left hand side) and macro-scale (right hand side) heterogeneities. . . . .	19
2.16	Dispersion due to two-phase processes as well as to local-scale (left hand side) and macro-scale (right hand side) heterogeneities. . . . .	20
2.17	Capillary diffusion as a function of saturation on the local scale. . . . .	21
2.18	Local-scale effects of mass transfer of components between the phases. . . . .	21
2.19	Effects of block heterogeneities—pooling. . . . .	21
2.20	Effects of block heterogeneities—trapping. . . . .	22
2.21	Effects of block heterogeneities—spreading. . . . .	22



2.22	Interfacial tension between water phase and gas phase (Source: Fonds der Chemischen Industrie, Germany; image series “Tenside”). . . . .	23
2.23	Wetting angle $\alpha$ between a wetting and a non-wetting fluid. . . . .	27
2.24	Two fluids in a capillary tube. . . . .	28
2.25	Capillary pressure–saturation relationship after Brooks-Corey and Van Genuchten. . . . .	30
2.26	Relative permeability—saturation relationship after Brooks-Corey and Van Genuchten. . . . .	32
2.27	Effect of 1. advection, 2. diffusion / dispersion, 3. sorption, and 4. biodegradation / reaction. . . . .	34
2.28	Numerical diffusion: the finer the grid, the better the steep front can be approximated. . . . .	36
2.29	Dispersion due to the velocity distribution within a pore throat on the micro scale. . . . .	36
2.30	Dispersion due to local-scale (left hand side) and macro-scale (right hand side) heterogeneities. . . . .	37
2.31	Dispersion due to two-phase processes as well as to local-scale (left hand side) and macro-scale (right hand side) heterogeneities. . . . .	38
2.32	Longitudinal macrodispersion as a function of travel time (modified after Rubin et al. [1999]). . . . .	39
2.33	Transversal macrodispersion as a function of travel time (modified after Rubin et al. [1999]). . . . .	39
2.34	Applicability of Henry’s law and Raoult’s law for a binary gas–liquid system (after Lüdecke and Lüdecke [2000]). . . . .	41
3.35	Control volume for the phase mass balance. . . . .	43
3.36	Control volume for the component mass balance. . . . .	45
3.37	Different 3p3c models. A: mass transfer is considered mutually between all three phases, B: no mass transfer between the liquid phases, and C: only LNAPL and water components can migrate into the gas phase. . . . .	57
4.38	Notation with respect to a one-dimensional element for the TVD–Runge-Kutta–DG discretization. . . . .	65
4.39	<i>minmod</i> function in the case of linear advection. The minimum of the three lines $\bar{u}_i - \bar{u}_{i-1}$ , $\tilde{u}_i$ , and $\bar{u}_{i+1} - \bar{u}_i$ is returned, in the given example $\bar{u}_i - \bar{u}_{i-1}$ . . . . .	67
4.40	Basis functions $P_2$ for DG discretization (First line: degree 0 polynomials, second line: degree 1, third line: degree 2). . . . .	69
4.41	Streamline in a two-dimensional grid-block (after Pollock [1988]). . .	79
4.42	Construction of a solution of the streamline equations using Riemann fans. . . . .	81

5.43	Overview of the solution strategy pursued in this work. . . . .	86
5.44	Averaging over a coarse-grid block. . . . .	87
5.45	Two-dimensional projection showing the averaging procedure for the total velocity. . . . .	90
5.46	Bilinear representation of the velocity components within a fine-scale element. . . . .	91
5.47	Linear representation of the velocity components within a coarse-scale element. . . . .	91
5.48	Approximation of the streamline length within a unit cell. . . . .	91
5.49	Schematic of steps 1. to 4. of the solution strategy for local 2p2c processes. . . . .	99
5.50	Schematic of steps 5. to 8. of the solution strategy for local 2p2c processes. . . . .	100
5.51	Schematic of steps 1. to 4. of the solution strategy for local 3p3c processes. . . . .	103
5.52	Schematic of steps 5. to 8. of the solution strategy for local 3p3c processes. . . . .	104
6.53	Schematic overview of the structure of the test examples. . . . .	108
6.54	Domain considered within the test examples. . . . .	110
6.55	Five test permeability fields corresponding to the geostatistic properties given in Table 6.4. . . . .	111
6.56	Multi-scale structure for test case <i>DG fine</i> . . . . .	112
6.57	Refinement of one grid block from ML 1 to ML 4. . . . .	113
6.58	Boundary and initial conditions used for the testing of the module <i>DG fine</i> . . . . .	114
6.59	Saturation profiles (y-averages) for different values of MAXLEVEL compared for linear and nonlinear DG as well as for linear SL simulations. . . . .	114
6.60	Saturation profiles (y-averages) for the five test permeability fields in the linear case. . . . .	116
6.61	Saturation fronts for different ML—SL results and output for DG in the linear and nonlinear case in a homogeneous domain. . . . .	116
6.62	Saturation fronts for the five test permeability fields—SL results and DG simulations in the linear and nonlinear case. . . . .	116
6.63	Multi-scale structure for test case <i>DG upscaled</i> . . . . .	119
6.64	Multi-scale structure for test case <i>DG coarse II</i> . On the right hand side, the preprocessing step (0a. and 0b.) is shown where the coarse-scale permeability tensor $\underline{K}^*$ is obtained by fine-grid pressure solutions over regions corresponding to coarse-grid blocks. . . . .	120

6.65	The fine-scale one-phase pressure equation is solved in regions corresponding to coarse-grid blocks (left hand side: x-direction, right hand side: y-direction). . . . .	122
6.66	Boundary and initial conditions used for the testing of the modules <i>DG upscaled</i> . . . . .	123
6.67	Saturation profiles (y-averaged values) for the linear and nonlinear case in a homogeneous domain and for the five test permeability fields.	125
6.68	Saturation fronts in a homogeneous domain for the linear and the nonlinear case for different coarse-scale models and the reference fine-scale solution <i>DG fine</i> . . . . .	125
6.69	Saturation fronts using the five test permeability fields for the linear case for different coarse-scale models and the reference fine-scale solution <i>DG fine</i> . . . . .	126
6.70	Saturation fronts using the five test permeability fields for the nonlinear case for different coarse-scale models and the reference fine-scale solution <i>DG fine</i> . . . . .	128
6.71	Saturation fronts for fine level 4 and coarse level 3 through 1 in the linear case. . . . .	130
6.72	Saturation fronts for fine level 4 and coarse level 3 through 1 in the nonlinear case. . . . .	130
6.73	Saturation profiles (y-averaged) in the linear and the nonlinear case for coarse levels ranging from level 3 to 1. A comparison of the upscaled solution ( <i>DG upscaled</i> ), the upscaled solution without macrodispersion ( <i>DG coarse I</i> ), and the reference fine-scale solution ( <i>DG fine</i> ) is shown. . . . .	130
6.74	Multi-scale structure for the reference test case <i>DG 2p2c</i> . . . . .	133
6.75	Boundary and initial conditions used for the testing of the modules <i>DG local 2p2c</i> . . . . .	134
6.76	Saturation fronts in a homogeneous domain for the linear and the nonlinear case for the module <i>DG local 2p2c</i> and its reference fine-scale solution <i>DG 2p2c</i> . . . . .	135
6.77	Saturation fronts for the five test permeability fields in the linear case—comparison of the module <i>DG local 2p2c</i> to its reference fine-scale solution <i>DG 2p2c</i> . . . . .	135
6.78	Saturation fronts for the five test permeability fields in the nonlinear case—comparison of the module <i>DG local 2p2c</i> to its reference fine-scale solution <i>DG 2p2c</i> . . . . .	136
6.79	Geometry for the studies on the dependence of the module <i>DG local 2p2c</i> on the upscaling level. . . . .	137
6.80	Log-permeability field on ML 4 for the studies on the dependence of <i>DG local 2p2c</i> on the upscaling level. . . . .	138

---

6.81	Saturation contour lines for <i>DG local 2p2c</i> on ML 4 and coarse levels 1 through 3 using linear and nonlinear model equations. The reference model is <i>DG 2p2c</i> on ML 4. . . . .	138
6.82	Multi-scale structure for the reference test case <i>DG 3p3c</i> . . . . .	141
6.83	Boundary and initial conditions used for the testing of the module <i>DG local 3p3c</i> . . . . .	142
6.84	Saturation contours in a homogeneous domain and for the heterogeneous test fields for the module <i>DG local 3p3c</i> and its reference fine-scale solution <i>DG 3p3c</i> . Results for both mass transfer model B and mass transfer model C are shown. . . . .	143
6.85	Mole fractions $x_g^k(t)$ as a function of time at location ( $x = 210.9375$ m, $y = 182.8125$ m). . . . .	145

# List of Tables

3.1	Overview of the 2p2c flash solution procedure. . . . .	56
3.2	Overview of the 3p3c flash solution procedure for mass transfer model B. . . . .	60
4.3	Parameters $a_{ik}$ , $b_{ik}$ , and $d_k$ for Runge-Kutta schemes of orders 2 and 3 (taken from Cockburn et al. [1990]) . . . . .	67
6.4	Geostatistical parameters of the five test permeability fields. . . . .	110
6.5	Parameters for the simulation examples. The index $w$ denotes the water phase, the index $n$ the non-wetting phase (gas). . . . .	110
6.6	System CPU times [s] for a homogeneous problem on different refinement levels. . . . .	117
6.7	System CPU times [s] for the five different permeability fields on refinement level ML 3. . . . .	117
6.8	System CPU times [s] for a homogeneous problem using different coarse-scale models (linear and nonlinear case). . . . .	124
6.9	Error norms $L_1$ and $L_2$ for a homogeneous problem using different coarse-scale models (linear and nonlinear case). The respective reference solution is the one provided by <i>DG fine</i> . . . . .	124
6.10	System CPU times [s] for the heterogeneous test cases using different coarse-scale models (linear case). . . . .	127
6.11	Error norms $L_1$ and $L_2$ for the heterogeneous test cases using different coarse-scale models (linear case). The respective reference solution is the one provided by <i>DG fine</i> . . . . .	127
6.12	System CPU times [s] for the heterogeneous test cases using different coarse-scale models (nonlinear case). . . . .	129
6.13	Error norms $L_1$ and $L_2$ for the heterogeneous test cases using different coarse-scale models (nonlinear case). The respective reference solution is the one provided by <i>DG fine</i> . . . . .	129
6.14	CPU times [s] for fine level 4 and coarse levels 3 through 1 in the linear and nonlinear case. . . . .	131
6.15	Error norms $L_1$ and $L_2$ for fine level 4 and coarse levels 3 through 1 in the linear and nonlinear case. . . . .	131

6.16	System CPU times [s] for a homogeneous problem with local and global 2p2c processes (linear and nonlinear case). . . . .	135
6.17	Error norms $L_1$ and $L_2$ for a homogeneous problem with local 2p2c processes (linear and nonlinear case). The module <i>DG 2p2c</i> serves as reference module. . . . .	135
6.18	System CPU times [s] for the five heterogeneous test cases with local and global 2p2c processes (linear and nonlinear case). . . . .	136
6.19	Error norms $L_1$ and $L_2$ for the five heterogeneous test cases with local 2p2c processes (linear and nonlinear case). The module <i>DG 2p2c</i> serves as reference module. . . . .	136
6.20	System CPU times [s] for <i>DG local 2p2c</i> on ML 4 and coarse level 1 through 3 as well as for <i>DG 2p2c</i> on ML 4 (linear and nonlinear case). . . . .	139
6.21	Error norms $L_1$ and $L_2$ for <i>DG local 2p2c</i> on ML 4 and coarse level 1 through 3 (linear and nonlinear case). . . . .	139
6.22	Fluid parameter values for the comparisomal studies to check the module <i>DG local 3p3c</i> ( <i>w</i> : water, <i>n</i> : xylol, and <i>g</i> : gas). . . . .	141
6.23	System CPU times [s] in the homogeneous and in the five heterogeneous domains with local and global 3p3c processes (mass transfer models B and C). . . . .	144
6.24	Error norms $L_1$ and $L_2$ for a homogeneous problem and the five heterogeneous domains with local 3p3c processes (mass transfer models B and C). The module <i>DG 3p3c</i> with mass transfer model B or C serves as reference module. . . . .	144
A.25	Vapor pressure of water and xylol, molar masses of water, xylol, and air as well as Henry constants of water–air and LNAPL–air systems used in this work. . . . .	154
B.26	Physical laws for the evaluation of the 3p3c mole equilibrium ratios. . . . .	155
C.27	Parameters $c_{ab}$ for $P_2$ basis functions for DG schemes of degree 0 (rows: index a, columns: index b). . . . .	160
C.28	A: parameters $c_{ab}$ for $P_2$ basis functions for DG schemes of degree 1 (rows: index a, columns: index b). . . . .	160
C.29	B: parameters $c_{ab}$ for $P_2$ basis functions for DG schemes of degree 1 (rows: index a, columns: index b). . . . .	160
C.30	A: parameters $c_{ab}$ for $P_2$ basis functions for DG schemes of degree 2 (rows: index a, columns: index b). . . . .	161
C.31	B: parameters $c_{ab}$ for $P_2$ basis functions for DG schemes of degree 2 (rows: index a, columns: index b). . . . .	161
C.32	C: parameters $c_{ab}$ for $P_2$ basis functions for DG schemes of degree 2 (rows: index a, columns: index b). . . . .	161

## Notation

symbol	meaning	dimension
$A$	area of a coarse-grid block	$[\text{m}^2]$
$A_\alpha$	exchange of mass of phase $\alpha$ over a control volume boundary	$[\text{kg}/(\text{m}^3 \text{ s})]$
BDM	Brezzi-Douglas-Marini	$[-]$
$C^\kappa$	total concentration of component $\kappa$	$[\text{kg}/\text{m}^3]$
$C_\alpha^\kappa$	concentration of component $\kappa$ in phase $\alpha$	$[\text{kg}/\text{m}^3]$
CFL	Courant-Friedrichs-Lewy	$[-]$
$\underline{\underline{D}}$	macrodispersion tensor	$[\text{m}^2/\text{s}]$
$\underline{\underline{D}}_c(S_w)$	tensor of capillary diffusion	$[\text{m}/\text{s}]$
$\underline{\underline{D}}_{pm}^\kappa$	tensor of hydrodynamic dispersion for component $\kappa$	$[\text{m}^2/\text{s}]$
$\underline{\underline{D}}_{m,pm,\alpha}^\kappa$	tensor of molecular diffusion for component $\kappa$ in phase $\alpha$	$[\text{m}^2/\text{s}]$
DG	discontinuous Galerkin	$[-]$
$E$	length of a coarse-grid edge	$[\text{m}]$
$E_h$	subdivision of $\Omega$	$[-]$
$F$	force	$[\text{N}]$
$\underline{F}_\alpha^\kappa$	diffusive Fickian flux of component $\kappa$ in phase $\alpha$	$[\text{kg}/\text{m}^2\text{s}]$
$FV$	finite volume	$[-]$
$\underline{G}$	gravity term	$[\text{kg}/\text{m}^2\text{s}^2]$
$H^\kappa$	Henry coefficient of component $\kappa$	$[1/\text{Pa}]$
$H_\alpha^\kappa$	Henry coefficient of component $\kappa$ in phase $\alpha$	$[1/\text{Pa}]$
$I_\alpha$	exchange of mass of phase $\alpha$ with other phases	$[\text{kg}/(\text{m}^3 \text{ s})]$
$J_i^c$	absolute correlation length	$[\text{m}]$
$\underline{K}$	matrix of absolute (intrinsic) permeability	$[\text{m}^2]$
$\underline{K}^\kappa$	mole equilibrium ratio for flash calculations	$[-]$
$\mathcal{K}^\kappa$	mass equilibrium ratio for flash calculations	$[-]$
$\underline{L}$	vector of length of a coarse-grid streamline	$[\text{m}]$
$L$	length of a domain	$[\text{m}]$
	macro-scale length scale	$[\text{m}]$
	mathematical operator	$[\text{m}]$
$M$	parameter for the TVB corrected minmod function	$[-]$
$M_\alpha$	storage term for the mass of phase $\alpha$	$[\text{kg}/(\text{m}^3 \text{ s})]$
$M^\kappa$	molecular weight of component $\kappa$	$[\text{g}/(\text{mole})]$
ML	MAXLEVEL (fine-grid level)	$[-]$
$N_{CFL}$	Courant number	$[-]$
NIPG	nonsymmetric interior penalty Galerkin method	$[-]$
ODE	ordinary differential equation	$[-]$
$P_r$	space of polynomial functions of degree $r$	$[-]$

PDE	partial differential equation	[-]
$Q_\alpha$	sink / source term for phase $\alpha$ in a control volume	[kg/(m <sup>3</sup> s)]
$S_\alpha$	saturation of phase $\alpha$	[-]
SL	streamline	[-]
$T$	temperature	[K]
TVB	total variation bounded	[-]
TVD	total variation diminishing	[-]
$V$	volume	[m <sup>3</sup> ]
$X_\alpha^\kappa$	mass fraction of component $\kappa$ in phase $\alpha$	[-]
$b$	fine-grid quantity ( $S_\alpha, \underline{v}_\alpha$ )	[?]
$c$	component	[-]
$d$	diameter	[m]
$f$	increment function for an ODE	[-]
$f_\alpha$	fractional flow function of phase $\alpha$	[-]
$\underline{g}$	vector of gravity	[m/s <sup>2</sup> ]
$h_i$	length of a coarse-grid edge in coordinate direction $i$	[m]
$k$	polynomial order of a DG scheme	[-]
$k_{r\alpha}$	relative permeability of phase $\alpha$	[-]
$l$	local-scale length scale	[m]
$l_i$	relative correlation length	[m]
$m$	mass	[kg]
	Van Genuchten parameter	[-]
	number of phases / components	[-]
	minmod function	[-]
$\bar{m}$	TVB corrected minmod function	[-]
$\underline{n}$	normal vector	[-]
$n$	number of moles	[mole]
	Van Genuchten parameter	[-]
$n_f$	number of fine-grid elements [-]	
$p$	pressure	[Pa]
	phase	[-]
$\tilde{p}$	global pressure	[Pa]
$p_\alpha$	pressure of phase $\alpha$	[Pa]
$p_\alpha^\kappa$	partial pressure of component $\kappa$ in phase $\alpha$	[Pa]
$p_c$	capillary pressure	[Pa]
$p_d$	entry pressure of a material	[Pa]
$p_{vap}^\kappa$	vapor pressure of pure component $\kappa$	[Pa]
$q$	parameter for the TVB corrected minmod function	[-]
$q_\alpha$	source/sink of phase $\alpha$	[1/s]
$q^\kappa$	source/sink of component $\kappa$	[kg/(m <sup>3</sup> s)]
$s$	sign of a value	[-]
$t$	time	[s]



$u$	unknown quantity	[?]
$\underline{v}$	vector of total velocity	[m/s]
$\underline{v}_\alpha$	vector of velocity of phase $\alpha$	[m/s]
$x_\alpha^\kappa$	mole fraction of component $\kappa$ in phase $\alpha$	[-]
$\Gamma$	boundary of a coarse-grid block	[-]
$\Lambda\Pi$	local projection maintaining TVD property	[-]
$\Omega$	domain in $R_2$	[-]
$\alpha$	coefficient accounting for variance of log permeability	[-]
	wetting angle	[rad]
	Van Genuchten parameter	[1/Pa]
$\epsilon$	parameter needed in Van-Genuchten relative permeability function	[-]
$\gamma$	angle deformation	[rad]
$\gamma$	parameter needed in Van-Genuchten relative permeability function	[-]
$\lambda$	total mobility	[(ms)/kg]
	Brooks-Corey parameter	[-]
$\lambda_\alpha$	mobility of phase $\alpha$	[(ms)/kg]
$\mu_\alpha$	dynamic viscosity of phase $\alpha$	[kg/(ms)]
$\phi$	porosity	[-]
$\rho_\alpha$	density of phase $\alpha$	[kg/m <sup>3</sup> ]
$\sigma$	standard deviation of log permeability	[-]
	interfacial tension	[N/m <sup>2</sup> ]
$\tau$	shear stress	[N/m <sup>2</sup> ]
	time of flight along a streamline	[s]
$\xi$	arc length along a streamline	[m]

**subscripts**

$2p$	referring to two-phase problem
$2p2c$	referring to two-phase–two-component problem
$3p3c$	referring to three-phase–three-component problem
$D$	Dirichlet boundary
$N$	Neumann boundary
$e$	effective
	element
$g$	gas phase
$h$	discretized with discretization length $h$
$i, j$	components of vectors and matrices
$w$	wetting phase
$n$	non-wetting phase
$r$	degree of polynomial

	residual
tof	time of flight
$\alpha$	referring to phase $\alpha$

**superscripts**

$C$	resulting from the total concentration equations
$S$	resulting from the saturation equation
$n$	time level
$s$	number of stages
$\kappa$	component

# Abstract

Flow and transport phenomena in porous media are the governing processes in many natural and industrial systems. Considering the flow and transport processes on the one hand, they occur on different spatial and temporal scales and may also differ locally. Highly complex processes may take place in one part of the system necessitating an examination of the processes on a fine spatial and temporal scale, while in other parts of the system, physically simpler processes may take place allowing an examination on a coarser scale. Considering the porous medium on the other hand, its heterogeneous structure shows a high dependence on the spatial scale. The porous medium is generally heterogeneous on every spatial scale, but different kinds of heterogeneities predominate on different scales.

To study these issues, a domain with randomly distributed heterogeneities is considered where complex multi-phase–multi-component processes are relevant only in a small (local) subdomain. This situation might well be an LNAPL contamination in the unsaturated zone of the groundwater, where complex three-phase–three-component processes take place in a subdomain in and around the contaminated zone. This subdomain needs fine resolution as the complex processes are governed by small-scale effects. For a comprehensive fine-scale model taking into account multi-phase–multi-component processes as well as heterogeneities in the whole (global) model domain, the data collection is often far too expensive and the computational effort is high.

Therefore, a general multi-scale concept is developed where on the one hand, the global flow field influences the local multi-phase–multi-component processes on the fine-scale. On the other hand, the coarse-scale effects of the fine-scale multi-phase–multi-component processes in the subdomain are captured by source / sink terms and the coarse-scale effects of fine-scale heterogeneities by a macrodispersion term. Specifically, a fine-scale pressure equation is solved globally to obtain a fine-scale velocity field. Equations accounting for the total concentrations of components are solved in a local domain on a fine scale. An averaged velocity as well as a source / sink term resulting from the concentration solution are passed to an upscaled coarse-scale saturation equation.

The overall algorithm is presented and tested for locally occurring two-phase–two-component as well as for locally occurring three-phase–three-component processes in homogeneous and different heterogeneous domains, for both linear and nonlinear model equations. Various test examples are used to investigate the quality of the algorithm by studying the error introduced due to the coarse-scale form of the saturation model. Furthermore, the computing times of the model in which the total concentration equations are solved only locally are compared to the computing times of the model in which the concentration equations are solved globally in the whole domain.

It is shown, that the algorithm developed in this work provides a convenient, general and expandable tool for modeling processes of different complexity occurring at different locations and on different scales.

# Zusammenfassung

## Problemdefinition und Ziel der Arbeit

Die vorliegende Arbeit beschäftigt sich mit der Entwicklung eines mathematischen und numerischen Modells, das die Einbindung physikalischer Prozesse unterschiedlicher Komplexität in heterogenen Modellgebieten erlaubt. Hierbei laufen die Prozesse auf unterschiedlichen räumlichen und zeitlichen Skalen ab und können lokal verschieden sein, während die Heterogenitäten ebenfalls eine ausgeprägte Abhängigkeit von der räumlichen Skala aufweisen. Ziel der Arbeit ist es, komplexe Prozesse nur in den Gebieten und Prozesse und Strukturen lediglich auf den Skalen abzubilden, wo sie einen relevanten Einfluss haben. Diese Herangehensweise bedeutet einerseits, dass hochkomplexe Prozesse, die eine feinskalige Betrachtung erfordern und deshalb nicht nur große Datenmengen benötigen sondern auch von einem extrem hohen Rechenaufwand begleitet sind, nur in einem kleineren Gebiet modelliert werden. Dadurch können sich erforderliche Datenmenge und Rechenzeit erheblich verringern. Andererseits sind einige hochkomplexe Prozesse stark von feinskaligen Parametern abhängig und erfordern daher eine feine Auflösung, während andere – meist einfachere – Prozesse ohne große Genauigkeitsverluste auf einer größeren Skala approximiert werden können. Der hier entwickelte Algorithmus zur Lösung dieser Problemstellung wird im Folgenden Mehrskalenalgorithmus genannt.

Ziel der Arbeit ist es, den Mehrskalenalgorithmus flexibel zu gestalten, so dass er leicht um weitere Prozesse erweitert werden kann oder auch ganze Prozessmodule ausgetauscht werden können. Um Ergebnisse zu erhalten, die nachvollziehbar sind und deren Qualität anhand von Referenzlösungen verifiziert werden kann, stellt die vorliegende Arbeit den Mehrskalenalgorithmus anhand eines konkreten Beispiels vor, nämlich der Kontamination der ungesättigten Zone eines Grundwassersystems mit einem sogenannten LNAPL (light non-aqueous phase liquid). Der Kontaminant LNAPL ist mit Wasser nicht oder nur in geringem Maße mischbar, das heißt, Wasser, LNAPL und Bodenluft bilden jeweils eine *Phase*. Diese Situation ist in Abbildung 1 dargestellt. Aus der Abbildung wird ersichtlich, dass das Grundwassersystem von zwei sich wechselseitig beeinflussenden Effekten geprägt ist:

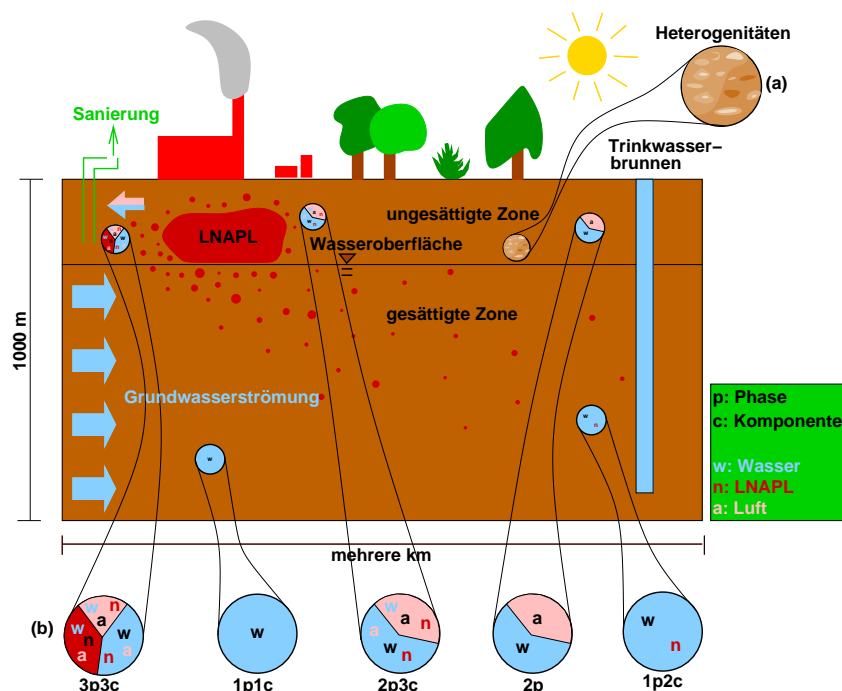


Abbildung 1: Grundwassersystem, dessen ungesättigte Zone mit einem LNAPL verunreinigt ist.

- (a) Einerseits ist die Bodenmatrix, d.h. das poröse Medium Boden, uneinheitlich – diese Uneinheitlichkeiten werden **Strukturheterogenitäten** oder kurz **Heterogenitäten** genannt. Sie treten auf den verschiedensten Skalen auf, angefangen von einer molekularen Skala, auf der einzelne Teilchen unterschieden werden können, bis hin zu einer Makroskala, die mehrere Kilometer umfassen kann und die die Zielskala für eine numerische Modellierung des Systems ist. Die Heterogenitäten auf jeder der Skalen haben Einfluss auf die jeweils größeren Skalen.
- (b) Andererseits ist das System von verschiedenen physikalischen **Prozessen** geprägt. Diese Prozesse finden nicht nur auf unterschiedlichen räumlichen und zeitlichen Skalen statt, sondern sie können auch von Ort zu Ort variieren. Betrachtet man das in Abbildung 1 dargestellte System, so dominieren in der Nähe der LNAPL-Kontamination andere Prozesse als in größerer Entfernung. An der Phasengrenzfläche zwischen LNAPL, umgebendem Grund- bzw. Bodenwasser und Bodenluft finden Massentransferprozesse statt, d.h. durch Verdunstung treten LNAPL und Wasser in die Gasphase über, während sich umgekehrt Luft in LNAPL und Wasser löst. Die Strömungs- und Transportprozesse sind stets mit einer bestimmten Anzahl von Phasen  $p$  und einer bestimmten Anzahl an Komponenten  $c$  verbunden. Komponenten sind entweder chemische Substanzen oder eine Einheit von chemischen Substanzen,

die physikalisch ähnliches Verhalten (z.B. Luft) aufweisen. Die oben diskutierten Prozesse in Nähe der LNAPL-Kontamination sind damit Dreiphasen-Dreikomponentenprozesse (3p3c-Prozesse) mit den Komponenten Luft (a), Wasser (w) und LNAPL (n) sowie den Phasen Gas, Wasser und LNAPL. Mit zunehmender Entfernung von der Verunreinigung nimmt der Massentransfer zwischen den Fluidphasen ab. In großer Entfernung von der Kontamination spielt der Massentransfer eine vernachlässigbar geringe Rolle und das System kann adäquat mit einem Zweiphasenmodell (2p: Wasser und Gas) beschrieben werden, in dem keine Massentransferprozesse berücksichtigt werden. Während die komplexen 3p3c-Prozesse eine feinskalige Auflösung benötigen, ist für die einfacheren Zweiphasenprozesse ein grobskaliges Modell ausreichend.

In der vorliegenden Arbeit werden daher Heterogenitäten bereits auf einer feinen Skala erfasst. Gleichzeitig werden Mehrphasen-Mehrkomponentenprozesse ebenfalls auf einer feinen Skala, aber lediglich in einem Teilgebiet des gesamten Untersuchungsgebiets modelliert. Auf einer groben Skala werden einfachere Zweiphasenprozesse betrachtet. Bei den Mehrphasen-Mehrkomponentenprozessen handelt es sich wie oben ausgeführt um 3p3c-Prozesse, zur besseren Überprüfbarkeit des Mehrskalenalgorithmus wird jedoch zunächst ein Zweiphasen-Zweikomponentenmodell (2p2c-Modell) konstruiert, siehe auch Abbildung 2.

Für die Vorstellung des Mehrskalenalgorithmus ist eine nähere Definition der betrachteten Skalen nötig. Die feine Skala entspricht demnach der **lokalen Skala**, auf

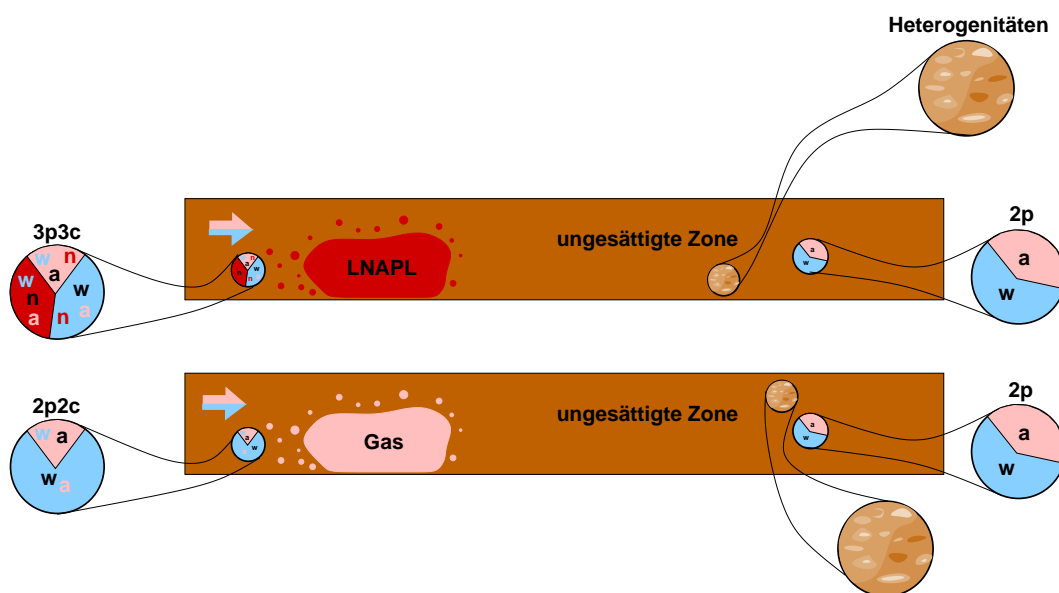


Abbildung 2: Betrachtung lokaler 3p3c-Prozesse (oben) bzw. lokaler 2p2c Prozesse (unten) in einem globalen Zweiphasenmodell.

der volumengemittelte Größen vorliegen. Diese entstehen ihrerseits bei der Mittelung der Prozesse auf einer Skala, in der einzelne Poren und Porennetzwerke betrachtet werden, über ein sogenanntes repräsentatives Elementarvolumen. Die Skala, auf der das gesamte Untersuchungsgebiet erfasst wird, ist die grobe Skala, welche auch **Makroskala** genannt wird und auf der teils andere, aber ebenfalls gemittelte, Größen bestimmend sind.

## Mathematische Modellbeschreibung

Da der in der vorliegenden Arbeit entwickelte Mehrskalenalgorithmus sehr komplex ist, werden zum Teil aus physikalischen Gründen, vor allem aber auch zur Verifizierbarkeit des Algorithmus vereinfachende Annahmen getroffen. Die wichtigsten umfassen die Vernachlässigung von Kapillar-, Kompressibilitäts- und Gravitationseffekten sowie die Annahme isothermer Verhältnisse.

Zur mathematischen Beschreibung der betrachteten Prozesse kann ein System von partiellen Differentialgleichungen aufgestellt werden. In der vorliegenden Arbeit wird eine fraktionale Durchflussformulierung (**fractional-flow-Formulierung**) der Erhaltungsgleichungen herangezogen, bei der die ansonsten voll gekoppelten partiellen Differentialgleichungen in eine Druckgleichung, eine Sättigungsgleichung sowie - in Abhängigkeit davon, ob lokal 2p2c- oder 3p3c-Prozesse betrachtet werden - eine bzw. zwei Gleichungen für die totalen Konzentrationen umgeformt werden können. Die Lösung der Sättigungsgleichung ist hierbei notwendig, da global auf der groben Skala Zweiphasenprozesse approximiert werden sollen. Die Druckgleichung hat elliptischen Charakter, während Sättigungsgleichung und Konzentrationsgleichung(en) hyperbolisch / parabolischen bzw. hyperbolischen Charakter haben.

Bei der Modellierung der Mehrphasen-Mehrkomponentenprozesse werden Konzentrationsgleichungen gelöst, aus denen totale Konzentrationen resultieren. Da für die Lösung der Druckgleichung die Sättigungsverteilung benötigt wird, muss aus dem gegebenen Druckfeld sowie dem Konzentrationsfeld ein Sättigungsfeld berechnet werden. Dies geschieht in sogenannten **Flash-Berechnungen**, in denen aus Gleichgewichtsbeziehungen für den Massentransfer zwischen Fluidphasen, wie dem Henry-, Dalton- oder Raoultgesetz, Sättigungen abgeleitet werden. Vorgestellt werden einerseits ein Modell für eine 2p2c-Flash-Berechnung, andererseits werden zwei verschieden komplexe Modelle für eine 3p3c-Flash-Berechnung präsentiert. Das einfachere dieser Modelle berücksichtigt lediglich den Transfer von LNAPL und Wasser in die Gasphase, während das komplexere zusätzlich die Lösung von Luft in LNAPL und Wasser einbezieht.



## Wahl des Diskretisierungsschemas

Um die partiellen Differentialgleichungen bestehend aus Druckgleichung, Sättigungsgleichung und Konzentrationsgleichung(en) numerisch lösen zu können, ist eine Diskretisierung in Raum und Zeit nötig. Diese muss einerseits flexibel genug sein, um sowohl elliptische als auch hyperbolische Gleichungen behandeln zu können, andererseits muss sie weitestgehend arm an numerischer Diffusion sein. Letzteres ist ein wichtiger Aspekt, da beim Hochskalieren der Sättigungsgleichung auf eine grobe Skala ein Makrodispersionsterm entsteht. Ist die numerische Diffusion von ähnlicher Größenordnung wie die Makrodispersion, so verlieren die Ergebnisse erheblich an Wert. Aus diesen Gründen kommt in dieser Arbeit eine **Diskontinuierliche Galerkin-Formulierung** (siehe Reed und Hill [1973], Oden et al. [1998], Cockburn und Shu [1989, 1998]) für die Raumdiskretisierung zur Anwendung, die sich für eine Finite Elemente-Diskretisierung höherer Ordnung anbietet.

In Bezug auf die Raumdiskretisierung ist anzumerken, dass eine bestimmte Skala auch immer mit einer bestimmten Diskretisierungslänge verknüpft ist. Während die feine Skala mit einem feinen Gitter belegt ist, wird auf der groben Skala auch ein grobes Gitter angewandt.

Die Zeitdiskretisierung ist für die elliptische Druckgleichung implizit, wohingegen die hyperbolischen, bzw. parabolisch / hyperbolischen Differentialgleichungen zeit-explizit gelöst werden. Hierbei kommt ein Runge-Kutta-Schema zur Anwendung, das einen modifizierten minmod-Slope-Limiter enthält. Die hier verwendete Diskontinuierliche Galerkin-Formulierung ist die von Bastian [2003] beschriebene und implementierte.

## Prinzip des Mehrskalenalgorithmus

Das Prinzip des hier entwickelten Algorithmus ist aus Abbildung 3 ersichtlich. Aus der Lösung der Druckgleichung ergibt sich ein Druckfeld, aus dem über die Darcy-Gleichung ein Geschwindigkeitsfeld berechnet werden kann. Da dieses mit der angewandten Diskretisierung diskontinuierlich über Elementkanten hinweg ist, wird es durch eine *BDM*-Projektion (Brezzi-Douglas-Marini-Projektion nach Brezzi et al. [1986] sowie Brezzi und Fortin [1991]) kontinuierlich gemacht. Diese Geschwindigkeiten gehen (in gemittelter Form) in die hochskalierte Sättigungsgleichung sowie in die lokalen feinskaligen Konzentrationsgleichungen ein (a).

Der nächste Schritt besteht in der Lösung einer oder zweier Konzentrationsgleichung(en). Aus den feinskaligen lokalen Konzentrationen sowie dem Druck kann in einer Flash-Berechnung das lokale feinskalige Sättigungsfeld rekonstruiert werden. Diese Sättigungen werden gemittelt und so auf die grobe Skala übertragen (b).

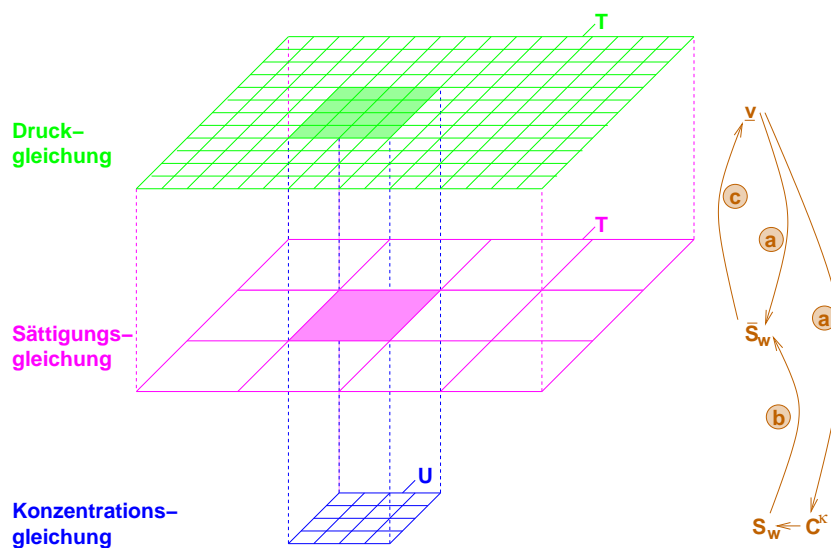


Abbildung 3: Prinzipübersicht des entwickelten Mehrskalenalgorithmus.

Nun werden aus der Differenz dieser gemittelten Sättigungen und der Sättigungen, die aus der letzten Lösung der Sättigungsgleichung resultieren, Quell- / Senkterme für jedes grobskalige Element berechnet. Diese ermöglichen die lokal massenkonserve Lösung der grobskaligen Sättigungsgleichung. Unter Einbeziehung der gemittelten Geschwindigkeiten und Sättigungen sowie der Quell- / Senkterme wird die hochskalierte Sättigungsgleichung gelöst. Das so berechnete Sättigungsfeld wird wieder zur nächsten Lösung der Druckgleichung herangezogen (c).

Drei wichtige Eigenheiten des Mehrskalenalgorithmus sind noch anzusprechen.

1. Zur **Hochskalierung** der Sättigungsgleichung wird die Technik der Volumenmittelung angewandt (Efendiev et al. [2000] sowie Efendiev und Durlofsky [2002]), bei der die unbekannt Größen über Grobgitterelemente gemittelt werden. Dadurch werden sie in gemittelte und fluktuierende Größe aufgespalten. Die Volumenmittelung der feinskaligen Sättigungsgleichung ergibt eine Gleichung, die noch feinskalige Unbekannte enthält. Durch geschickte Manipulation der Gleichungen kann eine Form der hochskalierten Sättigungsgleichungen erhalten werden, die nur bekannte feinskalige Größen enthält.
2. Am Rand der lokalen Domain werden Dirichlet-**Randbedingungen** für die totalen Konzentrationen der Komponenten formuliert. Da die totalen Konzentrationen sättigungsabhängig sind, werden sie mit den grobskaligen Sättigungen aus der hochskalierten Sättigungsgleichung aktualisiert. Damit sind diese Randbedingungen instationär.
3. Die zeit-explicite Lösung von Sättigungs- und Konzentrationsgleichung

erfordert die Einhaltung der Courant-Friedrichs-Lewy-Bedingung (**CFL-Bedingung**, siehe Courant et al. [1928]), welche den maximalen Zeitschritt festsetzt. Da die Konzentrationsgleichung(en) auf einem feineren Gitter als die Sättigungsgleichung gelöst werden, sind hier kleinere Zeitschritte anzusetzen. Aus diesem Grund wird die Konzentrationsgleichung in mehreren Mikrozeitschritten gelöst, bevor wieder in einem Makrozeitschritt Sättigungs- und Druckgleichung gelöst werden.

## Ergebnisse und abschließende Bemerkungen

Da der vorgestellte Mehrskalenalgorithmus komplex ist und aus verschiedenen Bausteinen besteht, werden die einzelnen Module des Algorithmus für numerische Untersuchungen zunächst zerlegt und schrittweise zum vollen und komplexen Algorithmus zusammengesetzt. Damit erfolgt eine Verifikation des Algorithmus von einem einfachen Modell zum kompletten Mehrskalenalgorithmus hin.

Untersucht werden sowohl ein homogenes Feld als auch eine Testserie von fünf heterogenen Feldern mit unterschiedlichen geostatistischen Eigenschaften. Für jedes dieser Permeabilitätsfelder werden eine lineare und eine nichtlineare, feinskalige und hochskalierte Sättigungsgleichung betrachtet. Neben einer visuellen Überprüfung der Qualität des Algorithmus mittels des Verlaufs von Isolinien der Sättigung wird die Genauigkeit mathematisch über die Berechnung der  $L_1$ - und der  $L_2$ -Fehlernorm bestimmt. Darüber hinaus werden die Rechenzeiten mit den CPU-Zeiten von feinskaligen Referenzlösungen verglichen.

Die schrittweise Überprüfung des Algorithmus erfolgt folgendermaßen:

- Zunächst wird ein Modul untersucht, in dem Druck- und Sättigungsgleichung global auf einer feinen Skala modelliert werden. Für den linearen Fall werden die Ergebnisse mit den Resultaten von Streamline-Verfahren verglichen, die in diesem speziellen Fall praktisch frei von numerischer Diffusion sind. Außerdem werden Netzverfeinerungsuntersuchungen durchgeführt, um für die folgenden Berechnungen eine geeignete Referenzskala für die Lösung der feinskaligen Gleichungen auszuwählen.
- Statt der feinskaligen Sättigungsgleichung wird nun die hochskalierte Sättigungsgleichung gelöst. Die Ergebnisse werden mit der feinskaligen Referenz und mit drei weiteren Modellen für die Lösung einer grobskaligen Sättigungsgleichung verglichen. Darüber hinaus wird die Abhängigkeit der Resultate vom Vergrößerungsgrad, d.h. dem Unterschied zwischen feinem und grobem Gitter, untersucht.

- Im nächsten Schritt wird zusätzlich zu feinskaliger Druckgleichung und grobskaliger Sättigungsgleichung lokal eine Konzentrationsgleichung gelöst. Dies entspricht einer lokalen Berücksichtigung von 2p2c-Prozessen. Referenzlösung ist hier ein Modell, welches feinskalige Druckgleichung und feinskalige Konzentrationsgleichung global löst. Auch in diesem Fall wird die Abhängigkeit der Resultate vom Verhältnis der Diskretisierungslängen des feinen und groben Gitters untersucht.
- Schließlich werden statt der lokalen 2p2c-Prozesse lokale 3p3c-Prozesse betrachtet. In diesem Fall werden auch die beiden oben vorgestellten Massentransfermodelle verglichen. Hierzu wird zusätzlich zu der Berechnung von Fehlernormen und dem Vergleich von CPU-Zeiten der zeitliche Verlauf der Massenfraktionen aller drei Komponenten in der Gasphase untersucht.

Die Resultate zeigen, dass der entwickelte Mehrskalalgorithmus die feinskaligen Referenzergebnisse sehr genau approximiert. Dies belegt sowohl der Verlauf von Isolinien der Sättigung als auch die Fehlernormen. In Bezug auf die Rechenzeiten bringt der Mehrskalalgorithmus in den betrachteten Fällen nicht immer eine Ersparnis. Dies liegt einerseits daran, dass die in der Arbeit betrachteten physikalischen Prozesse noch nicht sehr komplex sind und relativ schnell gelöst werden können. Andererseits benötigen auch die Transferoperationen zwischen den Gittern Rechenzeit. Es ist jedoch davon auszugehen, dass bei der Betrachtung komplexerer physikalischer Prozesse der Mehrskalalgorithmus im Vergleich zur Referenzlösung besser abschneiden wird. Auch konnte gezeigt werden, dass für höhere Vergrößerungsgrade der Mehrskalalgorithmus hinsichtlich der Rechenzeit vorteilhafter ist als die herkömmliche feinskalige Lösung. Der Vergleich der beiden Massentransfermodelle im 3p3c-Fall ergab keinen großen Unterschied, so dass für die betrachteten Beispiele das vergleichsweise einfachere Modell ausreichend ist.

Aus dem entwickelten Modell ergibt sich vielfältiger weiterer Forschungsbedarf. Eine Ergänzung des physikalischen und mathematischen Modells um eine Vielzahl weiterer Prozesse ist möglich und erforderlich, wenn praktische Anwendungsbeispiele modelliert werden sollen. Darüber hinaus kann die numerische Diskretisierung der elliptischen Druckgleichung verbessert werden. Einerseits kann auch diese Gleichung hochskaliert werden, was erheblich Rechenzeit einsparen kann, aber eine kompliziertere und ungenauere Bestimmung des feinskaligen Geschwindigkeitsfelds mit sich bringt, andererseits kann hier die Diskontinuierliche Galerkin-Diskretisierung durch eine – für diese elliptische Gleichung geeignetere – Finite-Volumen-Diskretisierung ersetzt werden. Schließlich stellt die Behandlung der Randbedingungen der lokalen Domain eine besondere Herausforderung dar; andere Ansätze als der hier verwendete relativ simple Ansatz sind denkbar, wie z.B. ein nicht-ortsfestes Netz für die Lösung der Konzentrationsgleichung(en), das sich mit der Kontamination mitbewegt.

# 1 Introduction

## 1.1 Motivation

Flow and transport phenomena in porous media are *the* governing processes in many natural and industrial systems. Classical applications comprise for example petroleum engineering where the flow of oil, water and gas in a reservoir is studied, civil engineering where stability issues of geotechnical systems are investigated, or environmental engineering where flow and transport of contaminants in the subsurface is considered. Recently, new disciplines dealing with flow and transport in porous media have evolved. They range from the study of the sequestration of carbon dioxide in deep geological formations and the investigation of the migration of methane emitted by abandoned coal mines to paper manufacturing and medical applications, like the description of fluid flow processes in the human body. This work focusses on flow and transport processes in subsurface hydrosystems, though findings may be transferred to other applications.

Figure 1.4 shows a schematic cut-out of the hydrosystem subsurface. As can be seen, the upper part of this subsurface system corresponds to the unsaturated zone, where air and water fill the void space between the soil particles. Going further down, at some point, the groundwater table is reached, and below, all the pores are filled with water. In the given example, the unsaturated zone is contaminated by an LNAPL (light non-aqueous phase liquid) which is immiscible with water and of a density smaller than that of water. It can be seen, that

- (a) the soil structure is heterogeneous. The distribution of small-scale heterogeneities has a high impact on all flow and transport processes.
- (b) processes of different complexity occur in different parts of the soil, involving a different number of phases  $p$  and components  $c$ . In and around the LNAPL contamination, mass transfer processes, e.g. the evaporation of LNAPL and water or the dissolution of air in water and LNAPL, play an important role, while further away from the plume, the mass transfer is negligibly small. In the vicinity of the contamination in the unsaturated zone, numerical studies require a complex three-phase–three-component model (3p3c) taking into account a liquid wetting phase (mainly water), an intermediate-wetting liquid

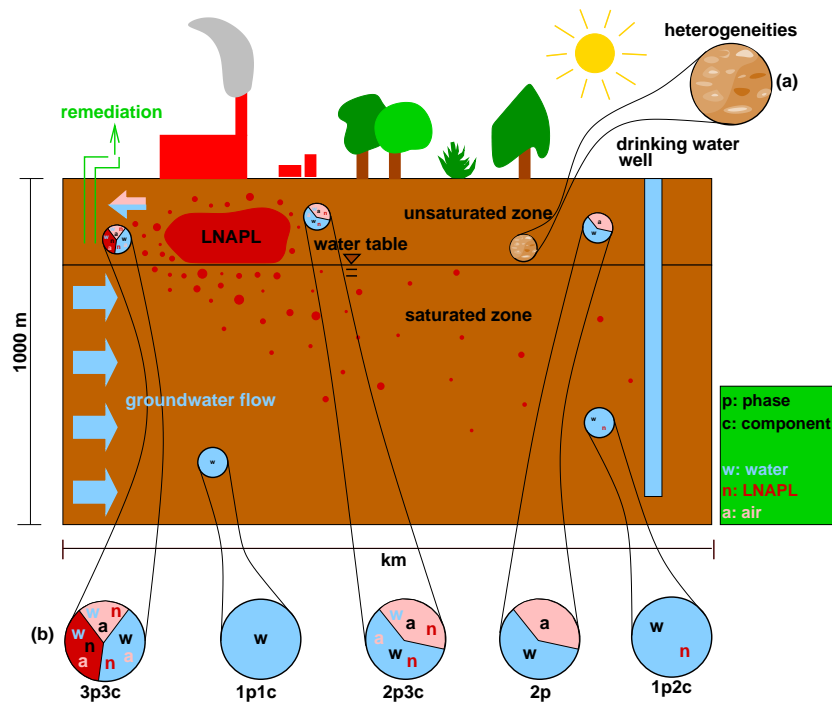


Figure 1.4: Processes in the hydrosystem subsurface.

phase (consisting mainly of LNAPL), and a non-wetting gaseous phase with the components water (w), air (a), and LNAPL (n). Further downstream of the contamination, a 2p3c or even a 2p model captures the physical processes accurately enough. In the saturated zone, i.e. below the groundwater table, a 1p1c model is sufficient for modeling flow upstream of the contamination, whereas a 1p2c model is required in the downstream region.

To investigate the multi-scale properties of both the porous medium and the occurring processes, they are studied separately. First, the heterogeneous soil structure where the fluid phases are neglected is focussed on (a), and second, the occurring processes are studied where in turn the heterogeneities of the porous medium are not accounted for (b).

- (a) First, the system given in Figure 1.5 is considered. When zooming in, the focus is only on the structural properties, i.e. the porous medium itself. One can see that in a first magnification step, further structural inhomogeneities become visible (see Figure 1.5, upper right picture) than those that could already be distinguished on the coarsest scale in the upper left picture. Zooming even further in, the single soil grains become visible. One can see that they have different shapes and sizes leading to heterogeneities on this scale. A last magnification finally shows, that not even a single grain is homogeneous but consists of different particles, i.e. crystals etc. While one could zoom in further, I

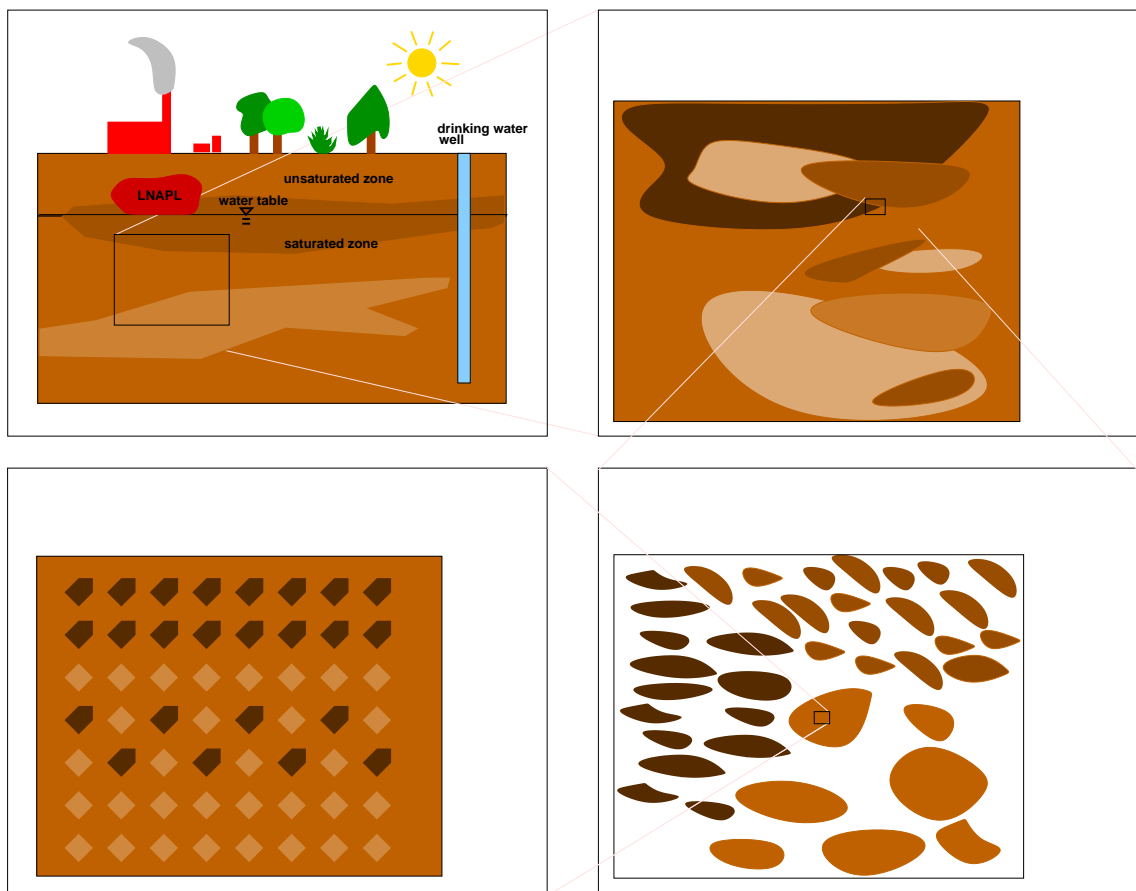


Figure 1.5: Heterogeneities on different scales without taking into account the fluid phases.

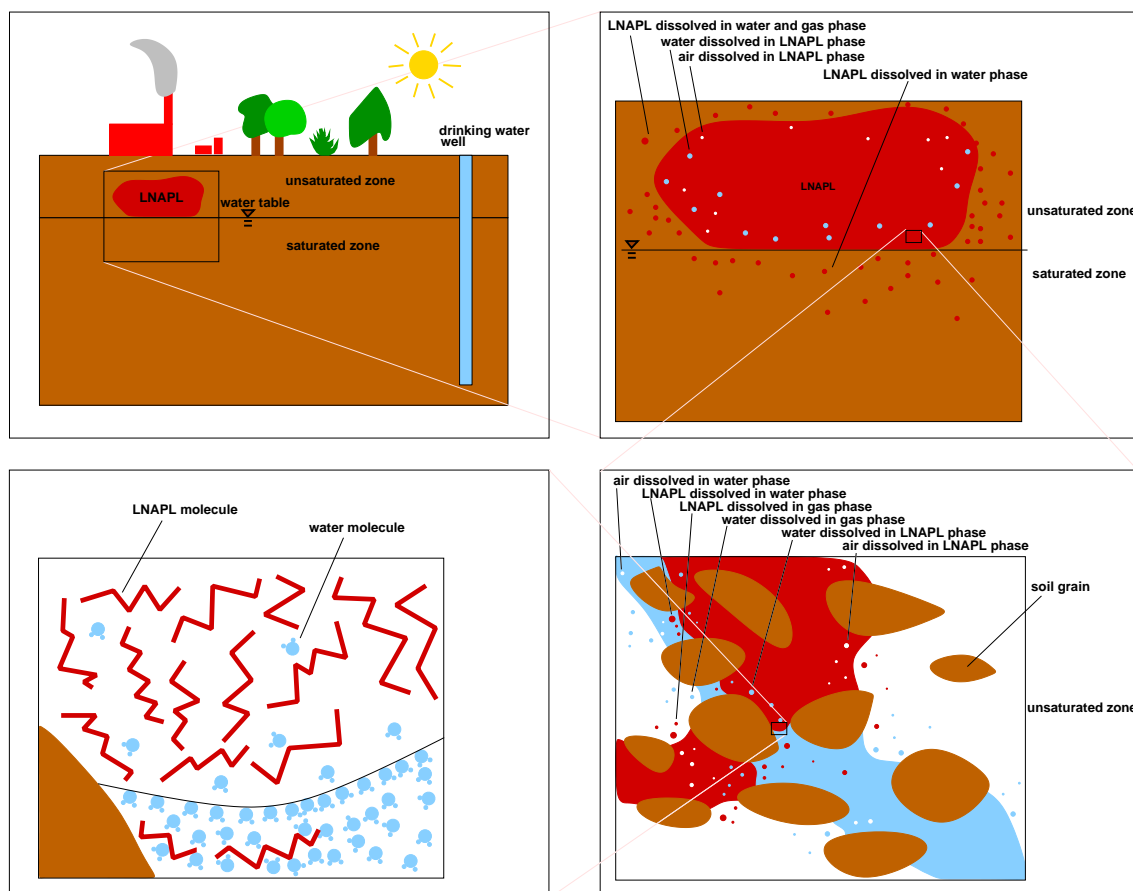


Figure 1.6: Different processes on different scales in a homogeneous medium.



will stop here and not consider finer scales than the scale where single particles (crystals, molecules, . . .) can be detected.

- (b) Second, the occurring mass transfer processes are considered in a homogeneous medium, i.e. in a system where the heterogeneities of the porous medium are neglected. When considering the situation given in Figure 1.4 from “far away”, i.e. on a coarse scale, one can only see that there is an LNAPL contamination in the unsaturated zone (left upper picture of Figure 1.6). One cannot detect any dissolution processes taking place. To detect them, one has to zoom in a smaller region around the contaminated zone (switch to a finer scale, see upper right picture of Figure 1.6). When zooming even further in, one can detect, that in fact the soil consists of single grains and that there exist interfaces between the fluid phases water, LNAPL, and gas. Mass transfer, i.e. exchange of components between the phases takes place across these interfaces and is thus highly dependent on interfacial areas (lower right picture). The last picture in the lower left corner shows a last magnification step where one can see that the phase interface is in fact formed by the specific orientation of the molecules (here the polar water molecules) at this interface.

In theory, the constitution of the molecules and their chemical and physical properties on the finest of the considered scales determines the behavior on all coarser scales. In general, all information about a scale is contained in the information given on the finer scales.

In the frame of this work, the complex setup of Figure 1.4 with a variety of spatially dependent multi-phase–multi-component systems is simplified in two steps. In both cases, only a cut-out of the system of Figure 1.4 is considered, the unsaturated zone. For the first setup, the most complex of the occurring processes are three-phase–three-component processes (occurring in and around the LNAPL contaminated zone); for the second setup, two-phase–two-component processes are the most complex occurring processes. Figure 1.7 depicts the first setup, where on the one hand, small-scale heterogeneities occur in the whole domain. On the other hand, complex 3p3c processes occur in a small part of the model domain, in and around a zone where a high amount of LNAPL is present. Further away from this zone, mass transfer processes become negligibly small and a 2p model is adequate.

Next, the even more simplified second setup of Figure 1.8 is studied. This setup does not have any connection to the real-life system of Figure 1.4 any more, but represents a tool to study the principle issues of the three-phase–three-component setup of Figure 1.7 for the easier case of local two-phase–two-component processes. As for the problem introduced in Figure 1.7, on the one hand, small-scale heterogeneities occur in the whole domain. On the other hand, complex 2p2c processes occur in a small part of the model domain, in and around a zone where a high amount of gas is

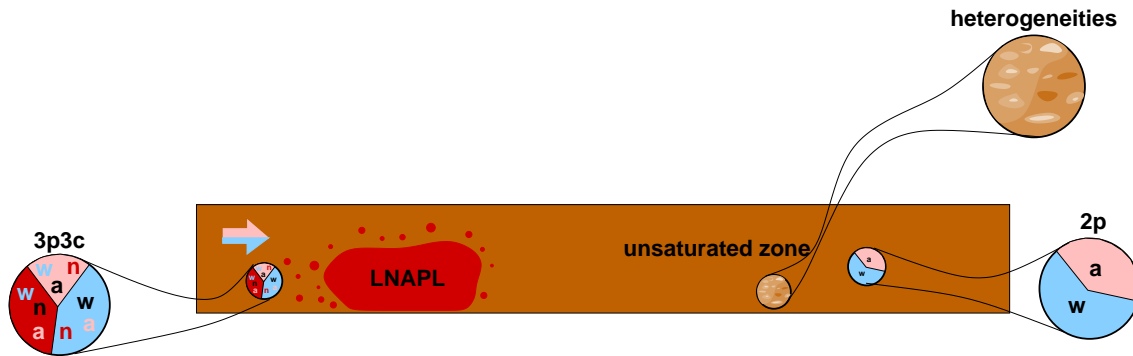


Figure 1.7: Three-phase–three-component setup considered in this work.

present. As for the first setup, further away from this zone, mass transfer processes become negligibly small and a 2p model is adequate. To accurately capture the influence of both heterogeneities and mass transfer processes, a fine-scale model is necessary, while for the physically simpler two-phase processes, a coarser resolution can already give reasonable results.

To investigate multi-scale issues, one can either perform laboratory experiments or use numerical modeling. In this work, the second alternative is pursued, i.e. the numerical approach to the multi-phase–multi-component problems under study.

When numerically modeling processes on different scales in porous media, one has in principal three possibilities:

1. The most accurate solution is a very well-resolved fine-scale solution. Sometimes, however, the physical laws describing the fine-scale processes are not known in detail. Furthermore, fine-scale modeling requires a large amount of data and takes long computing times.
2. To reduce the amount of data to be collected and to speed up the computation, upscaling approaches have been developed for a variety of flow and trans-

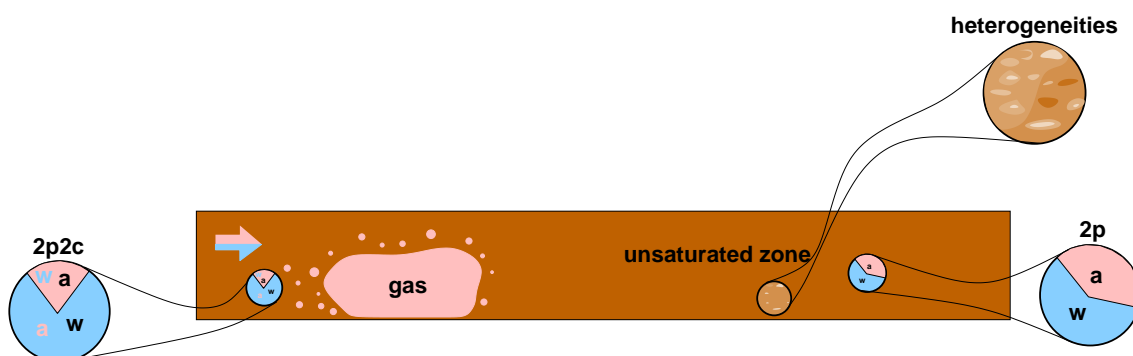


Figure 1.8: Two-phase–two-component setup considered in this work.

port equations. Upscaled models represent a mathematically justified description of fine-scale processes on a larger scale. Nevertheless, depending on the fine-scale equations and the considered scales, such an upscaled model cannot always be designed.

3. A further possibility to deal with multi-scale problems are multi-scale approaches which model different processes on different scales depending on their impact on each scale.

The aim of this work is to develop a framework for dealing with problems of different complexity at different locations and on different scales. This framework combines the advantages of all three approaches.

So far, the issue of structural heterogeneity and the issue of scales have been identified as two of the aspects with the highest impact on flow and transport in porous media. The quantity which has a decisive influence on both heterogeneities and on multi-phase–multi-component processes and which is extremely scale-dependent, is the “interface”. For heterogeneities, the relevant interfaces are defined by the interfaces between different materials (different block heterogeneities), whereas for multi-phase–multi-component processes, the interface between two different fluids is the governing parameter.

First, the issue of material interfaces is studied considering a heterogeneous soil. Figure 1.9 shows a photo of a laboratory experiment carried out at the VEGAS facility at the Universität Stuttgart. The color red represents a DNAPL (dense non-aqueous phase liquid), i.e. a liquid that is not miscible with water, which is infiltrated in a water-saturated soil sample of coarse sand. Within the coarse sand, there is a lense of fine sand. As can be seen, the DNAPL flows around the large block heterogeneity of fine sand and cannot enter. Looking at the coarse sand to the left of the fine sand lense, one can see that the DNAPL continues to spread laterally within the coarse sand instead of flowing downwards in the direction of gravity. The lateral spreading is due to heterogeneities within the coarse sand, i.e. small-scale heterogeneities called intrinsic heterogeneities.

Between two immiscible fluids, such as water and DNAPL in Figure 1.9, one can distinguish a sharp phase interface. The interfacial area between these two fluids, which is only visible on such a small scale where single soil grains can be detected, is *the* decisive parameter for physical processes such as dissolution, evaporation—in general, all kinds of mass transfer between fluid phases. Figure 1.10 shows two fluids (red and transparent) at a temperature of 20°C (left hand side) and at 70°C (right hand side), see Hiester et al. [2003]. One can see that the amount of red fluids decreases with increasing temperature as it is dissolved in the transparent fluid. For reasons of data collection and computer power, it is impossible to numerically model large domains with such complex processes occurring on a very small scale.

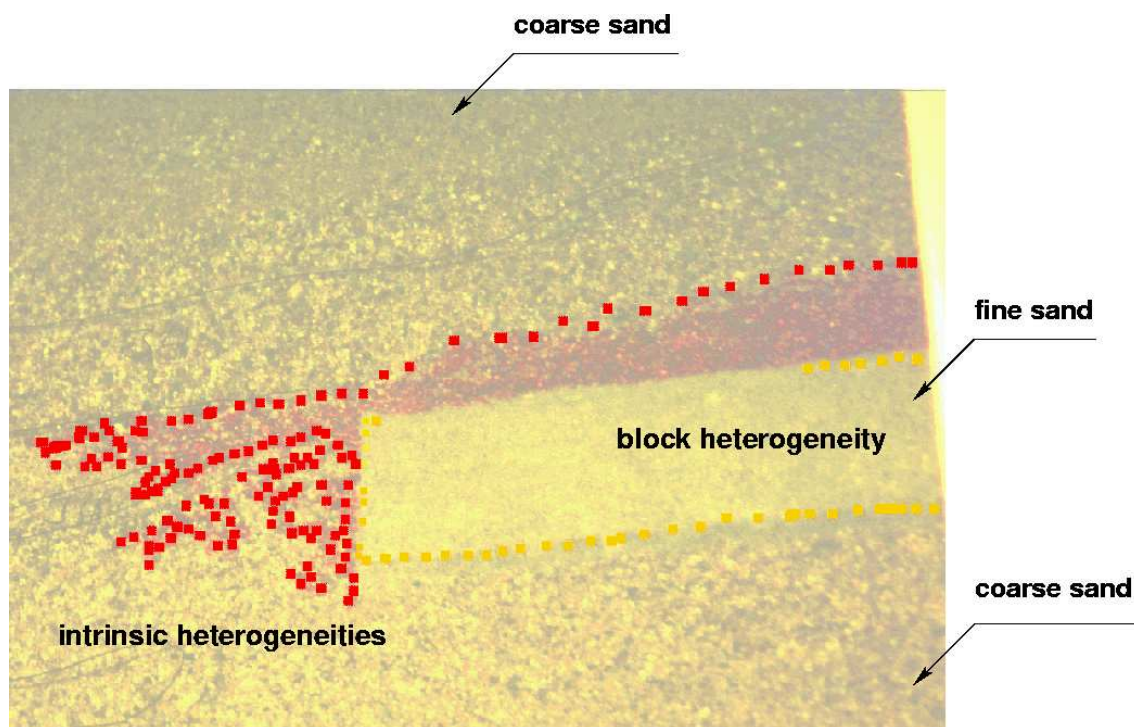


Figure 1.9: Block and intrinsic heterogeneities (photo taken from an experiment carried out at the VEGAS research facility, Universität Stuttgart).

However, as it is necessary to account for these processes, the aim of this work is to develop a multi-scale-upscaling framework adequate for tackling these issues.

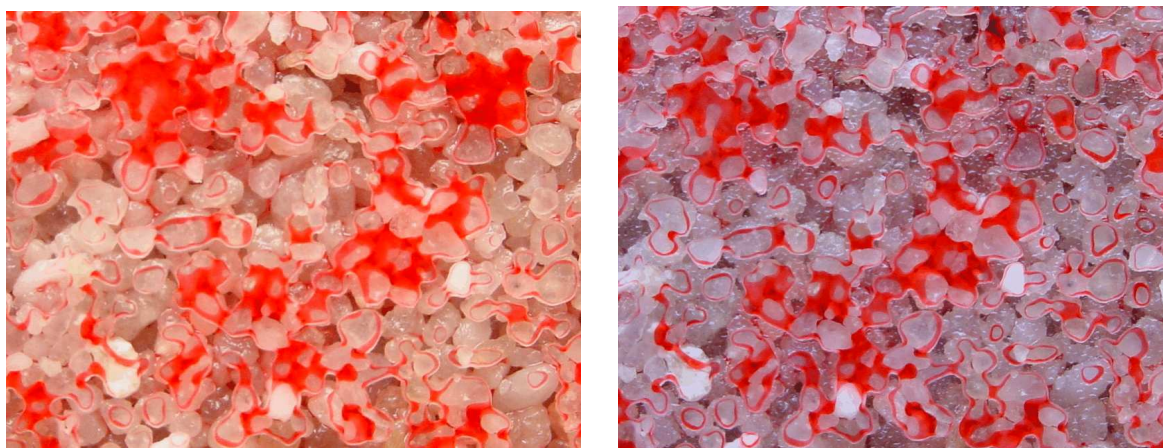


Figure 1.10: Interface between wetting and non-wetting phase at 20°C (left hand side) and 70°C (right hand side) (taken from Hiester et al. [2003]).

## 1.2 Literature Overview

This work deals with the modeling of multi-phase–multi-component processes in heterogeneous porous media on multiple scales. Therefore, existing literature on the basics of multi-phase and multi-phase–multi-component modeling will first be introduced. Second, the issue of scales will be addressed by presenting literature on multi-scale techniques. Furthermore, strategies of dealing with different physical processes in one model domain, also called multi-physics strategies, are dealt with. Next, upscaling techniques will be presented as a possibility to handle heterogeneities on different scales and finally, literature on the numerical simulators used in this work will be focussed on.

### **Multi-phase and multi-phase–multi-component modeling.**

Numerical simulation of multi-phase flow came up in the field of petroleum engineering in the 1960s. First simulators were developed by Aziz and Settari [1979] and Peaceman [1977]. Later, in the 1980s, multi-phase simulation was also applied to environmental problems, like the pollution of the subsurface and the simulation of adequate remediation strategies. First approaches including mass transfer between fluid phases, i.e. multi-phase–multi-component models, have been derived by Falta et al. [1992a,b], and Forsyth [1993]. The theory and modeling of multi-phase and also of multi-phase–multi-component flow and transport in porous media is widely discussed in literature, a broad overview is given by Helmig [1997]. This work is an extension of Helmig [1993] where first approaches for the modeling of multi-phase flow, also in fractured porous media, have been discussed. Detailed investigation of two-phase–two-component flow and transport has been done by Emmert [1996], whereas Class [2001] has studied a three-phase–three-component model for nonisothermal processes. A good overview of problems arising for multi-phase–multi-component modeling in heterogeneous porous media can be found in Miller et al. [1998]. The work of Huber [1999] revisits the issue of different formulations of the governing equations describing both multi-phase and multi-phase–multi-component processes.

### **Multi-scale modeling and multi-physics strategies.**

Multi-scale modeling has been applied to many different applications, not only in the frame of flow and transport modeling in porous media. E et al. [2003] as well as E and Engquist [2003] give a general motivation and a broad overview of multi-scale modeling for a variety of research fields.

When modeling phenomena of flow and transport on different scales, it is possible to directly include the knowledge about the scales in the numerical scheme (multi-scale finite element method given in Hou and Wu [1997], and in Chen and Hou [2002] or multi-scale finite volume method, see Jenny et al. [2003]).

Multi-physics strategies refer to models where different physical processes are

solved in one model domain. One can distinguish horizontal coupling where different model concepts are solved on the same scale in different subdomains and vertical coupling where only one model concept is applied, but on different scales.

**Vertical** coupling has been widely used in atmospheric and ocean modeling, where usually a fine-scale model is nested into a coarse-scale model. Here, the boundary conditions for the fine-scale model represent the crucial issue. Koch [1987], e.g. gives an overview of these nested techniques for weather-forecasting models. In these models, the coarse-scale problem influences the fine-scale problem, but generally, there is no transfer of information from the fine-scale model to the coarse-scale model.

**Horizontal** coupling has been developed for multi-phase issues by Wheeler et al. [1999] and Yotov [2002], who subdivided their system into a number of non-overlapping subdomains according to the relevance of physical processes. However, the issue of coupling these different models in a physically and mathematically correct way still represents a crucial issue.

#### **Upscaling flow and transport in heterogeneous porous media.**

To upscale the governing flow and transport equations in heterogeneous media, various approaches have been taken. They are distinct with respect to the upscaling technique itself, with respect to the underlying assumptions and with respect to the equation or model problem they are applied to. Durlofsky [1998] gives an overview of different upscaling techniques, like the use of pseudo relative permeabilities, nonuniform coarsening and the use of higher moments of the fine-scale variables in the frame of the volume-averaged saturation equation. A review of upscaling techniques for the pressure equation is given by Farmer [2002], and an ample overview of calculating equivalent permeability has been asserted by Renard and de Marsily [1997] as well as by Wen and Gómez-Hernández [1996].

Pruess [1996], for example, studied formations with randomly distributed long, thin obstacles and showed that these medium heterogeneities have a dispersive effect analogous to Fickian diffusion. The author demonstrated that the longitudinal dispersivity grows with time. Analytical solutions for macrodispersion in one-dimensional stratified media have been found by Didierjean et al. [2004]. Efendiev et al. [2000] derived a subgrid term for the one-phase transport equation applying the upscaling technique of volume averaging and Efendiev and Durlofsky [2002] extended it for the two-phase equation for water transport, the saturation equation. Both approaches explicitly take into account the length and time dependence of macrodispersion. Falta [2003] uses a dual-domain approach to study subgrid-scale DNAPL pool dissolution. The time-dependence of macrodispersion is only valid in a preasymptotic range, while for large times macrodispersion approaches an asymptotic value. Rubin et al. [1999, 2003] developed closed-form analytical results for the block-effective macrodispersion. Other approaches use a fully stochastic framework

for the solution of the coarse-scale saturation equation (Langlo and Espedal [1994]).

For certain setups, scale separation and periodicity of the heterogeneity pattern of the porous medium are reasonable assumptions. Then the equations can be up-scaled by the mathematically restrictive method of asymptotic expansions or homogenization. A short overview of the technique and its separation from other upscaling approaches is given in Auriault [2002].

Other authors, like Durlafsky [1991], also developed strategies for the upscaling of the water flow equation (the two-phase pressure equation) avoiding the global fine-grid solution of the pressure field by computing coarse-grid permeabilities from local fine-grid solutions over regions corresponding to coarse-grid blocks. Chen et al. [2003] extended this approach for a coupled local–global strategy which can handle even highly heterogeneous media.

### **Numerical modeling and simulator used in this work.**

The numerical model used in this thesis is based on the work of Bastian et al. [1997], and Bastian [1999, 2003]. The toolbox UG (unstructured grids) is a software toolbox capable of solving partial differential equations on general (unstructured) grids. The numerical discretization scheme used here is a Runge-Kutta discontinuous Galerkin scheme, described in Bastian [2003] for both the pressure and the saturation equation. Detailed studies on the use of a discontinuous Galerkin formulation for the pressure equation are performed in Reichenberger et al. [2004]. The discontinuous Galerkin scheme for flow is based on the method developed by Oden et al. [1998], the scheme for transport is basically founded on the work of Cockburn and Shu [1989], Cockburn et al. [1990], and Cockburn and Shu [1998]. In order to create reference solutions for other discretization schemes, e.g. for discontinuous Galerkin schemes, streamline simulation can be used under certain conditions, as they are in special cases basically free of numerical diffusion. Therefore, streamlines have to be traced and the streamline equations have to be solved along a streamline. Most tracing schemes are based on the method of Pollock [1988], more sophisticated schemes improving the mapping forth and back to the grid (Mallison et al. [2004]) or the accuracy of the tracing algorithm have been developed, e.g. by Matringe [2004]. Extensions for unstructured and curvilinear grids have been done by Cordes and Kinzelbach [1992], Prévost [2000], and Prévost [2003]. Juanes et al. [2004] and Juanes and Lie [2005] developed a front tracker to solve one-dimensional streamline equations along each streamline which is applicable also to three-phase flow.

In this work, a new multi-scale algorithm is developed which combines horizontal and vertical coupling by modeling complex multi-phase–multi-component processes in a local domain of interest on a fine scale and by including the effects of these fine-scale processes in a physically simpler two-phase model on a coarse scale. Fine-scale processes and coarse-scale processes influence each other mutually. The coarse-scale model comprises the upscaled form of the saturation equation derived

in Efendiev et al. [2000] and in Efendiev and Durlafsky [2002] which is converted from a finite volume discretization to the discontinuous Galerkin scheme described in Bastian [2003].

### 1.3 Goal and Structure

The aim of this work is to make one first step to model complex systems as the example of an LNAPL contamination in the unsaturated zone discussed in Section 1.1. The solution strategy developed here is designed to be general and transferable to other kinds of problems, where different processes occur at different locations in one model domain and on different scales.

The leading rationale is to save wherever and whatever is possible. To save wherever possible means that processes are only modeled in regions where they are actually relevant. To save whatever is possible means, that whatever is possible is modeled on a large scale and only the parts which are necessary on a fine scale. The processes for which there exist mathematically or physically motivated upscaling approaches are modeled on a large scale whereas those processes for which no upscaled model exists or which for some physical reason need fine resolution are modeled on a fine scale. Note, that the purpose of the developed algorithm is *not* to improve the physical model, but to reduce the required amount of data and to increase computational efficiency.

For the example of an LNAPL contamination in the unsaturated zone, it has been shown that one has to deal with fine-scale (intrinsic) heterogeneities everywhere in the domain of interest. Next, one could observe, that locally in certain regions, physically complex processes occur, e.g. dissolution processes. Thus, an efficient use of computational power is to apply a complex physical model accounting for dissolution only in a small domain where these processes are actually relevant and to use a simpler model in the rest of domain. Last but not least, the occurring processes are split into processes which can be accounted for on a large scale and into those which need fine resolution.

To develop and test a fundamental multi-scale framework capable of solving different kinds of problems on different scales and at different locations, it is not practical to blow up the physical and mathematical model and to include all kinds of occurring processes. Processes, which are of secondary importance or which would extremely complicate the algorithm are therefore neglected. In the frame of this work,

- only one- and two-dimensional problems are considered,



- it is assumed that the locally complex processes are either two-phase–two-component or three-phase–three-component processes,
- only two scales are considered,
- gravitational forces are neglected,
- capillary forces are neglected,
- local-scale diffusion is neglected,
- it is assumed that the considered system is isothermal,
- constant phase densities are assumed,
- constant phase viscosities are assumed,
- it is assumed that the soil matrix does not change, and
- external sinks and sources are not considered.

These assumptions are thoroughly discussed and justified when introducing the multi-scale solution strategy in Section 5.1. When tackling the basic physical and mathematical issues of multi-phase and of multi-phase–multi-component modeling, however, a general and comprehensive overview of all possibly occurring processes is given. Only where a general treatment of the physics or mathematics would extremely blow up the analysis, the above simplifications are applied.

The thesis is structured as follows.

In **Chapter 2**, the physical background necessary for the description of multi-phase–multi-component flow and transport on multiple scales is given. After a definition of spatial scales and the processes on these scales, the basic definitions are presented and then, parameters defining the fluids, parameters defining the solid matrix, and parameters accounting for fluid–matrix interaction are discussed. In the end, it is differentiated between diffusion and dispersion which are important processes dealt with in this work. Also, some basic physical laws for mass transfer between fluid phases are revisited.

The mathematical description of multi-phase and of multi-phase–multi-component processes is described in **Chapter 3**. Moreover, the choice of the formulation of the governing equations is discussed and flash calculations are explained. For the chosen formulation of the balance equations, flash calculations are required when mass transfer between fluid phases takes place.

The discretization of the model equations in space and time is introduced in **Chapter 4**. Therefore, discontinuous Galerkin Runge-Kutta methods as well as streamline methods are described.

**Chapter 5** contains the heart of this work, i.e. the multi-scale approach for multi-phase–multi-component modeling in heterogeneous porous media. Here, the algorithm is explained in detail for local two-phase–two-component processes as well as for local three-phase–three-component processes.

**In Chapter 6**, thorough numerical investigations are performed studying both the accuracy and the computing time of simulations using the new algorithm. Results for several test cases are presented and discussed.

**Chapter 7** summarizes the results obtained in this work. It is discussed which future research fields result from the investigations.

## 2 Physical Background

### 2.1 Scales and Processes

In this section, the definition of scales used in this work is given, being conscious of the fact, that a variety of different definitions is in use. It is pointed out which scales are considered in this work and an overview of the physical processes occurring on these scales is given. To define the scales and processes, some parameters have to be used which are then discussed in detail in the following sections of this chapter.

In theory, all physical processes and properties could be derived from the properties of single molecules and their interactions on a very small scale, the **molecular scale**, see Figure 2.11. Fluid properties, such as boiling point, density, viscosity, interfacial tensions can be explained by the structure, steric order and dipolar moments of these molecules. However, as one would have to deal with a very large number of molecules (1 g of water contains  $3.3 \cdot 10^{22}$  molecules of  $H_2O$ ), it is not possible to make computations on scales of practical interest for engineering purposes. For this reason, it is averaged over a large number of molecules which is equivalent to assuming matter to be continuous. Single molecules can then no longer be detected, but one can describe substances by new physical parameters representing a large number of molecules, like density (see Section 2.3.1), viscosity (Section 2.3.2), boiling point etc. This continuity assumption leads to the **micro scale**. This is the largest scale, where a clear separation of phases can be detected, i.e. one can observe interfaces between the fluid phases as well as fluid–solid interfaces. Therefore, phase-interface oriented processes, such as mass transfer between fluid phases, reaction, or capillarity should optimally be considered on this scale, otherwise phase interfaces and their interfacial areas will not be correctly resolved. In fluid mechanics, the Navier-Stokes equation is the appropriate description of micro-scale processes.

A further averaging procedure, the averaging of micro-scale properties over a **representative elementary volume** (REV) does not only give new effective parameters, such as porosity (see Section 2.4.1) and saturation (see Section 2.5.1) as well as so-called constitutive relationships (Sections 2.5.2 and 2.5.3) needed to bridge the gap from the micro scale to the **local scale**, but also entirely new equations. Considering one of these parameters, e.g. porosity  $\phi$ , it becomes obvious, that if a small averaging volume is chosen it might well lie either totally within solid rock or totally within the

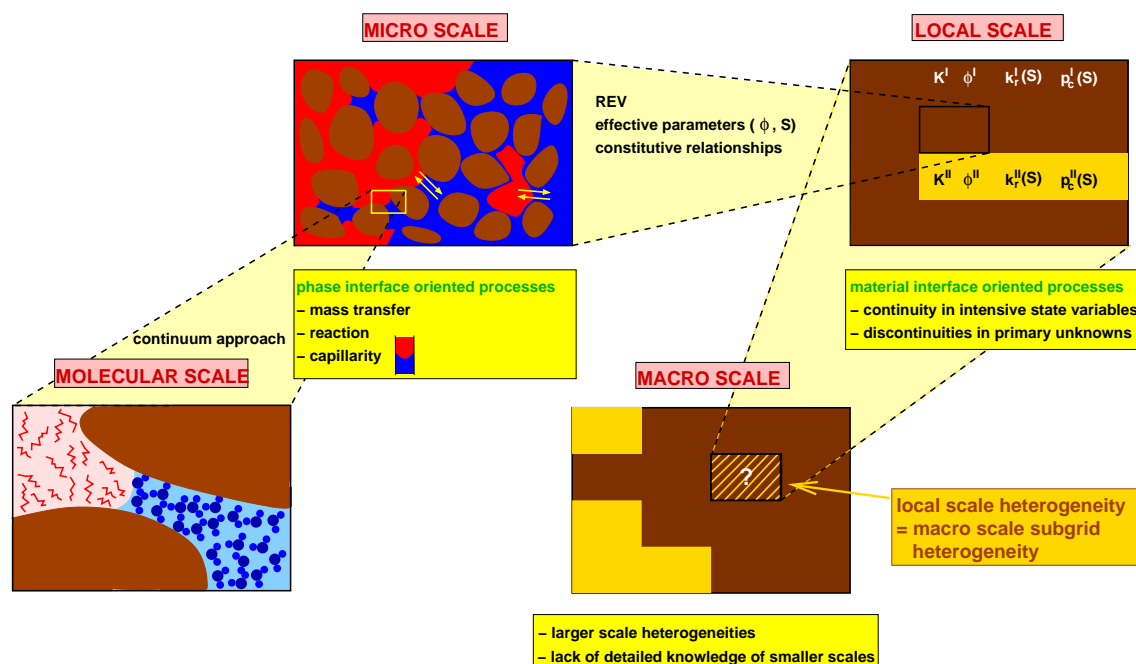


Figure 2.11: Definition of scales.

pore space, i.e.  $\phi = 0$  or  $\phi = 1$ , see Figure 2.12 left hand side. Enlarging this volume, one will encounter porosity oscillations starting from extreme values and stabilizing at a more or less constant value, until larger scale heterogeneities are included in the averaging volume. The REV is the minimum volume for which the averaging parameters remain constant for the first time when further enlarging this volume, see Figure 2.12, right hand side. The inclusion of larger scale heterogeneities leads to derivations from this constant value.

Due to the averaging process over the REV, discontinuities and interfaces between the fluid phases disappear, but one now has to deal with material discontinuities. These material discontinuities provide new challenges as they may lead to discontinuities in primary variables (saturation) when assuming continuity of intensive thermodynamical variables (capillary pressure). The Darcy law is the appropriate model for fluid mechanical problems on the local scale.

Often, one is interested in larger-scale simulations with high spatial extensions. Only applying the local-scale laws on this so-called **macro scale** underestimates interface-related processes, as the interfaces (phase interfaces as well as material interfaces, see Figure 2.11) cannot be resolved. Thus, it is a very important task to better account for interface dependent processes (both types) by better resolving these interfaces while solving the model problem on a coarse scale. On the macro scale, the same effective parameters as on the local scale do occur, but new terms in the equations are needed to account for the subgrid effects coming from the smaller

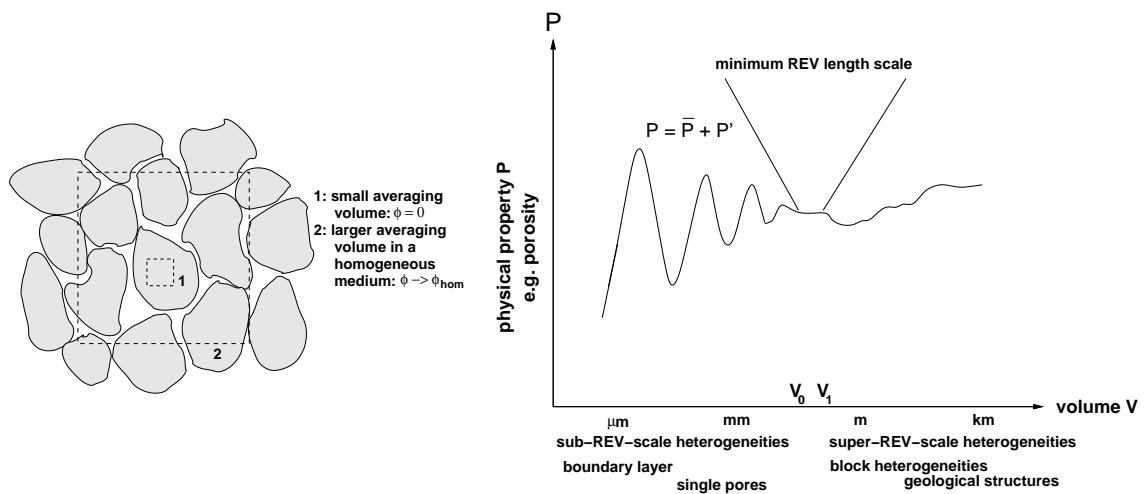


Figure 2.12: Definition of the representative elementary volume (picture on the right hand side after Bear [1972]).

scales.

For the multi-scale studies, the focus is put on this last pair of scales (local scale  $\rightarrow$  macro scale, see Figure 2.11). In the following, the term “fine scale” is used synonymously for the local scale, and the term “coarse scale” is applied to the macro scale. However, to get insight into certain physical processes, I might go back and consider the micro scale or even the molecular scale, where necessary.

Figure 2.13 sums up the principal issues of this work keeping in mind the motivation example of Figure 1.4. On the one hand, the influence of fine-scale heterogeneities of the soil matrix on the coarse scale processes has to be accounted for, see Figure 2.13

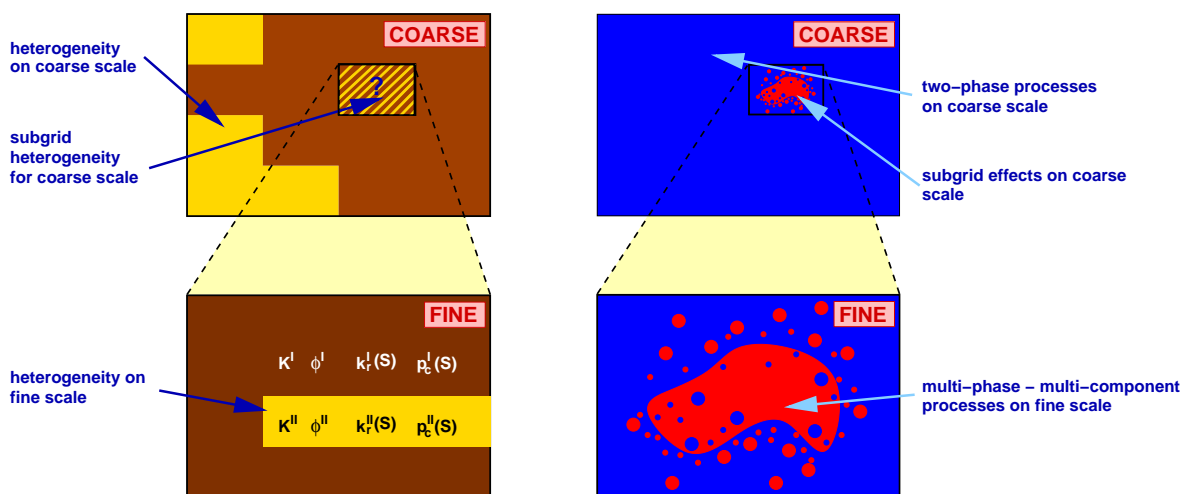


Figure 2.13: Heterogeneities and multi-phase–multi-component processes on fine and coarse scale.

(left hand side). On the other hand, complex multi-phase–multi-component processes occur in certain parts of the model domain on the fine scale (Figure 2.13, right hand side). Their influence on the saturation distribution on the coarse scale will be modeled.

Figure 2.14 shows the principle ideas more specifically. The influence of fine-scale heterogeneities is captured by a macrodispersion term on a coarse scale. The influence of the locally occurring mass transfer processes, by contrast, is captured by source / sink terms in the coarse-scale model. For a detailed description of the solution strategy, the reader is referred to Chapter 5.

Now, the main physical processes and effects are studied occurring on the two scales of interest. One can distinguish

1. **Dispersion due to local-scale and macro-scale heterogeneities (Figure 2.15).**  
Dispersion occurs due to a nonuniform velocity distribution in the porous medium. Heterogeneities on both local scale and macro scale cause nonuniformities of the velocity field, see Figure 2.15. The parameter accounting for this effect is absolute permeability  $\underline{K}$ , see Section 2.4.2. The local-scale heterogeneities lead to local-scale dispersion  $\underline{D}_{\text{local}}$ , while both local-scale and macro-scale heterogeneities lead to macro-scale dispersion  $\underline{D}_{\text{macro}}$ . Both local-scale and macro-scale dispersion depend on the local-scale flow velocity  $\underline{v}$ , and macro-scale dispersion additionally depends on the macro-scale velocity  $\underline{v}^{\text{coarse}}$ . This type of dispersion occurs in one-phase as well as in two-phase systems.
2. **Dispersion due to multi-phase flow behavior on the local and on the macro scale (Figure 2.16).**  
The presence of a second phase in a heterogeneous medium (Figure 2.16 compared to Figure 2.15) further increases the tortuosity of the porous medium and thus, further increases dispersion. This process takes place additionally to the dispersion due to the heterogeneous structure of the medium explained in 1. The described effect is represented by the relative permeability  $k_{r\alpha}$  introduced in Section 2.5.3. As for 1., the local-scale heterogeneities lead to local-scale dispersion  $\underline{D}_{\alpha\text{local}}$ , while both local-scale and macro-scale heterogeneities lead to macro-scale dispersion  $\underline{D}_{\alpha\text{macro}}$ . The local-scale dispersion, on the one

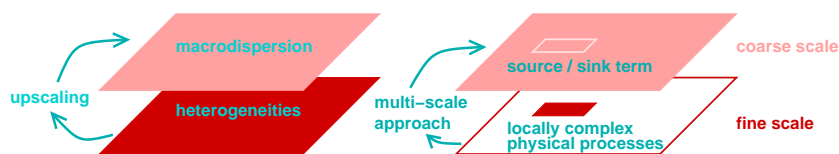


Figure 2.14: Treatment of heterogeneities (left hand side) and of locally complex processes (right hand side) in the frame of this work.

hand, depends on the fine-scale velocity field as well as on the fine-scale saturation distribution. The macro-scale dispersion, on the other hand, is dependent on the velocity and saturation distribution on both local scale and macro scale.

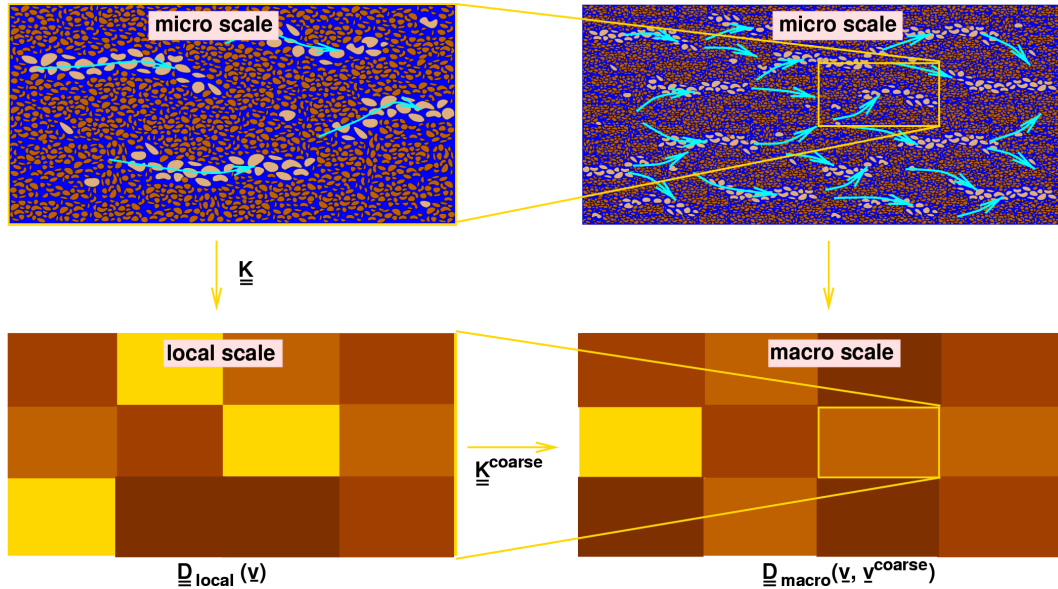


Figure 2.15: Dispersion due to local-scale (left hand side) and macro-scale (right hand side) heterogeneities<sup>1</sup>. The pictures in the upper row show the situation on the micro scale.

### 3. Effects of capillary diffusion on the local scale (Figure 2.17).

Capillary pressure has a diffusive effect which depends on saturation, see Figure 2.17. Capillary effects are further discussed in Section 2.5.2 while saturation is addressed in Section 2.5.1. Capillary diffusion vanishes where the two-phase system passes into a one-phase system, i.e. for  $S_w = 1$  as well as for  $S_w = 0$ , and it has a maximum in between.

### 4. The local-scale effects of mass transfer of components between the phases (Figure 2.18).

The mass transfer of components between fluid phases is an effect coming from the micro scale, as it is dependent on the interfacial area between two phases. As on the local scale the fluid interfaces are averaged out, empirical relations are needed. Examples are Henry's law or Raoult's law which are depicted in Figure 2.18 and which account for the local-scale effects of mass transfer between fluid phases. These local-scale laws for mass transfer are discussed in Section 2.7.

<sup>1</sup>upper-row pictures taken from the lecture notes "Model Concepts and Simulation Methods for Single and Multi-Phase Flow"

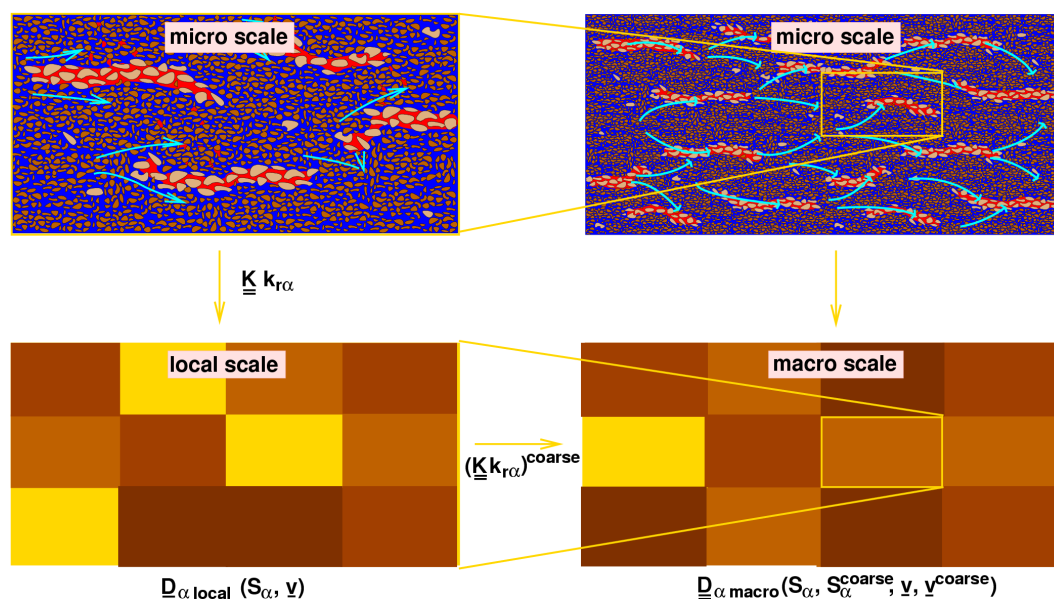


Figure 2.16: Dispersion due to two-phase processes as well as to local-scale (left hand side) and macro-scale (right hand side) heterogeneities<sup>1</sup>. The pictures in the upper row show the situation on the micro scale.

##### 5. The effects of block heterogeneities on the local scale (Figures 2.19 through 2.21).

The effects of block heterogeneities are shown in Figures 2.19 through 2.21 and can be characterized by the terms **pooling**, **trapping**, and **spreading**. They can only be understood having a deep insight into the physics of capillary pressure defined in Section 2.5.2. When a DNAPL reaches a fine sand lense embedded in coarse sand (Figure 2.19), the DNAPL cannot infiltrate, until the pressure needed to enter the fine sand is reached (entry pressure). This causes a **pooling** of the DNAPL on top of the fine sand lense. If, vice versa, a coarse sand lense is embedded in fine sand (Figure 2.20), the DNAPL can easily enter the coarse sand. However, the DNAPL cannot leave the coarse sand lense until the entry pressure of the fine sand is reached. If it is never reached, the DNAPL cannot re-enter the fine sand and stays **trapped** within the coarse sand lense. To understand the effect of **spreading**, the setup of a fine sand lense in ambient coarse sand is considered once again. If the entry pressure of the fine sand is not reached, the DNAPL is forced to flow laterally around the fine sand lense. Thus, the block heterogeneity causes a lateral spreading of the non-wetting phase (in this case DNAPL).



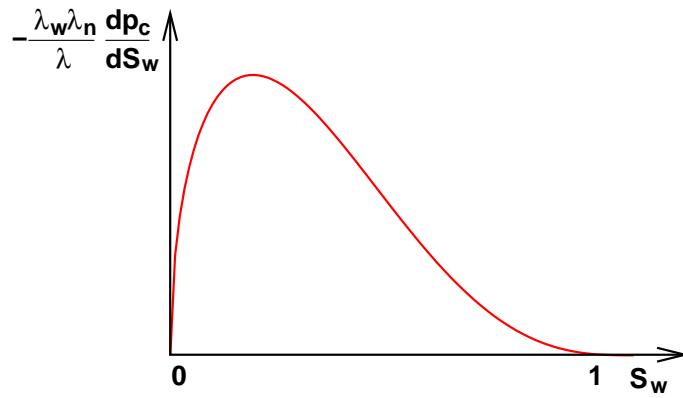


Figure 2.17: Capillary diffusion as a function of saturation on the local scale.

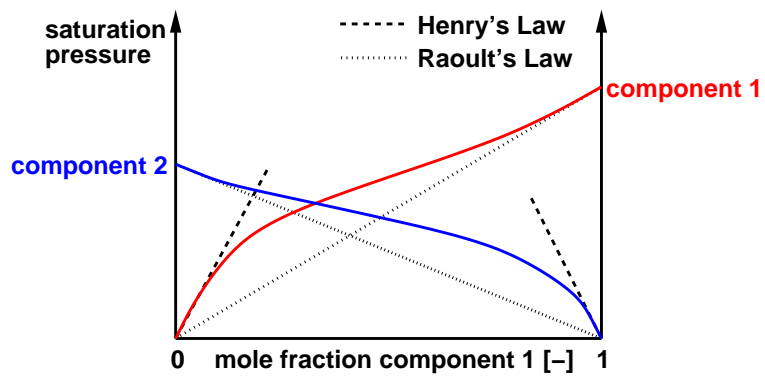


Figure 2.18: Local-scale effects of mass transfer of components between the phases.

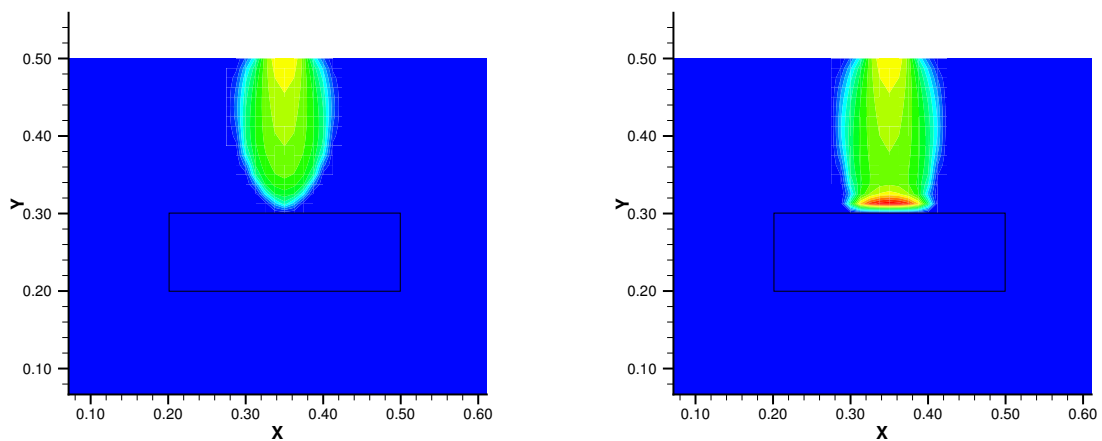


Figure 2.19: Effects of block heterogeneities—pooling.

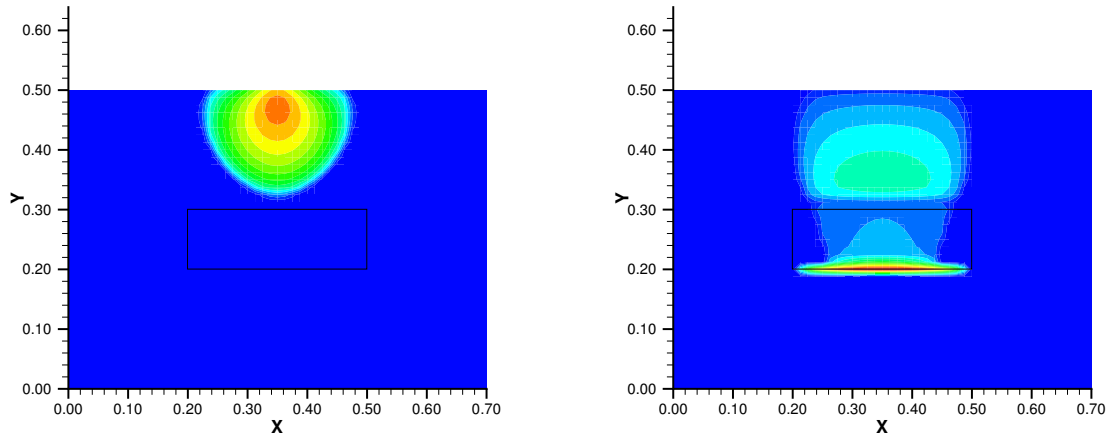


Figure 2.20: Effects of block heterogeneities—trapping.

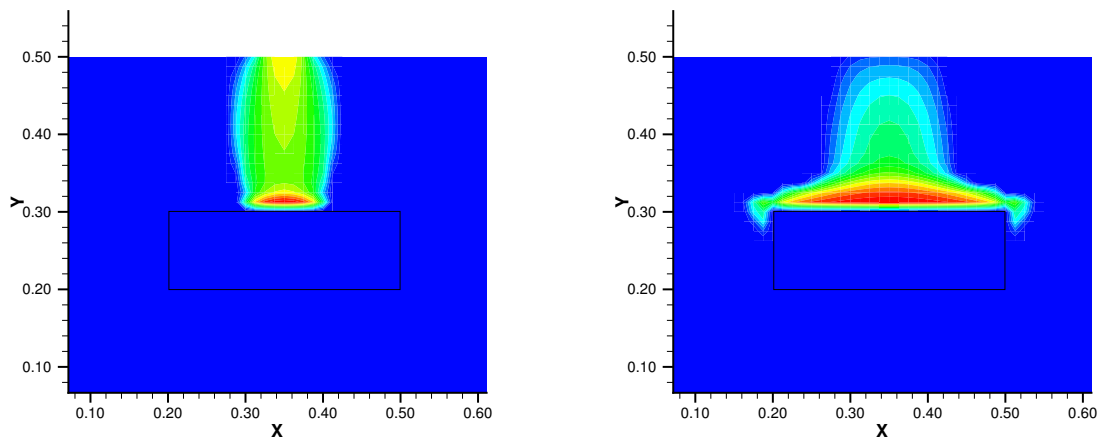


Figure 2.21: Effects of block heterogeneities—spreading.

## 2.2 Basic Definitions

In this section, the terms **phase** needed for multi-phase modeling and the term **component**, additionally needed for multi-phase–multi-component modeling, are defined.

### 2.2.1 Phase

In a micro-scale consideration, a fluid phase is a continuum of fluid which has a sharp interface to other such continua. Physical fluid properties are discontinuous across this interface. Two phases are by definition immiscible. In reality, however, two fluids are *always* soluble in each other in small amounts. If the solubility of the two fluids in one another is negligibly small (e.g. the solubility of water in oil and vice versa) and a sharp interface between the two fluids can be detected, they are considered as two separate phases.

To understand, why this sharp interface between two fluids is formed, one has to look at the molecular scale, see Figure 2.22 which depicts water as an example. Within the water phase (case A), a water molecule is surrounded by other water

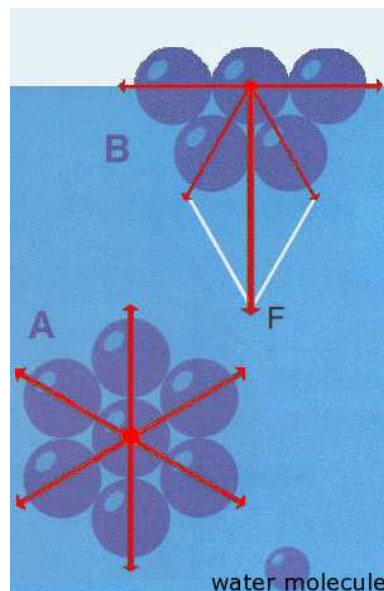


Figure 2.22: Interfacial tension between water phase and gas phase (Source: Fonds der Chemischen Industrie, Germany; image series “Tenside”).

molecules in all directions. The resulting force of the attracting forces is zero (red arrows). Considering the surface of the water, i.e. the interface between water and gas,

one can see that the situation is different. Further water molecules are only found in one hemisphere around a water molecule at the surface (case B), the other hemisphere is occupied by gas. Thus, the resulting force  $F$  caused by the dipolar moment of the water molecules points downwards into the water. The result is an interfacial tension  $\sigma$  between water and gas which in turn leads to a pressure difference across the phase interface called capillary pressure  $p_c$ .

Note, that gases are always easily miscible with one another and thus, only form one phase. That means, that while a system might consist of several liquid phases, there will always be one single gas phase.

Strictly speaking, the solid matrix also forms a phase, the solid phase. However, speaking of phases in this work, it is only referred to fluid phases, i.e. a “two-phase system” represents a system with two fluids which are not soluble in one another and a solid matrix. To denote systems with insoluble (negligibly soluble) phases, the term “multi-phase system” is used; if the phases are soluble in one another, the term “multi-phase–multi-component system” is applied.

## 2.2.2 Component

A phase usually consists of several components considering the fact that in reality phases are never absolutely insoluble. Components can either be pure chemical substances—elements or molecules, or consist of several substances which form a unit with constant physical properties, such as air. Thus, it depends on the model problem which substances or mixtures of substances are considered as a component. The choice of the components is essential, as balance equations for multi-phase–multi-component systems are in general formulated with respect to components.

## 2.3 Fluid Parameters

In this section, fluid density and viscosity are discussed as the parameters depending only on the properties of the fluid phases, but not on the solid matrix.

### 2.3.1 Density

The density  $\rho$  of a substance is the ratio of the mass  $m$  of that substance in a certain volume  $V$  over that volume:

$$\rho = \frac{m}{V}. \quad (2.1)$$

For a fluid phase  $\alpha$ , it is in general dependent on the phase pressure  $p_\alpha$  and temperature  $T$ , as well as on the composition  $x_\alpha^\kappa$  of the phase:

$$\rho_\alpha = \rho_\alpha(p_\alpha, T, x_\alpha^\kappa). \quad (2.2)$$

For more details on the parameter  $x_\alpha^\kappa$  accounting for the mole fraction of component  $\kappa$  in phase  $\alpha$ , the reader is referred to Section 2.5.4.

However, the compressibility of the **solid matrix** as well as its temperature-dependence can usually be neglected. Therefore, one can generally assign a constant density to solids.

For **water**, the pressure dependence of density is very low and the solubility of both NAPL and air is not significant. Therefore, it can be assumed that the density of the water phase is only dependent on temperature,

$$\rho_\alpha = \rho_\alpha(T). \quad (2.3)$$

For isothermal systems, the temperature is constant and thus, the density of the water phase is also constant.

The density of **gases** is highly dependent on temperature as well as on pressure. Assuming that the gas phase behaves like an ideal gas, its density is independent of the composition. For isothermal systems, only the pressure dependence of density has to be considered.

### 2.3.2 Viscosity

Viscosity is a measure for the resistance of a fluid to deformation under shear stress. For Newtonian fluids, the fluid shear stress  $\tau$  is proportional to the temporal angle deformation  $\gamma$ ,

$$\tau = \mu \frac{\partial \gamma}{\partial t}. \quad (2.4)$$

The proportionality factor  $\mu$  is called *dynamic viscosity*.

The viscosity of the **water** phase is primarily determined by its composition and by temperature. With increasing temperature, the viscosity of water decreases.

Contrarily, the **gas** viscosity increases with increasing temperature.

## 2.4 Matrix Parameters

Parameters describing the properties of the solid matrix only are porosity and absolute permeability. They will be focussed on in this section.

### 2.4.1 Porosity

For the determination of porosity, the definition of the REV (representative elementary volume) is needed which was introduced in Section 2.1. The porosity  $\phi$  is defined as the ratio of the volume of the pore space within an REV over the total volume of the REV. This implies the assumption that the fluids can flow through the whole pore space. In reality, however, the pore space is only partly available for flow due to dead end pores and adsorption processes. In the following, the term porosity will be used for the *effective* porosity, i.e. the volume fraction of the porous medium available for flow.

Actually, the pore space is also dependent on pressure and temperature, for swelling or shrinking soils like clay, it is additionally dependent on saturation.

### 2.4.2 Absolute Permeability

The absolute permeability  $\underline{\underline{K}}$  of a porous medium is in the general case a tensor,

$$\underline{\underline{K}} = \begin{pmatrix} K_{xx} & K_{xy} & K_{xz} \\ K_{yx} & K_{yy} & K_{yz} \\ K_{zx} & K_{zy} & K_{zz} \end{pmatrix}. \quad (2.5)$$

A layering of the porous medium which is usually encountered in natural soils, leads to **anisotropy** of the porous medium, implying that  $K_{xx} \neq K_{yy} \neq K_{zz}$ . This means, that the physical properties are different in the spatial directions. If the main flow direction is different from the principal directions of the tensor of absolute permeability, this leads to significant off-diagonal entries. However, these off-diagonal entries vanish, if the coordinate system is turned such that it coincides with the main flow direction.

A spatial dependence  $\underline{\underline{K}} = \underline{\underline{K}}(x)$ , leads to **inhomogeneity**, also called **heterogeneity** of the porous medium.

## 2.5 Parameters Describing Fluid–Matrix Interaction

Besides the parameters accounting for fluid properties or matrix properties alone, the transition from the micro scale to the local scale brings along quantities describing the fluid–matrix interaction, like capillary pressure and relative permeability.

### 2.5.1 Saturation

The saturation  $S_\alpha$  of a phase  $\alpha$  is defined as the ratio of phase  $\alpha$  within the REV over the total pore volume in the REV. Assuming that in an  $m$ -phase system the pore space is entirely occupied by the  $m$  fluids, it becomes obvious that the sum of the saturations in each REV has to be equal to 1:

$$\sum_{\alpha=1}^m S_\alpha = 1, \quad (2.6)$$

where  $m$  is the number of phases in the model.

The phase saturations are one of the decisive local-scale parameters which determine the magnitude of other quantities, like capillary pressure or relative permeability.

### 2.5.2 Capillary Pressure

To understand the physics of capillarity, one has to go back to the micro scale. In Section 2.2.1, an explanation was given how the molecular behavior at the interface between two fluids causes an interfacial tension  $\sigma$  and thus, leads to a pressure jump across the fluid–fluid interface which is called capillary pressure.

To study what happens with the fluid–fluid interface at the interface to a solid matrix, Figure 2.23 is considered. The fluid with a wetting angle  $\alpha < 90^\circ$  is called

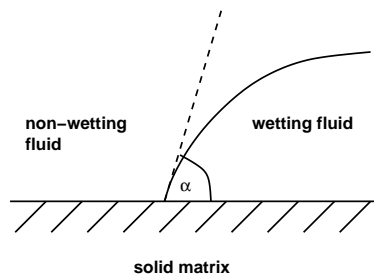


Figure 2.23: Wetting angle  $\alpha$  between a wetting and a non-wetting fluid.

**wetting fluid** with respect to the solid phase and is denoted by the subscript  $w$ , and the fluid with an obtuse wetting angle is called **non-wetting fluid** (subscript  $n$ ).

The capillary pressure  $p_c$  as the pressure difference across the fluid–fluid interface is calculated as the difference between non-wetting phase pressure  $p_n$  and wetting phase pressure  $p_w$ :

$$p_c = p_n - p_w. \quad (2.7)$$

Considering a capillary tube, this pressure jump results in a vaulted interface, see Figure 2.24. According to the Laplace equation, the capillary pressure can be calcu-

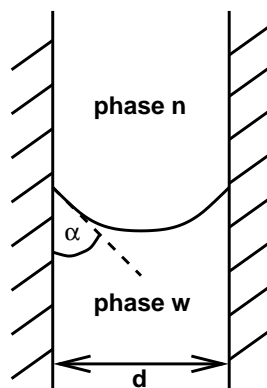


Figure 2.24: Two fluids in a capillary tube.

lated as

$$p_c = \frac{4\sigma \cos \alpha}{d}, \quad (2.8)$$

where  $d$  is the diameter of the capillary tube. Note, that capillary pressure is dependent on both solid phase ( $d, \alpha$ ) and fluid phases ( $\sigma, \alpha$ ). From the Laplace equation, it becomes obvious that the capillary pressure is higher in smaller pores and that they are occupied by the wetting fluid whereas the non-wetting fluid occupies the larger pores. Already from micro-scale considerations, one can see that each material is characterized by a certain pressure which has to be reached, before a non-wetting fluid can enter. This pressure is called the **entry pressure** and is exactly the pressure needed to enter the coarsest pore of the material with a maximum pore diameter  $d_{max}$ .

It has already been shown that for a local-scale description of capillary pressure, the entry pressure of the matrix has to be accounted for. Then, the case of a porous medium is considered which is fully saturated with a wetting fluid and where a non-wetting fluid infiltrates. As already found out, the non-wetting fluid occupies the larger pores. With increasing saturation of the non-wetting phase, the wetting phase has to retreat into smaller and smaller pores. This leads to an increase in capillary pressure as the pore diameter  $d$  of pores filled by the wetting phase decreases. Thus, it is intuitively clear that a relationship

$$p_c = p_c(S_w) \quad (2.9)$$

exists which is decreasing with increasing  $S_w$  and which has to have the property

$$p_c(1) = p_d, \quad (2.10)$$



where  $p_d$  is the entry pressure of the considered porous medium.

The exact relationship between saturation and capillary pressure can only be investigated experimentally. These experimentally found relationships can then be parameterized. Among the most famous relationships are the ones of Brooks and Corey [1964] and of Van Genuchten [1980]. Both approaches use the effective wetting-phase saturation  $S_e$  instead of the saturation  $S_w$

$$S_e = \frac{S_w - S_{wr}}{1 - S_{wr}}, \quad (2.11)$$

where  $S_{wr}$  is the residual wetting-phase saturation. This residual saturation  $S_{\alpha r}$  of phase  $\alpha$  is in general the transition between coherent and incoherent phase distribution. Below the residual saturation, the respective phase is immobile.

The Brooks-Corey capillary pressure–saturation relationship

$$p_c = p_d S_e^{-\frac{1}{\lambda}} \quad (2.12)$$

directly includes the entry pressure into the model equation. The parameter  $\lambda$  accounts for the nonuniformity of the pore size distribution. A high  $\lambda$  parameter means, that the pores all have similar pore size, a low  $\lambda$  means, that the pore size distribution is nonuniform and ranges from small pores to large pores.

The Van-Genuchten capillary pressure–saturation relationship

$$p_c = \frac{1}{\alpha} \left( S_e^{-\frac{1}{m}} - 1 \right)^{\frac{1}{n}} \quad (2.13)$$

has three fitting parameters  $m$ ,  $n$ , and  $\alpha$ , where usually  $m = 1 - \frac{1}{n}$ . The Brooks-Corey parameters can be converted to Van-Genuchten parameters and vice versa.

Figure 2.25 shows the basic difference between the two approaches. Whereas the Brooks-Corey model actually includes the entry pressure  $p_d$  in the model formulation which is a physical requirement founded on the Laplace equation on the micro scale, this is not the case for the Van Genuchten formulation. Close to a wetting-phase saturation of 1, the capillary pressure function is regularized in the Van Genuchten case and reaches a value of zero, see Figure 2.25 (Van Genuchten [1980]). It is not only numerically advantageous to avoid the discontinuity of capillary pressure at  $S_w = 1$ , but it makes also sense to have no capillary pressure for a fully saturated system, as the system then reduces to a one-phase system. In practice, the choice of the relationship depends on the problem. Often, both formulations can be applied.

For three-phase systems, different other relationships exist (see Parker and Lenhard [1987], Lenhard and Parker [1988], and Lenhard et al. [1988]) which are mostly based

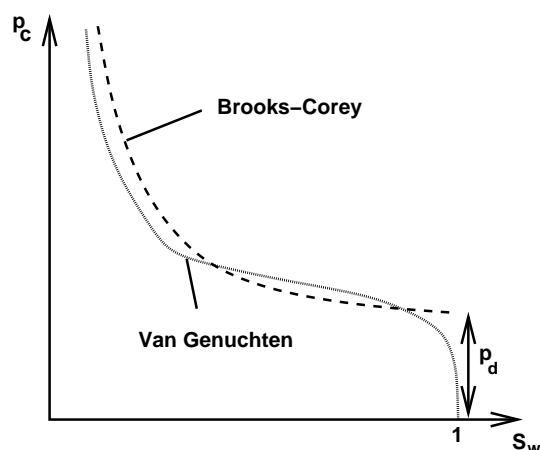


Figure 2.25: Capillary pressure–saturation relationship after Brooks-Corey and Van Genuchten.

on the two-phase relations given above. The underlying assumption is that the intermediate-wetting phase is spreading, meaning that the most and the least wetting phase are not in contact with one another.

The constitutive relationships discussed above represent a simplification of the real-life system. Actually, the capillary pressure–saturation relationship is non-unique and only valid under static conditions.

The non-uniqueness of the capillary pressure function is generally captured by the term “hysteresis” and results in different drainage and imbibition paths. For further details on hysteresis as well as possible parameterizations, the reader is referred to the work of Mualem [1976], Stauffer and Dracos [1984], Kool and Parker [1987], as well as Lenhard et al. [1993].

The capillary pressure–saturation relationships introduced here only apply to static conditions. When modeling transient flow, these models show various shortcomings which can be overcome by introducing a so-called “dynamic capillary pressure”, see e.g. Hassanizadeh and Gray [1990, 1993a], or Kalaydjian [1987], as well as Stauffer [1978] and Manthey et al. [2005].

### 2.5.3 Relative Permeability

To understand the physics of relative permeability, one has to go back to the micro scale. In Section 2.1, it was shown that material heterogeneities increase the length of the flow path of a particle through a porous medium, and in Section 2.4.2, absolute permeability has been introduced as the parameter describing material inhomogeneities. Considering a porous medium with two fluid phases present, it is

obvious that the presence of the second phase further increases the tortuosity of the flow paths. Thus, the presence of a second phase disturbs the flow of the other phase.

First, a fully wetting-phase-saturated medium is considered—all the flow paths are available for flow of the wetting-phase. A small amount of non-wetting phase will force the wetting phase to flow around the parts of the porous medium which are occupied by non-wetting phase. A large amount of non-wetting phase will force the wetting-phase particles to take large “deviations” and significantly disturb their flow. These effects are captured by the relative permeability  $k_{r\alpha}$  of each phase  $\alpha$ .

With these considerations, the local-scale behavior of relative permeability is obvious. Increasing saturation of the wetting phase will lead to increased wetting-phase relative permeability. The same is valid for the non-wetting phase. Thus, the relative permeability–saturation function for the wetting phase in a two-phase system,

$$k_{rw} = k_{rw}(S_w) \quad (2.14)$$

is increasing in  $[0, \dots, 1]$ , whereas the respective function for the non-wetting phase

$$k_{rn} = k_{rn}(S_w) \quad (2.15)$$

is decreasing in that interval.

The exact relationships again have to be found experimentally and again, famous functions can be found in Brooks and Corey [1964] and Van Genuchten [1980]. The Brooks-Corey approach is given by

$$k_{rw} = S_e^{\frac{2+3\lambda}{\lambda}} \quad (2.16)$$

$$k_{rn} = (1 - S_e)^2 \left(1 - S_e^{\frac{2+\lambda}{\lambda}}\right), \quad (2.17)$$

where  $\lambda$  is the same parameter as the  $\lambda$  defined for the Brooks-Corey capillary pressure–saturation relationship given in Section 2.5.2. The Van Genuchten model can be formulated as

$$k_{rw} = S_e^\epsilon \left[1 - \left(1 - S_e^{\frac{1}{m}}\right)^{m\gamma}\right]^2 \quad (2.18)$$

$$k_{rn} = (1 - S_e)^\gamma \left[1 - S_e^{\frac{1}{m}}\right]^{2m}, \quad (2.19)$$

where usually  $\epsilon = \frac{1}{2}$  and  $\gamma = \frac{1}{3}$ , and  $m$  is the well-known parameter introduced in Section 2.5.2. As can be seen from Figure 2.26, there is no significant difference between the two approaches—contrary to the capillary pressure–saturation relationships.

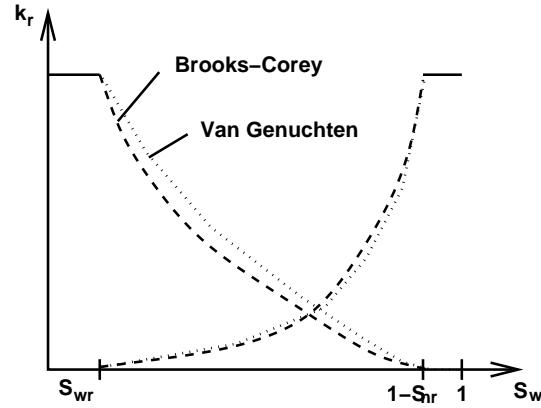


Figure 2.26: Relative permeability—saturation relationship after Brooks-Corey and Van Genuchten.

As for capillary pressure, the most commonly used models for relative permeability–saturation relationships of three-phase systems are derived from the relationships for two-phase systems. Amongst others, the two most commonly used models are the ones of Stone [1970, 1973], as well as the one of Parker et al. [1987].

In this work, the model of Parker et al. [1987] is used to calculate the relative permeability of the intermediate-wetting phase, i.e. the NAPL relative permeability  $k_{rn}$  for a water–NAPL–gas system,

$$k_{rn} = \left[ \frac{S_n}{1 - S_{wr}} \right]^{\frac{1}{2}} \left[ \left( 1 - S_e^{\frac{n}{n-1}} \right)^{\frac{n-1}{n}} - \left( 1 - \bar{S}_t^{\frac{n}{n-1}} \right)^{\frac{n-1}{n}} \right]^2, \quad (2.20)$$

with

$$\bar{S}_t = \frac{S_n + S_w - S_{wr}}{1 - S_{wr}}, \quad (2.21)$$

where  $n$  is the Van Genuchten parameter as introduced in Section 2.5.2.

## 2.5.4 Mass and Mole Fraction, Concentrations

Modeling multi-phase–multi-component processes, the knowledge about the phase saturations alone is not sufficient—it is only an information about the volume fraction of a fluid within an REV. As mass transfer processes between fluid phases take place, parameters accounting for the phase composition, that is the amount of fluid components contained in the fluid phases, are needed.

One possibility is, to give the dimensionless **mass fraction**  $X_\alpha^\kappa$  of a component  $\kappa$  in phase  $\alpha$ . It is defined as the mass of component  $\kappa$  in phase  $\alpha$  over the total mass of

phase  $\alpha$ ,  $X_\alpha^\kappa = \frac{m_\alpha^\kappa}{\sum_\kappa m_\alpha^\kappa}$ . Thus, it is clear that

$$\sum_\kappa X_\alpha^\kappa = 1, \quad (2.22)$$

i.e. the sum of the mass fractions of all components in a phase has to be equal to 1.

Analogously to the definition of mass fractions, it is also possible to define **mole fractions**  $x_\alpha^\kappa$  of a component  $\kappa$  in phase  $\alpha$ . They describe the number of moles of component  $\kappa$  in phase  $\alpha$ ,  $n_\alpha^\kappa$ , over the total number of moles  $n_\alpha$  of phase  $\alpha$ ,

$$x_\alpha^\kappa = \frac{n_\alpha^\kappa}{n_\alpha} = \frac{n_\alpha^\kappa}{\sum_\kappa n_\alpha^\kappa}. \quad (2.23)$$

Like the mass fractions, the mole fractions also sum up to 1,  $\sum_\kappa x_\alpha^\kappa = 1$ .

Next, it is also possible to use the **concentrations**  $C_\alpha^\kappa$ ,

$$C_\alpha^\kappa = \rho_\alpha \cdot X_\alpha^\kappa, \quad (2.24)$$

to quantify the amount of component  $\kappa$  in phase  $\alpha$ . Unlike mass fractions and mole fractions, these concentrations are not dimensionless, but have the unit  $[kg/m^3]$ .

The **total concentration**  $C^\kappa$  finally is the sum of the saturation-weighted single-phase concentrations  $C_\alpha^\kappa$  multiplied by the porosity  $\phi$  of the porous medium:

$$C^\kappa = \phi \cdot \sum_\alpha (\rho_\alpha S_\alpha X_\alpha^\kappa). \quad (2.25)$$

## 2.6 Diffusion and Dispersion

Considering the injection of a small amount of a tracer into a porous medium, one can generally distinguish four effects, see Figure 2.27 where flow is from left to right. First, the tracer is transported with the underlying flow field without change of the form of the plume (**advection**), see Figure 2.27, picture 1. Second, the peak is getting smaller and wider while the mass A of the tracer is conserved (**diffusion and dispersion**) as can be seen in picture 2 of Figure 2.27. Third, the tracer is retarded which is due to **sorption** processes (picture 3), and four, the mass of the tracer decreases from A to B (**reaction / biodegradation**), see picture 4.

In this work, only advection, diffusion and dispersion are considered. While the effect of diffusion and dispersion is the same and can be mathematically described in a similar way, the difference between the two phenomena lies in their dependence on the velocity of the flow field. Diffusive processes are velocity-independent, whereas

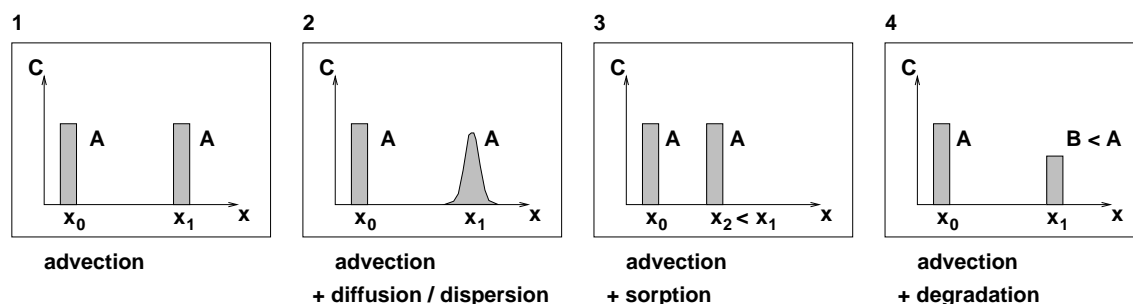


Figure 2.27: Effect of 1. advection, 2. diffusion / dispersion, 3. sorption, and 4. biodegradation / reaction.

dispersive processes always depend on velocity. In this section, **molecular diffusion** (Section 2.6.1), **capillary diffusion** (Section 2.6.2), as well as **numerical diffusion** are discussed (Section 2.6.3), although numerical diffusion is not a physical effect, but only occurs in numerical simulations due to discretization of the mathematical model equations. Next, in Section 2.6.4, **dispersion**, its scale-dependence and the preasymptotic / asymptotic behavior of macrodispersion are studied.

## 2.6.1 Molecular Diffusion

As the name indicates, molecular diffusion is a process taking place on the molecular scale. It is caused by the *Brownian* motion of the molecules which has a balancing effect on concentration gradients. This effect can be described by the Fickian law,

$$\underline{F}_\alpha^\kappa = -\nabla \cdot \left( \underline{D}_{m,pm,\alpha}^\kappa \nabla (C_\alpha^\kappa) \right), \quad (2.26)$$

where  $\underline{D}_{m,pm,\alpha}^\kappa$  is the tensor of molecular diffusion for component  $\kappa$  in phase  $\alpha$ , and  $\underline{F}_\alpha^\kappa$  is the diffusive flux. One can see, that it is proportional to the gradient of the mass fraction  $X_\alpha^\kappa = \frac{C_\alpha^\kappa}{\rho_\alpha}$  for incompressible systems. The tensor  $\underline{D}_{m,pm,\alpha}^\kappa$  is homogeneous and isotropic—thus, it is in fact a scalar quantity. However, in Equation (2.26), the molecular diffusion is interpreted as a tensor. This is to show the analogies to dispersion which is a genuine tensorial quantity. Often, molecular diffusion can be neglected compared to dispersion and advection. Only for very low permeable materials with consequently long travel times or for small flow velocities due to small pressure gradients, it can play a significant role.

## 2.6.2 Capillary Diffusion

Capillary forces are insofar of diffusive nature as they act in all space dimensions in the same way and thus, also cause “smearing” of fronts and a decrease of peaks.

When mathematically modeling multi-phase and multi-phase–multi-component processes as will be done in Section 3, one term describing capillary pressure occurs. Rewriting this capillary term  $\nabla \cdot (\rho_w f_w \lambda_n \underline{K} \nabla p_c)$ , of Equation (3.79) as  $\nabla \cdot \left( \rho_w f_w \lambda_n \underline{K} \frac{dp_c}{dS_w} \nabla S_w \right)$ , one can see that it is of a form similar to the Fickian law discussed in Section 2.6.1, with  $\underline{D}_c(S_w) = f_w \lambda_n \underline{K} \frac{dp_c}{dS_w}$  as the tensor of capillary diffusion.

In Figure 2.17, the dependence of capillary diffusion on saturation has been shown using Brooks-Corey relative permeability–saturation and capillary pressure–saturation relationships. One sees, that capillary diffusion vanishes for one-phase systems ( $S_w = 0$  or  $S_w = 1$ ) and that it shows a maximum in between. Thus, capillary diffusion depends on the constitutive relationships and its parameters (material dependence) as well as on saturation.

### 2.6.3 Numerical Diffusion

Numerical diffusion is no physically based process, it is only due to a discretization of the mathematical equations describing multi-phase and multi-phase–multi-component processes. However, it is mentioned here for the sake of completeness.

If the differential equations become too complex to solve them analytically, one has to use a numerical scheme. In order to do so, the differential equations are not solved at all (infinitely many) points in space, but only at a discrete number of points corresponding to a so-called *grid* or *mesh*. Therefore, one can imagine already at this point, that the finer the grid is, the more points the equations will be solved at and the more accurate the solution will get.

If e.g. an advection equation is solved numerically, it can be observed that the corresponding steep fronts smear out in a diffusion-like process known as numerical diffusion. The reason for this is that one grid point will always lie upstream of the steep front, while the next one lies downstream of the shock. In between these two points, one can only interpolate the values of unknown quantities. No matter which interpolation scheme is chosen, the solution will never reproduce the steep front exactly. These issues are illustrated for a one-dimensional problem in Figure 2.28, where a linear interpolation of the unknown  $u$  between grid points is applied. For the coarse grid, the steep front is represented rather badly and shows some diffusion-like spreading behavior, as the nodes upstream and downstream of the shock are far away from each other. This “numerical diffusion” reduces when taking the finer grid.

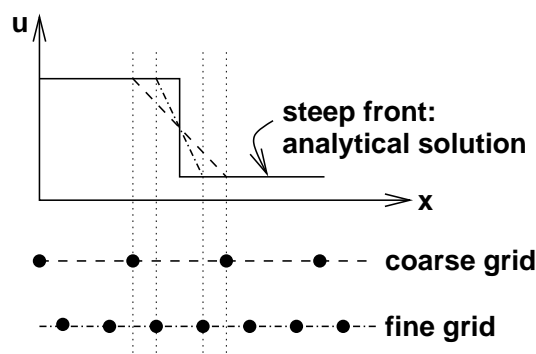


Figure 2.28: Numerical diffusion: the finer the grid, the better the step front can be approximated.

## 2.6.4 Dispersion

Dispersion is always caused by a nonuniform velocity distribution which may occur on all possible scales starting from the micro scale.

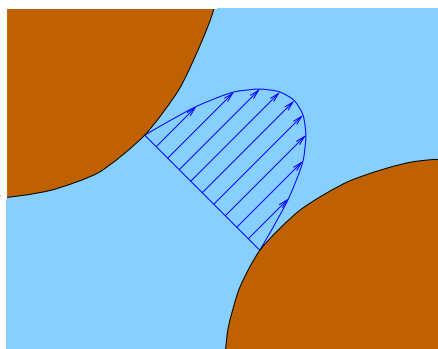


Figure 2.29: Dispersion due to the velocity distribution within a pore throat on the micro scale<sup>2</sup>.

Figure 2.29 shows the velocity distribution within a pore throat on the **micro scale**. As the soil matrix is not supposed to move, the velocity has to vanish at the fluid–solid interfaces. This condition of zero velocity at fluid–solid interfaces is called *no-slip condition*. In between these points of zero velocity, a parabolic velocity profile is established. Therefore, particles within a cross section travel with different velocities leading to a smearing of steep fronts on the micro scale.

Figure 2.30 shows dispersion caused by a heterogeneous distribution of absolute permeability on the **local scale** and on the **macro scale**.

<sup>2</sup>pictures taken or adapted from the lecture notes “Model Concepts and Simulation Methods for Single and Multi-Phase Flow”



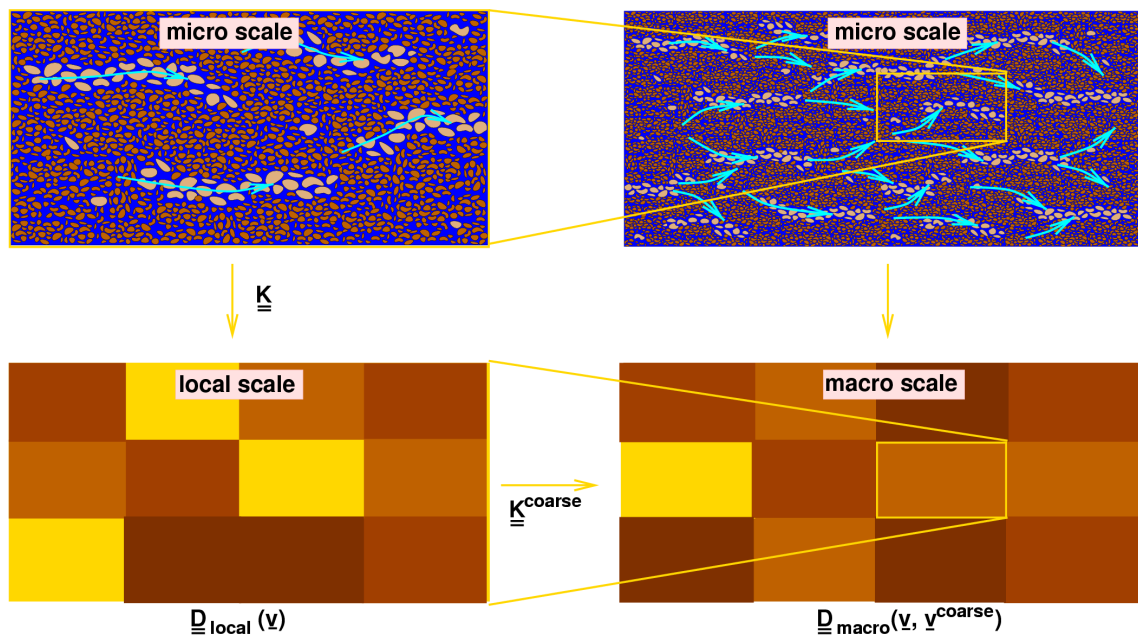


Figure 2.30: Dispersion due to local-scale (left hand side) and macro-scale (right hand side) heterogeneities<sup>2</sup>.

In a multi-phase system, the presence of other phases further increases the tortuosity of the flow paths and thus, further increases dispersion, see Figure 2.31. This circumstance is represented by the relative permeability.

The theory of dispersion on the macro scale (also called “macrodispersion”) has been derived e.g. by Dagan [1989] and Gelhar [1993]. In this work, the theory of macrodispersion will not be discussed in a stochastic framework, but it is referred to the above-mentioned work for details. Instead, only its physical basics and its effects are explained.

One can imagine that a set of particles released at a certain point in space and time will encounter the more heterogeneities the longer it travels. The longer it travels, the longer the longitudinal dispersion parallel to the main velocity direction can act. Thus, it becomes clear that longitudinal dispersion is growing with travel length and therefore with time. However, it is assumed that there is an upper limit for longitudinal dispersion which is approached asymptotically. Depending on the scale separation, i.e. the ratio between a typical length scale  $l$  on the local scale where the heterogeneities are present and a typical length  $L$  on the macro scale, which is the scale of interest, this asymptotic value will be reached almost immediately or only after a certain time. If the local-scale length scale is very small compared to the macro-scale length scale ( $l/L \ll 1$ ), the asymptotic value is approached very fast (after a small travel time), see Figure 2.32, right hand side. If by contrast, the local length scale  $l$  becomes larger compared to the macro length scale  $L$ , it takes longer for the asymp-

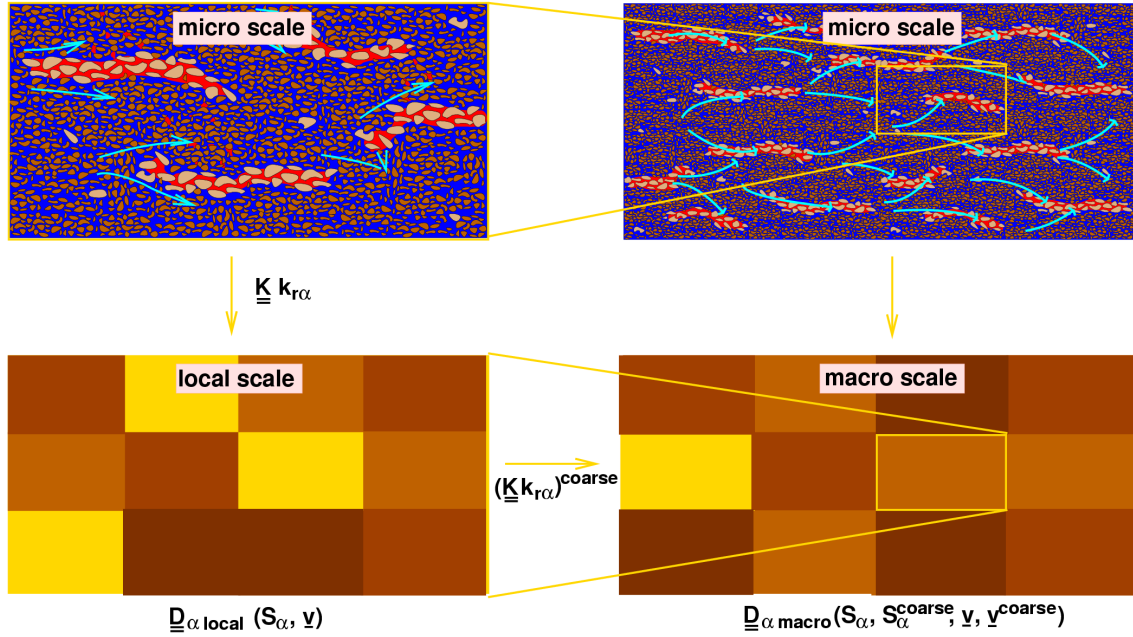


Figure 2.31: Dispersion due to two-phase processes as well as to local-scale (left hand side) and macro-scale (right hand side) heterogeneities<sup>2</sup>.

otic range to be reached. Before the asymptotic range is reached where the entry  $D_{xx}$  of the macrodispersion matrix is approximated up to a certain error  $\epsilon$ , allowing a constant entry  $D_{xx,as}$ , one is in the preasymptotic range for macrodispersion,

$$D_{xx} \begin{cases} < D_{xx,as} - \epsilon & \rightarrow \text{preasymptotic} \\ \geq D_{xx,as} - \epsilon & \rightarrow \text{asymptotic.} \end{cases} \quad (2.27)$$

When the second condition is fulfilled, one says that the asymptotic (or ergodic) range for the longitudinal macrodispersion  $D_{xx}$  has been reached, see Figure 2.32, left hand side.

Considering transversal dispersion  $D_{yy}$  and  $D_{zz}$ , dispersion first increases fast, then decreases and asymptotically approaches zero, see Figure 2.33. If the ratio of  $(l/L)$  is very small, again, the asymptotic value is reached rather quickly. Within the asymptotic range, it is assumed that the macrodispersion matrix can be approximated by a constant tensor.

In the work of Rubin et al. [1999], analytical results for planar flow in a domain using an anisotropic exponential variogram for a stationary log-permeability covariance are shown. The authors calculated the dependence of the longitudinal and transversal macrodispersion  $D_{xx}$  and  $D_{yy}$  on travel time and block scale. Four years later, Rubin et al. [2003] extended and tested this concept and they derived conditions of applicability. They also show that the asymptotic range is reached rather fast for slightly heterogeneous media with small variances.

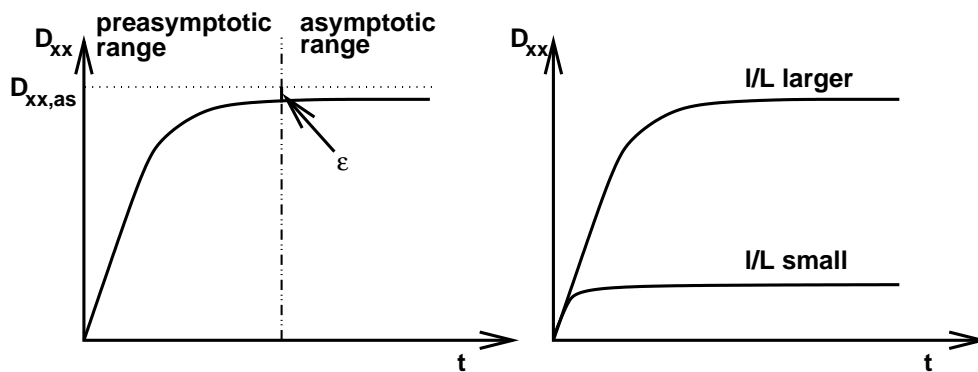


Figure 2.32: Longitudinal macrodispersion as a function of travel time (modified after Rubin et al. [1999]).

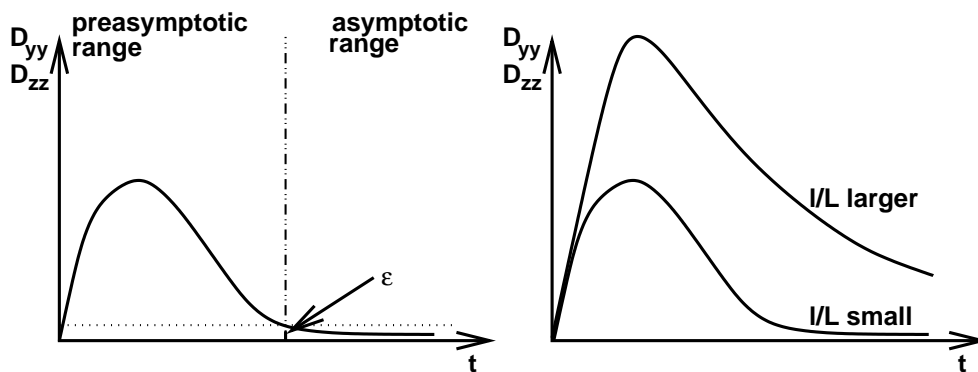


Figure 2.33: Transversal macrodispersion as a function of travel time (modified after Rubin et al. [1999]).

It is to question whether the asymptotic range for the longitudinal and the transversal macrodispersion is reached at the same travel time.

In macro-scale considerations, the effect of spatial variability is partly captured directly, i.e. by modeling heterogeneities explicitly. This can be done for heterogeneities corresponding to the model scale, i.e. the macro scale. Partly, for local-scale heterogeneities, spatial variability is accounted for by a macrodispersion term.

## 2.7 Laws for Fluid Phase Equilibria

In this section, a short summary is given tackling the physical relationships which govern the equilibrium state between fluid phases and thus, the mass transfer processes, i.e. the exchange of components between phases. While in real-life system kinetics might play an important role, it is a common assumption in hydraulic en-

engineering to assume chemical equilibrium, if flow velocities are slow in comparison to kinetic processes. This means, that a certain system state clearly defines the phase composition, which is—by definition—the equilibrium composition at that system state. While a variety of other relationships can be found in literature, only the relations used in this work are presented. Dalton's law, Raoult's law, as well as Henry's law are treated.

### Dalton's Law

The English scientist John Dalton studied the properties of gas mixtures and stated the following law, known as Dalton's Law:

*The total pressure of a gas mixture equals the sum of the pressures of the gases that make up the mixture,*

$$p_g = \sum_{\kappa} p_g^{\kappa}, \quad (2.28)$$

where  $p^{\kappa}$  is the pressure of a single component  $\kappa$  ("partial pressure"). The partial pressure  $p_g^{\kappa}$  is by definition the product of the mole fraction of the respective component in the gas phase and the total pressure of the gas phase,

$$p_g^{\kappa} = x_g^{\kappa} p_g. \quad (2.29)$$

### Raoult's Law

Raoult's law describes the lowering of the vapor pressure of a pure substance in a solution. It relates the vapor pressure of components to the composition of the solution under the simplifying assumption of an ideal solution. The relationship can be derived from the equality of fugacities, see Prausnitz et al. [1967]. According to Raoult's law, the vapor pressure of a solution of component  $\kappa$  is equal to the vapor pressure of the pure substance times the mole fraction of component  $\kappa$  in phase  $\alpha$ .

$$p_g^{\kappa} = x_{\alpha}^{\kappa} \cdot p_{vap}^{\kappa} \quad (2.30)$$

Here,  $p_{vap}^{\kappa}$  denotes the vapor pressure of pure component  $\kappa$  which is generally a function of temperature—for isothermal systems as the one considered here, it is constant.

### Henry's Law

Henry's law is valid for ideally diluted solutions and ideal gases. It is especially used for the calculation of the solution of gaseous components in liquids. Considering a system with gaseous component  $\kappa$ , a linear relationship between the mole fraction  $x_{\alpha}^{\kappa}$  of component  $\kappa$  in the liquid phase and the partial pressure  $p_g^{\kappa}$  of  $\kappa$  in the gas phase is obtained,

$$x_{\alpha}^{\kappa} = H_{\alpha}^{\kappa} \cdot p_g^{\kappa}. \quad (2.31)$$

The parameter  $H_{\alpha}^{\kappa}$  denotes the Henry coefficient of component  $\kappa$  in phase  $\alpha$  which is dependent on temperature.

Figure 2.34 shows the range of applicability of both Henry's law and Raoult's law for a binary system, where component 1 is a component forming a liquid phase, e.g. water, and component 2 is a component forming the gaseous phase, e.g. air. One can see, that for low mole ratios of component 1 in the system (small amounts of liquid in the gas phase), Henry's law can be applied whereas for mole ratios of component 1 close to 1 (small amounts of component 2 in the liquid phase), Raoult's law is the appropriate description. In general, the solvent follows Raoult's law as it is present in excess, whereas the dissolved substance follows Henry's law as it is highly diluted.

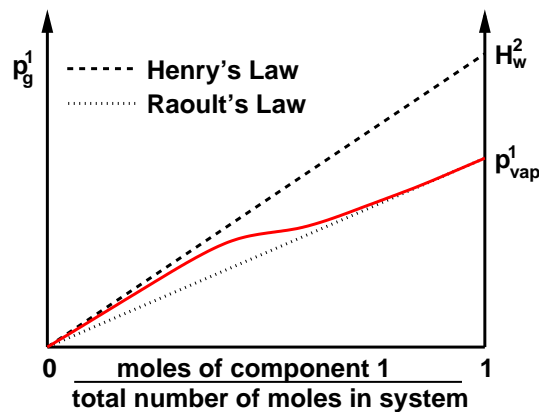


Figure 2.34: Applicability of Henry's law and Raoult's law for a binary gas-liquid system (after Lüdecke and Lüdecke [2000]).

## 3 Mathematical Modeling

In this chapter, first the basic balance equations describing multi-phase and multi-phase–multi-component processes are discussed. Next, the advantages and disadvantages of different mathematical formulations of the governing equations are studied. Finally, flash calculations are explained, as they are needed in multi-phase–multi-component modeling in order to compute saturations from total concentrations when using the mathematical formulation applied in this work.

It is emphasized that all the equations presented in this chapter are only valid on the local scale. For macro-scale models, an upscaling approach has to be applied. The upscaling technique used in this work is volume averaging, for further details see Section 5.4.

A general form of the balance equations for multi-phase–multi-component flow and transport in porous media has first been derived by Hassanizadeh and Gray [1979] and then further developed by Hassanizadeh and Gray [1980, 1990, 1993b, 1997].

### 3.1 Equations for Multi-Phase Processes

Considering a control volume with e.g. two fluid phases, see Figure 3.35, a part of the volume is occupied by the solid matrix, a part by the wetting phase and the rest by the non-wetting phase. Balancing the mass within the control volume, the temporal change of mass  $M_\alpha$  within one phase is governed by the exchange of mass  $I_\alpha$  with the other phase, by sources and sinks  $Q_\alpha$  of phase  $\alpha$  within the control volume and by the exchange of mass  $A_\alpha$  with other control volumes. Thus, a mass balance can be set up which is of the form

$$M_\alpha + A_\alpha - I_\alpha - Q_\alpha = 0, \quad (3.32)$$

where *inflow* of mass  $A_\alpha$  into the control volume, the flux of mass  $I_\alpha$  to phase  $\alpha$ , and a *source*  $Q_\alpha$  have positive sign by definition.

Now, the single terms are considered in more detail.

The **storage term**  $M_\alpha$  is the temporal change of mass resulting from the integral over a control volume  $\Omega$  of the phase density  $\rho_\alpha$  multiplied by porosity  $\phi$  and the

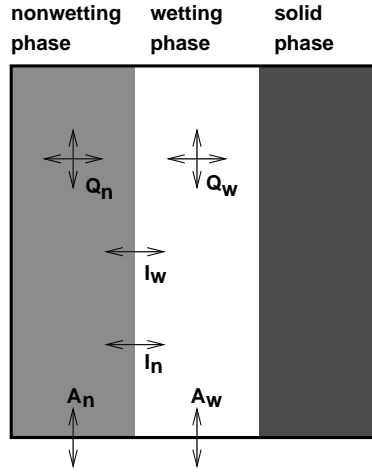


Figure 3.35: Control volume for the phase mass balance.

saturation  $S_\alpha$  of phase  $\alpha$ :

$$M_\alpha = \frac{\partial}{\partial t} \int_{\Omega} \phi \rho_\alpha S_\alpha d\Omega. \quad (3.33)$$

To determine the **flux term**  $A_\alpha$  across the boundary of a control volume, the advective flux across the boundary  $\Gamma$  of the control volume  $\Omega$  is considered:

$$A_\alpha = \int_{\Gamma} (\rho_\alpha \underline{v}_\alpha) \cdot \underline{n} d\Gamma, \quad (3.34)$$

where  $\underline{v}_\alpha$  is the Darcy velocity of phase  $\alpha$  which will be discussed later on in this section.

To transform Equation (3.34), the Gauss theorem

$$\int_{\Gamma} \underline{f} \cdot \underline{n} d\Gamma = \int_{\Omega} \nabla \cdot \underline{f} d\Omega \quad (3.35)$$

is applied which is valid for any vector function  $\underline{f}$ . This yields

$$A_\alpha = \int_{\Omega} \nabla \cdot (\rho_\alpha \underline{v}_\alpha) d\Omega. \quad (3.36)$$

Finally, the **mass exchange term** between fluid phases for multi-phase systems is zero by definition, i.e.

$$I_\alpha = 0. \quad (3.37)$$

The **source / sink term** is given by

$$Q_\alpha = \int_{\Omega} (\rho_\alpha q_\alpha) d\Omega, \quad (3.38)$$

where  $q_\alpha$  is a source or sink of phase  $\alpha$  (wells, groundwater recharge, etc.), depending on its sign.

Inserting Equations (3.33), (3.36), (3.37), and (3.38) into Equation (3.32) results in

$$\frac{\partial}{\partial t} \int_{\Omega} \phi \rho_\alpha S_\alpha d\Omega + \int_{\Omega} \nabla \cdot (\rho_\alpha \underline{v}_\alpha) d\Omega - \int_{\Omega} \rho_\alpha q_\alpha d\Omega = 0. \quad (3.39)$$

Under certain mathematical assumptions, it is possible to write this equation in differential form as

$$\frac{\partial(\phi \rho_\alpha S_\alpha)}{\partial t} + \nabla \cdot (\rho_\alpha \underline{v}_\alpha) - \rho_\alpha q_\alpha = 0. \quad (3.40)$$

The quantity which still needs further discussion is the phase velocity  $\underline{v}_\alpha$ . For small flow velocities (Reynold's numbers  $< 1$ ), the generally accepted way to calculate these velocities is to apply the extended form of Darcy's law for several phases:

$$\underline{v}_\alpha = -\frac{k_{r\alpha}}{\mu_\alpha} \underline{K} (\nabla p_\alpha - \rho_\alpha \underline{g}), \quad (3.41)$$

where  $\underline{g}$  is the vector of gravity pointing to the earth's midpoint. The Darcy's law is a simplification of the general momentum balance equation.

## 3.2 Equations for Multi-Phase–Multi-Component Processes

For the mass balance of a multi-phase–multi-component system with  $m$  phases and  $m$  components, similar considerations can be made as for the system without mass transfer between phases. One only has to balance over components  $\kappa$  instead of phases

$$M^\kappa + A^\kappa - I^\kappa - Q^\kappa = 0, \quad (3.42)$$

see Figure 3.36. The signs are defined analogously to the balance equation for a multi-phase system given in Equation (3.32).

To set up the mass balance for components, it is possible to either balance over each component in each phase, or to balance over the total mass of a component which is both consistent with Figure 3.36. The balance over the total masses is advantageous as then only  $m$  balance equations instead of  $m^2$  equations are needed and the exchange terms  $I^\kappa$  disappear, similar to the multi-phase case. As for the multi-phase case, the remaining terms  $M^\kappa$ ,  $A^\kappa$ , and  $Q^\kappa$  have to be given which are directly



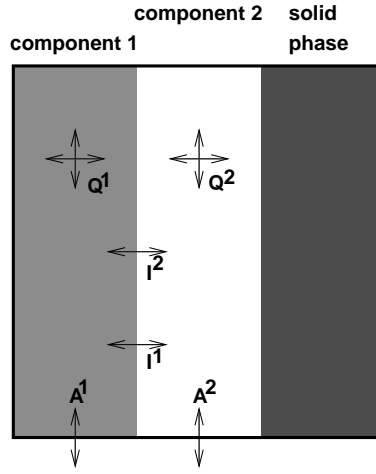


Figure 3.36: Control volume for the component mass balance.

considered to be in differential form:

$$M^\kappa = \frac{\partial \phi \sum_\alpha C_\alpha^\kappa}{\partial t}, \quad (3.43)$$

$$A^\kappa = \sum_\alpha \nabla \cdot (C_\alpha^\kappa \underline{v}_\alpha + \underline{\underline{D}}_{pm}^\kappa \nabla C_\alpha^\kappa), \text{ and} \quad (3.44)$$

$$Q^\kappa = q^\kappa, \quad (3.45)$$

where  $q^\kappa$  is a source / sink term for component  $\kappa$  and  $\underline{\underline{D}}_{pm}^\kappa$  is the tensor of hydrodynamic dispersion of component  $\kappa$ . In this tensor  $\underline{\underline{D}}_{pm}^\kappa$ , both diffusion and dispersion are subsumed.

Inserting the single terms into Equation (3.42) gives

$$\frac{\partial C^\kappa}{\partial t} + \sum_\alpha \nabla \cdot (C_\alpha^\kappa \underline{v}_\alpha + \underline{\underline{D}}_{pm}^\kappa \nabla C_\alpha^\kappa) - q^\kappa = 0. \quad (3.46)$$

### 3.3 Fully Coupled vs. Fractional Flow Formulation

In Equation (3.40), the general mass balance for multi-phase flow has been introduced, whereas in Equation (3.46) the mass balance equation for multi-phase–multi-component flow and transport has been tackled.

Considering the example of a multi-phase, say, an  $m$ -phase system, one has the possibility either to solve the  $m$  balance equations for the  $m$ -phase system directly in the form of Equation (3.40). In this case, there are  $m$  balance equations that are

all coupled to one another. This approach is called the *fully coupled* formulation and is further studied in Section 3.3.1. An analogous formulation can be constructed for multi-phase–multi-component systems.

The other possibility for multi-phase systems is to transform the system of  $m$  balance equations into one equation for pressure, the *pressure equation*, and  $(m - 1)$  equations for selected saturations, the *saturation equations*. This approach is the so-called *fractional flow formulation*. These  $(1 + (m - 1))$  equations are usually solved sequentially. The easiest and most common approach is the IMPES scheme (IMplicit pressure, Explicit Saturation), where the pressure equation is first solved implicitly to yield the velocity field which then enters into the  $(m - 1)$  saturation equations. Like the fully coupled formulation, the fractional flow formulation can also be applied to multi-phase–multi-component systems.

An overview of different formulations for multi-phase–multi-component systems with varying numbers of phases and components is given in Huber [1999]. Binning and Celia [1999] make a detailed study on the advantageous and disadvantageous of the fractional flow formulation for one-dimensional systems. The fractional flow formulation for both multi-phase and for multi-phase–multi-component systems is presented in Section 3.3.2.

### 3.3.1 Fully Coupled Formulation

In this section, the fully coupled formulation for both multi-phase and for multi-phase–multi-component models is reviewed.

#### Multi-phase systems.

First, general  $m$ -phase flow is considered. Inserting the extended Darcy's law given in Equation (3.41) into the mass balance given by Equation (3.40) gives  $m$  equations, one for each of the  $m$  phases:

$$\frac{\partial(\phi\rho_\alpha S_\alpha)}{\partial t} - \nabla \cdot \left( \rho_\alpha \frac{k_{r\alpha}}{\mu_\alpha} \underline{\underline{K}} (\nabla p_\alpha - \rho_\alpha \underline{\underline{g}}) \right) - \rho_\alpha q_\alpha = 0. \quad (3.47)$$

The unknown quantities are the pressures of the  $m$  phases,  $p_1, \dots, p_m$ , and the phase saturations,  $S_1, \dots, S_m$ . That means, only  $m$  equations for  $2m$  unknowns can be formulated. The common strategy to tackle this problem is to choose  $m$  primary variables among the  $2m$  unknowns and to use  $m$  closure relations to substitute the  $m$  secondary unknowns. In the following considerations, it is assumed that the pressures, as well as the saturations are ordered according to their wettability, i.e. fluid 1 is the most wetting fluid, and fluid  $m$  the least wetting fluid. Then, these

$m$  closure relations are

$$\sum_{i=1}^m S_i = 1 \quad (3.48)$$

$$p_{c12} = p_2 - p_1 = p_c(S_1) \quad (3.49)$$

$$p_{c23} = p_3 - p_2 = p_c(S_2) \quad (3.50)$$

$$\vdots = \vdots$$

$$p_{c(m-1)m} = p_m - p_{m-1} = p_c(S_{m-1}), \quad (3.51)$$

i.e. the  $m$  closure relations consist of the condition that the sum of the saturations has to be equal to 1, and  $(m - 1)$  capillary pressure–saturation relationships that relate the phase pressures to saturations.

Note, that for the fully coupled approach, the  $m$  differential equations are all of the same structure. Mathematically, they represent a parabolic nonlinear partial differential equation system.

#### Multi-phase–multi-component systems.

Similar considerations can be made for multi-phase–multi-component flow and transport. Here, a system with  $m$  phases and  $m$  components is considered. Inserting the extended Darcy's law given in Equation (3.41) into the mass balance for multi-phase–multi-component systems of Equation (3.46) results in

$$\frac{\partial C^\kappa}{\partial t} - \sum_{\alpha} \nabla \cdot \left( C_{\alpha}^{\kappa} \frac{k_{r\alpha}}{\mu_{\alpha}} \underline{\underline{K}} (\nabla p_{\alpha} - \rho_{\alpha} \underline{g}) - \underline{\underline{D}}_{pm}^{\kappa} \nabla C_{\alpha}^{\kappa} \right) - q^{\kappa} = 0. \quad (3.52)$$

In this case, there are  $m$  governing equations for  $m^2 + m$  unknowns ( $m$  pressures, and  $m^2$  concentrations  $C_{\alpha}^{\kappa}$ ). To close the equation system, the same  $m$  condition as for multi-phase flow are needed

$$\sum_{i=1}^m S_i = 1 \quad (3.53)$$

$$p_{c12} = p_2 - p_1 = p_c(S_1) \quad (3.54)$$

$$p_{c23} = p_3 - p_2 = p_c(S_2) \quad (3.55)$$

$$\vdots = \vdots \quad (3.56)$$

$$p_{c(m-1)m} = p_m - p_{m-1} = p_c(S_{m-1}), \quad (3.57)$$

and again,  $m$  independent primary variables are chosen. With Equation (2.25)

$$C^{\kappa} = \phi \sum_{\alpha} (\rho_{\alpha} S_{\alpha} X_{\alpha}^{\kappa}), \quad (3.58)$$

$m$  equations are given, but at the same time,  $m^2$  new unknowns  $X_\alpha^\kappa$  are introduced. However, it is known from Equation (2.24) that

$$C_\alpha^\kappa = \rho_\alpha \cdot X_\alpha^\kappa. \quad (3.59)$$

Equation (2.22) gives  $m$  conditions for the mass fractions  $X_\alpha^\kappa$ :

$$\sum_{\kappa} X_\alpha^\kappa = 1, \quad (3.60)$$

and then, one has to formulate equations of state to relate the mass fractions  $X_\alpha^\kappa$  or the mole fractions  $x_\alpha^\kappa$  to the primary variables, see e.g. Section 2.7.

The key point for the fully coupled multi-phase–multi-component system is again, that the partial differential equation system is solved in the form of Equation (3.52), i.e. as a parabolic, nonlinear, and coupled system of equations, that are all of the same type.

### 3.3.2 Fractional Flow Formulation

This section comprises the fractional flow formulations for both multi-phase and for multi-phase–multi-component systems.

#### Multi-phase systems.

It is not as straightforward as for the fully coupled formulation to derive a general representation of the fractional flow formulation for an  $m$ -phase system. Therefore, a two-phase systems is discussed, i.e., a wetting phase  $w$  and a non-wetting phase  $n$  are focussed on. Remember, that in the frame of this work, the considered macro-scale model is *always* a two-phase gas–water model. Therefore, this section contents itself with the presentation of the fractional flow formulation for a two-phase system. Details on the this formulation, also for three-phase flow, can be found in the work of Chen and Ewing [1997] and Huber [1999]. First, the two-phase flow equation system in the form of Equation (3.40) is considered,

$$\frac{\partial(\phi\rho_\alpha S_\alpha)}{\partial t} + \nabla \cdot (\rho_\alpha \underline{v}_\alpha) - \rho_\alpha q_\alpha = 0, \quad (3.61)$$

with the closure relations

$$S_w + S_n = 1, \text{ and} \quad (3.62)$$

$$p_c = p_n - p_w = p_c(S_w), \quad (3.63)$$

and the Darcy velocity

$$\underline{v}_\alpha = -\frac{k_{r\alpha}}{\mu_\alpha} \underline{\underline{K}}(\nabla p_\alpha - \rho_\alpha \underline{g}) \quad (3.64)$$

Adding up Equations (3.61) for  $\alpha = w$  and  $\alpha = n$ , one is left with

$$\nabla \cdot \sum_{\alpha} \underline{v}_{\alpha} = -\frac{\partial \phi}{\partial t} - \sum_{\alpha} \frac{1}{\rho_{\alpha}} \left( \phi S_{\alpha} \frac{\partial \rho_{\alpha}}{\partial t} + \underline{v}_{\alpha} \nabla \rho_{\alpha} - \rho_{\alpha} \underline{q}_{\alpha} \right). \quad (3.65)$$

For the fractional flow formulation, two new variables are introduced, the *total velocity*  $\underline{v}$ , and a *global pressure*  $\tilde{p}$ . These new variables are “artificial” variables which are only defined for the fractional flow formulation, but do not represent measurable physical quantities. The sum of the phase velocities is denoted as the total velocity  $\underline{v}$

$$\underline{v} = \sum_{\alpha} \underline{v}_{\alpha}. \quad (3.66)$$

The global pressure is defined in a way, that a relationship similar to Darcy’s law can be established between global pressure and total velocity,

$$\underline{v} = -\lambda \underline{K} \cdot (\nabla \tilde{p} - \underline{G}), \quad (3.67)$$

where  $\lambda$  is the total mobility defined as

$$\lambda = \sum_{\alpha} \lambda_{\alpha}. \quad (3.68)$$

The phase mobilities  $\lambda_{\alpha}$  are calculated as

$$\lambda_{\alpha} = \frac{k_{r\alpha}}{\mu_{\alpha}}, \quad (3.69)$$

and  $\underline{G}$  is the gravity term

$$\underline{G} = \sum_{\alpha} \rho_{\alpha} f_{\alpha} \underline{g}. \quad (3.70)$$

The variables  $f_{\alpha}$  denote the fractional flow function of phase  $\alpha$  which gave the name to this formulation. It is defined as

$$f_{\alpha} = \frac{\lambda_{\alpha}}{\lambda}. \quad (3.71)$$

Following Chen and Ewing [1997] and Chavent and Jaffré [1986], the global pressure is given by

$$\tilde{p} = p_n - \int_{S_c}^{S_w} f_w \frac{dp_c(\xi)}{dS_w} d\xi, \quad (3.72)$$

where  $S_c$  is defined such that  $p_c(S_c) = 0$ . The integral in Equation (3.72) has to be evaluated numerically, which means, that it either lacks accuracy or—when accurately computing the integral—that the calculation is time consuming.

Having this information, already one of the two equations of a fractional flow formulation for two-phase flow is defined, i.e. the *pressure equation*. The total set of equations defining the pressure equation is

$$\nabla \cdot \underline{v} = -\frac{\partial \phi}{\partial t} - \sum_{\alpha} \frac{1}{\rho_{\alpha}} \left( \phi S_{\alpha} \frac{\partial \rho_{\alpha}}{\partial t} + \underline{v}_{\alpha} \nabla \rho_{\alpha} - \rho_{\alpha} \underline{q}_{\alpha} \right) \quad (3.73)$$

$$\underline{v} = -\lambda \underline{K} \cdot (\nabla \tilde{p} - \underline{G}), \text{ and} \quad (3.74)$$

$$\tilde{p} = p_n - \int_{S_c}^{S_w} f_w \frac{dp_c(\xi)}{dS_w} d\xi. \quad (3.75)$$

The other equation to be defined is the *saturation equation*. One can choose to formulate the equation either for the wetting phase saturation  $S_w$  or for the non-wetting phase saturation  $S_n$ . Here, the wetting phase saturation  $S_w$  is chosen.

Considering the definitions of the phase velocities

$$\underline{v}_w = -\lambda_w \underline{K} (\nabla p_w - \rho_w \underline{g}) \quad (3.76)$$

$$\underline{v}_n = -\lambda_n \underline{K} (\nabla p_n - \rho_n \underline{g}) = -\lambda_n \underline{K} (\nabla p_w + \nabla p_c - \rho_n \underline{g}), \quad (3.77)$$

both equations can be resolved for  $\underline{K} \nabla p_w$  and equated. With the condition  $\underline{v} = \underline{v}_w + \underline{v}_n$ , one gets after resolving for  $\underline{v}_w$

$$\underline{v}_w = f_w \underline{v} + \lambda_n f_w (\rho_w - \rho_n) \underline{K} \underline{g} + \lambda_n f_w \underline{K} \nabla p_c. \quad (3.78)$$

Inserting this expression into Equation (3.61) with  $\alpha = w$ , one obtains the final saturation equation

$$\underbrace{\frac{\partial(\phi \rho_w S_w)}{\partial t}}_1 + \underbrace{\nabla \cdot (\rho_w f_w \underline{v})}_2 + \underbrace{\nabla \cdot (\rho_w \lambda_n f_w (\rho_w - \rho_n) \underline{K} \underline{g})}_3 + \underbrace{\nabla \cdot (\rho_w f_w \lambda_n \underline{K} \nabla p_c)}_4 - \underbrace{\rho_w \underline{q}_w}_5 = 0. \quad (3.79)$$

In this form, one can clearly identify the mathematical character of the different terms. The term 1 is the accumulation term, while the terms 2 and 3 have advective character, and 4 is of diffusive nature while term 5 is a sink / source term.

### Multi-phase–multi-component systems.

First, the differential equations for multi-phase–multi-component flow and transport are considered, given by Equation (3.46),

$$\frac{\partial C^{\kappa}}{\partial t} + \sum_{\alpha} \nabla \cdot (C_{\alpha}^{\kappa} \underline{v}_{\alpha} + \underline{D}_{pm}^{\kappa} \nabla C_{\alpha}^{\kappa}) - q^{\kappa} = 0. \quad (3.80)$$

The pressure equation for a multi-phase–multi-component model is identical to the pressure equation of a multi-phase model

$$\nabla \cdot \underline{v} = -\frac{\partial \phi}{\partial t} - \sum_{\alpha} \frac{1}{\rho_{\alpha}} \left( \phi S_{\alpha} \frac{\partial \rho_{\alpha}}{\partial t} + \underline{v}_{\alpha} \nabla \rho_{\alpha} - \rho_{\alpha} q_{\alpha} \right) \quad (3.81)$$

$$\underline{v} = -\lambda \underline{K} \cdot (\nabla \tilde{p} - \underline{G}). \quad (3.82)$$

The concentration equations can also be derived analogously to multi-phase flow. Following the derivations in Huber [1999], the resulting equations are

$$\begin{aligned} \frac{\partial C^{\kappa}}{\partial t} + \nabla \cdot \left[ \sum_{\alpha} C_{\alpha}^{\kappa} f_{\alpha} \underline{v} \right] - \nabla \cdot \left[ \sum_{\alpha} C_{\alpha}^{\kappa} (-1)^{\delta_{n\alpha}} \lambda_n f_w (\rho_w - \rho_n) \underline{K} g \right] \\ - \nabla \cdot \left[ \sum_{\alpha} C_{\alpha}^{\kappa} (-1)^{\delta_{n\alpha}} \lambda_n f_w \underline{K} \nabla p_c \right] - \nabla \cdot \left[ \phi \sum_{\alpha} S_{\alpha} \underline{D}_{pm}^{\kappa} \cdot C_{\alpha}^{\kappa} \right] - q^{\kappa} \\ = 0, \end{aligned} \quad (3.83)$$

where  $\delta_{n\alpha}$  is the Kronecker delta which is equal to 1 if  $n = \alpha$ , else it is zero.

## 3.4 Flash Calculations

Flash calculations are necessary for multi-phase–multi-component modeling to reconstruct mass fractions and saturations from the total concentrations which are obtained when solving the concentration equations in a fractional flow formulation, see Section 3.3.2.

Thus, it is pointed out that flash calculations are only needed when modeling

- multi-phase–multi-component processes
- in the fractional flow formulation.

The usual flash calculations can either be a simple equilibrium ratio flash (so-called  $K^{\kappa}$  flash) which was first described by Young and Stephenson [1983], or a more sophisticated approach where equality of the phase fugacities is assumed which can be solved either by iterative successive substitution or by a Newton–Raphson type procedure (Fussel and Yanosik [1978]). In this work, the simple approach of Young and Stephenson [1983] is applied. For the case of local two-phase–two-component processes, the flash calculations are explained in Section 3.4.1 taking into account the phases water and gas, and the two components water and air. In Section 3.4.2, by contrast, an adequate flash for a three-phase–three-component system will be

derived. Here, the phases are water, LNAPL, and gas phase while the components are water, LNAPL, and air component.

After giving a detailed description and derivation of the underlying equations for both the two-phase–two-component flash and the three-phase–three-component flash, a schematic overview of the algorithm is given at the end of each section. As the derivation of a generally valid flash procedure is extremely complex, the general algorithm and mass transfer relations are not presented. Instead, the assumptions valid for this work are taken into account, specifically, it is presumed that capillary forces can be neglected and that the system is isothermal.

### 3.4.1 Flash for a Two-Phase–Two-Component System

The (mole) equilibrium ratio  $K^\kappa$  relates the mole fraction of a component  $\kappa$  in phase  $w$  to the mole fraction of  $\kappa$  in phase  $n$ :

$$x_n^\kappa = K^\kappa \cdot x_w^\kappa, \quad (3.84)$$

where in this work, a two-phase gas–water system is considered with  $w$  indicating the water phase and  $n$  as the gas phase. This means, it is assumed that a component is distributed among the phases in a known ratio  $K^\kappa$  which is in the general case a function of pressure, density, temperature, and total concentration. With the assumptions made in this work, it is only dependent on pressure. For the two-phase–two-component flash, the vapor pressure of water, the Henry constant for a water–air system as well as the molar masses of both water and air are needed. Values are given in Appendix A.

Here, it is assumed that component 1 is a water component and that component 2 is air. Considering the **water component**, the mole equilibrium ratio is given by

$$K^1 = \frac{x_n^1}{x_w^1}. \quad (3.85)$$

Using the mass transfer relationships introduced in Section 2.7, one can calculate the ratios  $K^\kappa$ .

*Raoult's law* gives a linear relationship between the mole fraction of water in the water phase and the vapor pressure  $p_n^1$  of water in the gas phase which is valid for small mole fractions  $x_w^2$  of air in the water phase,

$$p_n^1 = x_w^1 \cdot p_{vap}^1. \quad (3.86)$$

Here,  $p_{vap}^1$  denotes the vapor pressure of water which is a constant for isothermal systems as the one considered here.



On the other hand, *Dalton's law* postulates, that the sum of the partial pressures of a gas or vapor has to be equal to the total pressure  $p_n$  of the gas,

$$p_n = p_n^1 + p_n^2. \quad (3.87)$$

As capillary pressure is neglected in this work, the gas pressure  $p_n$  is at the same time equal to the water pressure  $p_w$  and denoted by  $p$ ,

$$p := p_w = p_n. \quad (3.88)$$

Thus, one can equate Equations (3.86) and (2.29) for  $\kappa = 1$ , yielding

$$x_w^1 \cdot p_{vap}^1 = x_n^1 \cdot p. \quad (3.89)$$

This gives the possibility to calculate the mole equilibrium ratio  $K^1$  for the water component as

$$K^1 = \frac{x_n^1}{x_w^1} = \frac{p_{vap}^1}{p}. \quad (3.90)$$

Similar considerations can be done for the **air component**. Its mole equilibrium ratio  $K^2$  is given by

$$K^2 = \frac{x_n^2}{x_w^2}. \quad (3.91)$$

*Henry's law* gives a linear relationship between the mole fraction  $x_w^2$  of air in the water phase and the partial pressure of air in the gas phase,

$$p_n^2 = \frac{x_w^2}{H^2}, \quad (3.92)$$

which is valid for small amounts of water in the gas phase, i.e. small values of  $x_n^1$ . The parameter  $H^2$  denotes the Henry coefficient of the air–water system at a given temperature.

Inserting Equation (3.92) into Equation (2.29) for  $\kappa = 2$  yields

$$x_n^2 p = \frac{x_w^2}{H^2}. \quad (3.93)$$

This gives a relationship for the mole equilibrium ratio  $K^2$  of air of the form

$$K^2 = \frac{x_n^2}{x_w^2} = \frac{1}{pH^2}. \quad (3.94)$$

Having calculated the mole equilibrium ratios  $K^1$  and  $K^2$ , it is now possible to calculate all four mole fractions  $x_w^1$ ,  $x_w^2$ ,  $x_n^1$  and  $x_n^2$ . Resolving Equation (3.85) for  $x_n^1$  and Equation (3.91) for  $x_n^2$  taking into account the constraint  $x_n^1 + x_n^2 = 1$  yields

$$K^1 x_w^1 + K^2 x_w^2 = 1. \quad (3.95)$$

Additionally considering the constraint for the mole fractions in the water phase  $x_w^2 = 1 - x_w^1$  and resolving for  $x_w^1$  gives

$$x_w^1 = \frac{1 - K^2}{K^1 - K^2}. \quad (3.96)$$

The three remaining mole fractions can be obtained using simple algebraic relationships,

$$x_w^2 = 1 - x_w^1 \quad (3.97)$$

$$x_n^1 = x_w^1 K^1 \quad (3.98)$$

$$x_n^2 = 1 - x_n^1. \quad (3.99)$$

As the total concentrations are formulated in terms of mass-dependent quantities (i.e. mass densities), it is necessary to switch from mole fractions  $x_\alpha^\kappa$  to mass fractions  $X_\alpha^\kappa$ . This can be done easily using the molecular weight  $M^\kappa$  of component  $\kappa$ , yielding

$$X_w^1 = \frac{x_w^1 M^1}{x_w^1 M^1 + x_w^2 M^2} \quad (3.100)$$

$$X_w^2 = 1 - X_w^1 \quad (3.101)$$

$$X_n^1 = \frac{x_n^1 M^1}{x_n^1 M^1 + x_n^2 M^2} \quad (3.102)$$

$$X_n^2 = 1 - X_n^1. \quad (3.103)$$

Following the above approach for the *mole* equilibrium ratios  $K^\kappa$ , *mass* equilibrium ratios  $\mathcal{K}^\kappa$  can be formulated in an analogous way as

$$\mathcal{K}^\kappa = \frac{X_n^\kappa}{X_w^\kappa}. \quad (3.104)$$

The equation defining the total concentration of a component  $\kappa$ ,

$$C^\kappa = \phi (\rho_w S_w X_w^\kappa + \rho_n S_n X_n^\kappa), \quad (3.105)$$

can be resolved for the mass fraction  $X_w^\kappa$  of  $\kappa$  in the wetting phase,

$$X_w^\kappa = \frac{C^\kappa / \phi - \rho_n S_n X_n^\kappa}{\rho_w S_w}. \quad (3.106)$$

Inserting Equation (3.106) in Equation (3.104) gives

$$X_n^\kappa = \frac{\mathcal{K}^\kappa C^\kappa / \phi}{\rho_w S_w} - \frac{\mathcal{K}^\kappa \rho_n S_n}{\rho_w S_w} X_n^\kappa, \quad (3.107)$$

which can be resolved for  $X_n^\kappa$ :

$$X_n^\kappa = \frac{\mathcal{K}^\kappa C^\kappa / \phi}{\rho_w S_w + \rho_n (1 - S_w) \mathcal{K}^\kappa}. \quad (3.108)$$

Inserting Equation (3.108) in Equation (3.104) gives a relationship for  $X_w^\kappa$ :

$$X_w^\kappa = \frac{C^\kappa / \phi}{\rho_w S_w + \rho_n (1 - S_w) \mathcal{K}^\kappa}. \quad (3.109)$$

Using the condition that the sum of the mass fractions of all components in a phase has to add up to 1, one can formulate a relationship between the total concentration  $C^\kappa$  and the wetting-phase saturation  $S_w$ :

$$\begin{aligned} 0 &= 1 - 1 = \sum_{\kappa} X_n^\kappa - \sum_{\kappa} X_w^\kappa = \sum_{\kappa} (X_n^\kappa - X_w^\kappa) \\ &= \sum_{\kappa} \frac{(\mathcal{K}^\kappa - 1) C^\kappa / \phi}{\rho_w S_w + \rho_n (1 - S_w) \mathcal{K}^\kappa} \end{aligned} \quad (3.110)$$

Resolving Equation (3.110) for  $S_w$  finally yields

$$S_w = \frac{C^1 / \phi \cdot \mathcal{K}^1 - C^1 / \phi \cdot \mathcal{K}^2 - \mathcal{K}^1 \cdot \rho_n + \mathcal{K}^1 \cdot \mathcal{K}^1 \cdot \rho_n}{(-1 + \mathcal{K}^2) \cdot (\mathcal{K}^1 \cdot \rho_n - \rho_w)} \quad (3.111)$$

Having given this detailed derivation of the flash procedure, the equations are displayed in a schematic form in Table 3.1. This flash procedure is called after having solved the pressure equation and one of the concentration equations (here for component 1) to obtain wetting-phase saturations. That means, that the pressure  $p$  and the concentration  $C^1$  of component 1 are known quantities at the beginning of a flash calculation. The steps of the 2p2c flash calculations are (see also Table 3.1):

1. Applying *Henry's law*, *Raoult's law*, and *Dalton's law*, the mole equilibrium ratios  $K^\kappa$  can be derived depending on the physical properties of component  $\kappa$  and the system pressure  $p$ .
2. Having calculated the mole equilibrium ratios, all mole fractions  $x_\alpha^\kappa$  can be calculated as a function of them.
3. Consequently, the mass fractions  $X_\alpha^\kappa$  can easily be computed with the help of the molecular weights  $M^\kappa$ .
4. In an analogous way to the mole equilibrium ratios, mass equilibrium ratios  $\mathcal{K}_\alpha^\kappa$  can be calculated as a ratio of the respective mass fractions.
5. Finally, all quantities needed to solve for the saturation  $S_w$  are known.

	calculated variable	equation
1	mole equilibrium ratios	$K^1 = \frac{p_{vap}^1}{p}$
		$K^2 = \frac{1}{H^2 p}$
2	mole fractions	$x_w^1 = \frac{1-K^2}{K^1-K^2}; \quad x_w^2 = 1 - x_w^1;$ $x_n^1 = x_w^1 K^1; \quad x_n^2 = 1 - x_n^1$
3	mass fractions	$X_w^1 = \frac{x_w^1 M^1}{x_w^1 M^1 + x_w^2 M^2}; \quad X_w^2 = 1 - X_w^1;$ $X_n^1 = \frac{x_n^1 M^1}{x_n^1 M^1 + x_n^2 M^2}; \quad X_n^2 = 1 - X_n^1$
4	mass equilibrium ratios	$\mathcal{K}^\kappa = \frac{X_n^\kappa}{X_w^\kappa}$
5	saturation	$S_w = \frac{C^1/\phi \cdot \mathcal{K}^1 - C^1/\phi \cdot \mathcal{K}^2 - \mathcal{K}^1 \cdot \rho_n + \mathcal{K}^1 \cdot \mathcal{K}^1 \cdot \rho_n}{(-1 + \mathcal{K}^2) \cdot (\mathcal{K}^1 \cdot \rho_n - \rho_w)}$

Table 3.1: Overview of the 2p2c flash solution procedure.

### 3.4.2 Flash for a Three-Phase–Three-Component System

Considering a setup with locally occurring mass transfer between three phases, a three-phase–three-component system, a flash calculation has to provide the saturations for all three phases,  $S_w$ ,  $S_n$ , and  $S_g$  given the pressure  $p$  and two of the total concentrations, e.g.  $C^1$  and  $C^2$ . Here,  $w$  denotes the water phase,  $n$  an LNAPL phase and  $g$  is the gas phase, while the components are denoted by 1 (water component), 2 (LNAPL component) and 3 (air component).

Considering Figure 3.37, one can see that mass transfer models of different complexity might be reasonable depending on the given situation. The mass transfer processes which occur in the general case mutually between all three fluid phases leading to six mass transfer relations, as is shown in picture A, can often be simplified. Many LNAPLs are highly hydrophobic, and thus, hardly soluble in water. Vice versa, water hardly solubilizes in these LNAPLs. In this case, model B is a sufficient description of the physical processes. Here, only four mass transfer relations are needed, two relations for the exchange between water phase and gas phase, and two relations for the exchange between LNAPL phase and gas phase. Going even further and considering only the main mass transfer processes, one can additionally simplify the situation given in model B and only model the transfer of water and LNAPL components into the gas phase. This is possible, because for most situations with an LNAPL contamination in the unsaturated zone of the groundwater, the mole fractions of water and LNAPL which evaporate into the gas phase are much higher than the mole fractions of air which dissolve in water and LNAPL phase. This situation corresponds to model C of Figure 3.37. The full model A is only sketched in Section 3.4.2.1, as this model will not be used in the frame of this work. Model B will be discussed in Section 3.4.2.2, whereas model C will be studied in Section 3.4.2.3. More in-depth information on the thermodynamics of interphase mass transfer can be found in the literature, e.g. in Lüdecke and Lüdecke [2000].

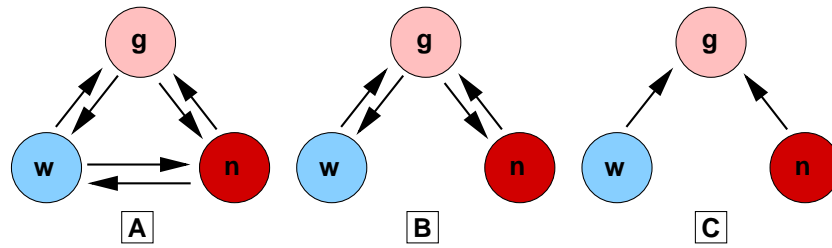


Figure 3.37: Different 3p3c models. A: mass transfer is considered mutually between all three phases, B: no mass transfer between the liquid phases, and C: only LNAPL and water components can migrate into the gas phase.

### 3.4.2.1 Flash for a 3p3c System—Mass Transfer Model A

As for the 2p2c flash, the relatively simple approach of a  $K^\kappa$  flash, can also be applied to a 3p3c system. In the three-phase–three-component case, there are two liquid phases, a water phase and an LNAPL phase. Therefore, 6 mass transfer relationships are needed, 3 relations for the components of the water phase  $K_w^\kappa$  and 3 relations for the components of the LNAPL phase  $K_n^\kappa$ .

Considering mass transfer between liquid phases in a three-phase system, one needs to take into account the activity of the liquid components leading to a rather complex thermodynamic model. In the frame of this work, this model will not be applied for two reasons:

1. The solubility of many LNAPLs in water is very small—for xylol, which is the LNAPL considered in these studies, it is  $< 0.1\%$ , and the solubility of water in these LNAPLs is similarly low.
2. In this work, a complex multi-scale–upscaling algorithm is introduced. That means, that the main interest is the development of this algorithm. Therefore, it is desirable to keep the physical and thermodynamic part of the model as simple as possible.

### 3.4.2.2 Flash for a 3p3c System—Mass Transfer Model B

Case B corresponds to a situation where mass transfer is not possible mutually between all three phases. Instead, a setup is studied where the solubility of one liquid component in the other liquid phase is negligibly small, corresponding to the situation B of Figure 3.37. The restrictions for model B are thus, that no water is present in the LNAPL phase,  $X_n^1 = 0$ , and that vice versa, no LNAPL is present in the water phase,  $X_w^2 = 0$ .

With these conditions, one has to consider only four mass transfer relations, the transfer

- water (component 1) → gas phase,
- air (component 3) → water phase,
- LNAPL (component 2) → gas phase, and
- air (component 3) → LNAPL phase.

To account for the mass transfer between liquid phases and gas phase, an equilibrium distribution of a component  $\kappa$  between the gas phase  $g$  and a liquid phase  $\alpha$  with  $\alpha \in \{w, n\}$  is assumed as

$$K_{\alpha}^{\kappa} = \frac{x_g^{\kappa}}{x_{\alpha}^{\kappa}}, \quad (3.112)$$

where  $K_{\alpha}^{\kappa}$  is the mole equilibrium ratio for component  $\kappa$  in phase  $\alpha$ .

The mole equilibrium ratios needed in mass transfer model B are  $K_w^1$ ,  $K_w^3$ ,  $K_n^2$ , and  $K_n^3$ . They are only dependent on the phase pressure  $p$  and can be obtained with the help of Dalton's law, Raoult's law and Henry's law as discussed in Appendix B.1.1,

$$K_w^1 = \frac{p_{vap}^1}{p}, \quad K_w^3 = \frac{1}{pH_w^3}, \quad K_n^2 = \frac{p_{vap}^2}{p}, \quad K_n^3 = \frac{1}{pH_n^3}. \quad (3.113)$$

Having calculated these mole equilibrium ratios, an equation system is considered which consists of the definition of the mole equilibrium ratios and of the condition that the mole fractions of all components in one phase have to sum up to one,

$$K_w^1 = \frac{x_g^1}{x_w^1} \quad (3.114)$$

$$K_w^3 = \frac{x_g^3}{x_w^3} \quad (3.115)$$

$$K_n^2 = \frac{x_g^2}{x_n^2} \quad (3.116)$$

$$K_n^3 = \frac{x_g^3}{x_n^3} \quad (3.117)$$

$$1 = x_w^1 + x_w^3 \quad (3.118)$$

$$1 = x_n^2 + x_n^3 \quad (3.119)$$

$$1 = x_g^1 + x_g^2 + x_g^3. \quad (3.120)$$

These are seven equations for the seven unknown quantities:

$x_w^1, x_w^3, x_n^2, x_n^3, x_g^1, x_g^2, x_g^3$ .

The solution of this equation system is given in Appendix B.1.2.

Knowing the mole fractions, the mass fractions  $X_\alpha^\kappa$  can be calculated as a function of the mole fractions  $x_\alpha^\kappa$  and the molar weights  $M^\kappa$ :

$$X_\alpha^\kappa = \frac{x_\alpha^\kappa M^\kappa}{\sum_{\kappa=1}^3 x_\alpha^\kappa M^\kappa}. \quad (3.121)$$

Finally, an equation system with three linear equations and three unknowns can be formulated,

$$1 = S_w + S_n + S_g \quad (3.122)$$

$$C^1/\phi = \rho_w S_w X_w^1 + \rho_n S_n X_n^1 + \rho_g S_g X_g^1 \quad (3.123)$$

$$C^2/\phi = \rho_w S_w X_w^2 + \rho_n S_n X_n^2 + \rho_g S_g X_g^2, \quad (3.124)$$

consisting of the condition that the saturations have to sum up to one as well as the definitions of the total concentrations. Solving this equation system yields the saturations  $S_w$ ,  $S_n$ , and  $S_g$ . These resulting saturations are given in Appendix B.1.3.

For mass transfer model B, the general solution procedure is shown in Table 3.2. The evaluation of the relatively long expressions can be found in Appendix B.1. The known variables at the beginning of a flash are the total concentrations  $C^1$  and  $C^2$  as well as the pressure  $p$ .

### 3.4.2.3 Flash for a 3p3c System—Mass Transfer Model C

The model C introduced in Figure 3.37 corresponds to a situation where the only occurring mass transfer processes are the evaporation of water and LNAPL components into the gas phase.

In this relatively simple model, it is not necessary to calculate mole or mass equilibrium ratios. Considering the liquid phases on the one hand, they consist of the pure components, i.e.  $x_w^1 = 1$ , and  $x_w^2 = x_w^3 = 0$  as well as  $x_n^2 = 1$ , and  $x_n^1 = x_n^3 = 0$ .

Considering the gas phase on the other hand, its partitioning into the components air, water, and LNAPL can be calculated using Dalton's law. As the liquid phases consist of 100% water, and 100% LNAPL, respectively, the partial pressure of both water and LNAPL in the gas phase corresponds to its vapor pressure. Thus, one can

	calculated variable		equation		
1	mole equilibrium ratio	w1	$K_w^1 = \frac{p_{vap}^1}{p}$		
		w3	$K_w^3 = \frac{1}{pH_w^3}$		
		n2	$K_n^2 = \frac{p_{vap}^2}{p}$		
2	mole fraction	n3	$K_n^3 = \frac{1}{pH_n^3}$		
		w1	$x_w^1 = x_w^1(K_\alpha^\kappa)$		
		w2	$x_w^2 = 0$		
		w3	$x_w^3 = 1 - x_w^1 - x_w^2$		
		n1	$x_n^1 = 0$		
		n2	$x_n^2 = x_n^2(K_\alpha^\kappa)$		
		n3	$x_n^3 = 1 - x_n^1 - x_n^2$		
		g1	$x_g^1 = x_g^1(K_\alpha^\kappa)$		
		g2	$x_g^2 = x_g^2(K_\alpha^\kappa)$		
g3	$x_g^3 = 1 - x_g^1 - x_g^2$				
3	mass fraction	w1	$X_w^1 = \frac{x_w^1 M^1}{x_w^1 M^1 + x_w^2 M^2 + x_w^3 M^3}$		
		w3	$X_w^3 = 1 - X_w^1 - X_w^2$		
		n2	$X_n^2 = \frac{x_n^2 M^2}{x_n^1 M^1 + x_n^2 M^2 + x_n^3 M^3}$		
		n3	$X_n^3 = 1 - X_n^1 - X_n^2$		
		g1	$X_g^1 = \frac{x_g^1 M^1}{x_g^1 M^1 + x_g^2 M^2 + x_g^3 M^3}$		
		g2	$X_g^2 = \frac{x_g^2 M^2}{x_g^1 M^1 + x_g^2 M^2 + x_g^3 M^3}$		
		g3	$X_g^3 = 1 - X_g^1 - X_g^2$		
		4	saturation	n	$S_n = S_n(C^1/\phi, C^2/\phi, X_\alpha^\kappa, \rho_w, \rho_n, \rho_g)$
				g	$S_g = S_g(C^1/\phi, C^2/\phi, X_\alpha^\kappa, \rho_w, \rho_n, \rho_g)$
w	$S_w = 1 - S_n - S_g$				

Table 3.2: Overview of the 3p3c flash solution procedure for mass transfer model B.



calculate all nine mole fractions as a function of pressure  $p$  only,

$$x_w^1 = 1 \quad (3.125)$$

$$x_w^2 = 0 \quad (3.126)$$

$$x_w^3 = 0 \quad (3.127)$$

$$x_n^1 = 0 \quad (3.128)$$

$$x_n^2 = 1 \quad (3.129)$$

$$x_n^3 = 0 \quad (3.130)$$

$$x_g^1 = \frac{p_{vap}^1}{p} \quad (3.131)$$

$$x_g^2 = \frac{p_{vap}^2}{p} \quad (3.132)$$

$$x_g^3 = 1 - x_g^1 - x_g^2, \quad (3.133)$$

where Dalton's law has been applied in Equations (3.131) and (3.132).

Having thus calculated the mole fractions, mass fractions can be derived as usual by

$$X_\alpha^\kappa = \frac{x_\alpha^\kappa M^\kappa}{\sum_{\kappa=1}^3 x_\alpha^\kappa M^\kappa}. \quad (3.134)$$

With the help of the mass fractions, the saturations can be directly calculated,

$$S_g = \frac{C^1/\phi\rho_n - \rho_w\rho_n + \rho_w C^2/\phi}{\rho_w\rho_g X_g^2 + \rho_g\rho_n X_g^1 - \rho_w\rho_n} \quad (3.135)$$

$$S_n = \frac{C^2/\phi - \rho_g X_g^2 S_g}{\rho_n} \quad (3.136)$$

$$S_w = 1 - S_g - S_n \quad (3.137)$$

The derivation of Equations (3.135) and (3.136) can be found in Appendix B.2.

## 4 Discretization

The partial differential equations describing multi-phase and multi-phase–multi-component processes that were discussed in Section 3.3 do not have an analytical solution. Therefore, one can discretize the equations and solve them numerically at certain points in space corresponding to an underlying grid. The multi-scale–upscaling concept presented in this work and discussed in Chapter 5 represents a special challenge for numerical modeling. On the one hand, an accurate solution of the mathematical model requires a fine resolution, and thus, a fine grid. However, the purpose of this work implies to solve a coarse-scale model for saturation on a coarse grid. The consequence is usually high numerical diffusion and the numerical solution is not very valuable any more. To generate reliable results, it is therefore essential to use a numerical scheme which does not introduce too much numerical diffusion into the solution. On the other hand, the predominance of different processes might change the mathematical character of the equations. Here, capillarity plays an important role. Although neglected here, the aim of this work is the development of a general multi-scale toolbox where more complex processes like capillarity can be included stepwise. While a system with small velocities may become parabolic–elliptic as the influence of capillary diffusion exceeds the influence of advection, the opposite is the case for advection-dominated systems which in turn may become parabolic–hyperbolic. Therefore, the discretization scheme has to be applicable to different types of mathematical problems ranging from elliptic to hyperbolic.

For these reasons, the discretization scheme applied to the developed multi-scale–upscaling framework is a discontinuous Galerkin (DG) method. DG methods were first introduced by Reed and Hill [1973] for linear equations, and further developed for nonlinear equations by Oden et al. [1998] who studied the flow equation and by Cockburn and Shu [1989], Cockburn et al. [1990], and Cockburn and Shu [1998] who focussed on the transport equation.

DG methods have some favourable qualities besides introducing only low numerical diffusion and being applicable to equations of different mathematical character. These further advantages are

- higher order convergence,
- local mass conservativity,

- “natural” representation of heterogeneities (by the use of discontinuous *Ansatz* functions),
- flexibility with respect to meshing which allows e.g. hanging nodes, and
- robustness with respect to highly varying coefficients.

However, DG schemes are not directly intellegible and it is not straightforward to apply them to more complex equations. Moreover, it is not always easy to adjust them as they may contain parameters in penalty terms which are not physically motivated.

Runge-Kutta schemes are used for time discretization as they can easily be combined with DG methods. Furthermore, they can be applied to explicit as well as to implicit schemes and the use of higher order methods is easily possible. The issue of time discretization is discussed in Section 4.2, while space discretization is addressed in Section 4.3 where the above-mentioned DG methods as well as streamline methods are studied. Streamline methods are used to construct reference solutions for the DG schemes in the case of linear advection and they serve for the approximation of streamline length occurring as a parameter in the upscaled saturation equation, see Sections 5.4.1 and 5.4.2.

## 4.1 Preliminary Remarks

An important issue to be addressed is the choice of the formulation of the governing equations. In Section 3.3.1 and Section 3.3.2, both the fully coupled and the fractional flow formulation have been introduced. In this work, the *fractional flow formulation* is applied. The reasons for that are

- that the fractional flow formulation allows to identify the physical meaning of each term in the equations,
- that it makes the solution of the pressure equation and the saturation on different scales possible,
- that upscaling approaches exist for the saturation equation taking into account the simplifications introduced in Section 1.3, and
- that discretization schemes accounting for the mathematical type of the equation can be used (e.g. the elliptic pressure equation can be solved time-implicitly and the hyperbolic saturation and concentration equations time-explicitly—for more details, see Section 4.2).

However, one has to be aware of the drawbacks of the fractional flow formulation. First, not all the quantities occurring in the fractional flow formulation do have a physical meaning, like the total velocity and the global pressure. With the assumptions made in this work, one only has to deal with the total velocity as an unphysical parameter. This is because without capillary forces, there is only one (physical) pressure in the system,  $\tilde{p} = p_w = p_n =: p$ . Next, it simplifies the solution of the equation system if both equations are of the same form, like in the fully coupled approach. Moreover, Binning and Celia [1999] showed that using general boundary conditions, problems with the fractional flow formulation may occur. And last but not least, when using an explicit discretization of the saturation and concentration equations as proposed above, the time step is restricted according to the CFL condition (Courant-Friedrichs-Lewy condition, see Section 4.2). This means that the time step might get very small when using fine grids.

As for DG schemes the discretized equations usually become long and complex, the assumptions and simplifications introduced in Section 1.3 are directly included and the DG formulation is not presented for the general multi-phase and multi-phase-multi-component case, but for the simplified model equations.

## 4.2 Time Discretization

The time discretization used in this work follows the Runge-Kutta method. For the elliptic pressure equation, a diagonally implicit scheme is applied, while for the saturation and concentration equations, an explicit scheme is used. In the following, the explicit Runge-Kutta scheme is further discussed as it represents the challenging part of the time discretization. This scheme is applied to the governing equations in a form, where they are already discretized in space by a DG method as developed by Cockburn et al. [1990]. First, the principal structure of this space-discretized equation is presented, for the exact formulation of the discretized hyperbolic equations, the reader is referred to Sections 4.3.1.2 for the saturation equation, and to Section 4.3.1.3 for the concentration equation.

Discretizing e.g. the saturation equation given in Equation (3.79) in space using DG as explained in Section 4.3.1.2 leads to an equation of ordinary differential equation (ODE) form:

$$\frac{d}{dt}S_w = L(S_w(t), t), \quad (4.138)$$

where  $L(S_w(t), t)$  is given by the DG discretization of the saturation equation. The time stepping is performed by forward steps of size  $\Delta t^n = t^{n+1} - t^n$ . The value of  $S_w$  at time step  $t^n$  is denoted by  $S_w^n$ .

Runge-Kutta methods are the most important class of one-step methods, meaning that the saturation at the new time step  $S_w^{n+1}$  is only dependent on  $S_w^n$ , but not on  $S_w^{n-k}$  with  $k \geq 0$ . The ODE given in Equation (4.138) can then be written in the semi-discrete form

$$S_w^{n+1} = S_w^n + \Delta t^n \cdot f(t^n, t^{n+1}, S_w^n, S_w^{n+1}), \quad (4.139)$$

where  $f(t^n, t^{n+1}, S_w^n, S_w^{n+1})$  is the so-called *increment function*.

The ODE is called *explicit* if the increment function  $f$  does not depend on  $S_w^{n+1}$ ; if  $f$  is dependent on  $S_w^{n+1}$ , then it is called *implicit*. Using Runge-Kutta methods, higher order schemes can easily be constructed.

The ODE is discretized in time using the total variation diminishing (TVD) Runge-Kutta scheme introduced by Shu and Osher [1988]. After calculating one whole time step, a slope limiter is applied to remove unphysical oscillations of higher order schemes. This slope limiter is a local projection  $\Lambda\Pi : V^r(E_h) \rightarrow V^r(E_h)$  that is applied in a postprocessing step, such that the TVD property is maintained, see Cockburn et al. [1990] and Cockburn and Shu [1998]. The space  $V^r(E_h)$  is the finite element space used in the DG method. It is further defined later on in this section.

Now, a closer look is taken at the slope limiting operator  $\Lambda\Pi$  applied to a one-dimensional function  $u$  as an example. This operator  $\Lambda\Pi$  was introduced by Cockburn and Shu [1998] and is used in this work. The slope limiter is only applied to the linear part  $u^1$  of  $u$  and therefore, satisfies the following properties

1. It is *accurate*: if  $u$  is linear, then  $\Lambda\Pi(u) = u$ .
2. It is *mass conservative*: for each element  $e$ :  $\int_e \Lambda\Pi u = \int_e u$ .

As an example, a one-dimensional element as given in Figure 4.38 is considered. The midpoint of element  $e_i$  is  $x_i$ , its corners are then given by  $x_{i-\frac{1}{2}}$  and  $x_{i+\frac{1}{2}}$ . The size of the element is  $\Delta x_i = x_{i+\frac{1}{2}} - x_{i-\frac{1}{2}}$ . The (linear) functions  $u_{e_i}^1$  on element  $e_i$  can

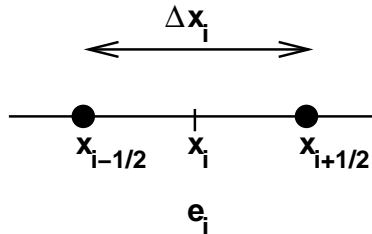


Figure 4.38: Notation with respect to a one-dimensional element for the TVD–Runge-Kutta–DG discretization.

then be written as

$$u_{e_i}^1(x) = \bar{u}_i + \tilde{u}_i \cdot \frac{x - x_i}{\frac{1}{2}\Delta x_i}. \quad (4.140)$$

The variables  $\bar{u}_i$  and  $\tilde{u}_i$  can be computed from  $u_{e_i}^1$  as

$$\bar{u}_i = u_{e_i}^1(x_i) \quad (4.141)$$

$$\tilde{u}_i = u_{e_i}^1(x_{i+\frac{1}{2}}) - u_{e_i}^1(x_i). \quad (4.142)$$

It gets obvious that  $\bar{u}_i$  is the cell-average of  $u_{e_i}^1$  and that  $\tilde{u}_i$  determines the slope of  $u_{e_i}^1$ . The slope limiter only changes the slope of the function while the cell-average  $\bar{u}_i$  remains unchanged in order to ensure mass-conservativity. The modified slope  $\tilde{u}_i^*$  on  $e_i$  is computed as

$$\tilde{u}_i^* = \bar{m}(\tilde{u}_i, q(\bar{u}_{i+1} - \bar{u}_i), q(\bar{u}_i - \bar{u}_{i-1})), \quad (4.143)$$

where  $\bar{m}$  is the TVB (total variation bounded) corrected *minmod* function defined as

$$\bar{m}(a_1, a_2, a_3) = \begin{cases} a_1, & \text{if } |a_1| \leq M\Delta x^2, \\ m(a_1, a_2, a_3), & \text{else.} \end{cases} \quad (4.144)$$

The function  $m(a_1, a_2, a_3)$  is the standard *minmod* function given by

$$m(a_1, a_2, a_3) = \begin{cases} s \min_i |a_i|, & \text{if } s = \text{sign}(a_1) = \text{sign}(a_2) = \text{sign}(a_3) \\ 0, & \text{else} \end{cases}, \quad (4.145)$$

i.e. the slope with the smallest value is selected if all slopes have the same sign, otherwise a local extremum has been detected and the slope is set to zero.

The TVB correction is applied to avoid unnecessary limiting near smooth extrema. In the following, the corresponding parameter  $M$  is taken to be 50, as suggested by Cockburn and Shu [1998]. The other user defined parameter is the nonlinearity parameter  $q$ . It is taken as  $q = 1$  for linear advection problems, and  $q = \frac{1}{2}$  for nonlinear advection.

An example to show the purpose of the *minmod* function in the case of a linear advection term is shown in Figure 4.39. Evaluating the *minmod* function as given in Equation (4.145), the lengths of three vertical lines have to be compared. In this example, the *minmod* function would return  $\bar{u}_i - \bar{u}_{i-1}$ .

The general Runge-Kutta time-stepping algorithm then has the form

1.  $S_w^{(0)} = S_w^n$ ;
2.  $S_w^{(i)} = \Lambda \Pi \left( \sum_{k=0}^i \left[ a_{ik} S_w^{(k)} + b_{ik} \Delta t^n L \left( t^n + d_k \Delta t^n, S_w^{(k)} \right) \right] \right)$ ;

$$3. S_w^{n+1} = S_w^{(s)},$$

where  $s$  is the number of stages. The operator  $L$  representing the DG space discretization will be explained in Section 4.3.1.2 for the saturation equation and in Section 4.3.1.3 for the concentration equation. Note, that Runge-Kutta schemes with  $b_{ii} = 0$  are explicit schemes, all the others are implicit.

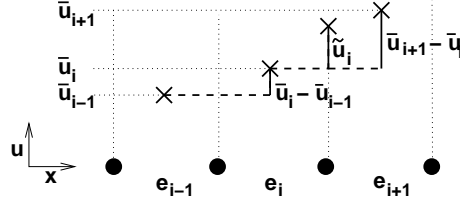


Figure 4.39: *minmod* function in the case of linear advection. The minimum of the three lines  $\bar{u}_i - \bar{u}_{i-1}$ ,  $\tilde{u}_i$ , and  $\bar{u}_{i+1} - \bar{u}_i$  is returned, in the given example  $\bar{u}_i - \bar{u}_{i-1}$ .

Table 4.3 shows some combinations of the parameters  $a_{ik}$ ,  $b_{ik}$ , and  $d_k$  for order 2 and order 3 schemes (taken from Cockburn et al. [1990]). For explicit schemes, the so-called Courant–Friedrichs–Lewy (or CFL) condition has to be fulfilled, claiming that the domain of dependence of a finite difference method should include the domain of dependence of a partial differential equation (PDE), see Courant et al. [1928]. This condition must be satisfied at least in the limit case where the discretization length tends to zero. The CFL condition is a necessary, but not sufficient condition for stability.

The Courant number  $N_{CFL}$  of a linear one-dimensional system with discretization length  $\Delta x$  is given by

$$N_{CFL} = \frac{v\Delta t}{\Delta x}. \tag{4.146}$$

The numerical scheme has to provide  $N_{CFL} \leq 1$  to ensure that information does not spread further than one grid step per time step.

order	$a_{ik}$		$b_{ik}$		$d_k$
2	1		1		1
	$\frac{1}{2}$	$\frac{1}{2}$	0	$\frac{1}{2}$	1
3	1		1		0
	$\frac{3}{4}$	$\frac{1}{4}$	0	$\frac{1}{4}$	1
	$\frac{1}{3}$	0	$\frac{2}{3}$	0	$\frac{1}{2}$

Table 4.3: Parameters  $a_{ik}$ ,  $b_{ik}$ , and  $d_k$  for Runge-Kutta schemes of orders 2 and 3 (taken from Cockburn et al. [1990])

## 4.3 Space Discretization

For discretization in space, DG finite element methods are used in the frame of this work. To check their accuracy, they will be compared to streamline methods in the numerical studies of Section 6. For the purpose of this work, the most favorable property of streamline methods is that they are—at least in the case of a linear saturation equation—basically free of numerical diffusion. In addition, tracing of streamlines is necessary for the solution of the upscaled saturation equation.

For these reasons, the DG discretization is studied in Section 4.3.1, while streamline methods are addressed in Section 4.3.2.

### 4.3.1 Discontinuous Galerkin Method

Solving the equations describing multi-phase–multi-component processes numerically, pressure equation, saturation equation and concentration equation(s) have to be discretized separately because of their different mathematical character.

The discretization of the pressure equation is studied in Section 4.3.1.1, while the saturation equation is considered in Section 4.3.1.2 and the concentration equations in Section 4.3.1.3.

#### 4.3.1.1 DG for the Pressure Equation

The following derivation principally follows the paper by Bastian [2003] and the work of Reichenberger et al. [2004].

Recalling the pressure equation given by Equations (3.73) through (3.75),

$$\nabla \cdot \underline{v} = -\frac{\partial \phi}{\partial t} - \sum_{\alpha} \frac{1}{\rho_{\alpha}} \left( \phi S_{\alpha} \frac{\partial \rho_{\alpha}}{\partial t} + \underline{v}_{\alpha} \nabla \rho_{\alpha} - \rho_{\alpha} q_{\alpha} \right) \quad \text{in } \Omega \quad (4.147)$$

$$\underline{v} = -\lambda \underline{K} \cdot (\nabla \tilde{p} - \underline{G}), \quad \text{and} \quad (4.148)$$

$$\tilde{p} = p_n - \int_{S_c}^{S_w} f_w \frac{dp_c(\xi)}{dS_w} d\xi, \quad (4.149)$$

where  $\Omega$  is a domain in  $\mathbb{R}_2$  with outward unit normal  $\underline{n}$ , an accurate approximation of the total velocity has to be obtained as this is the parameter needed for the solution of the saturation equation. The DG scheme for the pressure equation is derived for the case  $\underline{G} = \underline{0}$ ,  $\rho_{\alpha} = \text{const.}$ ,  $\phi = \text{const.}$ ,  $q_{\alpha} = 0$  and  $p_c = 0$  implying  $\tilde{p} = p_w = p_n =: p$ , which corresponds to the simplifications applied within this work, see Section 1.3.



For a given wetting-phase saturation  $S_w$ , the pressure equation is elliptic. The parameter  $E_h$  is defined as a non-degenerate subdivision of  $\Omega$  which does not have to be a triangulation and which may contain elements of mixed type, i.e. a combination of triangles and quadrilaterals is allowed.

For basis and test functions, the space of polynomial functions of degree  $r$  on an element  $e \in E_h$  is defined as

$$P_r(\Omega_e) = \{w : \Omega_e \rightarrow \mathbb{R} | w(x, y) = \sum_{0 \leq a+b \leq r} c_{ab} x^a y^b\}, \quad (4.150)$$

where  $P_r$  can be a basis for triangles and quadrilaterals. These basis polynomials  $P_r$  are chosen to be  $L_2$  orthogonal on the reference element. They are created from the monomials by *Gram-Schmidt orthonormalization*. This is a procedure which takes a non-orthogonal set of linearly independent functions and constructs an orthogonal basis over an arbitrary interval with respect to an arbitrary weighting function, see Arfken [1985].

As an example, the resulting  $P_2$  polynomials

$$P_2(\Omega_e) = c_{00} + c_{10}x + c_{01}y + c_{11}xy + c_{20}x^2 + c_{02}y^2 \quad (4.151)$$

with coefficients  $c_{ab}$  as given in Appendix C are plotted in Figure 4.40. One can see that there are six of these  $P_2$  polynomials, one of degree 0, two of degree 1, and three of degree 2.

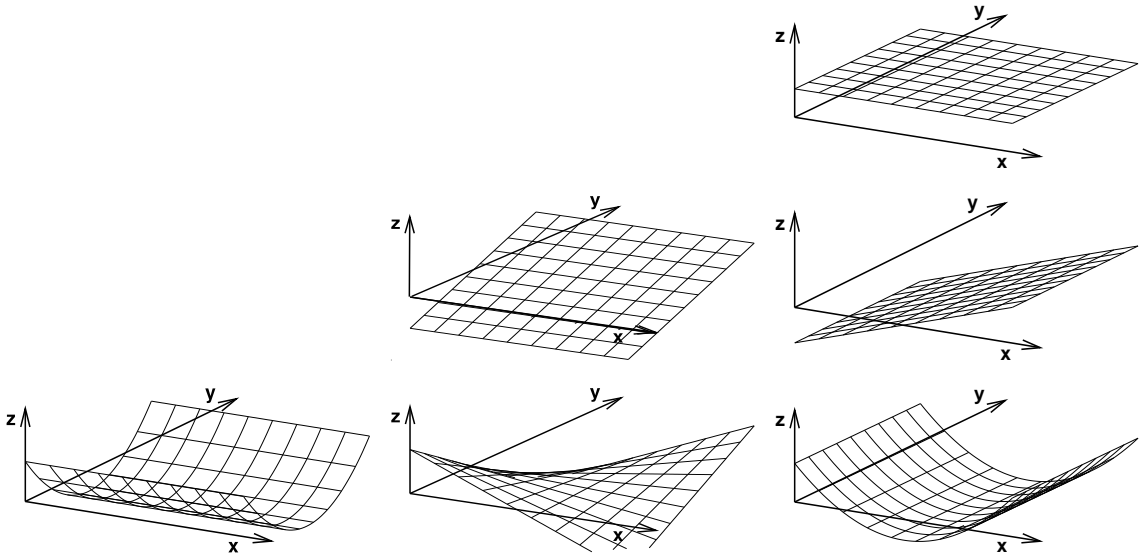


Figure 4.40: Basis functions  $P_2$  for DG discretization (First line: degree 0 polynomials, second line: degree 1, third line: degree 2).

The space of trial functions  $V^r(E_h)$  is taken as

$$V^r(E_h) = \prod_{e \in E_h} P_r(\Omega_e). \quad (4.152)$$

For DG schemes, functions in  $V^r(E_h)$  are discontinuous on the internal skeleton  $\Gamma_{int}$  consisting of the interior boundaries between two elements  $e$  and  $f$ ,

$$\Gamma_{int} = \{\Gamma_{e,f} | \Gamma_{e,f} = \partial\Omega_e \cap \partial\Omega_f \forall e, f \in E_h, e \neq f\}. \quad (4.153)$$

The exterior skeleton  $\Gamma_{ext}$  is defined in an analogous way as the set of the element edges at the boundary  $\partial\Omega$  of domain  $\Omega$ ,

$$\Gamma_{ext} = \{\Gamma_e | \Gamma_e = \partial\Omega_e \cap \partial\Omega \forall e \in E_h\}. \quad (4.154)$$

A unique normal vector  $\underline{n}$  is associated with every interior edge  $\Gamma_{e,f}$  in considering the numbering of the elements. Thus, the normal vector  $\underline{n}$  points from element  $e$  to element  $f$  if the element number of  $e$  is larger than that of  $f$ , whereas it points from  $f$  to  $e$  if the element number of  $f$  is the larger one.

Furthermore, the jump  $[N]$  of a function  $N \in V^r(E_h)$  is defined as

$$[N](\underline{x}) = \lim_{\epsilon \rightarrow 0^+} N(\underline{x} + \epsilon \underline{n}) - \lim_{\epsilon \rightarrow 0^+} N(\underline{x} - \epsilon \underline{n}), \quad (4.155)$$

and the average  $\{N\}$  of  $N \in V^r(E_h)$  as

$$\{N\}(\underline{x}) = \frac{1}{2} \left( \lim_{\epsilon \rightarrow 0^+} N(\underline{x} + \epsilon \underline{n}) + \lim_{\epsilon \rightarrow 0^+} N(\underline{x} - \epsilon \underline{n}) \right). \quad (4.156)$$

With these definitions, one sees that

$$[NM] = [N]\{M\} + \{N\}[M] \quad (4.157)$$

is valid.

One now has the ingredients to actually derive a DG discretization of the pressure equation. First, the pressure equation for an element is considered taking into account the simplifying assumptions mentioned above,

$$\int_{\Omega_e} (\nabla \cdot (\lambda(S_w) \underline{K} \nabla p)) \, d\underline{x} = 0. \quad (4.158)$$

Multiplication by a test function  $N \in P^r(\Omega_e)$  and integration by parts gives for element  $e$

$$\int_{\Omega_e} \lambda(S_w) \underline{K} \nabla p \cdot \nabla N \, d\underline{x} - \int_{\Gamma_e} \lambda(S_w) \underline{K} \nabla p \cdot \underline{n} N \, d\underline{s} = 0. \quad (4.159)$$

Next, it is summed over all elements  $e$  in  $E_h$  and boundary integrals are separated into integrals belonging to the interior and exterior skeleton:

$$\begin{aligned}
& \sum_{e \in E_h} \int_{\Omega_e} \lambda(S_w) \underline{\underline{K}} \nabla p \cdot \nabla N d\mathbf{x} \\
& - \sum_{\Gamma_{e,f} \in \Gamma_{int}} \int_{\Gamma_{e,f}} [\lambda(S_w) \underline{\underline{K}} \nabla p \cdot \underline{n} N] d\mathbf{s} \\
& - \sum_{\Gamma_e \in \Gamma_{ext}} \int_{\Gamma_e} \lambda(S_w) \underline{\underline{K}} \nabla p \cdot \underline{n} N d\mathbf{s} \\
& = 0.
\end{aligned} \tag{4.160}$$

Considering the integral over interior edges,  $\int_{\Gamma_{e,f} \in \Gamma_{int}} [\lambda(S_w) \underline{\underline{K}} \nabla p \cdot \underline{n} N] d\mathbf{s}$ , one has to formulate two interface conditions to deal with the pressure equation as a second order elliptic equation. These two conditions are:

1. continuity of pressure,  $[p] = 0$ , and
2. continuity of normal flux,  $[\lambda(S_w) \underline{\underline{K}} \nabla p \cdot \underline{n}] = 0$ .

This second condition helps to reformulate the integral over interior edges,

$$[\lambda(S_w) \underline{\underline{K}} \nabla p \cdot \underline{n} N] = [\lambda(S_w) \underline{\underline{K}} \nabla p \cdot \underline{n}] \{N\} + \{\lambda(S_w) \underline{\underline{K}} \nabla p \cdot \underline{n}\} [N] = \{\lambda(S_w) \underline{\underline{K}} \nabla p \cdot \underline{n}\} [N]. \tag{4.161}$$

The bilinear form follows by inserting this flux boundary condition, separating boundary integrals into the Dirichlet ( $\Gamma_D$ ) and the Neumann part  $\Gamma_N$  and moving terms independent of  $p$  to the right hand side term  $f_h(N)$ ,

$$\begin{aligned}
a_h(p, N) &= \sum_{e \in E_h} \int_{\Omega_e} \lambda(S_w) \underline{\underline{K}} \nabla p \cdot \nabla N d\mathbf{x} \\
&+ \sum_{\Gamma_{e,f} \in \Gamma_{int}} \int_{\Gamma_{e,f}} \{\lambda(S_w) \underline{\underline{K}} \nabla N \cdot \underline{n}\} [p] - \{\lambda(S_w) \underline{\underline{K}} \nabla p \cdot \underline{n}\} [N] d\mathbf{s} \\
&+ \sum_{\Gamma_e \in \Gamma_D} \int_{\Gamma_e} (\lambda(S_w) \underline{\underline{K}} \nabla N \cdot \underline{n}) p - (\lambda(S_w) \underline{\underline{K}} \nabla p \cdot \underline{n}) N d\mathbf{s}, \tag{4.162}
\end{aligned}$$

$$\begin{aligned}
f_h(N) &= \sum_{\Gamma_e \in \Gamma_D} \int_{\Gamma_e} (\lambda(S_w) \underline{\underline{K}} \nabla N \cdot \underline{n}) p_D d\mathbf{s} \\
&+ \sum_{\Gamma_e \in \Gamma_N} \int_{\Gamma_e} N q_N d\mathbf{s}, \tag{4.163}
\end{aligned}$$

where  $q_N$  is the Neumann flux boundary condition, and  $p_D$  denotes the Dirichlet boundary condition for pressure.

Following the Baumann–Oden DG method introduced in Baumann and Oden [1999], and Oden et al. [1998], the mathematical problem can be formulated as:

Find  $p \in V^r(E_h)$  such that  $\forall N \in V^r(E_h)$

$$a_h(p, N) = f_h(N). \quad (4.164)$$

Other approaches like the nonsymmetric interior penalty Galerkin method (NIPG) by Rivière and Wheeler add an additional penalty term which depends on user-defined parameters. While the NIPG method is already stable for a polynomial order  $k$  of one (it is stable for all  $k \geq 1$ ), the Baumann–Oden scheme requires  $k \geq 2$ . Within this work, the Baumann–Oden approach is chosen because it is independent of user-defined parameters and because it is computationally cheaper.

Note, that the Darcy velocities

$$\underline{v} = -\lambda(S_w)\underline{K} \cdot \nabla p \quad (4.165)$$

resulting from the solution of the discretized pressure equation are discontinuous across element boundaries and do not have continuous normal components  $\underline{v} \cdot \underline{n}$ . That means, that the average flux  $\{\underline{v} \cdot \underline{n}\}$  at an edge is not equal to the fluxes evaluated inside the adjacent elements. For most transport simulations (solution of saturation equation and concentration equation), however, continuous normal components of the velocity are required to ensure a locally mass-conservative discretization. One possibility to transform the discontinuous velocity field into one that is continuous across element edges, is to apply a Brezzi-Douglas-Marini ( $BDM_1$ , Brezzi et al. [1986], Bastian and Rivière [2003]) projection coming from the mixed finite element formulation, which makes the velocity field continuous across element boundaries without reducing the accuracy of the DG scheme.

Since the velocity field should be divergence-free, the space of divergence-free velocities  $BDM_1^0$  is defined in the  $BDM_1$  space as

$$BDM_1^0(e) = \{\underline{v} | \underline{v} \in BDM_1(e), \nabla \cdot \underline{v} = 0\}. \quad (4.166)$$

For Cartesian elements in 2D, the space  $BDM_1(e)$  is given by

$$BDM_1(e) = \{\underline{v} | \underline{v} = \underline{p}_1(x, y) + p \nabla \times (x^2 y) + q \nabla \times (y^2 x), \underline{p}_1 \in (P_1)^2, p, q \in R\}, \quad (4.167)$$

see Brezzi and Fortin [1991]. This helps to evaluate  $v_x$  and  $v_y$  as

$$v_x = a_1 + b_1 x + c_1 y - p x^2 - 2q x y \quad (4.168)$$

$$v_y = a_2 + b_2 x + c_2 y + 2p x y + q y^2. \quad (4.169)$$

Applying the condition that the velocity field should be divergence-free gives

$$b_1 + c_2 = 0. \quad (4.170)$$

Thus, one can formulate the velocity field in  $BDM_1^0(e)$  as

$$v_x = a_1 + b_1x + c_1y - px^2 - 2qxy \quad (4.171)$$

$$v_y = a_2 + b_2x - b_1y + 2pxy + qy^2. \quad (4.172)$$

The unknowns  $a_1, a_2, b_1, b_2, c_1, p$ , and  $q$  are determined by inserting the boundary conditions at the edges of the element.

#### 4.3.1.2 DG for the Saturation Equation

For the derivation of the DG discretization of the saturation equation, i.e. the determination of the operator  $L$  introduced in Section 4.2, the saturation equation given in Equation (3.79) is considered with  $p_c = 0$ , and  $\underline{g} = \underline{0}$  as well as  $q_\alpha = 0, \rho_\alpha = \text{const.}$  and  $\phi = 1$  (the porosity is constant and used as a rescaling factor for time). These are the assumptions made within this work and given in Sections 1.3.

Thus, one is left with a saturation equation of the form

$$\frac{\partial S_w}{\partial t} + \nabla \cdot (f_w \underline{v}) = 0. \quad (4.173)$$

As will be discussed in Section 5.4, an upscaling of the saturation equation introduces a macrodispersion tensor  $\underline{D}$ . Therefore, the discretization of the upscaled saturation equation has to tackle an equation of the type

$$\frac{\partial S_w}{\partial t} + \nabla \cdot (f_w \underline{v} - \underline{D}(\underline{v}) \nabla S_w) = 0. \quad (4.174)$$

When deriving the multi-scale algorithm with local multi-phase–multi-component processes, one will see that it is necessary to introduce a source / sink term in order to maintain local mass conservation, see Section 5.5. Therefore, the saturation equation is considered in its upscaled form

$$\frac{\partial S_w}{\partial t} + \nabla \cdot (f_w \underline{v} - \underline{D}(\underline{v}) \nabla S_w) - q_w = 0, \quad (4.175)$$

where one has to be aware of the fact that the unknowns might partly represent coarse-scale quantities. For further details, the reader is referred to Chapter 5.

The general procedure is similar to the procedure for the pressure equation and follows the steps taken in Cockburn et al. [1990].

First, Equation (4.175) is multiplied by  $N \in V^r(E_h)$ , and integrated over element  $e$ :

$$\frac{\partial}{\partial t} \int_{\Omega_e} S_w N \, d\underline{x} + \int_{\Omega_e} \nabla \cdot (f_w \underline{v} - \underline{\underline{D}}(\underline{v}) \nabla S_w) N \, d\underline{x} - \int_{\Omega_e} q_w N \, d\underline{x}. \quad (4.176)$$

Integrating by parts gives

$$\begin{aligned} \frac{\partial}{\partial t} \int_{\Omega_e} S_w N \, d\underline{x} &- \int_{\Gamma_{e,f}} (f_w \underline{v} - \underline{\underline{D}}(\underline{v}) \nabla S_w) \cdot \underline{n} N \, d\underline{s} + \int_{\Omega_e} (f_w \underline{v} - \underline{\underline{D}}(\underline{v}) \nabla S_w) \cdot \nabla N \, d\underline{x} \\ &- \int_{\Omega_e} q_w N \, d\underline{x} = 0, \end{aligned} \quad (4.177)$$

where the direction of  $\underline{n}$  is defined as given in Section 4.3.1.1.

Then, it is summed over all elements  $e$  in  $E_h$  and boundary integrals are separated into integrals belonging to the interior and to integrals belonging to the exterior skeleton:

$$\begin{aligned} &\frac{\partial}{\partial t} \sum_{e \in E_h} \int_{\Omega_e} S_w N \, d\underline{x} - \sum_{\Gamma_{e,f} \in \Gamma_{int}} \int_{\Gamma_{e,f}} (f_w \underline{v} - \underline{\underline{D}}(\underline{v}) \nabla S_w) \cdot \underline{n} N \, d\underline{s} \\ &+ \sum_{e \in E_h} \int_{\Omega_e} (f_w \underline{v} - \underline{\underline{D}}(\underline{v}) \nabla S_w) \cdot \nabla N \, d\underline{x} - \sum_{\Gamma_e \in \Gamma_{ext}} \int_{\Gamma_e} (f_w \underline{v} - \underline{\underline{D}}(\underline{v}) \nabla S_w) \cdot \underline{n} N \, d\underline{s} \\ &- \sum_{e \in E_h} \int_{\Omega_e} q_w N \, d\underline{x} = 0. \end{aligned} \quad (4.178)$$

Next, exterior boundaries are split into Dirichlet inflow ( $\Gamma_D^{in}$ ) and outflow ( $\Gamma_D^{out}$ ) as well as Neumann ( $\Gamma_N$ ) boundaries. The equation is then further transformed to

yield

$$\begin{aligned}
& \frac{\partial}{\partial t} \sum_{e \in E_h} \int_{\Omega_e} S_w N \, d\mathbf{x} + \sum_{e \in E_h} \int_{\Omega_e} (f_w \underline{v} - \underline{D}(\underline{v}) \nabla S_w) \cdot \nabla N \, d\mathbf{x} \\
& - \sum_{\Gamma_{e,f} \in \Gamma_{int}} \int_{\Gamma_{e,f}} [N] f_w^* \{ \underline{v} \cdot \underline{n} \} d\mathbf{s} \\
& - \sum_{\Gamma_{e,f} \in \Gamma_{int}} \int_{\Gamma_{e,f}} \{ \underline{D} \nabla N \cdot \underline{n} \} [S_w] - [N] \{ \underline{D} \nabla S_w \cdot \underline{n} \} d\mathbf{s} \\
& - \sum_{\Gamma_e \in \Gamma_D} \int_{\Gamma_e} \underline{D} \nabla N \cdot \underline{n} S_w - N \underline{D} \nabla S_w \cdot \underline{n} \, d\mathbf{s} \\
& - \sum_{\Gamma_e \in \Gamma_D^{out}} \int_{\Gamma_e} N f_w \underline{v} \cdot \underline{n} \, d\mathbf{s} \\
& = \sum_{e \in E_h} \int_{\Omega_e} q_w N \, d\mathbf{x} - \sum_{\Gamma_e \in \Gamma_N} \int_{\Gamma_e} q_N N \, d\mathbf{s} \\
& + \sum_{\Gamma_e \in \Gamma_D^{in}} \int_{\Gamma_e} N f_w(S_w^0) \underline{v} \cdot \underline{n} \, d\mathbf{s} - \sum_{\Gamma_e \in \Gamma_D} \int_{\Gamma_e} \underline{D} \nabla N \cdot \underline{n} S_w^0 \, d\mathbf{s}, \tag{4.179}
\end{aligned}$$

where  $S_w^0$  is the Dirichlet condition for the wetting-phase saturation and  $q_N$  is the Neumann flux boundary condition. The parameter  $f_w^*$  is the upwinded convective term,

$$f_w^*(S_w(\underline{x}, \underline{x})) = \begin{cases} \lim_{\epsilon \rightarrow 0^+} f_w(S_w(\underline{x} - \epsilon \underline{n}), \underline{x} - \epsilon \underline{n}) & \text{if } \{ \underline{v} \cdot \underline{n} \} \geq 0 \\ \lim_{\epsilon \rightarrow 0^+} f_w(S_w(\underline{x} + \epsilon \underline{n}), \underline{x} + \epsilon \underline{n}) & \text{else} \end{cases}. \tag{4.180}$$

#### 4.3.1.3 DG for the Concentration Equations

The simplified concentration equations which take into account the assumptions of Section 1.3 are of a form similar to the simplified saturation equation. The only principal differences are

- that the advective term is summed up over the phases,
- that no diffusive / dispersive term has to be taken into account, and finally
- that no source / sink term has to be considered.

Thus, a discretization of the simplified concentration equation

$$\frac{\partial C^\kappa}{\partial t} + \nabla \cdot \left[ \sum_{\alpha} C_{\alpha}^{\kappa} f_{\alpha} \underline{v} \right] = 0 \tag{4.181}$$

is searched.

The discretized equation for the total concentration of component  $\kappa$  can be directly written in analogy to the saturation equation of Section 4.3.1.2 as

$$\begin{aligned}
& \frac{\partial}{\partial t} \sum_{e \in E_h} \int_{\Omega_e} C^\kappa N \, d\underline{x} \\
& + \sum_{\alpha} \left( \sum_{e \in E_h} \int_{\Omega_e} (C_{\alpha}^{\kappa} \underline{v}) \cdot \nabla N \, d\underline{x} \right) \\
& - \sum_{\alpha} \left( \sum_{\Gamma_{e,f} \in \Gamma_{int}} \int_{\Gamma_{e,f}} [N] C_{\alpha}^{\kappa,*} \{ \underline{v} \cdot \underline{n} \} \, d\underline{s} \right) \\
& - \sum_{\alpha} \left( \sum_{\Gamma_e \in \Gamma_D^{out}} \int_{\Gamma_e} N C_{\alpha}^{\kappa} \underline{v} \cdot \underline{n} \, d\underline{s} \right) \\
& = - \sum_{\Gamma_e \in \Gamma_N} \int_{\Gamma_e} q_N N \, d\underline{s} \\
& + \sum_{\alpha} \left( \sum_{\Gamma_e \in \Gamma_D^{in}} \int_{\Gamma_e} N f_{\alpha} (C_{\alpha}^{\kappa,0}) \underline{v} \cdot \underline{n} \, d\underline{s} \right). \tag{4.182}
\end{aligned}$$

Again,  $C_{\alpha}^{\kappa,*}$  is the upwinded value of the concentration of component  $\kappa$  in phase  $\alpha$ .

### 4.3.2 Streamline Methods

Streamline methods are increasingly famous in reservoir engineering because they are easy, accurate and efficient. However, while they are appropriate for hyperbolic problems, their application to equations with diffusive / dispersive terms is limited. Here, they are only applied to purely hyperbolic problems and used as a verification method for DG results in the case of a linear saturation equation where the streamline methods show a minimum amount of numerical diffusion.

In this work, streamline methods are used for two purposes:

#### 1. Calculation of streamline length:

For the solution of an upscaled saturation equation (see Section 5.4), a macrodispersion term has to be evaluated depending on streamline lengths  $\underline{L}(\underline{x}, t)$ . For the evaluation of these streamline lengths, streamlines have to be traced back from element edges. Therefore, *streamline tracing* is needed which is discussed in Section 4.3.2.1.



## 2. Construction of reference solutions:

Based on the streamline tracing, one-dimensional streamline equations can be solved along each streamline. As streamline methods can provide very accurate solutions for linear hyperbolic equations, streamline simulation is used for the linear fine-scale saturation equation to check the results obtained using DG schemes. The issue of streamline simulation is discussed in Section 4.3.2.2.

In the following, the main steps of streamline simulation are reviewed to clarify which parts of the entire streamline procedure are needed for both of the above purposes. In this work, the focus is on the case where gravity, capillary pressure as well as external sinks and sources are absent. Moreover, both the porous medium and the fluid phases are assumed to be incompressible. All this corresponds to the assumptions of Section 1.3.

Starting with the pressure equation as well as Darcy's law given in Equations (3.73) and (3.74), one obtains after including the above assumptions:

$$\nabla \cdot \underline{v} = 0, \text{ and} \quad (4.183)$$

$$\underline{v} = -\lambda(S_w)\underline{K} \cdot \nabla p. \quad (4.184)$$

Taking into account the assumptions, the saturation equation given in Equation (3.79) yields

$$\frac{\partial S_w}{\partial t} + \underline{v} \cdot \nabla f_w = 0. \quad (4.185)$$

To project the saturation equation onto a streamline, one needs the identity

$$\underline{v} \cdot \nabla = |\underline{v}| \frac{\partial}{\partial \xi}, \quad (4.186)$$

where  $\xi$  is the arc length along a streamline. Thus, the saturation equation given by Equation (4.185) can be reformulated as

$$\frac{\partial S_w}{\partial t} + |\underline{v}| \frac{\partial f_w}{\partial \xi} = 0. \quad (4.187)$$

The arc length  $\xi$  can then be transformed into a so-called *time of flight* coordinate  $\tau$  along a streamline given by

$$|\underline{v}| \frac{\partial}{\partial \xi} = \frac{\partial}{\partial \tau}. \quad (4.188)$$

This yields the final form of the saturation equation along a streamline as

$$\frac{\partial S_w}{\partial t} + \frac{\partial f_w}{\partial \tau} = 0. \quad (4.189)$$

Solving the pressure equation using the DG scheme given in Section 4.3.1.1, returns a pressure field. From the pressure field, velocities can be reconstructed using

Darcy's law given by Equation (4.184). Applying the  $BDM_1$  projection given in Section 4.3.1.1, the new velocity field is continuous across element edges. These continuous velocities are used to trace streamlines as will be described in Section 4.3.2.1. The saturation distribution which is known on the finite element grid, is projected onto the streamlines. Next, the one-dimensional saturation equation is solved along each streamline as discussed in Section 4.3.2.2. The new saturation distribution is then mapped back to the finite element grid and can then be used to update the pressure field, to recalculate the velocities and to trace a new set of streamlines.

Mostly, it is not necessary to update the pressure field at each time step in order to obtain accurate solutions, and several steps of the streamline solver can be done before recomputing the pressures.

In the frame of this work, streamline simulation is only performed for the case of linear relative permeability functions and a total mobility of  $\lambda = 1$ . In this case, the velocity field is stationary and can be calculated once at the beginning of the simulation. The special advantage in this case is that the mapping of the saturations back to the underlying grid has to be done only once at the end of the simulation. Thus, only a minimum amount of numerical diffusion is introduced.

#### 4.3.2.1 Streamline Tracing

Streamline tracing has been introduced by Pollock [1988] for regular grids. It is the standard technique used in most commercial simulators nowadays. Its advantages are that it provides flux conservative streamlines and that it is formulated in terms of time of flight  $\tau$ . Even though various improvements of Pollock's algorithm have been proposed in literature considering either the accuracy of the tracing itself and the mapping of saturations back and forth to the grid (Mallison et al. [2004], Matringe [2004]) or the extension to irregular grids (Cordes and Kinzelbach [1992], and Prévost [2000, 2003]), this work is restricted to the simplest and original tracing method proposed by Pollock [1988].

A streamline is a line in a flow field which runs at each point  $\underline{x}$  in space in the direction of the velocity  $\underline{v}(\underline{x})$  at this point. That means, that the velocity vectors represent at each location in a flow field the tangent to the streamline. Thus, it becomes clear that the velocity field is needed as a basis for streamline tracing.

We will review Pollock's method for the two-dimensional case, as the entire multi-scale-upscaling approach proposed in this work is formulated for two space dimensions. Using Pollock's method, the velocity field within an element is linearly

interpolated from the velocities at the element edges as

$$v_x = v_{x0} + A(x - x_0) = \frac{dx}{dt}, \quad (4.190)$$

$$v_y = v_{y0} + B(y - y_0) = \frac{dy}{dt}, \quad (4.191)$$

where

$$A = \frac{v_{x1} - v_{x0}}{x_1 - x_0}, \quad \text{and} \quad (4.192)$$

$$B = \frac{v_{y1} - v_{y0}}{y_1 - y_0}, \quad (4.193)$$

see Figure 4.41. Note that the velocities in each coordinate direction do only depend on this coordinate.

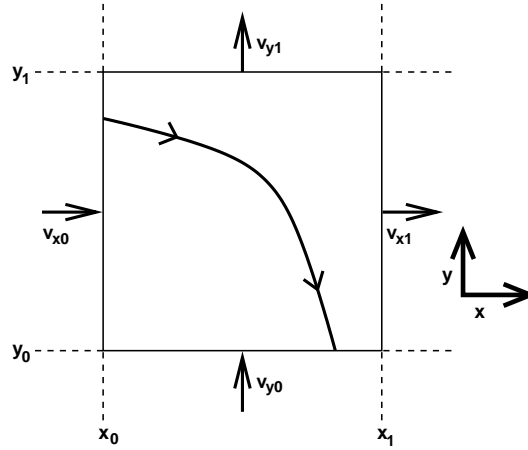


Figure 4.41: Streamline in a two-dimensional grid-block (after Pollock [1988]).

Reformulating Equation (4.190) yields

$$dt = \frac{dx}{v_{x0} + A(x - x_0)}. \quad (4.194)$$

This equation is integrated between the x-coordinate of the entry point,  $x_{in}$ , and the x-coordinate of a possible exit point  $x_{out}^*$ . This gives the time  $\Delta t^* = t_{out}^* - t_{in}$  needed for a particle to cross the considered grid block leaving the block through the considered face,

$$\Delta t^* = \frac{1}{A} \ln \left( \frac{v_{x,in}}{v_{x,out}^*} \right). \quad (4.195)$$

The time a particle would need to leave the grid block through one of the other faces, can be computed analogously. The actual exit face is then the face with the

minimum positive travel time  $\Delta t = \{\Delta t \mid \min(\Delta t^*), t \geq 0\}$ . This time period is called the *time of flight* of the particle through the considered grid block.

This time of flight is then used to compute the coordinates of the actual exit point  $\underline{x}_{out}$  as

$$x_{out} = \frac{1}{A} (v_{x,in} \exp(A\Delta t)) + x_0 \quad (4.196)$$

$$y_{out} = \frac{1}{A} (v_{y,in} \exp(B\Delta t)) + y_0. \quad (4.197)$$

When coding Pollock's method, several cases have to be treated separately, e.g. the case where both inflow and outflow velocity of one coordinate direction have opposite sign. For further details, see Pollock [1988] and the work of Hægland [2003] for the case of irregular grids.

Within the frame of this work, the length of a streamline within a grid block has to be approximated as it is needed for the macrodispersion term in the upscaled saturation equation. The details of this computation are discussed directly in connection with the upscaling technique in Section 5.4.1.

We will now further proceed in discussing how the streamline method can be used to solve the saturation equation.

#### 4.3.2.2 Front Tracking

As mentioned in the introductory Section 4.3.2, the (generally two- or three-dimensional) saturation equation on an initial finite element grid can be reformulated in terms of one-dimensional saturation equations along streamlines resulting in Equation (4.189).

This work follows the approach of Juanes et al. [2004] and Juanes and Lie [2005] who use a front tracking method to track saturations along streamlines. Therefore, only a rough outline of their approach is given and it is referred to the above-mentioned papers for further details. Whereas front tracking usually refers to numerical schemes using finite differences coupled with some scheme to detect discontinuities, the approach of Juanes et al. [2004] and Juanes and Lie [2005] is different in the sense, that all waves are represented as discontinuities. The solution of the transport equation is given as a set of moving discontinuities. These discontinuities are tracked along time-space rays. Whenever and wherever two of these rays cross, a Riemann problem is solved. Considering these Riemann problems, shocks are represented by shocks, and rarefaction waves are also resolved by a series of small discontinuities. This is done to ensure that the solution is always piecewise constant. Using front

tracking, discontinuities are represented exactly and rarefaction waves are represented approximately. Moreover, the method shows no grid-dependence and is unconditionally stable. Using a fast Riemann solver, the method can be very efficient.

A Riemann problem for the saturation equation is given by a piecewise constant initial condition in  $x$ -direction separated by one discontinuity,

$$S_w^0(x) = \begin{cases} S_w^L & \text{if } x < 0 \\ S_w^R & \text{if } x \geq 0, \end{cases} \quad (4.198)$$

where  $S_w^L$  denotes the left state, an injection boundary, and  $S_w^R$  is the right state, which is also identical to the initial condition.

Each Riemann problem is solved exactly, leading to a so-called local Riemann fan in the  $(x, t)$  plane. As wave speed, the Rankine-Hugoniot wave speed is used. When two rays of different Riemann fans cross, the corresponding Riemann fans interact. Therefore, a new Riemann fan has to be constructed each time two rays cross. This construction is sketched in Figure 4.42

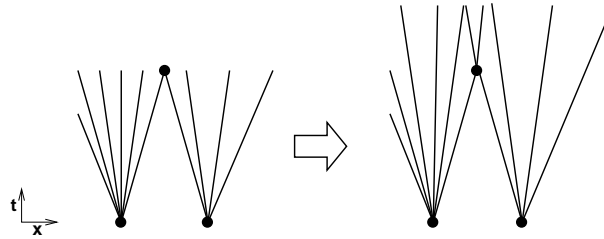


Figure 4.42: Construction of a solution of the streamline equations using Riemann fans.

The construction can be repeated up to an arbitrary level of accuracy. As rarefaction waves are also represented by a series of small shocks, the streamline equations given in Equation (4.189) can be solved in the same way. A drawback of front tracking is thus, that the number of discontinuities may blow up quickly. To mitigate this problem, waves which are smaller than some given tolerance are removed. Moreover, weak waves are treated in a simplified way by approximating them by only one or two shocks.

In this work, a front tracking code provided by Vegard Kippe and Knut-Andreas Lie from SINTEF technologies in Oslo, Norway, is used which is based on the work of Juanes et al. [2004] and Juanes and Lie [2005].

# 5 Multi-Scale Approach

## 5.1 Preliminary Remarks

This work is designed to be a first step into the direction of modeling complex systems as shown in Section 1.1. Therefore, some simplifying assumptions are made, being aware of the fact that the description of real-life systems requires further extensions. Specifically, presently

- only two-dimensional problems are considered,
- either two phases and two components (*phases*: water, gas, *components*: water, air), or three phases and three components are considered (*phases*: water, LNAPL, gas, *components*: water, LNAPL, air),
- only two scales (local scale and macro scale) are taken into account,
- gravitational forces are neglected ( $\underline{g} = \underline{0}$ ),
- capillary forces are neglected ( $p_c = 0$ ),
- local-scale hydrodynamic dispersion is neglected ( $\underline{\underline{D}}_{pm}^\kappa = 0$ ),
- the system is assumed to be isothermal ( $T = \text{const.}$ ),
- constant phase densities are assumed ( $\rho_\alpha = \text{const.}$ ),
- constant phase viscosities are assumed ( $\mu_\alpha = \text{const.}$ ),
- no change in the soil matrix  $\phi = \text{const.}$  is considered—the porosity is even set to one,  $\phi = 1$ , as it is simply a rescaling factor for time, and
- no external sinks and sources are considered in the domain, implying  $q_w = q_n = 0$  (no wells etc.).

The most severe simplification is the neglect of capillary forces. However, as mentioned above, the aim of this work is to make a first step into the direction of modeling processes of different complexity occurring on different scales. Therefore, the

principal aim is to create a framework and a platform for the handling of multi-scale processes. The complexity of the processes can in theory be easily extended. The neglect of capillary effects is especially due to the fact that the upscaling of the saturation equation is not an easy task in the capillary dominated case. Moreover, one might encounter problems with the choice of the formulation of the governing equations applied in this work, i.e. the fractional flow formulation. The reason for that is that for dominating capillary forces, pressure and saturation equation are strongly coupled. Despite or because of these challenges, it is planned to address the issue of capillarity in future work.

The neglect of gravity represents no restriction in the horizontal two-dimensional case that is considered in the frame of this work, however, for vertical two-dimensional or general three-dimensional problems, gravity has to be accounted for.

Another strong assumption is, that besides water and potential NAPL phase, also the gas phase is incompressible. This simplification is mainly done for the same two reasons, firstly, to be able to easily find an upscaled model, and secondly, the idea behind is to keep the model physically simple for the time being and to extend an existing multi-scale-upscaling framework for even more complex processes later on.

The assumption of an isothermal system is a simplification, but reasonable for the system under consideration. Within the saturated zone of the groundwater, temperature changes are often negligibly small—in middle Europe, e.g. an almost constant groundwater temperature of 10° C (283.15 K) is observed. In the unsaturated zone which is the system studied in this work, slight temperature changes may still occur, but the assumption of a constant temperature captures the main behavior of the natural system. However, in future research it is planned to examine the influence of possible temperature changes.

## 5.2 General Remarks

The final aim of the multi-scale strategy developed in this work is to model complex heterogeneous systems with locally occurring complex processes while being computationally efficient. Examples for such systems are shown in the application example in Figure 1.4 of Section 1.1.

In a local subdomain of interest, complex  $m$ -phase- $m$ -component processes are considered with  $m = 2$  or  $m = 3$ . As they are dependent on small-scale effects, they are modeled on the local scale. In the rest of the domain, the  $m$ -phase- $m$ -component

processes are of negligible impact. Therefore, a two-phase (gas–water) model is applied. This two-phase model is still dependent on local-scale heterogeneities. However, it is possible to apply an upscaling approach to model only one of the two two-phase equations on the local scale (the pressure equation, using a fractional flow formulation), and to model an upscaled saturation equation on the macro scale. The upscaled saturation equation accounts for subgrid effects, i.e. local-scale heterogeneities, by a subgrid term. An overview of the solution strategy is given in Section 5.3. while a detailed presentation is given in Section 5.5. This subdivision in two parts is due to the fact, that the developed multi-scale algorithm is highly coupled to the upscaling approach which is explained in detail in Section 5.4.

A challenging task is the choice of the boundary conditions for the local  $m$ -phase– $m$ -component system. The problem is that they are dependent on the solution of the global two-phase problem. That means, that these boundary conditions have to be updated each time step.

The issue of scales is directly related to the discretization discussed in Chapter 4. The local scale is associated with a fine resolution, i.e. a fine grid, whereas a macro-scale element contains a number of local-scale elements, i.e. a coarse grid is chosen on the macro scale. Also, the applied upscaling approach is semi-discrete, i.e. it can only be understood in connection with a certain grid. In this work, only grids with square elements are used, although the equations presented are also valid for rectangular grids.

Due to the fact, that saturation and concentration equations are solved time-explicitly, the CFL condition has to be fulfilled on the fine grid as well as on the coarse grid. This means, that a local time stepping has to be applied for the solution of the fine-grid concentration equations using a local time step corresponding to the ratio of discretization lengths.

Now, an overview of the differential equations on the local scale is given which have to be solved taking into account the above assumptions:

- the pressure equation:

$$\nabla \cdot \underline{v} = \nabla \cdot (\lambda(S_w) \underline{K} \nabla p) = 0, \quad (5.199)$$

- the saturation equation (to be upscaled!):

$$\frac{\partial S_w}{\partial t} + \underbrace{\nabla \cdot (f_w \underline{v})}_{=\underline{v} \cdot \nabla f_w} = 0, \quad (5.200)$$



- one or two concentration equations (with  $\kappa = 1$  for a local 2p2c problem and  $\kappa \in \{1, 2\}$  for a local 3p3c problem):

$$\frac{\partial C^\kappa}{\partial t} + \underbrace{\nabla \cdot \left[ \sum_{\alpha} C_{\alpha}^{\kappa} f_{\alpha} \underline{v} \right]}_{=\underline{v} \cdot \nabla \sum_{\alpha} C_{\alpha}^{\kappa} f_{\alpha}} = 0. \quad (5.201)$$

The fine-scale saturation equation given in Equation (5.200) corresponds to the well-known Buckley-Leverett problem for which Buckley and Leverett [1942] found an analytical solution. This solution serves as a verification method for numerical schemes modeling advection-dominated multi-phase flow without capillary effects.

## 5.3 Overview of the Solution Concept

In this Section, the general solution concept developed in this work to solve the model problem outlined in Section 5.2 is explained only schematically. The detailed form of the concept is explained in Section 5.5 after having studied the upscaling of the saturation equation.

Figure 5.43 gives an overview of the solution strategy. The pressure equation is solved in the whole domain on a fine grid, i.e. a small scale, the local scale. The saturation equation is solved also in the whole domain, but in its upscaled form on a coarse grid, representing the macro scale. The  $m - 1$  concentration equations finally are solved only in a subdomain of the solution domain, where  $m$ -phase- $m$ -component processes have a non-negligible influence. As they are highly dependent on local-scale processes, they are also solved on a fine grid, coinciding with the one that is used for the solution of the pressure equation.

From the solution of the pressure equation which gives the pressure field in the whole domain, one can calculate phase velocities  $v_{\alpha}$  and the total velocities  $\underline{v}$ . These velocities are needed for the solution of the upscaled saturation equation as well as for the solution of the  $m - 1$  concentration equations (a). After solving the pressure equation, the concentration equations are solved. The resulting quantities are the fine-grid total concentrations. Using flash calculations as introduced in Section 3.4, saturations can be reconstructed from the total concentrations which then enter (in averaged form) into the solution of the upscaled saturation equation (b). The new saturation distribution is then used to determine the pressure field of the next time step (c).

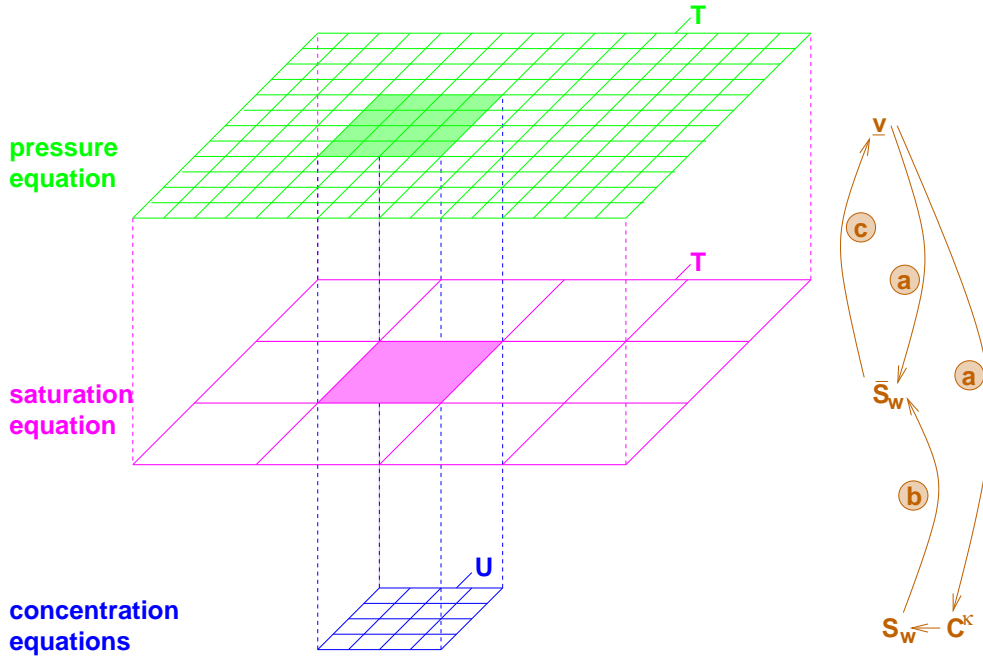


Figure 5.43: Overview of the solution strategy pursued in this work.

## 5.4 Upscaling: the Concept of Volume Averaging

In this section, the upscaling approach taken in this work is described which serves to scale up the fine-scale (local-scale) saturation equation to the coarse scale (macro scale). This approach follows the work of Efendiev et al. [2000] for a linear Buckley-Leverett problem and the paper of Efendiev and Durlofsky [2002] for a nonlinear Buckley-Leverett problem. Their approach is semi-discrete, i.e. it is directly associated with a certain numerical scheme, in their case, a classical finite volume scheme. Large parts of this section are directly taken from the work of Efendiev et al. [2000] and Efendiev and Durlofsky [2002]. Note, that the given upscaling approach is only valid in the preasymptotic case, i.e. for relatively large correlation length, before macrodispersion reaches its constant value, see Section 2.6.4. Efendiev et al. [2000] and Efendiev and Durlofsky [2002] connected their volume averaged saturation equation with a finite volume (FV) discretization, while in this work, it is connected with the DG discretization discussed in Section 4.3.1.2.

The general idea of volume averaging, here for a 2D element with area  $A$  can be understood considering Figure 5.44. The unknown parameters, here water saturation  $S_w$  and total velocity  $\underline{v}$ , are averaged over the coarse-grid blocks, i.e.

$$\begin{aligned} \underline{v} &= \bar{v} + v', & S_w &= \bar{S}_w + S'_w \\ \text{with } \bar{\cdot} &= \frac{1}{A} \int_A \cdot(\underline{x}, t) dA, \end{aligned} \quad (5.202)$$

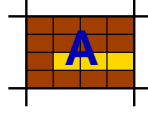


Figure 5.44: Averaging over a coarse-grid block.

where the overbar denotes coarse-grid (block-averaged) quantities and the prime denotes fluctuating quantities.

The upscaling of the linear saturation equation is discussed in Section 5.4.1, whereas the nonlinear equation is treated in Section 5.4.2.

### 5.4.1 Volume Averaging for a Linear Buckley-Leverett Problem

In this section, the upscaling of the saturation equation is studied including two further restrictions. This is done in order to start with a mathematically relatively simple linear hyperbolic equation. First, the Buckley-Leverett equation given in Equation (5.200) is recalled which represents the fine-scale saturation equation

$$\frac{\partial S_w}{\partial t} + \underline{v} \cdot \nabla f_w = 0. \quad (5.203)$$

It is now assumed that the relative permeabilities of each phase are a linear function of the saturation of that phase and that there are no residual saturations,  $S_{wr} = S_{nr} = 0$ , i.e.

$$k_{rw} = S_w, \text{ and} \quad (5.204)$$

$$k_{rn} = 1 - S_w. \quad (5.205)$$

Furthermore, equality of the viscosities is assumed  $\mu_w = \mu_n = 1$ . Then, one is left with a linear transport equation of the form

$$\frac{\partial S_w}{\partial t} + \underline{v} \nabla S_w = 0. \quad (5.206)$$

The corresponding pressure equation reduces to

$$\nabla \cdot (\underline{K} \nabla p) = 0, \quad (5.207)$$

as  $\lambda = \lambda_w + \lambda_n = \frac{k_{rw}}{\mu_w} + \frac{k_{rn}}{\mu_n} = \frac{S_w}{1} + \frac{1-S_w}{1} = 1$ . That means, the pressures are constant in time and the total velocity field is stationary.

Next, the volume averaging approach for the linear saturation equation given by Equation (5.206) is studied. Inserting the representations of  $S_w$  and  $\underline{v}$  of Equation

(5.202) in Equation (5.206) and averaging the resulting relationship over coarse-grid blocks leads to the averaged saturation equation

$$\frac{\partial \bar{S}_w}{\partial t} + \bar{\underline{v}} \cdot \nabla \bar{S}_w + \overline{\underline{v}' \cdot \nabla S'_w} = 0. \quad (5.208)$$

One can see, that the third term of this averaged saturation equation still contains fine-grid quantities ( $\underline{v}'$ ,  $S'_w$ ). To estimate them, the first step is to calculate a fluctuating saturation equation.

The fluctuating equation can be obtained by subtracting Equation (5.208) from Equation (5.206)

$$\frac{\partial S'_w}{\partial t} + \bar{\underline{v}} \cdot \nabla \bar{S}_w + \underline{v}' \cdot \nabla \bar{S}_w + \underline{v}' \cdot \nabla S'_w = \overline{\underline{v}' \cdot \nabla S'_w}. \quad (5.209)$$

It can be seen, that the right hand side of Equation (5.209) contains exactly the same subgrid quantity as the third term of Equation (5.208). The strategy is to treat the fluctuating equation given by Equation (5.209) in order to get an estimate of the subgrid term  $\overline{\underline{v}' \cdot \nabla S'_w}$  in the averaged saturation equation.

Therefore, Equation (5.209) is projected onto coarse-grid streamlines  $\frac{d\underline{x}}{dt} = \underline{v}$  which allows to combine the terms  $\frac{\partial S'_w}{\partial t}$  and  $\bar{\underline{v}} \cdot \nabla \bar{S}_w$  to  $\frac{\partial S'_w(t, \underline{x}(t))}{dt}$ . This leads to

$$\frac{dS'_w(t, \underline{x}(t))}{dt} + v'_j \cdot \nabla_j \bar{S}_w + v'_j \cdot \nabla_j S'_w = \overline{v'_j \cdot \nabla_j S'_w}, \quad (5.210)$$

where  $j \in \{x, y\}$  and where it is summed over repeated indices.

Next, integration of Equation (5.210) along streamlines from time  $\tau = 0$  to time  $\tau = t$  yields

$$\begin{aligned} S'_w(t, \underline{x}) = & - \int_0^t [v'_j(\underline{x}(\tau)) \nabla_j \bar{S}_w(\tau, \underline{x}(\tau)) \\ & + v'_j(\underline{x}(\tau)) \nabla_j S'_w(\tau, \underline{x}(\tau))] d\tau \\ & + \int_0^t \overline{v'_j(\underline{x}(\tau)) \nabla_j S'_w(\tau, \underline{x}(\tau))} d\tau, \end{aligned} \quad (5.211)$$

with  $(\underline{x}, t)$ , such that  $\underline{x}(t) = \underline{x}$ .

Then, it is multiplied by  $v'_i(\underline{x})$  and averaged over coarse-grid blocks. This gives

$$\begin{aligned} \int_A S'_w(t, \underline{x}) v'_i(\underline{x}) n_i dA = & - \int_A \int_0^t v'_i(\underline{x}) v'_j(\underline{x}(\tau)) \nabla_j \bar{S}_w(\tau, \underline{x}(\tau)) d\tau dA \\ & - \int_A \int_0^t v'_i(\underline{x}) v'_j(\underline{x}(\tau)) n_i \nabla_j S'_w(\tau, \underline{x}(\tau)) d\tau dA \\ & + \int_A \int_0^t v'_i(\underline{x}) n_i \overline{v'_j(\underline{x}(\tau)) \nabla_j S'_w(\tau, \underline{x}(\tau))} d\tau dA. \end{aligned} \quad (5.212)$$

The last term is definitely zero, as  $\bar{v}' = 0$  for each coarse-grid block. Furthermore, terms that are third order in varying quantities are neglected, i.e. the second term containing  $\underline{v}'\underline{v}'S'_w$ . This leaves

$$\int_A S'_w(t, \underline{x}) v'_i(\underline{x}) n_i dA \approx - \int_A \int_0^t v'_i(\underline{x}) v'_j(\underline{x}(\tau)) n_i \nabla_j \bar{S}_w(\tau, \underline{x}(\tau)) d\tau dA. \quad (5.213)$$

Inserting this estimation of the subgrid term in the averaged relationship given in Equation (5.208) results in

$$\begin{aligned} \frac{\partial \bar{S}_w}{\partial t} + \bar{v} \cdot \nabla \bar{S}_w = \\ \frac{1}{A} \nabla \cdot \int_A \int_0^t v'_i(\underline{x}) v'_j(\underline{x}(\tau)) \nabla_j \bar{S}_w(\tau, \underline{x}(\tau)) d\tau dA. \end{aligned} \quad (5.214)$$

As the time derivative of  $\bar{S}_w$  along streamlines is small, one can further transform the equation to

$$\begin{aligned} \frac{\partial \bar{S}_w}{\partial t} + \bar{v} \cdot \nabla \bar{S}_w = \\ \frac{1}{A} \nabla \cdot \int_A \left[ \int_0^t v'_i(\underline{x}) v'_j(\underline{x}(\tau)) d\tau \right] \nabla_j \bar{S}_w(t, \underline{x}) dA. \end{aligned} \quad (5.215)$$

Being aware of the fact that the covariance of the velocities represents in fact a dispersion term, it is possible to rewrite Equation (5.215) as

$$\frac{\partial \bar{S}_w}{\partial t} + \bar{v} \cdot \nabla \bar{S}_w = \nabla \cdot \frac{1}{A} \int_A \underline{D}(\underline{x}, t) \nabla \bar{S}_w(t, \underline{x}) dA \quad (5.216)$$

with the macrodispersion tensor

$$D_{ij}(\underline{x}, t) = \frac{1}{E} \int_E \left[ v'_i(\underline{x}) \int_0^t v'_j(\underline{x}(\tau)) d\tau \right] dE. \quad (5.217)$$

As numerical difficulties may occur when modeling the full two-point correlation of the variation of the velocities  $v'_i(\underline{x}, t) v'_j(\underline{x}(\tau), \tau)$ , one approximates the diagonal entries of the macrodispersion tensor by

$$D_{ii}(\underline{x}, t) \approx \alpha(\sigma, l_x, l_y) L_i(\underline{x}, t) |v'_i(\underline{x})|, \quad (5.218)$$

where  $L_i$  is the length of the coarse-grid streamline in direction  $i$ , and the parameters  $l_i$  are the respective correlation lengths, whereas  $\sigma$  is the standard deviation of the log-permeability field. The off-diagonal entries are equal to zero. Showing a high dependence on the standard deviation and a low dependence on the correlation length, the parameter  $\alpha$  is estimated as  $\alpha = \left(\frac{\sigma}{2}\right)^4$ .

Having so far derived an upscaled saturation equation, two issues still need to be addressed in more detail, i.e.

1. the exact evaluation of the coarse-scale velocity and
2. the approximation of the streamline lengths needed in the macrodispersion term.

### 1. Velocity averaging

To obtain coarse-scale velocities, one can simply apply a volume-averaging approach as given in Equation (5.202), where coarse-grid velocities are obtained as averages over coarse-grid cells. However, this velocity field will be discontinuous across coarse-element edges i.e., the flux from an element  $e$  to its neighbor  $f$  will be different from the flux from  $f$  to  $e$  and thus, this averaging approach will not be mass-conservative. A mass-conservative scheme is essential when modeling transport processes. Therefore, a different strategy for velocity averaging is pursued.

The principle averaging procedure is shown in Figure 5.45 in a 2D projection where, as an example, a coarse element contains four fine-scale elements along the coarse-grid edge. The DG solution of the pressure equation as described in Section 4.3.1.1 returns a pressure field that is discontinuous across fine-grid edges. Applying Darcy's law, a discontinuous velocity field is obtained. A  $BDM_1^0$  or short,  $BDM$ , projection as given in Section 4.3.1.1 is applied to make the velocity field continuous across fine-grid edges. Within a fine-grid element, the velocities are interpolated bilinearly. Next, the transition to the macro scale has to be considered. The fine-grid velocities are averaged over each coarse-element edge. This is an important point with respect to the mass-conservativity of the whole scheme. Within a coarse-grid element, the velocities are then linearly interpolated in  $x$ -direction and in  $y$ -direction. Note, that the fine-scale velocities are bilinear within an element for

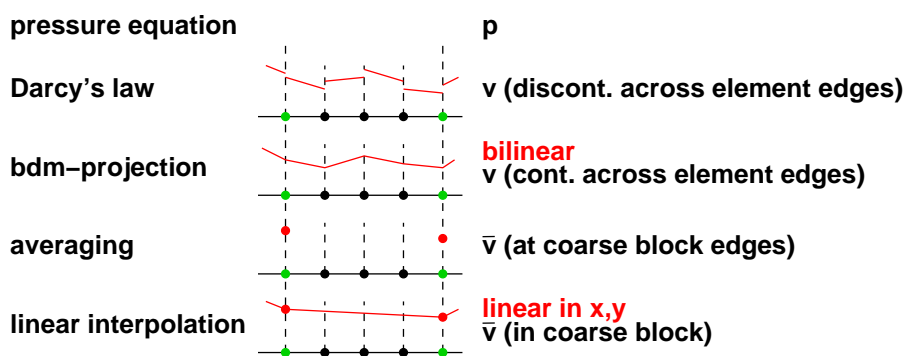


Figure 5.45: Two-dimensional projection showing the averaging procedure for the total velocity.

each velocity component  $v_i$ , see Figure 5.46, whereas the coarse-scale velocities are linear in each coordinate direction for both  $\bar{v}_x$  and  $\bar{v}_y$  as is illustrated in Figure 5.47.

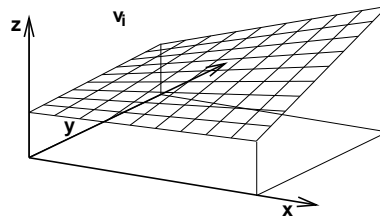


Figure 5.46: Bilinear representation of the velocity components within a fine-scale element.

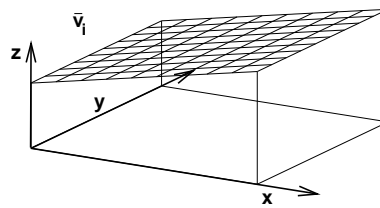


Figure 5.47: Linear representation of the velocity components within a coarse-scale element.

## 2. Streamline lengths

As can be seen, the evaluation of the macrodispersion tensor necessitates the calculation of the coarse-grid streamline length  $\underline{L}(\underline{x}, t) = \int_0^t v_j(\underline{x}(\tau)) d\tau$  which is growing with time. The backtracing of the streamlines is performed as discussed in Section 4.3.2.1. The actual length of the streamline has to be approximated numerically.

The approximation  $L_{j,\text{cell}}$  of  $L_j$  is derived for a unit cell, see Figure 5.48. The actual streamline length can then be obtained by simple scaling. The streamline length in

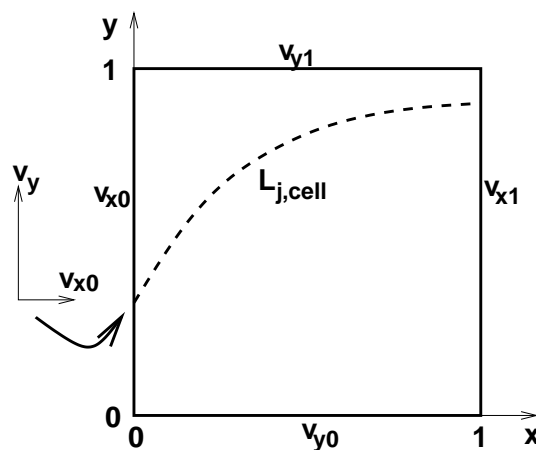


Figure 5.48: Approximation of the streamline length within a unit cell.

direction  $j$  is given by

$$L_{j,\text{cell}} = \int_0^{t_{\text{TOF}}} |v_j| dt, \quad (5.219)$$

where  $t_{\text{TOF}}$  is the time of flight within the unit cell.

The streamline length  $L_{j,\text{cell}}$  inside a cell is approximated numerically by  $m$  segments with constant velocity via

$$L_{j,\text{cell}} \approx \sum_{n=1}^m L_{j,n}, \quad (5.220)$$

where  $L_{j,\text{cell}}$  is calculated as the sum of the  $m$  small segments  $L_{j,n}$ . Being conscious of the fact that the velocity field of a unit cell is assumed linear in  $x$  and  $y$  direction,

$$v_x = (v_{x1} - v_{x0}) \cdot x + v_{x0} \quad (5.221)$$

$$v_y = (v_{y1} - v_{y0}) \cdot y + v_{y0}, \quad (5.222)$$

such a segment  $L_{j,n}$  can be calculated as

$$\begin{aligned} L_{j,n} &= |x_{j,n} - x_{j,n-1}| \\ &= |(v_{j,n-1} \Delta t + x_{j,n-1}) - x_{j,n-1}| \\ &= |[(v_{j1} - v_{j0})x_{j,n-1} + v_{j0}] \Delta t, \end{aligned} \quad (5.223)$$

where  $\Delta t = \frac{t_{\text{TOF}}}{m}$ .

### 5.4.2 Volume Averaging for a Nonlinear Buckley-Leverett Problem

This section deals with the upscaling of the general Buckley-Leverett equation, given in Equation (5.200)

$$\frac{\partial S_w}{\partial t} + \underline{v} \cdot \nabla f_w(S_w) = 0, \quad (5.224)$$

that means, a nonlinear hyperbolic equation is considered.

Again, the explanations given here follow the approach of Efendiev et al. [2000] and Efendiev and Durlofsky [2002], while adapting their FV-discretized equations to a DG scheme and again, the volume averaging technique introduced in Section 5.4 is used.

Inserting expressions for  $S_w$  and  $\underline{v}$  according to Equation (5.202) as well as an analogous expression for  $f_w$  in Equation (5.224) and averaging the resulting relationship over coarse-grid blocks gives

$$\frac{\partial \bar{S}_w}{\partial t} + \bar{\underline{v}} \cdot \nabla \bar{f}_w + \overline{\underline{v}' \cdot \nabla f'_w} = 0. \quad (5.225)$$



To estimate the subgrid term  $\overline{v' \cdot \nabla f'_w}$  in Equation (5.225), the fluctuating saturation equation is again calculated by subtracting Equation (5.225) from Equation (5.224). This results in

$$\frac{\partial S'_w}{\partial t} + \bar{v} \cdot \nabla \bar{f}'_w + \underline{v}' \cdot \nabla \bar{f}'_w + \underline{v}' \nabla f'_w = \overline{v' \cdot \nabla f'_w}. \quad (5.226)$$

Again, the right hand side term is identical to the subgrid term in the averaged equation. However, due to the nonlinearity of the fractional flow function  $f_w(S_w)$ , subgrid effects additionally occur in the term  $\bar{v} \cdot \nabla \bar{f}'_w$ .

Expanding the fractional flow function  $f_w(S_w)$  in terms of  $\bar{S}_w$  up to first order in  $\overline{v' S'_w}$  and  $\overline{S'_w S'_w}$  yields

$$f_w(S_w) = f_w(\bar{S}_w + S'_w) = f_w(\bar{S}_w) + f_{w,S}(\bar{S}_w)S'_w + \frac{1}{2}f_{w,SS}(\bar{S}_w)S'^2_w, \quad (5.227)$$

where

$$f_{w,S} = \frac{df_w(S_w)}{dS_w}, \text{ and} \quad (5.228)$$

$$f_{w,SS} = \frac{d^2 f_w}{(dS_w)^2}. \quad (5.229)$$

Averaging over Equation (5.227) gives an estimate for  $\bar{f}'_w$ , while calculating the difference between this averaged equation and Equation (5.227) gives an estimate for  $f'$ :

$$\bar{f}'_w = f_w(\bar{S}_w) + \frac{1}{2}f_{w,SS}(\bar{S}_w)\overline{S'^2_w} \quad (5.230)$$

$$f'_w = f_{w,S}(\bar{S}_w)S'_w. \quad (5.231)$$

Inserting these approximations of  $\bar{f}'_w$  and  $f'_w$  in Equation (5.225) and profiting of the fact that  $\nabla \cdot \underline{v} = 0$  yields

$$\frac{\partial \bar{S}_w}{\partial t} + \bar{v} \cdot \nabla f_w(\bar{S}_w) + \underbrace{\frac{1}{2} \nabla \cdot (\bar{v} f_{w,SS} \overline{S'^2_w})}_{F_{SS}} + \underbrace{\nabla \cdot (\underline{v}' f_{w,S}(\bar{S}_w) S'_w)}_{F_{vS}} = 0, \quad (5.232)$$

where the fluxes including varying quantities are denoted by  $F_{vS}$  for the term involving  $\underline{v}'$  and  $S'_w$ , and by  $F_{SS}$  for the term involving  $S'^2_w$ . For the linear case, the flux  $F_{SS}$  was equal to zero. In the work of Durlofsky [1997] and Durlofsky [1998], it was shown that the correlation of upscaled functions with  $F_{SS}$  is secondary. Therefore, like in the work of Efendiev and Durlofsky [2002], only the upscaling of  $F_{vS}$  is pursued while the term  $F_{SS}$  is neglected.

Averaging Equation (5.232) over the boundary of a coarse-grid block  $D$  with area  $A$  yields

$$\frac{\partial \bar{S}'_w}{\partial t} + \frac{1}{A} \int_{\partial D} \bar{v}_j f(\bar{S}_w) n_j dl + \frac{1}{A} \int_{\partial D} f_{w,S}(\bar{S}_w) v'_j S'_w n_j dl + \frac{1}{A} \int_{\partial D} \frac{1}{2} \bar{v}_j f_{w,SS}(\bar{S}_w) S'^2_w n_j dl = 0. \quad (5.233)$$

As for the unit mobility case discussed in Section 5.4.1, terms which are third order in varying quantities are neglected. Analogously to the proceeding there, the fluctuating equation is treated to estimate  $F_{v,S}$  in the averaged equation. And again in analogy to the proceeding in the linear case, the equation will be multiplied by the velocity variation  $\underline{v}'$  after several further transformation steps. Therefore, one can from now on neglect terms which are second order in varying quantities which allows to transform Equation (5.226) after inserting the approximations of  $\bar{f}_w$  and  $f'_w$  to

$$\frac{\partial S'_w}{\partial t} + \bar{v}_j S'_w f_{w,SS}(\bar{S}_w) \nabla_j \bar{S}_w + \bar{v}_j f_{w,S}(\bar{S}_w) \nabla_j S'_w + v'_j f_{w,S}(\bar{S}_w) \nabla_j \bar{S}_w - \overline{\nabla_j f_{w,S}(\bar{S}_w) v'_j S'_w} = 0, \quad (5.234)$$

where summation over repeated indices is implied.

The further procedure is to project Equation (5.234) onto coarse-grid streamlines given by  $\frac{d\underline{x}}{dt} = \underline{v} f_{w,S}(\bar{S}_w)$ . Taking into account the fact that

$$\frac{dS'_w(\underline{x}, t)}{dt} = \frac{\partial S'_w}{\partial t} + \bar{v}_j f_{w,S}(\bar{S}_w) \nabla_j S'_w, \quad (5.235)$$

Equation (5.234) can be formulated as

$$\frac{dS'_w(\underline{x}, t)}{dt} + \bar{v}_j S'_w f_{w,SS}(\bar{S}_w) \nabla_j \bar{S}_w + v'_j f_{w,S}(\bar{S}_w) \nabla_j \bar{S}_w - \overline{\nabla_j f_{w,S}(\bar{S}_w) v'_j S'_w} = 0. \quad (5.236)$$

Using the equality for an integrable function  $a(t)$

$$\frac{dS'_w}{dt} + a(t) S'_w = \exp\left(-\int_0^t a(\tau) d\tau\right) \frac{d}{dt} \left[ S'_w \exp\left(\int_0^t a(\tau) d\tau\right) \right], \quad (5.237)$$

where

$$a(t) = \bar{v}_j f_{w,SS}(\bar{S}_w) \nabla_j \bar{S}_w, \quad (5.238)$$

the fluctuating equation yields

$$\begin{aligned} & \exp\left(-\int_0^t \bar{v}_j(\underline{x}(\tau), \tau) f_{w,SS}(\bar{S}_w(\underline{x}(\tau), \tau)) \nabla_j \bar{S}_w(\underline{x}(\tau), \tau) d\tau\right) \\ & \cdot \frac{d}{dt} \left[ S'_w(\underline{x}(t), t) \exp\left(\int_0^t \bar{v}_j(\underline{x}(\tau), \tau) f_{w,SS}(\bar{S}_w(\underline{x}(\tau), \tau)) \nabla_j \bar{S}_w(\underline{x}(\tau), \tau) d\tau\right) \right] \\ & + v'_j(\underline{x}(t), t) f_{w,S}(\bar{S}_w(\underline{x}(t), t)) \nabla_j \bar{S}_w(\underline{x}(t), t) \\ & - \overline{\nabla_j f_{w,S}(\bar{S}_w(\underline{x}(t), t)) v'_j(\underline{x}(t), t) S'_w(\underline{x}(t), t)} = 0. \end{aligned} \quad (5.239)$$

After defining the coarse-scale function

$$H(\underline{x}(t), t) = \bar{v}_j(\underline{x}(t), t) f_{w,SS}(\bar{S}_w(\underline{x}(t), t)) \nabla_j \bar{S}_w(\underline{x}(t), t), \quad (5.240)$$

multiplying by  $\exp\left(\int_0^t H(\underline{x}(\tau), \tau) d\tau\right)$  and integrating over  $(0, t)$ , one obtains

$$\begin{aligned} S'_w(\underline{x}(t), t) \exp\left(\int_0^t H(\underline{x}(\tau), \tau) d\tau\right) &= - \int_0^t \exp\left(\int_0^\tau H(\underline{x}(\eta), \eta) d\eta\right) \\ &\cdot v'_j(\underline{x}(\tau), \tau) f_{w,S}(\bar{S}_w(\underline{x}(\tau), \tau)) \nabla_j \bar{S}_w(\underline{x}(\tau), \tau) d\tau \\ &+ \int_0^t \overline{\nabla_j f_{w,S}(\bar{S}_w(\underline{x}(\tau), \tau)) v'_j(\underline{x}(\tau), \tau) S'_w(\underline{x}(\tau), \tau)} \\ &\cdot \exp\left(\int_0^t H(\underline{x}(\tau), \tau) d\tau\right). \end{aligned} \quad (5.241)$$

Here, it is assumed that the initial conditions are given on the coarse grid, i.e.  $S'_w(\underline{x}(0), 0) = 0$ .

In the following, the last term will be denoted by

$$\Psi(\underline{x}(t), t) = \int_0^t \overline{\nabla_j f_{w,S}(\bar{S}_w(\underline{x}(\tau), \tau)) v'_j(\underline{x}(\tau), \tau) S'_w(\underline{x}(\tau), \tau)} \exp\left(\int_0^\tau H(\underline{x}(\eta), \eta) d\eta\right) d\tau. \quad (5.242)$$

Multiplying Equation (5.241) by  $\exp\left(-\int_0^t H(\underline{x}(\tau), \tau) d\tau\right)$  results in

$$\begin{aligned} S'_w(\underline{x}(t), t) &= - \int_0^t v'_j(\underline{x}(\tau), \tau) f_{w,S}(\bar{S}_w(\underline{x}(\tau), \tau)) \nabla_j \bar{S}_w(\underline{x}(\tau), \tau) \\ &\cdot \exp\left(-\int_\tau^t H(\underline{x}(\eta), \eta) d\eta\right) d\tau + \Gamma, \end{aligned} \quad (5.243)$$

with  $\Gamma = \Psi(\underline{x}(t), t) \exp\left(-\int_0^t H(\underline{x}(\tau), \tau) d\tau\right)$ .

The next step is to multiply Equation (5.243) by  $v'_i(\underline{x}, t) f_{w,S}(\bar{S}_w) n_i$  and to average it over the boundary of a coarse-grid block  $D$ . This yields

$$\begin{aligned} F_{vS}(\underline{x}, t) &= -\frac{1}{A} \int_{\partial D} v'_i(\underline{x}, t) f_{w,S}(\bar{S}_w) n_i \int_0^t v'_j(\underline{x}(\tau), \tau) f_{w,S}(\bar{S}_w(\underline{x}(\tau), \tau)) \\ &\cdot \nabla_j \bar{S}_w(\underline{x}(\tau), \tau) \exp\left(-\int_\tau^t H(\underline{x}(\eta), \eta) d\eta\right) d\tau dl \end{aligned} \quad (5.244)$$

The term including  $\Gamma$  vanishes as the average of  $\bar{v}' = 0$  over a coarse-grid edge.

To avoid numerical difficulties when modeling the full two-point correlation of the variation of velocities  $v'_i(\underline{x}, t) v'_j(\underline{x}(\tau), \tau)$ , one approximates its diagonal components by

$$v'_i(\underline{x}, t) v'_i(\underline{x}(\tau), \tau) \approx \alpha(\sigma, l_x, l_y) |v'_i(\underline{x}, t)| \bar{v}_i(\underline{x}(\tau), \tau), \quad (5.245)$$

whereas the off-diagonal entries are equal to zero. As for the linear case, the parameter  $\alpha$  is approximated as  $\alpha = \left(\frac{\sigma}{2}\right)^4$ .

Inserting this simplification into Equation (5.244) yields

$$F_{vS}(\underline{x}, t) = -\frac{\alpha}{A} \int_{\partial D} |v'_i(\underline{x}, t)| f_{w,S}(\bar{S}_w) n_i \int_0^t \bar{v}_j(\underline{x}(\tau), \tau) f_{w,S}(\bar{S}_w(\underline{x}(\tau), \tau)) \cdot \nabla_j \bar{S}_w(\underline{x}(\tau), \tau) \exp\left(-\int_\tau^t H(\underline{x}(\eta), \eta) d\eta\right) d\tau dl. \quad (5.246)$$

The original term for  $H(\underline{x}(\eta), \eta)$  is now re-inserted. Then the time integral over  $(0, t)$  can be expressed as

$$\begin{aligned} & \int_0^t v'_j(\underline{x}(\tau), \tau) f_{w,S}(\bar{S}_w(\underline{x}(\tau), \tau)) \cdot \nabla_j \bar{S}_w(\underline{x}(\tau), \tau) \\ & \cdot \exp\left(-\int_\tau^t \bar{v}_j \nabla_j \bar{S}_w f_{w,SS}(\bar{S}_w) d\eta\right) d\tau \\ & = \int_0^t \frac{f_{w,S}(\bar{S}_w(\underline{x}(\tau), \tau))}{f_{w,SS}(\bar{S}_w(\underline{x}(\tau), \tau))} \frac{d}{d\tau} \cdot \exp\left(-\int_\tau^t \bar{v}_j \nabla_j \bar{S}_w f_{w,SS}(\bar{S}_w) d\eta\right) d\tau \end{aligned} \quad (5.247)$$

Next, it is assumed that the time derivative of  $\bar{S}_w$  along streamlines is small as has been done for the linear case. This means, one can take the fraction  $f_{w,S}/f_{w,SS}$  out of the time integral which leads to

$$F_{vS}(\underline{x}, t) = -\frac{\alpha}{A} \int_{\partial D} |v'_i(\underline{x}, t)| f_{w,S}^2(\bar{S}_w) \cdot \frac{[1 - \exp(-\int_0^t \bar{v}_j(\underline{x}(\eta), \eta) d\eta f_{w,SS}(\bar{S}_w) \nabla_j \bar{S}_w)]}{f_{w,SS}(\bar{S}_w)} n_i dl. \quad (5.248)$$

Expanding the exponential term up to second order gives the form of the subgrid term, which is actually implemented,

$$F_{vS}(\underline{x}, t) = -\frac{\alpha}{A} \int_{\partial D} |v'_i(\underline{x}, t)| f_{w,S}^2(\bar{S}_w) \left[ L_j \nabla_j \bar{S}_w - \frac{1}{2} (L_j \nabla_j \bar{S}_w)^2 f_{w,SS} \right] n_i dl, \quad (5.249)$$

where  $L_j = \int_0^t \bar{v}_j(\underline{x}(\eta), \eta) d\eta$  is the length of the coarse-grid streamline. Note, that with  $f_w = S_w$ , exactly the same results as for the linear case are obtained and thus, the results are consistent with the results from Section 5.4.1.

One crucial issue occurring only in the nonlinear case still has to be addressed, that is, the determination of *fine-grid velocities*. As for the linear case, fine-grid quantities  $v'$  enter the subgrid term in the upscaled equation and furthermore, fine-scale velocities  $v$  are needed for the solution of the local fine-scale concentration equation(s). However, it is not obvious in the nonlinear case how to obtain these fine-scale velocities, as they depend—unlike in the linear case—on fine-scale saturations.

Considering the pressure equation given in Equation (5.199) as

$$\nabla \cdot \underline{v} = \nabla \cdot (\lambda(S_w) \underline{K} \nabla p) = 0, \quad (5.250)$$

it becomes obvious, that in order to resolve for fine-scale velocities, one needs to solve the fine-scale pressure equation. The crucial point is, that the fine-scale saturation field needed for the evaluation of  $\lambda(S_w)$  is not known, as the saturation equation is solved on the coarse grid. Therefore,  $\lambda(S_w)$  is approximated by  $\lambda(\bar{S}_w)$ . Numerical studies have shown that this approximation is reasonable for a wide range of correlation lengths, see e.g. Efendiev and Durlofsky [2002]. Furthermore, for highly heterogeneous porous media, the variation of absolute permeability governs the variation of fine-scale velocities.

To obtain fine-grid velocities, different other techniques besides the solution of a global fine-scale flow problem exist and have already been applied. One possibility is to solve fine-scale one-phase problems over regions corresponding to coarse-grid blocks or some extended coarse-grid block. This has been done in the work of Chen et al. [2003], Efendiev et al. [2000], and Efendiev and Durlofsky [2002]. A further possibility to mitigate a global fine-grid pressure solution is to include the different scales directly in the numerical model and to use multi-scale finite volumes or multi-scale finite elements as discretization technique, see e.g. Chen and Hou [2002] and Jenny et al. [2003]. Last but not least, one can also reconstruct coarse-scale permeabilities from a given fine-scale permeability field and solve the pressure equation entirely on the coarse scale. Fine-scale velocities can then be reconstructed using a downscaling approach.

As the emphasis of this work is not on sophisticated approaches to obtain fine-scale velocity fields, I stick to the easiest though expensive possibility of solving a global fine-scale pressure equation.

## 5.5 General Solution Strategy

Having studied volume averaging as the upscaling concept applied in this work, a closer look is taken at the general solution strategy to tackle the issue of multi-scale modeling in heterogeneous porous media which can be applied to systems as were shown in Figures 1.7 and 1.8. This is a detailed outline of the solution strategy briefly introduced in Section 5.3.

As has been shown in Figure 5.43, there are three different equations or equation systems to consider which are distinct with respect to the domain and the scale they are solved on:

1. the elliptic pressure equation is solved in the whole domain on the fine scale,

2. the upscaled parabolic or hyperbolic saturation equation is dealt with also in the whole domain, but on the coarse scale, and
3. the equation(s) for the total concentrations are solved only in a subdomain where mass transfer between the two (respectively three) fluid phases takes place in significant amount.

For simplicity's sake, the subdomain where multi-phase–multi-component processes are relevant is called  $U$ , whereas the total domain is denoted by  $T$ .

The basic assumption is that within the subdomain  $U$ , multi-phase–multi-component processes are governing. That means, that the saturation distribution in  $U$  is determined by these processes. For the global saturation distribution (domain  $T$ ), source / sink terms have to be introduced for all elements coinciding with the area of  $U$  in order to ensure a conservative solution of the saturation equation. These source / sink terms have to account for the difference in saturations resulting from the saturation equation and saturations resulting from the concentration equations.

The solution strategy for 2p2c processes in  $U$  will be discussed in Section 5.5.1, and the solution strategy for 3p3c processes taking place inside  $U$ , in Section 5.5.2.

### 5.5.1 Solution Strategy for Local 2p2c Processes

This section discusses the solution strategy to calculate one whole time step. As both saturation equation and concentration equation are solved explicitly in time, the CFL condition has to be fulfilled in both cases. For the saturation equation, the CFL condition has to be fulfilled on the coarse grid while for the concentration equation, it has to be fulfilled on the fine grid. Therefore, a local time stepping has to be applied and the concentration equation has to be solved in several micro time steps such that the CFL condition is fulfilled on the fine grid using a micro time step and that it is fulfilled on the coarse grid using a macro time step. In the following, the time step taken on the coarse grid will be called “macro time step” or “time step”, and the time step taken on the fine grid will be called “micro time step”. The known variables of the new time level are given for each step of the algorithm, and values resulting from the current equation are printed in bold letters. The algorithm is also shown schematically in Figures 5.49 and 5.50.

1. *Solve the modified fine-scale pressure equation in  $T$ :*

$$\nabla \cdot [\lambda(\bar{S}_w)\underline{K} \cdot \nabla p] = 0, \quad \underline{v}^{\text{discont.}} = -\lambda(\bar{S}_w)\underline{K} \cdot \nabla p, \quad (5.251)$$

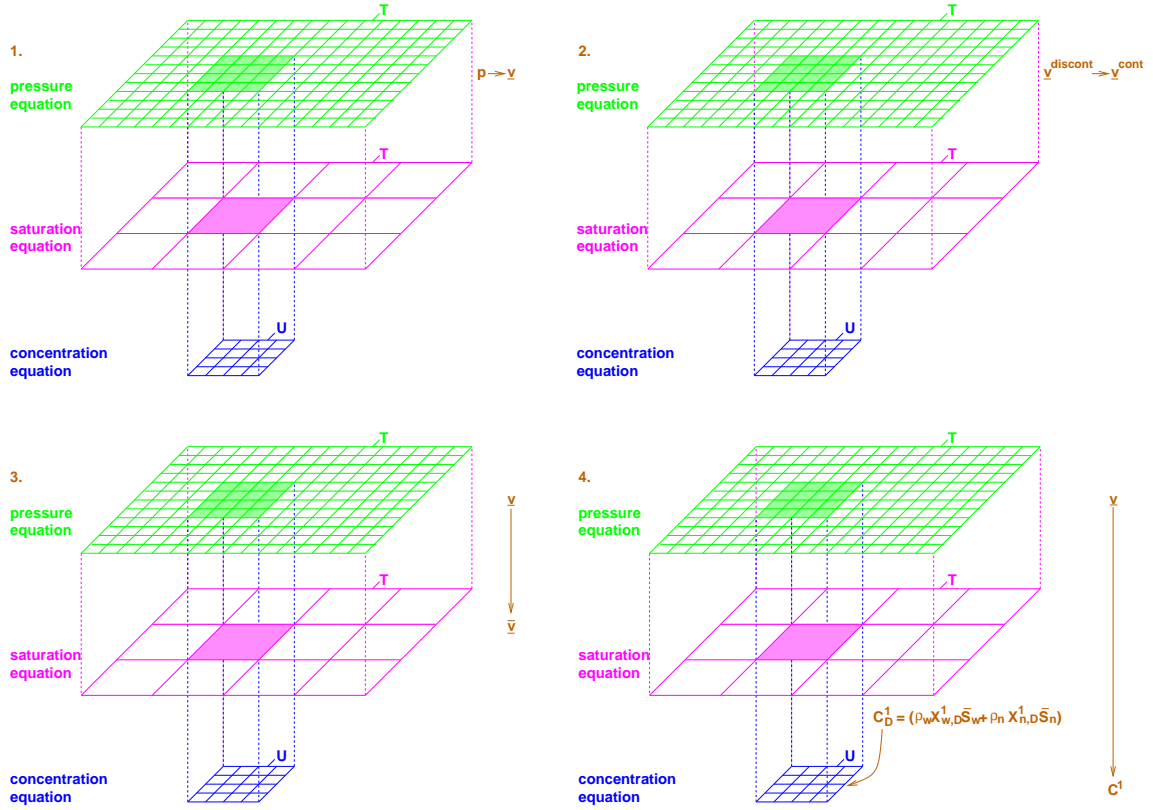


Figure 5.49: Schematic of steps 1. to 4. of the solution strategy for local 2p2c processes.

where the total mobility is approximated by the coarse-scale mobility  $\lambda(\bar{S}_w)$ . The resulting quantities are the fine-scale pressures and the fine-scale total velocities in the entire domain.

known:  $p, \underline{v}^{\text{discont.}}$ .

2. Make the fine-scale velocity field in  $T$  continuous across element edges:

$$\underline{v}^{\text{discont.}} \rightarrow \underline{v}^{\text{cont.}} =: \underline{v}. \quad (5.252)$$

A  $BDM_1^0$  projection as discussed in Section 4.3.1.1 is applied to make the discontinuous velocity field obtained from the solution of 1. continuous across element edges. This property is needed to ensure a locally mass-conservative discretization.

known:  $p, \underline{v}^{\text{discont.}}, \underline{v}$ .

3. Volume averaging for the total velocity  $\underline{v}$  in  $T$ :

$$\underline{v} = \bar{\underline{v}} + \underline{v}', \quad \bar{\underline{v}} = \frac{1}{E} \int_E \underline{v}(\underline{x}, t) dE \quad (5.253)$$

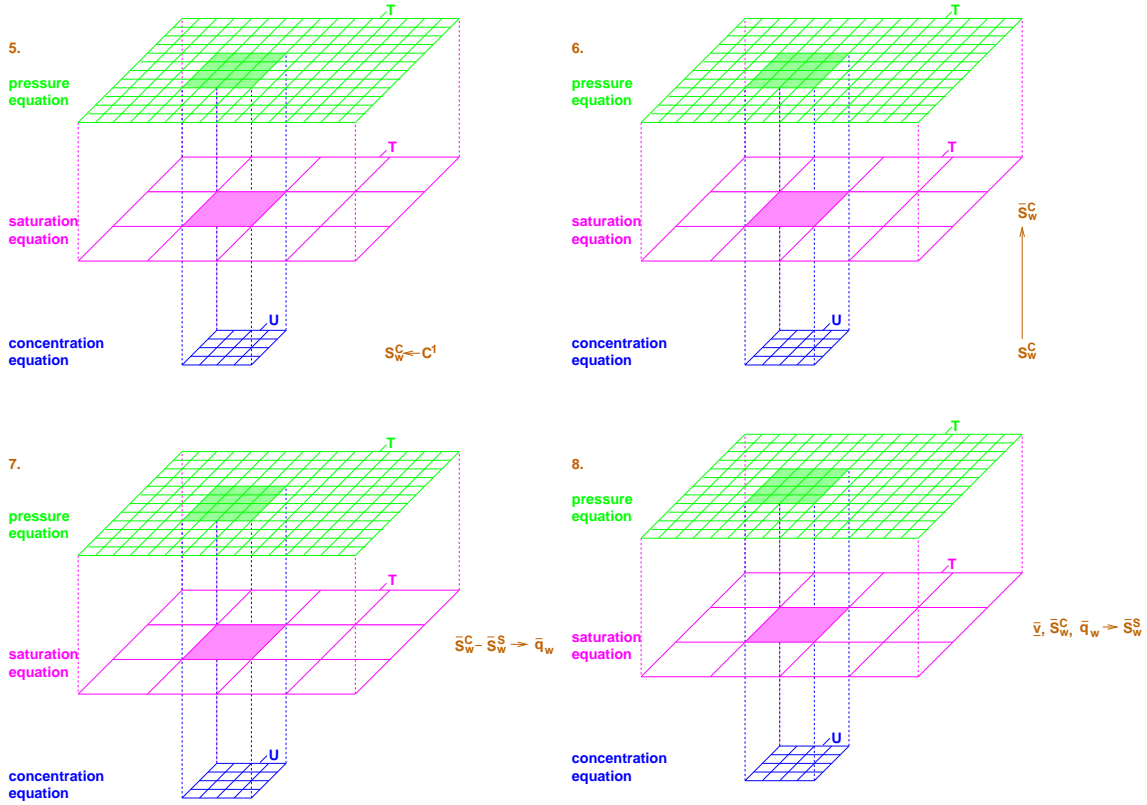


Figure 5.50: Schematic of steps 5. to 8. of the solution strategy for local 2p2c processes.

Thus, additionally, the coarse-scale total velocities as well as the fluctuating components of the total velocity in  $T$  along coarse-grid edges are known. Values inside coarse-grid elements are obtained by linear interpolation.

known:  $p, \underline{v}^{\text{discont.}}, \underline{v}, \bar{\underline{v}}, \underline{v}'$ .

4. *Solve one fine-scale total concentration equation in  $U$ :* This step is done within a sub-time loop taking micro time steps. If a coarse-grid edge consists of  $n$  fine-grid edges,  $n$  micro time steps are taken.

$$\frac{\partial C^1}{\partial t} + \underline{v} \cdot \nabla \sum_{\alpha} (f_{\alpha} C_{\alpha}^1) = 0 \quad (5.254)$$

Giving Dirichlet boundary conditions at  $\partial U$ , these boundary conditions may change if the saturations at the boundary change. The parameters which are actually fixed at  $\partial U$ , are the mass fractions  $X_{\alpha}^{\kappa}$  as  $U$  is chosen sufficiently large such that the dissolution process only takes place within  $U$ , but not at the boundary  $\partial U$  and not for all  $\underline{x} \in \{T \setminus U\}$ . That means, the total concentrations have to be updated at each macro time step according to

$$C_D^1 = \bar{S}_w^S \rho_w X_{w,D}^1 + \bar{S}_n^S \rho_n X_{n,D}^1, \quad (5.255)$$



where the upper index  $S$  emphasizes that the saturation comes from the solution of the saturation equation calculated in step 8. of the last macro time step.

That means, that the total concentrations on the fine scale in  $T$  are determined for the new time step.

known:  $p, \underline{v}^{\text{discont.}}, \underline{v}, \bar{v}, \underline{v}', C^1$ .

5. Calculate the fine-scale wetting-phase saturations in  $U$  from the concentration equation in  $U$ :

$$S_w^C = S_w^C(C^1, p), \quad (5.256)$$

where  $S_w^C(C^1, p)$  is obtained using flash calculations, see Section 3.4.1. The upper index  $C$  indicates, that these saturations result from the solution of the concentration equation.

known:  $p, \underline{v}^{\text{discont.}}, \underline{v}, \bar{v}, \underline{v}', C^1, \mathbf{S}_w^C$ .

6. Volume averaging for the saturation in  $U$ :

$$S_w^C = \bar{S}_w^C + S_w'^C, \quad \bar{S}_w^C = \frac{1}{A} \int_A S_w^C(\underline{x}, t) dA \quad (5.257)$$

This volume averaging procedure gives coarse-scale wetting-phase saturations  $\bar{S}_w^C$  in the subdomain  $U$ .

known:  $p, \underline{v}^{\text{discont.}}, \underline{v}, \bar{v}, \underline{v}', C^1, S_w^C, \bar{S}_w^C$ .

7. Ensuring mass conservativity of the coarse-scale saturation equation to be solved in 8.: For the solution of the upscaled saturation equation (step 8.), the coarse-scale saturations are used which have been calculated in 5. and in 6. from the total concentrations on the fine scale. Therefore, one has to calculate source / sink terms accounting for the difference in mass caused by the difference in saturation between saturations resulting from the concentration equation and saturations resulting from the saturation equation,

$$\bar{q}_w = \frac{\bar{S}_w^S - \bar{S}_w^C}{\partial t}. \quad (5.258)$$

known:  $p, \underline{v}^{\text{discont.}}, \underline{v}, \bar{v}, \underline{v}', C^1, S_w^C, \bar{S}_w^C, \bar{q}_w$ .

8. Solve the coarse-scale saturation equation in  $T$ :

$$\begin{aligned} \frac{\partial \bar{S}_w}{\partial t} + \frac{1}{A} \int_{d\Gamma} \bar{v}_j f(\bar{S}_w) n_j d\Gamma = \frac{\alpha}{A} \int_{d\Gamma} |v'_i(\underline{x}, t)| \frac{d^2 f(\bar{S}_w)}{dS_w^2} \\ \cdot \left( L_j \nabla_j \bar{S}_w - \frac{1}{2} (L_j \nabla_j \bar{S}_w)^2 \frac{d^2 f(\bar{S}_w)}{dS_w^2} \right) n_i dl + \bar{q}_w \end{aligned} \quad (5.259)$$

This finally yields the coarse-scale wetting-phase saturation distribution of the new time step, which enters into the mobility calculation in the pressure equation of the next time step.

known:  $p, \underline{v}^{\text{discont.}}, \underline{v}, \bar{v}, \underline{v}', C^1, S_w^C, \bar{S}_w^C, \bar{S}_w^S$ .

### 5.5.2 Solution Strategy for Local 3p3c Processes

The solution strategy for locally occurring 3p3c processes is very similar to the one for local 2p2c processes—the only major differences are the use of three-phase relative permeability functions in  $U$ , the solution of two instead of one concentration equation and the use of the more complex 3p3c flash calculation presented in Section 3.4.2.

As globally a two-phase problem is solved, but three phases are present in a part of the domain (gas and water as mobile phases and LNAPL as an immobile phase), gas and water saturation do no longer some up to unity throughout the whole model domain,

$$S_w + S_g = 1 - S_{nr}. \quad (5.260)$$

In order to remedy this shortcoming, gas and water saturation are rescaled in a way that they are again in a range between zero and one. Therefore, the effective water saturation is calculated as

$$S_{we} = \frac{1 - S_g - S_n}{1 - S_{nr}}. \quad (5.261)$$

The effective gas saturation is then simply  $S_{ge} = 1 - S_{we}$ .

For simplicity, the subscript  $e$  is dropped in the following demonstration of the algorithm. However, one should keep in mind, that all of the saturations used within the two-phase model are in fact effective phase saturations.

The known variables of the new time level are given for each step of the algorithm, and values resulting from the current equation are printed in bold letters. The algorithm is also shown schematically in Figures 5.51 and 5.52. One can see, that it is very similar to the 2p2c algorithm. The only principal differences in this representation are, that two concentration equations have to be solved and that both water phase saturation  $S_w^C$  and NAPL phase saturation  $S_n^C$  are calculated and need to be averaged over the coarse-grid elements corresponding to the local domain  $U$ .

1. Solve the modified fine-scale pressure equation in  $T$ :  
if in  $U$ :

$$\nabla \cdot [\lambda(\bar{S}_w, \bar{S}_n) \underline{K} \cdot \nabla p] = 0, \quad \underline{v}^{\text{discont.}} = -\lambda(\bar{S}_w, \bar{S}_n) \underline{K} \cdot \nabla p, \quad (5.262)$$

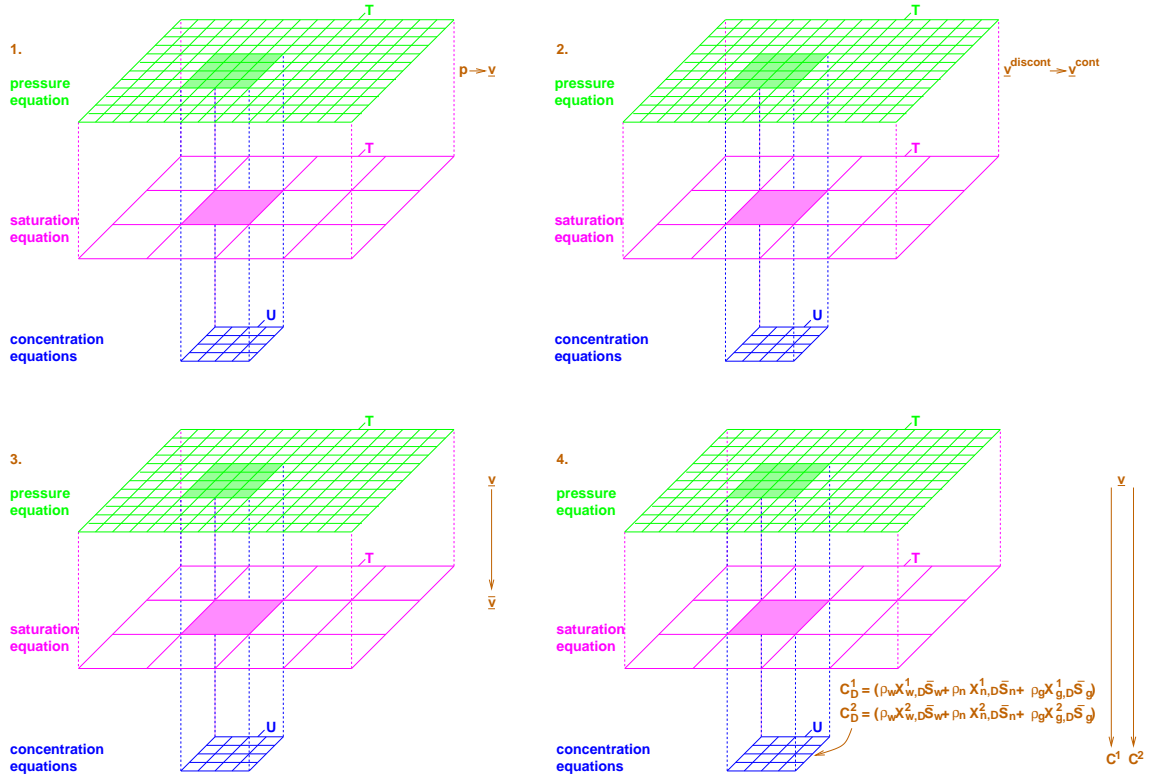


Figure 5.51: Schematic of steps 1. to 4. of the solution strategy for local 3p3c processes.

if in  $\{T \setminus U\}$ :

$$\nabla \cdot [\lambda(\bar{S}_w) \underline{K} \cdot \nabla p] = 0, \quad \underline{v}^{\text{discont.}} = -\lambda(\bar{S}_w) \underline{K} \cdot \nabla p, \quad (5.263)$$

where the total mobility in  $U$  is approximated by the coarse-scale three-phase mobility  $\lambda(\bar{S}_w, \bar{S}_n)$  and outside  $U$  by the two-phase mobility  $\lambda(\bar{S}_w)$ . The resulting quantities are the fine-scale pressures and the fine-scale total velocities in the entire domain.

known:  $p, \underline{v}^{\text{discont.}}$ .

2. Make the fine-scale velocity field in  $T$  continuous across element edges:

$$\underline{v}^{\text{discont.}} \rightarrow \underline{v}^{\text{cont.}} =: \underline{v}. \quad (5.264)$$

A  $BDM_1^0$  projection as discussed in Section 4.3.1.1 is applied to make the discontinuous velocity field obtained from the solution of 1. continuous across element edges. This property is needed to ensure a locally mass-conservative discretization.

known:  $p, \underline{v}^{\text{discont.}}, \underline{v}$ .

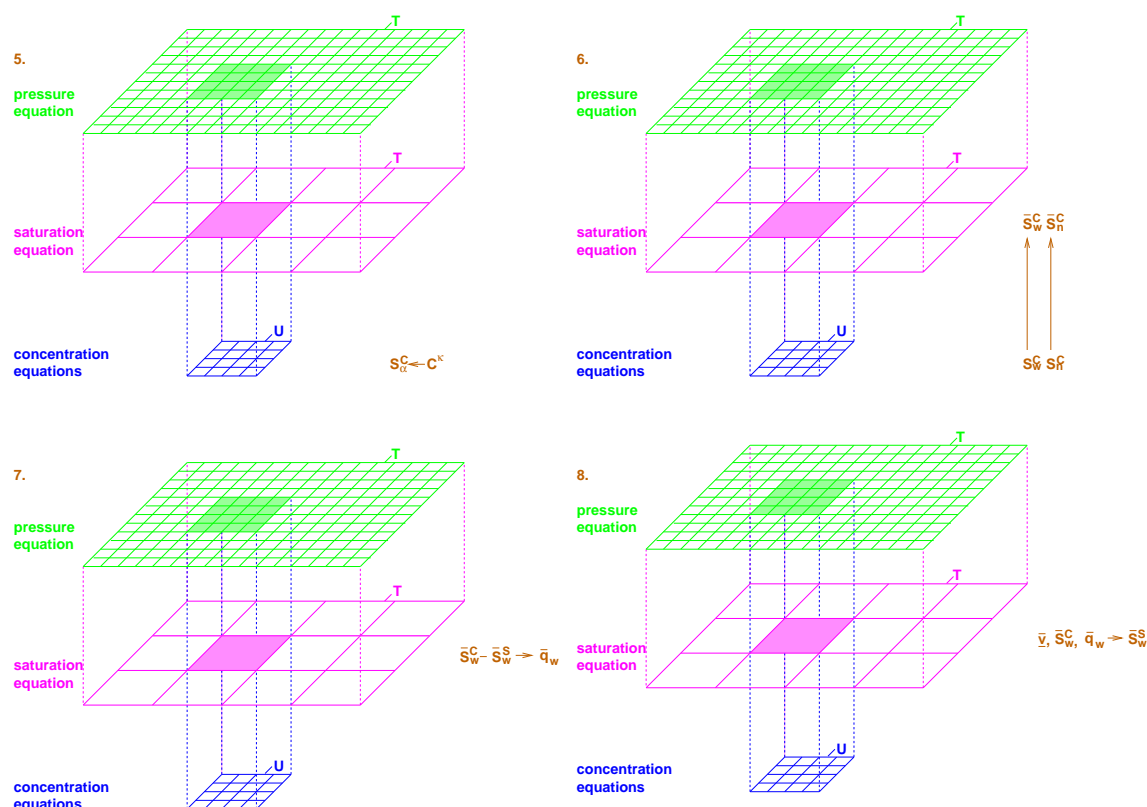


Figure 5.52: Schematic of steps 5. to 8. of the solution strategy for local 3p3c processes.

3. *Volume averaging for the total velocity  $\underline{v}$  in  $T$ :*

$$\underline{v} = \bar{\underline{v}} + \underline{v}', \quad \bar{\underline{v}} = \frac{1}{E} \int_E \underline{v}(\underline{x}, t) dE \quad (5.265)$$

Thus, additionally, the coarse-scale total velocities as well as the fluctuating components of the total velocity in  $T$  along coarse-grid edges are known. Values inside coarse-grid elements are obtained by linear interpolation.

known:  $p, \underline{v}^{\text{discont.}}, \underline{v}, \bar{\underline{v}}, \underline{v}'$ .

4. *Solve two fine-scale total concentration equations in  $U$ :* This step is done within a sub-time loop taking micro time steps. If a coarse-grid edge consists of  $n$  fine-grid edges,  $n$  micro time steps are taken.

$$\frac{\partial C^1}{\partial t} + \underline{v} \cdot \nabla \sum_{\alpha} (f_{\alpha} C_{\alpha}^1) = 0 \quad (5.266)$$

$$\frac{\partial C^2}{\partial t} + \underline{v} \cdot \nabla \sum_{\alpha} (f_{\alpha} C_{\alpha}^2) = 0 \quad (5.267)$$

Considering the boundaries of  $U$ , total concentrations are given as boundary condition. However, the parameters which are actually fixed at  $\partial U$  are the mass fractions  $X_\alpha^\kappa$ , as  $U$  is chosen sufficiently large such that the dissolution process only takes place within  $U$ , but not at the boundary  $\partial U$  and not for all  $\underline{x} \in \{T \setminus U\}$ . That means, one has to update the total concentrations at each macro time step according to

$$C_D^\kappa = \bar{S}_w^S \rho_w X_{w,D}^\kappa + \bar{S}_n^S \rho_n X_{n,D}^\kappa + \bar{S}_g^S \rho_g X_{g,D}^\kappa, \quad (5.268)$$

for  $\kappa \in \{1, 2\}$ . The upper index  $S$  emphasizes that the saturation comes from the solution of the saturation equation calculated in step 8. of the last macro time step.

That means, that the total concentrations on the fine scale in  $T$  are determined for the new time step.

known:  $p, \underline{v}^{\text{discont.}}, \underline{v}, \bar{v}, \underline{v}', \mathbf{C}^1, \mathbf{C}^2$ .

5. Calculate the fine-scale wetting-phase saturations in  $U$  from concentration equation in  $U$ :

$$S_w^C = S_w^C(C^1, C^2, p), \quad (5.269)$$

$$S_n^C = S_n^C(C^1, C^2, p), \quad (5.270)$$

where  $S_w(C^\kappa, p)$  and  $S_n(C^\kappa, p)$  are obtained using flash calculations, see Section 3.4. The upper index  $C$  indicates that these saturations result from the solution of the concentration equations.

known:  $p, \underline{v}^{\text{discont.}}, \underline{v}, \bar{v}, \underline{v}', C^1, C^2, \mathbf{S}_w^C, \mathbf{S}_n^C$ .

6. Volume averaging for the saturations in  $U$ :

$$S_w^C = \bar{S}_w^C + S_w'^C, \quad \bar{S}_w^C = \frac{1}{A} \int_A S_w^C(\underline{x}, t) dA \quad (5.271)$$

$$S_n^C = \bar{S}_n^C + S_n'^C, \quad \bar{S}_n^C = \frac{1}{A} \int_A S_n^C(\underline{x}, t) dA \quad (5.272)$$

This volume averaging procedure gives coarse-scale water-phase and LNAPL-phase saturations  $\bar{S}_w^C$  and  $\bar{S}_n^C$  in the subdomain  $U$ .

known:  $p, \underline{v}^{\text{discont.}}, \underline{v}, \bar{v}, \underline{v}', C^1, C^2, S_w^C, S_n^C, \mathbf{S}_w^C, \mathbf{S}_n^C$ .

7. Ensuring mass conservativity of the coarse-scale wetting-phase saturation equation to be solved in 8.:

For the solution of the upscaled saturation equation (step 8.), the coarse-scale saturations calculated in 5. and in 6. from the total concentrations on the fine scale are used. Therefore, one has to calculate source / sink terms accounting

for the difference in mass caused by the difference in saturation between saturations resulting from the concentration equation and saturations resulting from the saturation equation,

$$\bar{q}_w = \frac{\bar{S}_w^S - \bar{S}_w^C}{\partial t}. \quad (5.273)$$

known:  $p, \underline{v}^{\text{discont.}}, \underline{v}, \bar{v}, \underline{v}', C^1, C^2, S_w^C, S_n^C, \bar{S}_w^C, \bar{S}_n^C, \bar{\mathbf{q}}_w$ .

8. Solve the coarse-scale saturation equation in  $T$ :

$$\frac{\partial \bar{S}_w}{\partial t} + \frac{1}{A} \int_{d\Gamma} \bar{v}_j f(\bar{S}_w) n_j d\Gamma = \frac{\alpha}{A} \int_{d\Gamma} |v'_i(\underline{x}, t)| \frac{d^2 f(\bar{S}_w)}{dS_w^2}. \quad (5.274)$$

$$\cdot \left( L_j \nabla_j \bar{S}_w - \frac{1}{2} (L_j \nabla_j \bar{S}_w)^2 \frac{d^2 f(\bar{S}_w)}{dS_w^2} \right) n_i dl + \bar{q}_w \quad (5.275)$$

This finally gives the coarse-scale wetting-phase saturation distribution of the new time step, which enters into the mobility calculation in the pressure equation of the next time step.

known:  $p, \underline{v}^{\text{discont.}}, \underline{v}, \bar{v}, \underline{v}', C^1, C^2, S_w^C, S_n^C, \bar{S}_w^C, \bar{S}_n^C, \bar{\mathbf{S}}_w^S$ .

## 6 Examples

To test the quality and the performance of the complex algorithm introduced in Section 5.5, a stepwise procedure is applied where the different building blocks of the algorithm are verified separately and sequentially. For all model runs, the quality of the model is checked by comparisons to a reference solution and, for all modules containing an upscaled saturation equation, by computation of error norms in  $L_1$  and  $L_2$ . Moreover, the computing time is registered to find out how the multi-scale-upscaling algorithm performs in comparison to standard schemes. Specifically, each model is checked using

- linear equations (i.e. linear relative permeabilities as well as mobilities of  $\lambda_\alpha = 1$ ), and it is also checked using
- nonlinear equations (nonlinear relative permeability–saturation relationships).

For each of the linear and for each of the nonlinear models, the degree and type of heterogeneity is varied. Each model is applied to a homogeneous permeability field and a set of five heterogeneous fields with different geostatistical properties which will be defined later on in this section. Consequently, a set of 12 test cases has to be considered, 6 linear test cases, and 6 nonlinear ones, where each of the sets of 6 test cases consists of a homogeneous test case and 5 heterogeneous test cases.

A schematic overview is given in Figure 6.53, where the testing procedure is compared to the building of a house. Each of the “floors” can only be stable if all the floors below are stable. Therefore, each floor is validated by comparing it to the floor below. The complexity of the algorithm increases in each of the coordinate directions. In x-direction, nonlinearity increases while with growing y-value, the heterogeneity of the medium also increases. In z-direction, the physical, mathematical, and numerical model become more complex, starting from a model where a pressure and a saturation equation are solved on the fine scale (*DG fine*), then passing over to a model where the pressure equation is still solved on the fine scale, but the saturation equation is solved in an upscaled form on the coarse scale (*DG upscaled*). Finally, a highly complex model is tested, where additionally either two-phase–two-component processes or three-phase–three-component processes are modeled in a local domain of interest (*DG local 2p2c* or *DG local 3p3c*, respectively).

In Section 6.1, the module *DG fine* is checked by comparisons to the solution of the streamline code (*SL*, the “basement”) which was discussed in Section 4.3.2.2 as well as by grid convergence studies. The comparisons to the results obtained by streamline simulation are only performed for the linear module, as one can only in this case profit of an excellent accuracy of the streamline results which are then basically free of numerical diffusion.

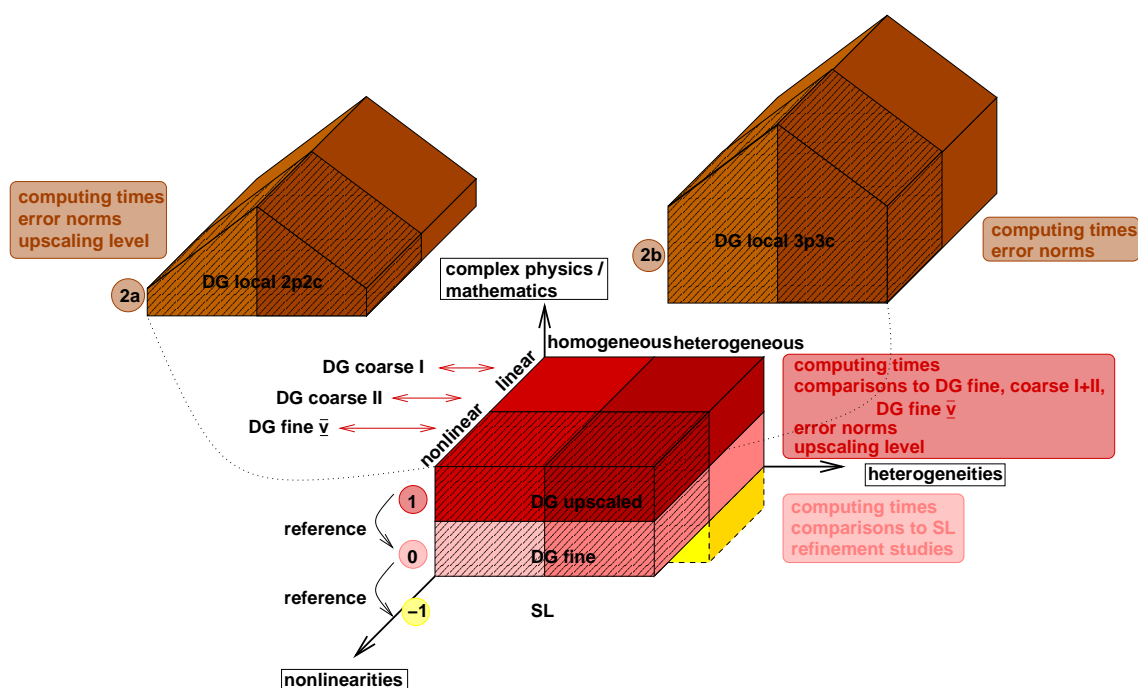


Figure 6.53: Schematic overview of the structure of the test examples.

The quality of *DG upscaled* (the “first floor”) is investigated by comparing this module to the above-defined reference solution (*DG fine*) on the one hand, see Section 6.2. Error norms in  $L_1$  and  $L_2$  can be computed to quantify the quality of the upscaled model, i.e. to quantify, how good the fine-scale solution can be reproduced. On the other hand, *DG upscaled* is compared to

- *DG coarse I*, which is given by a simulation of the upscaled saturation equation without macrodispersion (the entries of the macrodispersion tensor are simply set to zero).
- *DG coarse II*, where a coarse-scale permeability field is obtained by the solution of fine-scale one-phase pressure equations over regions corresponding to one coarse-grid block. The pressure equation as well as the saturation equation in its hyperbolic local-scale form are solved on the coarse grid.



- *DG fine*  $\bar{v}$ , where volume averaging is applied to the fine-scale velocity field. Using the averaged velocities, the saturation equation is still solved on the fine grid.

Finally, the dependence of the quality of *DG upscaled* on the level of coarsening is investigated.

Having studied the performance of the two-phase model, the top of the “building” is still missing. This top is either the modeling of locally occurring two-phase–two-component processes (Section 6.3), or of locally occurring three-phase–three-component processes (Section 6.4). Computing times and error norms are compared for both alternatives. In this case, the error norms are calculated with respect to a reference which is computed by solving globally (i.e. in the whole domain) a two-phase–two-component or a three-phase–three-component model, respectively. For *DG local 2p2c*, the dependence of both accuracy and computing time on the upscaling level is investigated.

In the end, all the results of Sections 6.1 through 6.4 are comprehensively analyzed and summed up in Section 6.5.

After this general overview, the permeability fields under study will be considered more closely. They are generated with the geostatistical simulator *simset* by A. Bárdossy which uses a turning-band algorithm with 36 bands. This simulator is based on the work of Brooker [1985], Journel and Huijbregts [1978], as well as Geckinli-Yavuz [1983] and gives a series of two-dimensional log-permeability fields fitting a number of given geostatistical properties.

Besides considering a homogeneous medium, five heterogeneous fields with different geostatistical properties are generated. One of the heterogeneous permeability fields with intermediate statistical properties is taken as a reference (“standard”). Besides, a field with a higher (“high  $l_i$ ”) and one with a lower correlation length (“low  $l_i$ ”) are taken. Moreover, the variance is varied and a smaller as well as a larger value compared to the heterogeneous standard example are taken (“high  $\sigma$ ” or “low  $\sigma$ ”, respectively). The exact geostatistical parameter values can be taken from Table 6.4. The mean value of absolute permeability was taken to be  $K = \bar{K} = 10^{-10} \text{ m}^2$  in all cases. Thus, it represents a quasi-scalar quantity. Correlation lengths are given as relative correlation lengths  $l_i$ , meaning that the absolute correlation length  $J_x^c$  in  $x$ -direction is scaled by the length  $L$  of the domain and the absolute correlation length  $J_y^c$  in  $y$ -direction is scaled by the height  $H$  of the domain, such that they are both within the interval  $[0, 1]$ ,

$$l_x = \frac{J_x^c}{L}, \quad (6.276)$$

$$l_y = \frac{J_y^c}{H}. \quad (6.277)$$

For the studies performed in this section, a domain as presented in Figure 6.54 is generally considered. The dimensions as well as the location of the local domain which is needed for 2p2c as well as for 3p3c modeling are depicted. The five test

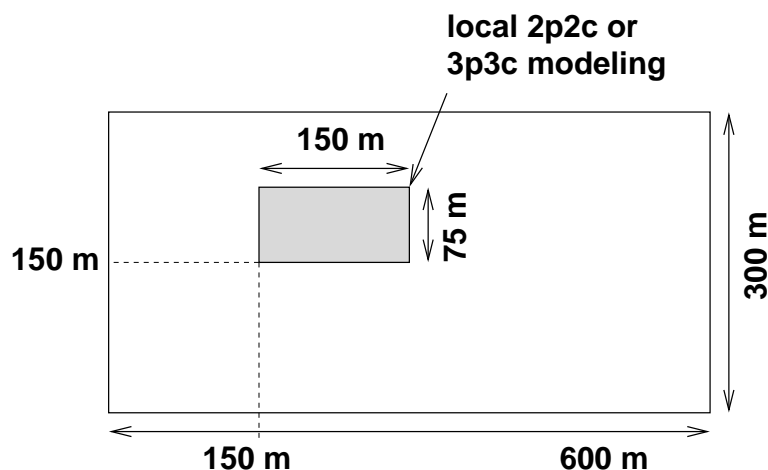


Figure 6.54: Domain considered within the test examples.

permeability fields generated with the parameters given in Table 6.4 are shown in Figure 6.55 where the logarithm of absolute permeability is the contour variable. Finally, for all of the following studies including two phases, the fluid properties as well as the Brooks-Corey parameter  $\lambda_{BC}$  for the nonlinear case are taken as given in Table 6.5, unless otherwise stated.

Considering discretization in time, the applied Runge-Kutta method is an S-stable 3-stage scheme of order 3. For the space discretization of pressure equation, saturation equation and concentration equations, DG schemes including polynomials of second order are used.

	standard	high $l_i$	low $l_i$	high $\sigma$	low $\sigma$
$l_x$ [m]	120	180	60	120	120
$l_y$ [m]	24	36	12	24	24
$\sigma$ [m]	1.5	1.5	1.5	2.0	1.0

Table 6.4: Geostatistical parameters of the five test permeability fields.

$\mu_w$ [kg/(ms)]	$\mu_n$ [kg/(ms)]	$\rho_w$ [kg/m <sup>3</sup> ]	$\rho_n$ [kg/m <sup>3</sup> ]	$\lambda_{BC}$ [-]
1.0	1.0	1000.0	0.9	2.0

Table 6.5: Parameters for the simulation examples. The index  $w$  denotes the water phase, the index  $n$  the non-wetting phase (gas).

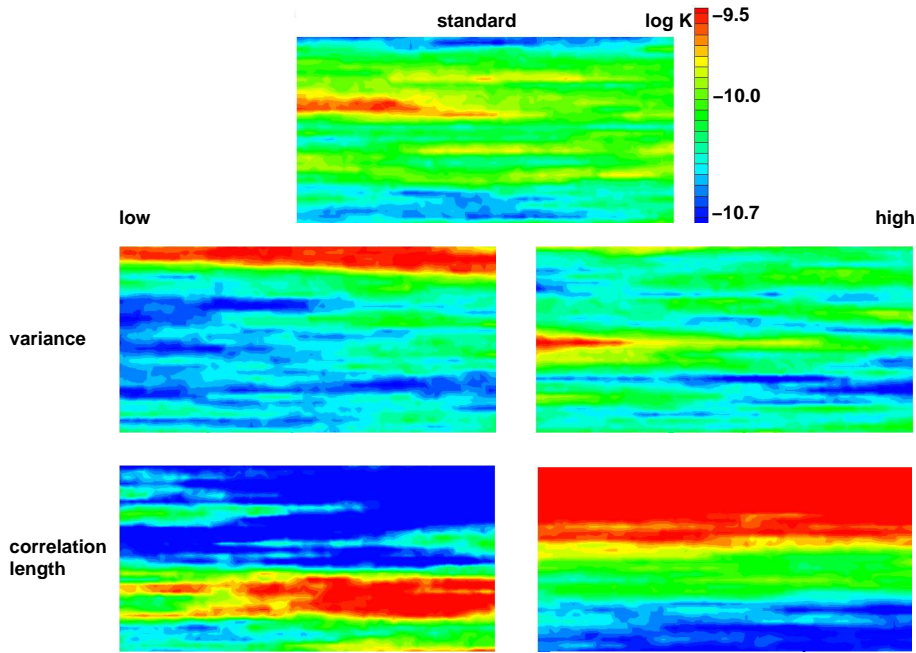


Figure 6.55: Five test permeability fields corresponding to the geostatistic properties given in Table 6.4.

## 6.1 Testing of *DG fine*

### 6.1.1 General Remarks and Algorithm

The quality and accuracy of the module *DG fine* is tested by two different studies,

1. **grid refinement** studies, where the grid is refined several times until no significant change of the results is obtained when further refining the mesh, and
2. for the linear cases, the results are compared to the results obtained by **stream-line simulation**. In the linear case, streamline simulation provides results which are basically free of numerical diffusion, and thus, results of an excellent accuracy, see Section 4.3.2.2.

The part of the algorithm of Section 5.5.1 that is used for the module *DG fine* is sketched in Figure 6.56 and is the following:

1. Solve the fine-scale pressure equation in  $T$ :

$$\nabla \cdot [\lambda(S_w)\underline{K} \cdot \nabla p] = 0, \quad \underline{v}^{\text{disc.}} = -\lambda(S_w)\underline{K} \cdot \nabla p, \quad (6.278)$$

The resulting quantities are the fine-scale pressures and the fine-scale total velocities in the entire domain.

known:  $\bar{p}, \underline{v}^{\text{discont.}}$ .

2. Make the fine-scale velocity field in  $T$  continuous across element edges:

$$\underline{v}^{\text{discont.}} \rightarrow \underline{v}^{\text{cont.}} =: \underline{v}. \quad (6.279)$$

A  $BDM_1^0$  projection as discussed in Section 4.3.1.1 is applied to make the discontinuous velocity field obtained from the solution of 1. continuous across element edges. This property is needed to ensure a locally mass-conservative discretization.

known:  $p, \underline{v}^{\text{discont.}}, \underline{v}$ .

8. Solve the fine-scale saturation equation in  $T$ :

$$\frac{\partial S_w}{\partial t} + \nabla \cdot (f_w(S_w)\underline{v}) = 0 \quad (6.280)$$

known:  $p, \underline{v}^{\text{discont.}}, \underline{v}, S_w$

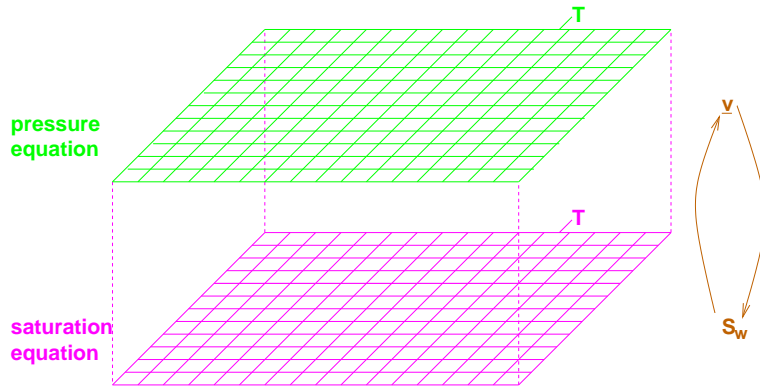


Figure 6.56: Multi-scale structure for test case *DG fine*.

## 6.1.2 Results

*Grid refinement* studies are carried out in order to check the convergence of the solution graphically when refining the mesh. With decreasing discretization length, the numerical solution should converge to the solution of the mathematical system of equations in the limit, while computing time increases. The results of a homogeneous and linear problem are compared for a series of refinement levels in order to be able to choose a reasonable fine-grid level for the further studies.

Considering the example domain with dimensions  $600 \text{ m} \times 300 \text{ m}$  as given in Figure 6.54, an initial grid is constructed in dividing the domain in  $8 \times 4$  grid cells. Thus, the initial grid consists of 32 grid cells of dimensions  $75 \text{ m} \times 75 \text{ m}$ . This refinement level is referred to as “MAXLEVEL 0” (ML 0). For each further grid refinement, a grid cell is halved in both x- and y-direction. Thus, the grid on ML 1 consists of  $16 \times 8$  cells of size  $37.5 \text{ m} \times 37.5 \text{ m}$  and so on, see Figure 6.57 for the refinement procedure for a single grid cell. In all of the results within this section, the saturation distribution at  $t = 944.44$  days is considered.

Furthermore, for the linear case, *comparisons to streamline simulation* results are carried through. In this case, streamline simulation introduces a minimum amount of numerical diffusion into the solution and can therefore be used as a reference solution.

Boundary and initial conditions for the fine-scale comparisons are given in Figure 6.58. Flow is from left to right and governed by the difference in Dirichlet pressure boundary conditions. Both top and bottom boundary are impermeable and given as Neumann no-flow boundary conditions. The initial wetting-phase saturation as well as the saturation at the right boundary is equal to 0.1, whereas the left boundary condition for saturation is equal to  $S_w^D = 0.9$ .

Figure 6.59 shows different plots of the y-averaged values of wetting-phase saturation  $S_w$  over the x-coordinate of the domain. The upper left picture shows the results for a linear homogeneous problem for ML 1 through 4 using a DG discretization. One can see that with increasing refinement level the solution comes closer to

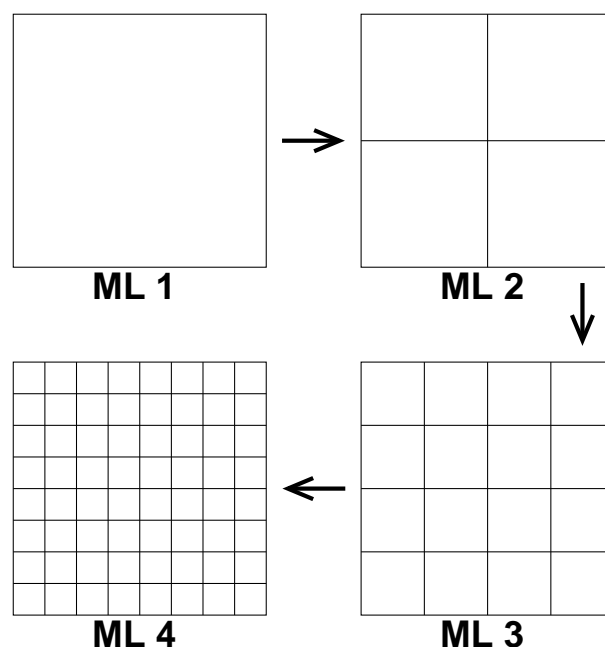


Figure 6.57: Refinement of one grid block from ML 1 to ML 4.

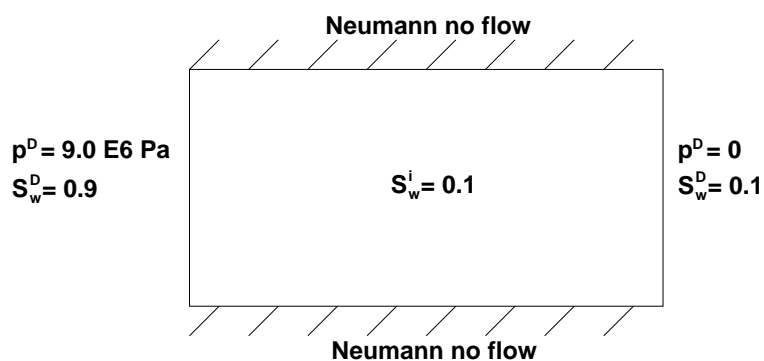


Figure 6.58: Boundary and initial conditions used for the testing of the module *DG fine*.

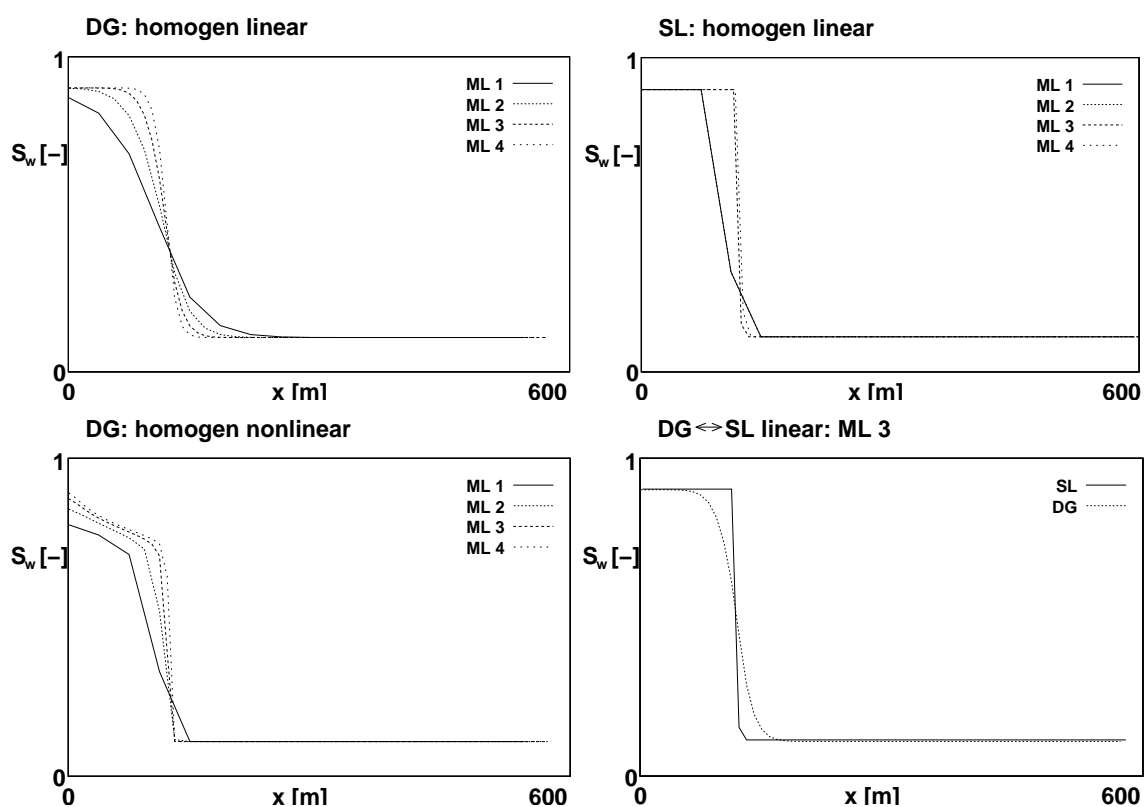


Figure 6.59: Saturation profiles (y-averages) for different values of MAXLEVEL compared for linear and nonlinear DG as well as for linear SL simulations.

the mathematically correct solution, i.e., a shock front. In the lower left picture, the same simulation is carried out for the nonlinear case, also using a DG discretization. One can identify the same effect as for the linear case—the finer the MAXLEVEL, the steeper the shock front. However, in the nonlinear case, a rarefaction wave occurs additionally to the sharp front for the  $x$ -values upstream of the shock. Furthermore, one can see that for the linear as well as for the nonlinear case, the difference between ML 3 and ML 4 becomes very small. Therefore, ML 3 is generally considered for the following fine-grid (fine-scale) DG computations, unless otherwise stated. Considering the streamline simulation (SL) results in the upper right picture of Figure 6.59, one can see, that the solution converges very fast with increasing MAXLEVEL. Starting from ML 2, the front is already almost perfectly represented showing a negligible difference to the result with ML 4. The last picture, i.e. the lower right picture, shows a comparison between DG and SL solution for the chosen fine level—i.e., ML 3. One can see that still there is a significant difference between the basically diffusion-free SL solution and the DG result. However, for the nonlinear cases and especially for the cases with mass transfer between fluid phases, the streamline code is either not appropriate any more with respect to the model equations, or it introduces—in the nonlinear cases—itsself a larger amount of numerical diffusion due to the mapping of saturations back and forth to the grid.

For the five test permeability fields, Figure 6.60 compares the DG solution of ML 3 to the SL solution. In all five cases, a very good agreement can be detected. Furthermore, the lower left picture shows a comparison of the five different fields for DG at a MAXLEVEL value of 3, so that the characteristics of the permeability fields can be directly compared. It becomes obvious that the permeability field with the high correlation length (high  $l_i$ ) allows an early arrival of the non-wetting phase at high  $x$ -coordinates. This is due to its layered structure with a high permeability in the upper layer.

To identify the actual shape of the front, two-dimensional contour plots of saturation within the domain are compared. Figure 6.61 shows the fronts in the homogeneous case on ML 1 through 4 for SL, as well as DG in the linear and nonlinear case. For the five test permeability fields on ML 3, SL results as well as DG results for the linear and nonlinear case are depicted in Figure 6.62.

Table 6.6 shows a comparison of the computing times (system CPU times) in the homogeneous case for different refinement levels, whereas Table 6.7 compares the computing times for the five chosen permeability fields.

It can be seen that streamline simulation is in the homogeneous case by a factor of 30-100 faster than the respective linear DG solution. For the heterogeneous fields, the computing times can only be considered separately for DG and for SL, as the simulations were carried through on different computers. Comparing the computing times for the linear and the nonlinear cases using a DG scheme, it gets obvious

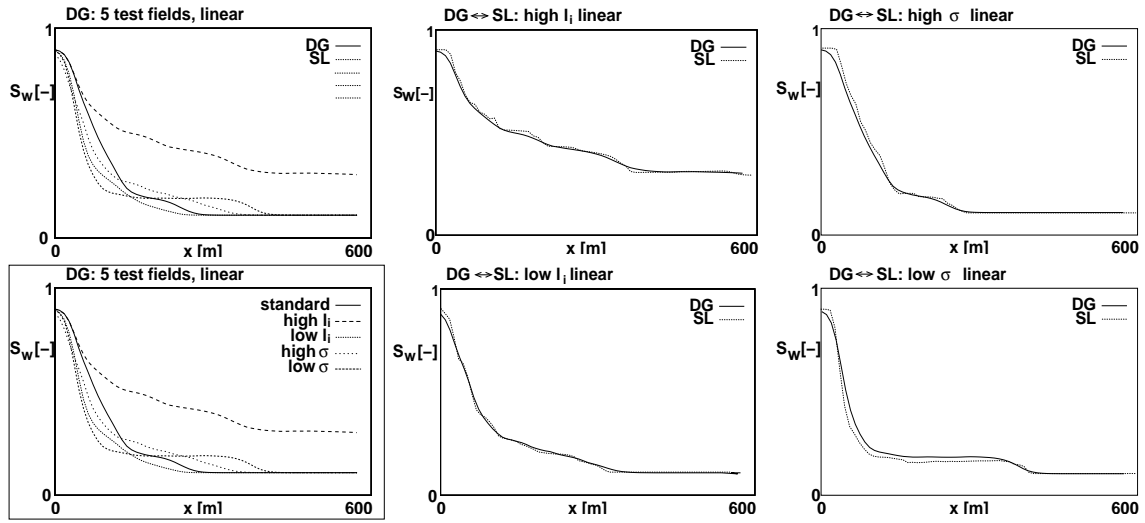


Figure 6.60: Saturation profiles (y-averages) for the five test permeability fields in the linear case.

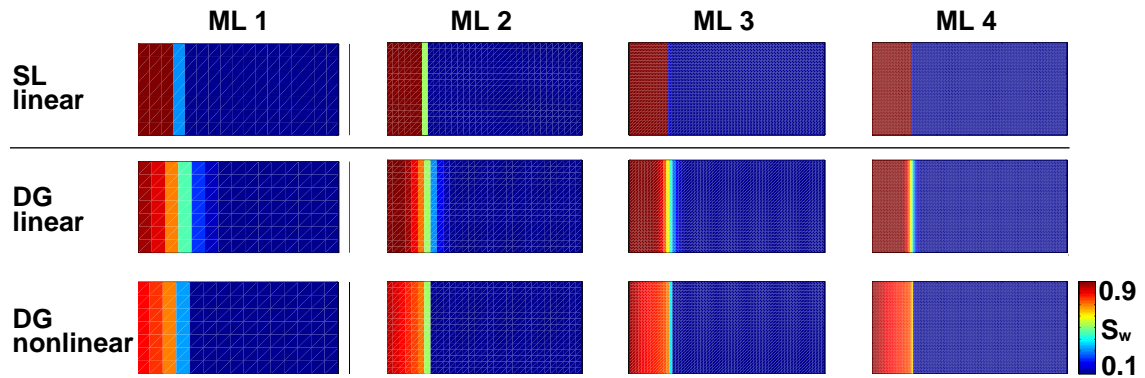


Figure 6.61: Saturation fronts for different ML—SL results and output for DG in the linear and nonlinear case in a homogeneous domain.

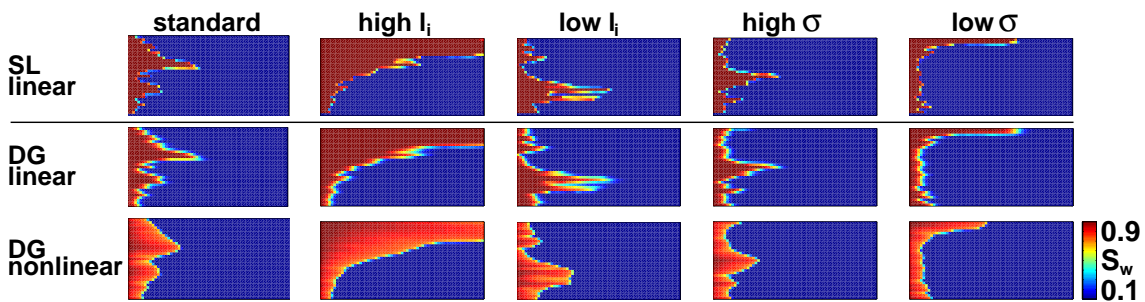


Figure 6.62: Saturation fronts for the five test permeability fields—SL results and DG simulations in the linear and nonlinear case.



that the linear scheme is always faster than the nonlinear one. This is due to the fact, that in the nonlinear case, the pressure equation is solved repeatedly whereas in the linear case, it is calculated only once. Finally, with increasing MAXLEVEL, the simulation time increases, as for every refinement step, four times more grid cells have to be evaluated.

ML	1	2	3	4
SL	0.014	0.012	0.021	0.739
DG linear	0.525	0.887	3.140	9.683
DG nonlinear	0.576	0.916	4.313	18.849

Table 6.6: System CPU times [s] for a homogeneous problem on different refinement levels.

K field	standard	high $l_i$	low $l_i$	high $\sigma$	low $\sigma$
SL	0.024	0.022	0.027	0.037	0.017
DG linear	731.134	697.694	719.653	748.444	707.856
DG nonlinear	753.711	748.948	728.029	763.02	794.222

Table 6.7: System CPU times [s] for the five different permeability fields on refinement level ML 3.

## 6.2 Testing of *DG upscaled*

The module *DG upscaled* consists of a fine-grid pressure solution in the global domain and a coarse-grid solution of the upscaled saturation equation. It is tested in various ways, namely by

- comparisons to *DG coarse I*, where the macrodispersion term in the upscaled saturation equation is set to zero (Section 6.2.1),
- comparisons to *DG coarse II*, where coarse-grid permeabilities are obtained from the solution of local fine-grid problems over regions corresponding to coarse-grid blocks, see Section 6.2.2. Both pressure equation and the purely hyperbolic form of the saturation equation are then solved on a coarse grid using the coarse-grid permeabilities for the coarse-grid pressure equation,
- comparisons to *DG fine  $\bar{v}$*  where coarse-grid velocities are obtained by volume-averaging of the fine-grid velocities which in turn are obtained by a fine-grid

pressure solution in the global domain. The saturation equation is solved on the fine grid using the coarse-grid velocities (Section 6.2.3). This is done in order to eliminate the influence of numerical diffusion resulting from the solution of the saturation equation on a coarser grid. Finally, it is tested by

- investigating the dependence of DG upscaled on the *upscaling level*, i.e. on the number of fine-grid elements per coarse-grid element.

As sketched in Figure 6.63, the corresponding algorithm of Section 5.5.1 reduces for DG upscaled to

1. Solve the modified fine-scale pressure equation in  $T$ :

$$\nabla \cdot [\lambda(\bar{S}_w)\underline{K} \cdot \nabla p] = 0, \quad \underline{v}^{\text{discont.}} = -\lambda(\bar{S}_w)\underline{K} \cdot \nabla p. \quad (6.281)$$

where the total mobility is approximated by the coarse-scale mobility  $\lambda(\bar{S}_w)$ . The resulting quantities are the fine-scale pressures and the fine-scale total velocities in the entire domain.

known:  $p, \underline{v}^{\text{discont.}}$ .

2. Make the fine-scale velocity field in  $T$  continuous across element edges:

$$\underline{v}^{\text{discont.}} \rightarrow \underline{v}^{\text{cont.}} =: \underline{v}. \quad (6.282)$$

A  $BDM_1^0$  projection is applied to make the discontinuous velocity field obtained from the solution of 1. continuous across element edges. This property is needed to ensure a locally mass-conservative discretization.

known:  $p, \underline{v}^{\text{discont.}}, \underline{v}$ .

3. Volume averaging for the total velocity  $\underline{v}$  in  $T$ :

$$\underline{v} = \bar{\underline{v}} + \underline{v}', \quad \bar{\underline{v}} = \frac{1}{E} \int_E \underline{v}(\underline{x}, t) dE \quad (6.283)$$

Thus, additionally, the coarse-scale total velocities in  $T$  are known.

known:  $p, \underline{v}^{\text{discont.}}, \underline{v}, \bar{\underline{v}}, \underline{v}'$ .

8. Solve the coarse-scale saturation equation in  $T$ :

$$\begin{aligned} \frac{\partial \bar{S}_w}{\partial t} + \frac{1}{A} \int_{d\Gamma} \bar{v}_j f(\bar{S}_w) n_j d\Gamma &= \frac{\alpha}{A} \int_{d\Gamma} |v'_i(\underline{x}, t)| \frac{d^2 f(\bar{S}_w)}{dS_w^2} \\ &\cdot \left( L_j \nabla_j \bar{S}_w - \frac{1}{2} (L_j \nabla_j \bar{S}_w)^2 \frac{d^2 f(\bar{S}_w)}{dS_w^2} \right) n_i dl \end{aligned} \quad (6.284)$$

This yields the coarse-scale wetting-phase saturation distribution of the new time step, which enters into the mobility calculation in the pressure equation of the next time step.

known:  $p, \underline{v}^{\text{discont.}}, \underline{v}, \bar{\underline{v}}, \underline{v}', \bar{S}_w$ .

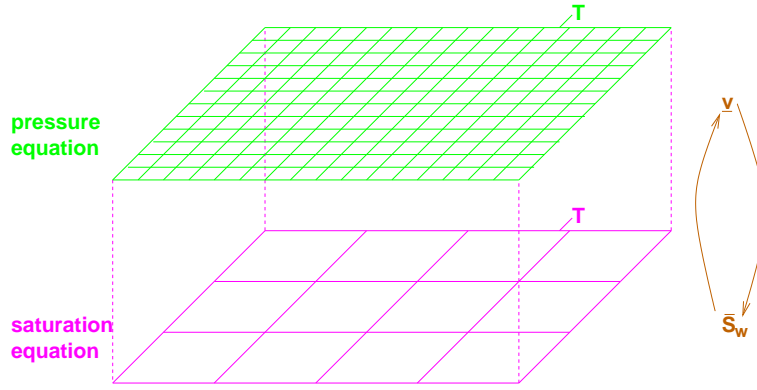


Figure 6.63: Multi-scale structure for test case *DG upscaled*.

For all the comparisnal studies of the module *DG upscaled*, the results of *DG fine* are taken as a reference solution. Error norms for *DG upscaled* as well as for the modules *DG coarse I*, *DG coarse II* as well as *DG fine*  $\bar{v}$  are computed with respect to that solution and the computing times are compared for the five modules. All these results as well as studies on the dependence of *DG upscaled* on the coarsening level are presented in Section 6.2.4.

Before having a closer look at the single modules and the outcome of their comparison, the computation of the error norms will be presented. The calculation of error norms takes place with respect to a reference solution, that is in this case the solution of the module *DG fine*. The  $L_1$  error is calculated by summing up the absolute value of the difference of the solution of *DG fine* and the coarse-scale model at the locations corresponding to the centers of fine-grid elements,

$$e_{L_1} = \sum_{i=1}^{n_f} |S_w^i - \bar{S}_w^i|, \quad (6.285)$$

where  $n_f$  is the number of fine-grid cells.

The error in the  $L_2$  norm is calculated analogously with the only difference being that the square root of the differences of the squares is summed up,

$$e_{L_2} = \sum_{i=1}^{n_f} \sqrt{(S_w^i)^2 - (\bar{S}_w^i)^2}. \quad (6.286)$$

### 6.2.1 The module *DG coarse I*

The numerical solution of the upscaled saturation equation shows a dispersed (diffusive) front. To be able to judge how much of the diffusive / dispersive behavior

is actually due to macrodispersion and how much due to numerical diffusion, the entries of the macrodispersion term are artificially set to zero and the algorithm is solved as given in Section 6.2.

### 6.2.2 The module *DG coarse II*

The module *DG coarse II* does not only use a coarse-grid form of the saturation equation, but it additionally uses an upscaled form of the pressure equation. Therefore, the algorithm differs from the one given in Section 5.4 as is shown in Figure 6.64. The principal procedure is the following:

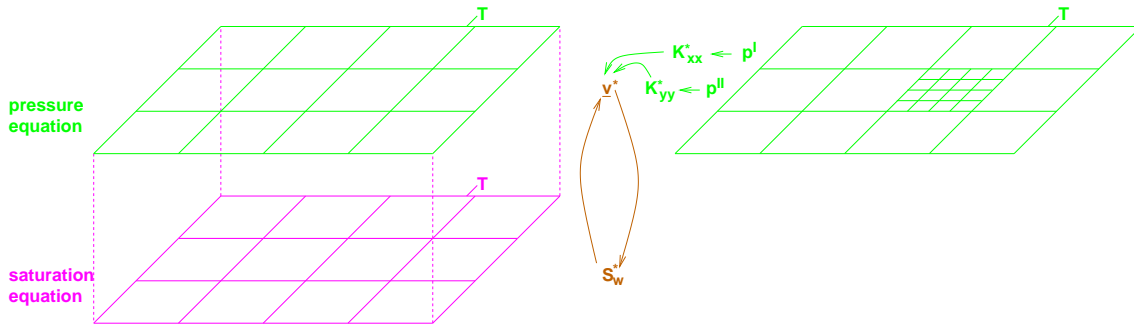


Figure 6.64: Multi-scale structure for test case *DG coarse II*. On the right hand side, the preprocessing step (0a. and 0b.) is shown where the coarse-scale permeability tensor  $\underline{K}^*$  is obtained by fine-grid pressure solutions over regions corresponding to coarse-grid blocks.

- 0a. Solve local one-phase problems on the fine scale in regions corresponding to one coarse-grid cell in  $T$

$$\nabla \cdot [\underline{K} \cdot \nabla p^I] = 0 \quad (6.287)$$

$$\nabla \cdot [\underline{K} \cdot \nabla p^{II}] = 0, \quad (6.288)$$

The first pressure equation given by Equation (6.287) is solved with boundary conditions as given in Figure 6.65 on the left hand side, whereas the boundary conditions used for the second pressure equation are given in the same figure on the right hand side. This gives a fine-scale pressure field  $p^I$  coming from the problem with flux in x-direction (Equation (6.287)) and a fine-scale pressure field  $p^{II}$  resulting from the problem in y-direction (Equation (6.288)).

known:  $p^I, p^{II}$

0b. Calculate coarse-grid permeabilities from the pressures obtained from the solution of local problems in  $T$

$$K_{xx}^* = \frac{\langle K \nabla_x p^I \rangle}{\langle \nabla_x p^I \rangle} \quad \text{with } \langle \cdot \rangle = \frac{1}{h_x h_y} \int_{E_x} \int_{E_y} \cdot dx dy \quad (6.289)$$

$$K_{xy}^* = 0 \quad (6.290)$$

$$K_{yx}^* = 0 \quad (6.291)$$

$$K_{yy}^* = \frac{\langle K \nabla_y p^{II} \rangle}{\langle \nabla_y p^{II} \rangle}, \quad (6.292)$$

where  $E_x$  and  $E_y$  are the edges oriented in x-direction, and in y-direction, respectively. Their dimensions are denoted by  $h_x$  and  $h_y$ . Note, that the absolute permeability is no longer a quasi-scalar quantity, but a diagonal tensor.

known:  $p^I, p^{II}, \mathbf{K}_{xx}^*, \mathbf{K}_{xy}^*, \mathbf{K}_{yx}^*, \mathbf{K}_{yy}^*$

1. Solve the coarse-scale pressure equation in  $T$

$$\nabla \cdot (\lambda(S_w^*) \underline{\underline{K}}^* \cdot \nabla p^*), \quad \underline{v}^{*,\text{discont.}} = -\lambda(S_w^*) \underline{\underline{K}}^* \cdot \nabla p^* \quad (6.293)$$

The pressure equation gives coarse-scale pressures  $p^*$  from which coarse-scale velocities  $\underline{v}^*$  can be calculated using Darcy's Law.

known:  $p^I, p^{II}, K_{xx}^*, K_{xy}^*, K_{yx}^*, K_{yy}^*, \mathbf{p}^*, \underline{v}^{*,\text{discont.}}$ .

2. Make the coarse-scale velocity field in  $T$  continuous across element edges:

$$\underline{v}^{*,\text{discont.}} \rightarrow \underline{v}^{*,\text{cont.}} =: \underline{v}^*. \quad (6.294)$$

A  $BDM_1^0$  projection is applied to make the discontinuous velocity field obtained from the solution of 1. continuous across element edges. This property is needed to ensure a locally mass-conservative discretization.

known:  $p^I, p^{II}, K_{xx}^*, K_{xy}^*, K_{yx}^*, K_{yy}^*, \mathbf{p}^*, \underline{v}^{*,\text{discont.}}, \underline{\mathbf{v}}^*$ .

8. Solve the fine-scale form of the saturation equation in  $T$  on the coarse grid using  $\underline{v}^*$ :

$$\frac{\partial S_w^*}{\partial t} + \nabla \cdot (f_w(S_w^*) \underline{v}^*) = 0 \quad (6.295)$$

This gives coarse-scale saturations  $S_w^*$  which again enter the mobility calculation in the coarse-scale pressure equation.

known:  $p^I, p^{II}, K_{xx}^*, K_{xy}^*, K_{yx}^*, K_{yy}^*, \mathbf{p}^*, \underline{v}^{*,\text{discont.}}, \underline{v}^*, \mathbf{S}_w^*$ .

Within this algorithm, steps 0a. and 0b. are preprocessing steps, i.e. they are solved before the start of the time loop.

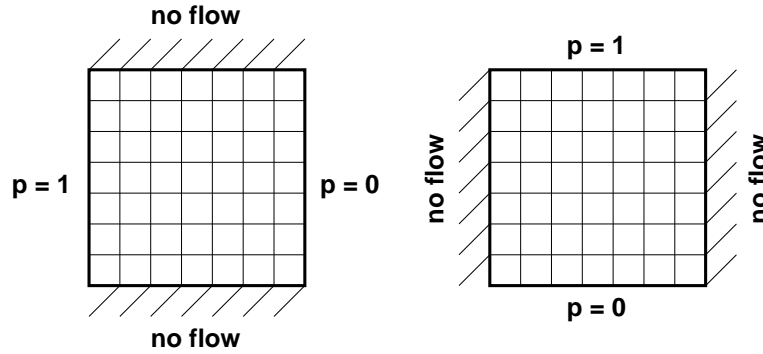


Figure 6.65: The fine-scale one-phase pressure equation is solved in regions corresponding to coarse-grid blocks (left hand side: x-direction, right hand side: y-direction).

### 6.2.3 The module *DG fine* $\bar{v}$

The module *DG fine*  $\bar{v}$  is introduced to check the influence of taking the averaged velocity field  $\bar{v}(\bar{x}, t)$  instead of the fine-scale velocity field  $v(x, t)$ . Therefore, the averaged velocity field is used, but the saturation equation is solved in its hyperbolic (fine-scale) form on the fine grid.

The part of the overall algorithm of Section 5.5.1 that is used in this module is the following:

1. Solve the fine-scale pressure equation in  $T$ :

$$\nabla \cdot [\lambda(S_w)\underline{K} \cdot \nabla p] = 0, \quad \underline{v}^{\text{discont.}} = -\lambda(S_w)\underline{K} \cdot \nabla p, \quad (6.296)$$

where the total mobility is approximated by the mobility  $\lambda(S_w)$  where  $S_w$  comes from the solution of the saturation equation. This mobility is no pure fine-grid quantity as the corresponding saturation  $S_w$  is calculated using the averaged velocities  $\bar{v}$ . The resulting quantities are the fine-scale pressures and the fine-scale total velocities in the entire domain.

known:  $p, \underline{v}^{\text{discont.}}$ .

2. Make the fine-scale velocity field in  $T$  continuous across element edges:

$$\underline{v}^{\text{discont.}} \rightarrow \underline{v}^{\text{cont.}} =: \underline{v}. \quad (6.297)$$

A  $BDM_1^0$  projection as discussed in Section 4.3.1.1 is applied to make the discontinuous velocity field obtained from the solution of 1. continuous across element edges. This property is needed to ensure a locally mass-conservative discretization.

known:  $p, \underline{v}^{\text{discont.}}, \underline{v}$ .

3. Volume averaging for the total velocity  $\underline{v}$  in  $T$ :

$$\underline{v} = \bar{v} + \underline{v}', \quad \bar{v} = \frac{1}{E} \int_E \underline{v}(x, t) dE \quad (6.298)$$

Thus, additionally, the coarse-scale total velocities in  $T$  are known.

known:  $p, \underline{v}^{\text{discont.}}, \underline{v}, \bar{v}, \underline{v}'$ .

8. Solve the fine-scale form of the saturation equation in  $T$  on the fine grid using  $\bar{v}$ :

$$\frac{\partial S_w}{\partial t} + \nabla \cdot (f_w(S_w)\bar{v}) = 0 \quad (6.299)$$

known:  $p, \underline{v}^{\text{discont.}}, \underline{v}, \bar{v}, \underline{v}', \mathbf{S}_w$ .

## 6.2.4 Results of the Comparisomal Studies

In this section, the simulation results of *DG upscaled* are compared to the module *DG coarse I* discussed in Section 6.2.1, to the module *DG coarse II* (Section 6.2.2) as well as to the module *DG fine*  $\bar{v}$  explained in Section 6.2.3. All of these coarse-scale or quasi coarse-scale models are compared to the reference fine-scale solution *DG fine*. In the end, a study on the dependence of *DG upscaled* on the coarsening level is done for the example of the permeability field “standard”.

Boundary and initial conditions for the coarse-scale models are given analogously to the fine-scale case in Section 6.1.2, the only difference being that saturation values are given on the coarse grid, see Figure 6.66.

Figure 6.67 shows the y-averaged wetting-phase saturation profiles over the x-coordinate of the domain both for the homogeneous domain and for the five heterogeneous cases using the linear as well as the nonlinear model equations. In all

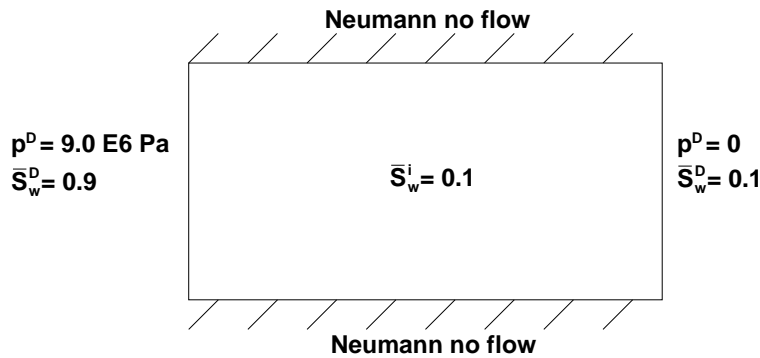


Figure 6.66: Boundary and initial conditions used for the testing of the modules *DG upscaled*.

twelve cases, a very good agreement between the fine model and all of the coarse-scale models can be detected.

The saturation fronts in the linear and the nonlinear case for the homogeneous domain can be taken from Figure 6.68. The respective CPU times are compared in Table 6.8 and the error norms are listed in Table 6.9. Visually, one can confirm the good agreement between fine and coarse-scale modules which seems to be even better in the nonlinear case.

Considering the CPU times in the homogeneous case, the coarse-scale models generally take more CPU time than the fine-scale models. This is due to the fact, that all of the considered coarse-scale models require additional evaluations like the averaging of velocities along coarse-block edges or the solution of local fine-grid problems which are entirely superfluous in the homogeneous linear case. In the homogeneous linear case, the fine-scale module *DG fine* is obviously not only the most accurate, but also the fastest model. For the homogeneous domain, only the module *DG coarse II* is in the nonlinear case faster than *DG fine*.

One can see, that the errors in  $L_1$  and  $L_2$  for the three coarse-scale models *DG upscaled*, *DG coarse I*, and *DG coarse II* for the linear as well as for the nonlinear case are approximately the same. The module *DG fine  $\bar{v}$*  does not make any error in the homogeneous case, as the velocity field is represented exactly, and the saturation equation is solved on the same (fine) grid as within *DG fine*.

Now, the five heterogeneous test cases are considered, at first only using the linear model equations. Figure 6.69 shows the respective saturation fronts whereas the

module	<i>DG upscaled</i>	<i>DG coarse I</i>	<i>DG coarse II</i>	<i>DG fine <math>\bar{v}</math></i>	<i>DG fine</i>
linear	4.912	8.051	0.887	9.963	0.633
nonlinear	7.865	8.033	0.916	13.986	4.313

Table 6.8: System CPU times [s] for a homogeneous problem using different coarse-scale models (linear and nonlinear case).

module	<i>DG upscaled</i>	<i>DG coarse I</i>	<i>DG coarse II</i>	<i>DG fine <math>\bar{v}</math></i>
linear $L_1$	369.92	350.32	362.10	0.00
linear $L_2$	15.69	14.42	15.66	0.00
nonlinear $L_1$	313.15	312.98	311.51	0.00
nonlinear $L_2$	14.22	14.21	14.21	0.00

Table 6.9: Error norms  $L_1$  and  $L_2$  for a homogeneous problem using different coarse-scale models (linear and nonlinear case). The respective reference solution is the one provided by *DG fine*.



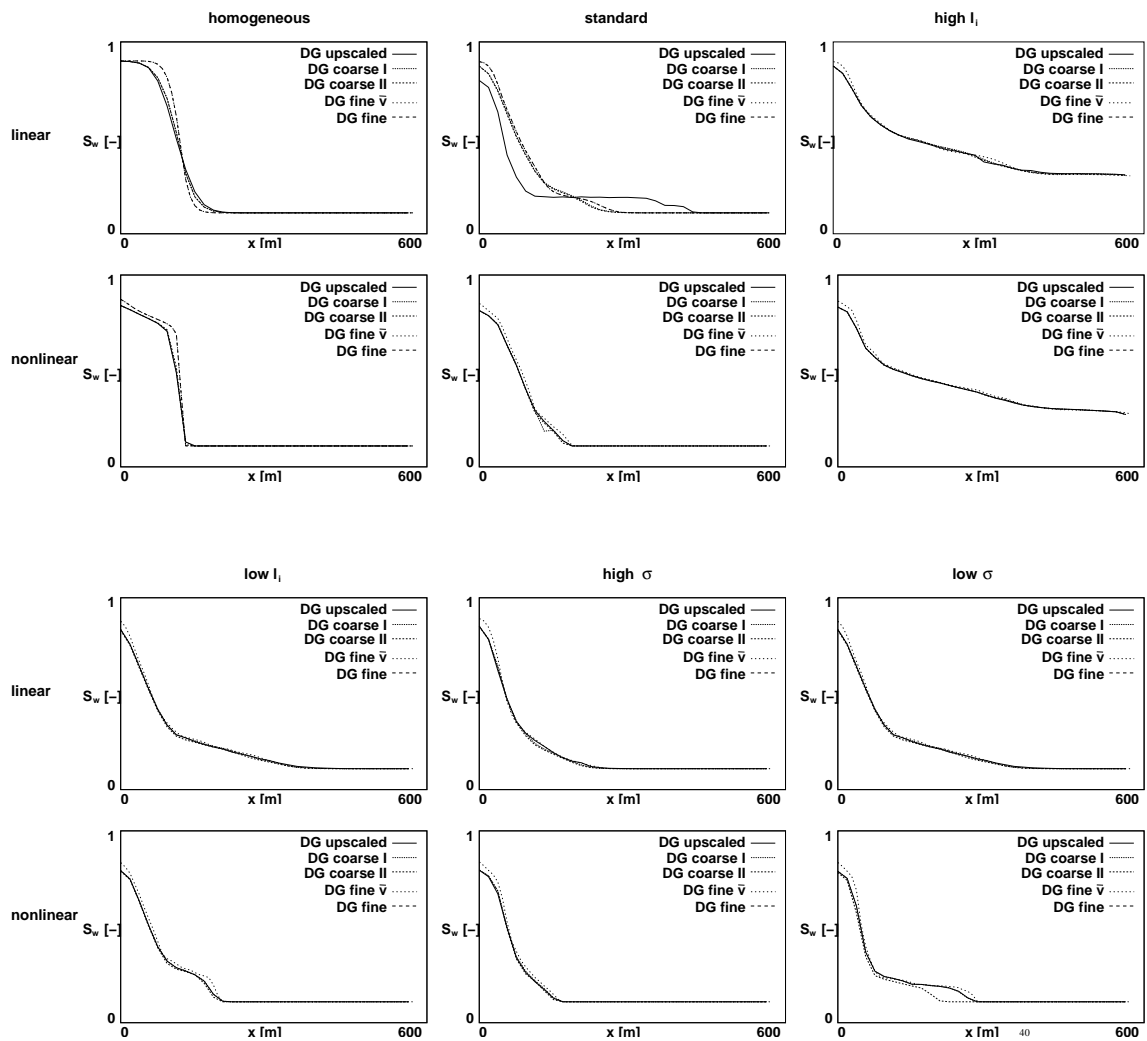


Figure 6.67: Saturation profiles (y-averaged values) for the linear and nonlinear case in a homogeneous domain and for the five test permeability fields.

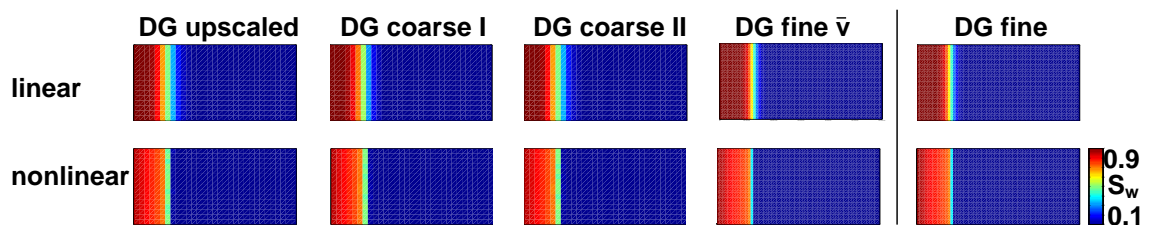


Figure 6.68: Saturation fronts in a homogeneous domain for the linear and the nonlinear case for different coarse-scale models and the reference fine-scale solution *DG fine*.

CPU times can be found in Table 6.10 and the error norms in Table 6.11.

Obviously, the coarse-scale models capture the main feature of the fine-scale reference solution, and the module *DG fine  $\bar{v}$*  captures them even very accurately as expected. This implies that a significant part of the error still comes from the numerical diffusion due to the coarse-scale solution of the saturation equation. However, the agreement with the reference solution is for all test cases very good.

With respect to CPU times, the modules *DG upscaled* and *DG coarse I* perform very similar as can be expected. For these heterogeneous cases, all of the three “real” coarse-scale modules *DG upscaled*, *DG coarse I* and *DG coarse II* are faster than the module *DG fine  $\bar{v}$*  which still includes a fine-scale saturation solution. However, in the linear case, the module *DG coarse II* is about three times faster than the upscaled module *DG upscaled*.

The error norms for *DG upscaled*, *DG coarse I* and *DG coarse II* are very similar for all five test fields. Only the module *DG fine  $\bar{v}$*  partly has an almost perfect agreement with the reference module resulting in very small error norms.

For the five heterogeneous test fields in the nonlinear case, saturation fronts are shown in Figure 6.70. The system CPU times are compared in Table 6.12 and the error norms can be found in Table 6.13.

The quality of the saturation fronts is visually very similar to the linear case. Whereas *DG upscaled*, *DG coarse I* and *DG coarse II* are able to reproduce the principal features of the fine-scale reference, *DG fine  $\bar{v}$*  seems to capture them very accurately.

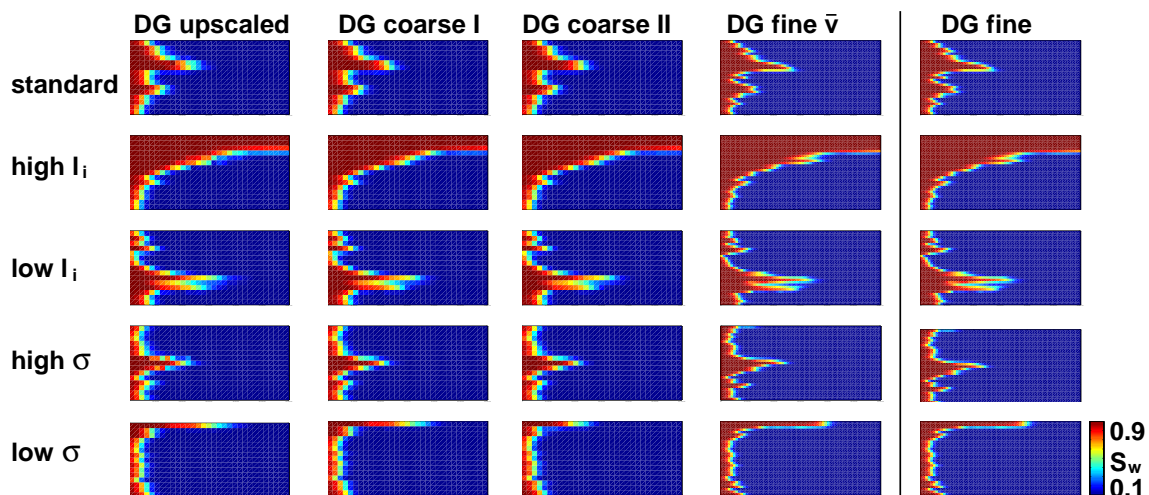


Figure 6.69: Saturation fronts using the five test permeability fields for the linear case for different coarse-scale models and the reference fine-scale solution *DG fine*.

module	<i>DG upscaled</i>	<i>DG coarse I</i>	<i>DG coarse II</i>	<i>DG fine</i> $\bar{v}$
standard	6.853	6.725	2.061	9.292
high $l_i$	5.958	5.168	1.791	15.858
low $l_i$	4.673	6.407	2.134	312.11
high $\sigma$	5.146	5.374	1.791	9.421
low $\sigma$	4.894	7.280	1.732	10.053

Table 6.10: System CPU times [s] for the heterogeneous test cases using different coarse-scale models (linear case).

module	<i>DG upscaled</i>	<i>DG coarse I</i>	<i>DG coarse II</i>	<i>DG fine</i> $\bar{v}$
standard $L_1$	317.41	315.02	315.01	0.15
standard $L_2$	14.08	14.07	14.08	0.01
high $l_i$ $L_1$	419.04	416.44	420.24	0.20
high $l_i$ $L_2$	16.18	16.35	16.43	0.01
low $l_i$ $L_1$	308.76	306.94	309.19	0.32
low $l_i$ $L_2$	13.49	13.49	13.50	0.02
high $\sigma$ $L_1$	250.35	251.76	251.58	0.11
high $\sigma$ $L_2$	12.21	12.22	12.24	0.01
low $\sigma$ $L_1$	280.64	279.61	312.03	0.14
low $\sigma$ $L_2$	13.19	13.18	13.95	0.01

Table 6.11: Error norms  $L_1$  and  $L_2$  for the heterogeneous test cases using different coarse-scale models (linear case). The respective reference solution is the one provided by *DG fine*.

Considering the CPU times, one can see that they are minimal for the upscaled modules *DG upscaled* and *DG coarse I*. So this nonlinear heterogeneous case is the one where the upscaled saturation equation gives the fastest solution.

The error times are again quite the same for the three pure coarse-scale models. One can see that the error is especially high for the permeability field “high  $l_i$ ”. This is due to the fact that this setup corresponds nearly to a layered medium implying that in the upper highly permeable layer, the flow velocity is very large. Over the whole width of the domain, the velocity component in x-direction might highly vary. Moreover, the saturation front reaches the right boundary which then has a strong influence.

Concludingly, one can say that for the considered test cases, no large differences in accuracy can be detected. Especially, the difference between *DG upscaled* and *DG coarse I* is small. This is due to the fact, that the macrodispersion term is very small. This is because due to the averaging over coarse-grid block edges only, the variation of velocity inside a grid-block is not taken into account. However, for the nonlinear and heterogeneous cases, the upscaled coarse-scale model is the fastest of the considered modules.

Having compared *DG upscaled* to alternative coarse-scale models and to its reference fine-scale solution *DG fine*, the dependence of *DG upscaled* on the coarsening level will now be studied and compared to the module without macrodispersion term, i.e. *DG coarse I*. For these investigations, a very fine resolved permeability field is generated. Figure 6.71 shows the saturation fronts for a fine-scale level of ML 4 and a coarse-scale level ranging from ML 3 to ML 1 in the linear case for a domain which

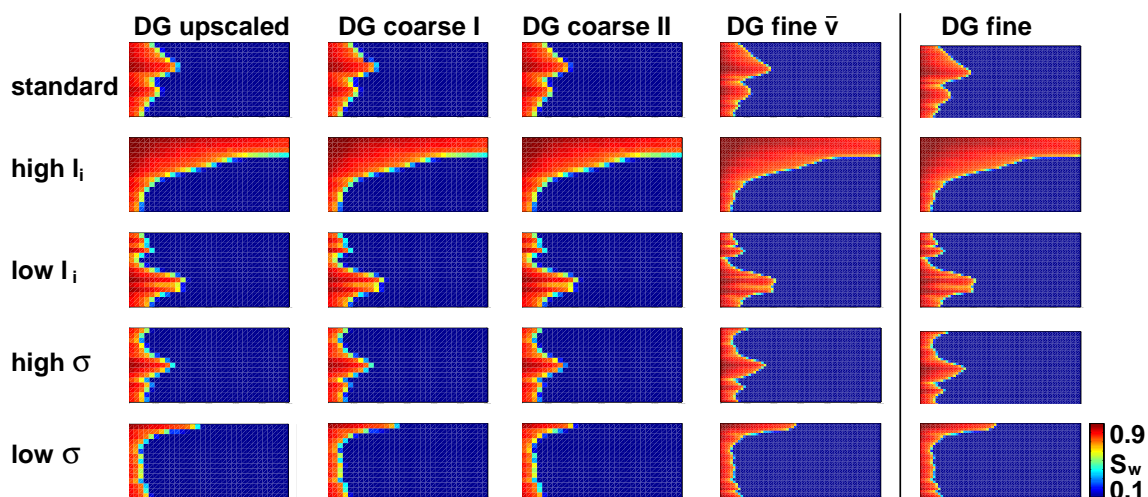


Figure 6.70: Saturation fronts using the five test permeability fields for the nonlinear case for different coarse-scale models and the reference fine-scale solution *DG fine*.

module	<i>DG upscaled</i>	<i>DG coarse I</i>	<i>DG coarse II</i>	<i>DG fine</i> $\bar{v}$
standard	10.195	6.629	173.658	14.278
high $l_i$	8.722	8.915	193.734	11.456
low $l_i$	8.341	7.858	197.108	14.717
high $\sigma$	6.361	9.028	200.078	11.748
low $\sigma$	5.979	7.947	186.474	12.009

Table 6.12: System CPU times [s] for the heterogeneous test cases using different coarse-scale models (nonlinear case).

module	<i>DG upscaled</i>	<i>DG coarse I</i>	<i>DG coarse II</i>	<i>DG fine</i> $\bar{v}$
standard $L_1$	269.40	271.66	268.56	1.01
standard $L_2$	12.93	13.03	12.94	0.09
high $l_i$ $L_1$	424.50	422.16	418.19	1.65
high $l_i$ $L_2$	15.22	15.24	15.16	0.09
low $l_i$ $L_1$	255.70	255.28	255.50	0.95
low $l_i$ $L_2$	12.40	12.41	12.44	0.08
high $\sigma$ $L_1$	215.29	214.00	214.88	1.02
high $\sigma$ $L_2$	11.38	11.37	11.40	0.10
low $\sigma$ $L_1$	228.62	228.81	247.05	0.64
low $\sigma$ $L_2$	11.79	11.80	12.27	0.06

Table 6.13: Error norms  $L_1$  and  $L_2$  for the heterogeneous test cases using different coarse-scale models (nonlinear case). The respective reference solution is the one provided by *DG fine*.

is homogeneous in its upper part and which shows a heterogeneous structure in its lower part. Figure 6.72 shows the corresponding saturation fronts for the nonlinear case, whereas Figure 6.73 compares the  $y$ -averaged saturation profiles, where the wetting-phase saturation is averaged over the height of the domain and displayed as a function of the longitudinal coordinate of the domain. CPU times and error norms can be found in Tables 6.14 and 6.15.

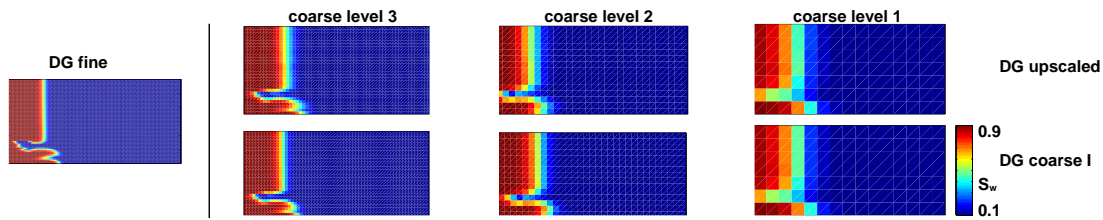


Figure 6.71: Saturation fronts for fine level 4 and coarse level 3 through 1 in the linear case.

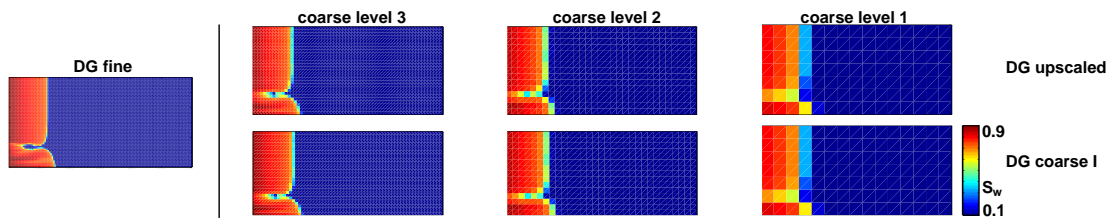


Figure 6.72: Saturation fronts for fine level 4 and coarse level 3 through 1 in the nonlinear case.

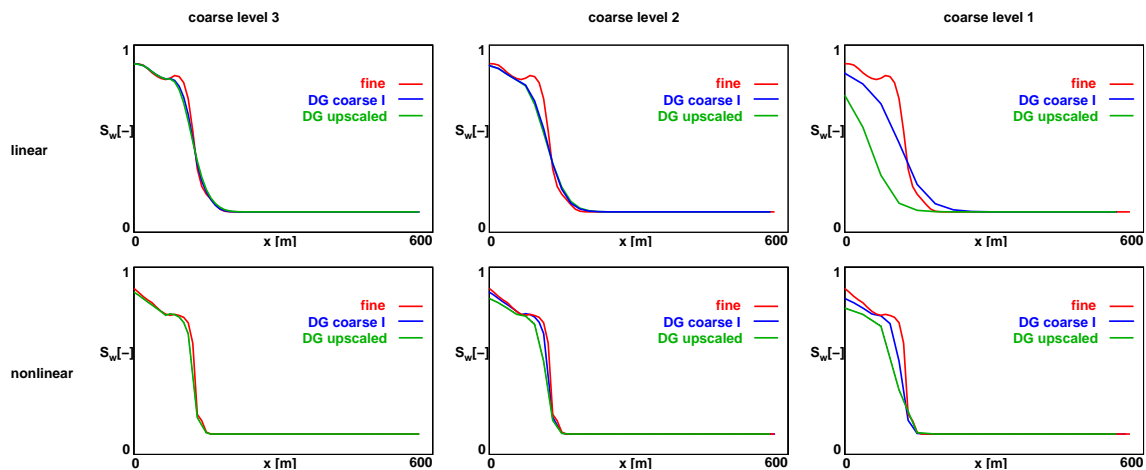


Figure 6.73: Saturation profiles ( $y$ -averaged) in the linear and the nonlinear case for coarse levels ranging from level 3 to 1. A comparison of the upscaled solution (*DG upscaled*), the upscaled solution without macrodispersion (*DG coarse I*), and the reference fine-scale solution (*DG fine*) is shown.

coarse level	3		2		1		<i>DG fine</i>
	<i>DG upscaled</i>	<i>coarse I</i>	<i>upscaled</i>	<i>coarse I</i>	<i>upscaled</i>	<i>coarse I</i>	
linear	13.916	22.018	6.577	5.702	4.351	4.639	5835.752
nonlinear	15.875	22.621	8.205	6.700	5.264	5.175	5872.959

Table 6.14: CPU times [s] for fine level 4 and coarse levels 3 through 1 in the linear and nonlinear case.

coarse level	3		2		1	
	<i>DG upscaled</i>	<i>coarse I</i>	<i>upscaled</i>	<i>coarse I</i>	<i>upscaled</i>	<i>coarse I</i>
linear $L_1$	1453.65	1424.12	4161.69	4145.49	9362.75	9362.03
linear $L_2$	31.73	31.67	54.42	54.39	81.04	81.04
nonlinear $L_1$	1251.82	1250.03	3665.84	3662.61	8350.66	8347.90
nonlinear $L_2$	28.80	28.80	49.55	49.54	73.92	73.92

Table 6.15: Error norms  $L_1$  and  $L_2$  for fine level 4 and coarse levels 3 through 1 in the linear and nonlinear case.

Studying the saturation profiles given in Figures 6.71 and 6.72 as well as the error norms, one can see that generally, the difference between *DG upscaled* and *DG coarse I* is not significant. Also, it can be remarked that the error norms are smaller for all coarse levels using the nonlinear model. In opposition to what one might expect, the error norms are for the considered permeability field smaller for the module *DG coarse I* which does not take a macrodispersion term into account.

One gets more insight into the magnitude of the error norms in having a look at Figure 6.73. One can see, that already the saturation profile of the module *DG coarse I* generally shows a too dispersive front. Adding a macrodispersion term further increases the dispersive effects. Thus, although using higher order schemes, numerical diffusion has a major influence and falsifies the results.

Considering the computing times, they are decreasing with decreasing coarse level, as the upscaled saturation equation has to be solved for less grid cells. Furthermore, they are always smaller for the linear model, as here, the pressure equation has to be solved only once, instead of every macro time step. Note, that the differences in computing times between the fine reference module and the coarse-scale modules are significant.

## 6.3 Testing of *DG local 2p2c*

### 6.3.1 General Remarks and Algorithm

To check the quality of the module *DG local 2p2c*, a 2p2c problem is solved not only locally within the small domain  $U$ , but globally in the whole domain  $T$ . This module will be called *DG 2p2c* and serves as a reference solution for the module *DG local 2p2c*. Like this, a comparison can be done to check the validity of the assumption that mass transfer processes only take place within  $U$ . Note, that the algorithm for the module of interest, i.e. *DG local 2p2c* was given in Section 5.5.1.

The algorithm for the reference module *DG 2p2c* is the following (see Figure 6.74):

1. Solve the fine-scale pressure equation in  $T$ :

$$\nabla \cdot [\lambda(S_w)\underline{K} \cdot \nabla p] = 0, \quad \underline{v}^{\text{discont.}} = -\lambda(S_w)\underline{K} \cdot \nabla p, \quad (6.300)$$

The resulting quantities are the fine-scale pressures and the fine-scale total velocities in the entire domain.

known:  $\mathbf{p}, \underline{v}^{\text{discont.}}$ .

2. Make the fine-scale velocity field in  $T$  continuous across element edges:

$$\underline{v}^{\text{discont.}} \rightarrow \underline{v}^{\text{cont.}} =: \underline{v}. \quad (6.301)$$

A  $BDM_1^0$  projection as discussed in Section 4.3.1.1 is applied to make the discontinuous velocity field obtained from the solution of 1. continuous across element edges. This property is needed to ensure a locally mass-conservative discretization.

known:  $p, \underline{v}^{\text{discont.}}, \underline{\mathbf{v}}$ .

4. Solve one fine-scale total concentration equation in  $T$ :

$$\frac{\partial C^1}{\partial t} + \underline{v} \cdot \nabla \sum_{\alpha} (f_{\alpha} C_{\alpha}^1) = 0 \quad (6.302)$$

This means, that the total concentrations on the fine scale in  $T$  are determined for the new time step.

known:  $p, \underline{v}^{\text{discont.}}, \underline{v}, \mathbf{C}^1$ .

5. Calculate the fine-scale wetting-phase saturations in  $T$  from the concentration equation in  $T$ :

$$S_w = S_w(C^1, p), \quad (6.303)$$

where  $S_w(C^1)$  is obtained using flash calculations, see Section 3.4.1. The fine-scale saturation distribution is needed for the next pressure solution.

known:  $p, \underline{v}^{\text{discont.}}, \underline{v}, C^1, \mathbf{S}_w$ .



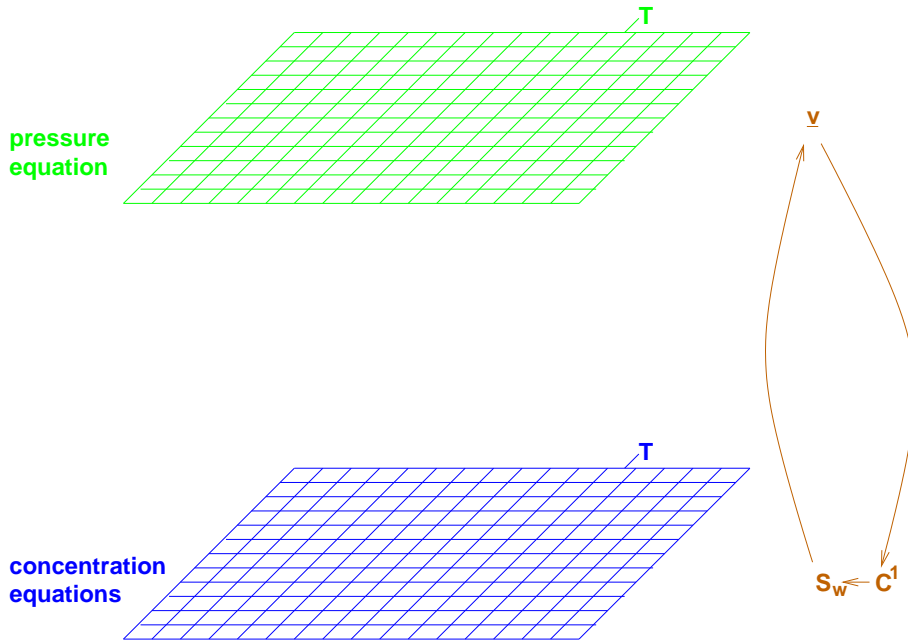


Figure 6.74: Multi-scale structure for the reference test case *DG 2p2c*.

### 6.3.2 Results of the Comparisomal Studies

Results for the module *DG local 2p2c* and its reference module *DG 2p2c* will be shown. Both linear and nonlinear case are studied in a homogeneous domain as well as for the five test permeability fields. Furthermore, a test case is set up to study the dependence of the quality of the module *DG local 2p2c* and of the computing times on the upscaling level.

Figure 6.75 shows the setup as well as the boundary and initial conditions for the domain introduced in Figure 6.54. This setup corresponds to the simplified motivation example of Figure 1.8. Flow is from left to right and governed by the difference in the Dirichlet pressure boundaries as given in Figure 6.75, resulting in a mean total velocity of  $1.5 \cdot 10^{-10} \frac{m}{s}$ . The top and bottom boundary of domain  $T$  are impermeable (Neumann no-flow boundaries), while Dirichlet boundaries are assumed for the wetting-phase saturation, taking  $S_w^D = 0.9$  at both left and right boundary. Initial conditions are given in a way that  $S_w^i = 0.1$  in a small part  $V$  of the model domain  $T$  which lies inside the domain  $U$ . At the boundary of  $U$ , Dirichlet boundaries for the total concentrations  $C^1$  are assumed. As the saturations at the boundary may change in the course of the simulation, these boundary conditions are instationary. They are updated as given in Section 5, where it is assumed that at the boundary of  $U$ , the wetting-phase only consists of water and the non-wetting-phase only of air, i.e.  $X_w^1 = 1$  and  $X_n^2 = 1$ . The initial conditions for  $C^1$  are given in a way that applying a flash calculation, the resulting wetting-phase saturation would be equal

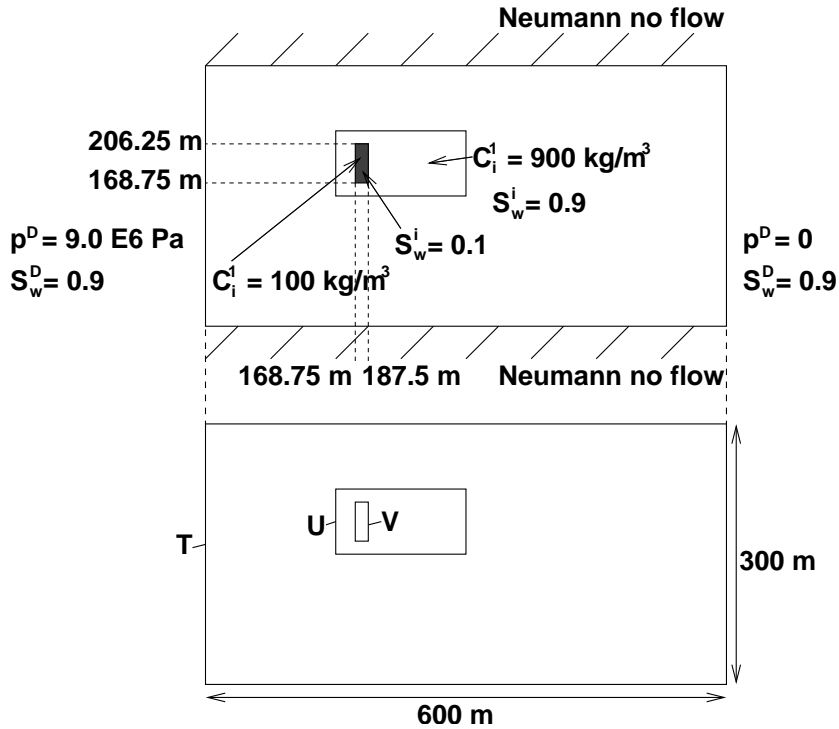


Figure 6.75: Boundary and initial conditions used for the testing of the modules *DG local 2p2c*.

to  $S_w = 0.9$  in  $\{U \setminus V\}$  ( $C_i^1 = 900 \frac{kg}{m^3}$ ), while within  $V$ , values for  $C^1$  are given such that the resulting wetting-phase saturation  $S_w = 0.1$ , i.e.,  $C_i^1 = 100 \frac{kg}{m^3}$ . The vapor pressures, Henry constants, and molar weights of water and air can be taken from Appendix A.

The discretization length is given by  $\Delta x = 9.375$  m for the fine grid and  $\Delta \bar{x} = 18.75$  m for the coarse grid. As both saturation and concentration equation are solved time-explicitly, both macro and micro time step are determined according to the CFL condition. In the following simulation results, the state of the system at a time of  $t = 627.17$  d is considered.

Figure 6.76 shows the saturation fronts in a homogeneous domain for both linear and nonlinear case comparing the module *DG local 2p2c* to *DG 2p2c*. The computing times for all four combinations are shown in Table 6.16, whereas the error norms in  $L_1$  and  $L_2$  are shown in Table 6.17.

For the five test permeability fields, Figure 6.77 shows the saturation fronts of *DG local 2p2c* in the linear case and compares it to the reference fine-scale solution. Figure 6.78 shows the corresponding saturation contours for the nonlinear case. For a better orientation, the permeability fields as well as the position of the local domain are plotted in the bottom line. CPU times and error norms can be taken from Tables 6.18 and 6.19, respectively.

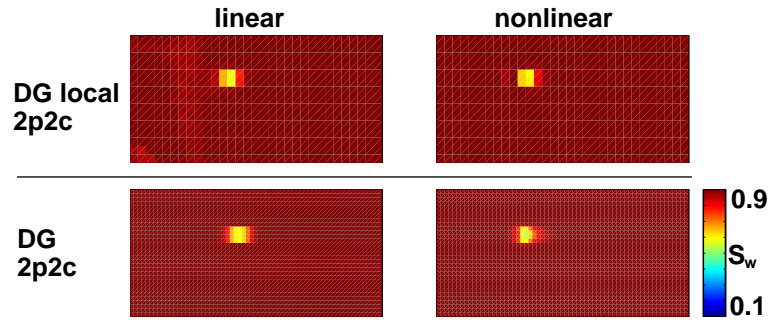


Figure 6.76: Saturation fronts in a homogeneous domain for the linear and the non-linear case for the module *DG local 2p2c* and its reference fine-scale solution *DG 2p2c*.

module	<i>DG local 2p2c</i>	<i>DG 2p2c</i>
linear	9.403	7.356
nonlinear	11.064	7.636

Table 6.16: System CPU times [s] for a homogeneous problem with local and global 2p2c processes (linear and nonlinear case).

module	<i>DG local 2p2c</i>
linear $L_1$	29.20
linear $L_2$	1.80
nonlinear $L_1$	10.41
nonlinear $L_2$	1.20

Table 6.17: Error norms  $L_1$  and  $L_2$  for a homogeneous problem with local 2p2c processes (linear and nonlinear case). The module *DG 2p2c* serves as reference module.

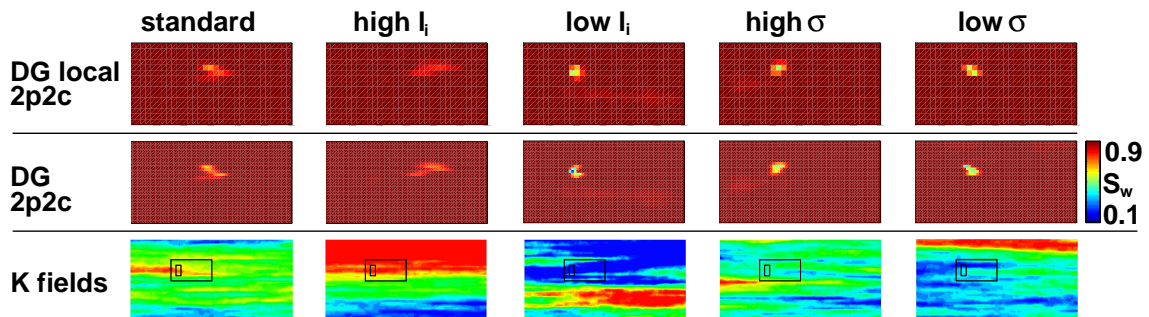


Figure 6.77: Saturation fronts for the five test permeability fields in the linear case—comparison of the module *DG local 2p2c* to its reference fine-scale solution *DG 2p2c*.

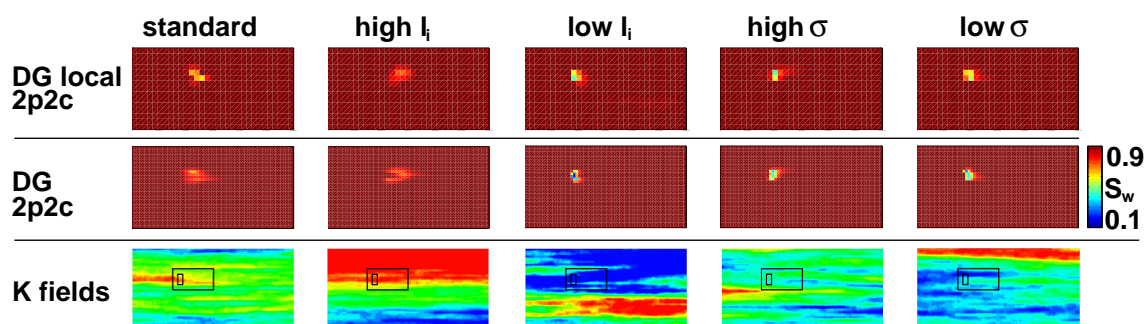


Figure 6.78: Saturation fronts for the five test permeability fields in the nonlinear case—comparison of the module *DG local 2p2c* to its reference fine-scale solution *DG 2p2c*.

module	<i>DG local 2p2c</i> <i>DG 2p2c</i>		<i>DG local 2p2c</i> <i>DG 2p2c</i>	
	linear		nonlinear	
standard	9.674	7.485	9.160	8.882
high $l_i$	9.153	7.325	13.241	11.249
low $l_i$	9.502	7.554	10.673	7.852
high $\sigma$	10.463	6.828	8.825	9.130
low $\sigma$	9.622	8.846	10.673	8.846

Table 6.18: System CPU times [s] for the five heterogeneous test cases with local and global 2p2c processes (linear and nonlinear case).

module	<i>DG local 2p2c</i> (linear)	<i>DG local 2p2c</i> (nonlinear)
standard $L_1$	11.56	12.17
standard $L_2$	1.02	1.01
high $l_i$ $L_1$	22.40	12.47
high $l_i$ $L_2$	1.05	0.92
low $l_i$ $L_1$	31.54	21.45
low $l_i$ $L_2$	1.74	1.86
high $\sigma$ $L_1$	21.16	13.98
high $\sigma$ $L_2$	1.38	1.50
low $\sigma$ $L_1$	25.16	17.84
low $\sigma$ $L_2$	1.56	1.65

Table 6.19: Error norms  $L_1$  and  $L_2$  for the five heterogeneous test cases with local 2p2c processes (linear and nonlinear case). The module *DG 2p2c* serves as reference module.

Both saturation fronts and error norms show, that the agreement between *DG local 2p2c* and the reference solution is excellent for both linear and nonlinear model equations. Even for the permeability field “high  $l_i$ ” with the high permeability in its upper layer, the reference solution can be reproduced, although the zone of high non-wetting phase saturation leaves the local domain  $U$  in the linear case, see Figure 6.77. This shows, that the implementation of the boundary conditions at  $\partial U$  as presented in this work makes sense.

The only issue which might appear unexpected at a first glance, are the CPU times. The module *DG local 2p2c* takes slightly longer computing times than *DG 2p2c*, although 2p2c processes are considered only locally. This is due to the fact that in the module *DG local 2p2c*, the upscaled saturation equation is solved at every macro time step, which is unnecessary using the reference module *DG 2p2c*. Including a more complex thermodynamic model leading to more expensive flash calculations, it has to be assumed, that the CPU times of *DG local 2p2c* will quickly fall below the CPU times of the module *DG 2p2c*.

In a further investigation, the dependence of the accuracy and performance of *DG local 2p2c* on the upscaling level is studied. As the definition of the source zone (domain  $V$ ) has to correspond to the coarse grid, we study the geometrically slightly modified setup of Figure 6.79. Boundary and initial conditions, however, are given exactly as presented in Figure 6.75. To study different upscaling levels, a fine grid corresponding to ML 4 ( $\Delta x = 4.6875$  m) is taken. The considered system state is the situation after a simulation time of 314.18 d.

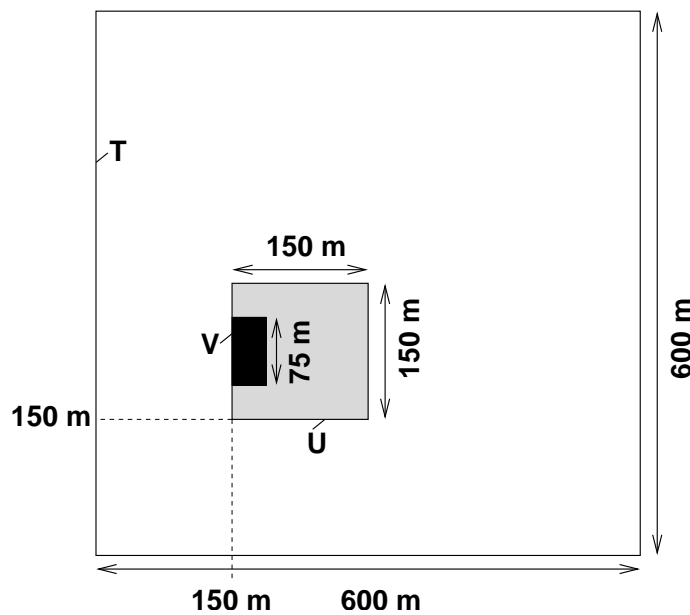


Figure 6.79: Geometry for the studies on the dependence of the module *DG local 2p2c* on the upscaling level.

For the generation of the corresponding log-permeability field, “standard” parameters are given. The resulting distribution of absolute permeability as well as the position of the local domain  $U$  and the position of the contaminated zone  $V$  are shown in Figure 6.80.

Saturation contour lines are shown in Figure 6.81 for coarse levels 1 through 3 and ML 4 using linear and nonlinear model equations. The results are compared to the reference solution  $DG\ 2p2c$  which is run on ML 4. Moreover, computing times are compared in Table 6.20 and error norms in  $L_1$  and  $L_2$  are displayed in Table 6.21.

Comparing the saturation contour lines given in Figure 6.81 as well as the error norms given in Table 6.21, a very good agreement between the solution provided by

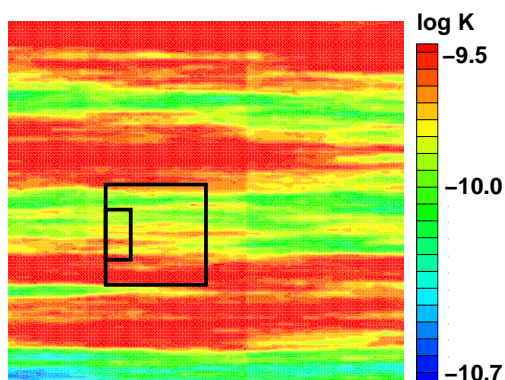


Figure 6.80: Log-permeability field on ML 4 for the studies on the dependence of  $DG\ local\ 2p2c$  on the upscaling level.

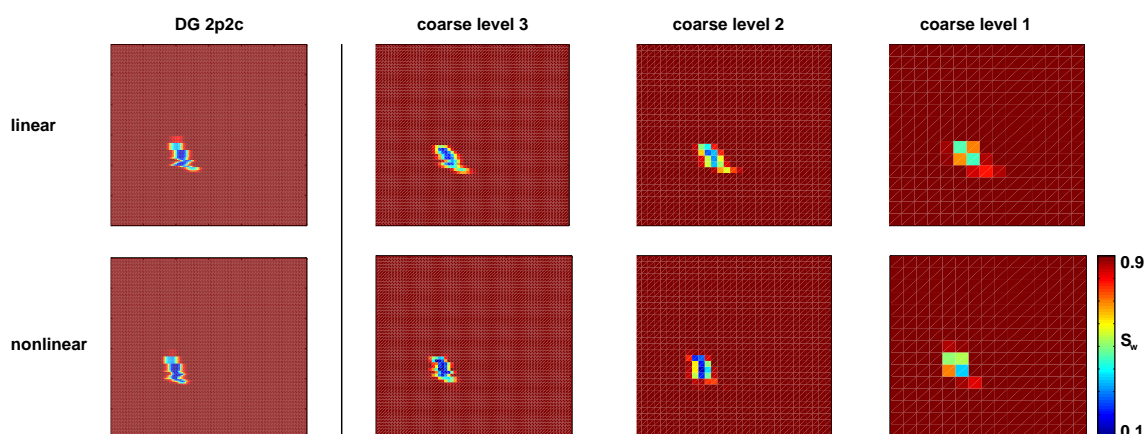


Figure 6.81: Saturation contour lines for  $DG\ local\ 2p2c$  on ML 4 and coarse levels 1 through 3 using linear and nonlinear model equations. The reference model is  $DG\ 2p2c$  on ML 4.

coarse level	1	2	3	<i>DG 2p2c</i>
linear	9.685	16.392	96.659	11.954
nonlinear	11.567	103.524	2696.978	18.29

Table 6.20: System CPU times [s] for *DG local 2p2c* on ML 4 and coarse level 1 through 3 as well as for *DG 2p2c* on ML 4 (linear and nonlinear case).

coarse level	1	2	3
linear $L_1$	2680.75	459.68	216.95
linear $L_2$	44.28	13.59	8.66
nonlinear $L_1$	2653.42	423.29	178.00
nonlinear $L_2$	44.52	13.68	8.34

Table 6.21: Error norms  $L_1$  and  $L_2$  for *DG local 2p2c* on ML 4 and coarse level 1 through 3 (linear and nonlinear case).

the module *DG local 2p2c* using the multi-scale algorithm and the reference solution *DG 2p2c* can be detected for a small coarsening level (coarse level 3). The visual agreement is very good for the linear as well as for the nonlinear case and the error is small. For higher levels of coarsening, the principal features of the reference solution can still be captured, but the error increases considerably, especially for the transition from coarse level 2 to 1.

Considering the CPU times, it can be seen that only for the highly coarsened model with a coarse level of 1, the multi-scale module *DG local 2p2c* is computationally more efficient than the reference fine-scale module *DG 2p2c*. This proves once more that the solution of the local processes, i.e. the solution of the fine-scale concentration equation requires few computing time compared to the transfer operations between grids and the solution of the upscaled saturation equation.

## 6.4 Testing of *DG local 3p3c*

### 6.4.1 General Remarks and Algorithm

In a way analogous to the testing of the module *DG local 2p2c*, a reference solution is created for *DG local 3p3c* which is then called *DG 3p3c*. While the solution strategy for the module *DG local 3p3c* was already introduced in Section 5.5.2, the principle solution strategy for *DG 3p3c* follows Figure 6.82 and is the following:

1. Solve the fine-scale pressure equation in  $T$ :

$$\nabla \cdot [\lambda(S_w, S_n) \underline{\underline{K}} \cdot \nabla p] = 0, \quad \underline{v}^{\text{discont.}} = -\lambda(S_w, S_n) \underline{\underline{K}} \cdot \nabla p, \quad (6.304)$$

The resulting quantities are the fine-scale pressures and the fine-scale total velocities in the entire domain.

known:  $\mathbf{p}, \underline{v}^{\text{discont.}}$ .

2. Make the fine-scale velocity field in  $T$  continuous across element edges:

$$\underline{v}^{\text{discont.}} \rightarrow \underline{v}^{\text{cont.}} := \underline{v}. \quad (6.305)$$

A  $BDM_1^0$  projection as discussed in Section 4.3.1.1 is applied to make the discontinuous velocity field obtained from the solution of 1. continuous across element edges. This property is needed to ensure a locally mass-conservative discretization.

known:  $p, \underline{v}^{\text{discont.}}, \underline{\mathbf{v}}$ .

4. Solve two fine-scale total concentration equations in  $T$ :

$$\frac{\partial C^1}{\partial t} + \underline{v} \cdot \nabla \sum_{\alpha} (f_{\alpha} C_{\alpha}^1) = 0 \quad (6.306)$$

$$\frac{\partial C^2}{\partial t} + \underline{v} \cdot \nabla \sum_{\alpha} (f_{\alpha} C_{\alpha}^2) = 0 \quad (6.307)$$

This means, that the total concentrations on the fine scale in  $T$  are determined for the new time step.

known:  $p, \underline{v}^{\text{discont.}}, \underline{v}, \mathbf{C}^1, \mathbf{C}^2$ .

5. Calculate the fine-scale water and NAPL saturations in  $T$  from the concentrations in  $T$ :

$$S_w = S_w(C^1, C^2, p) \quad (6.308)$$

$$S_n = S_n(C^1, C^2, p), \quad (6.309)$$

where  $S_w(C^1, C^2, p)$  and  $S_n(C^1, C^2, p)$  are obtained using flash calculations, see Section 3.4.2.

known:  $p, \underline{v}^{\text{discont.}}, \underline{v}, C^1, C^2, \mathbf{S}_w, \mathbf{S}_n$ .

## 6.4.2 Results of the Comparisomal Studies

Studying the module *DG local 3p3c*, a cut-out of the unsaturated zone is considered as given in the motivation example of Figure 1.7, where a residual contamination of



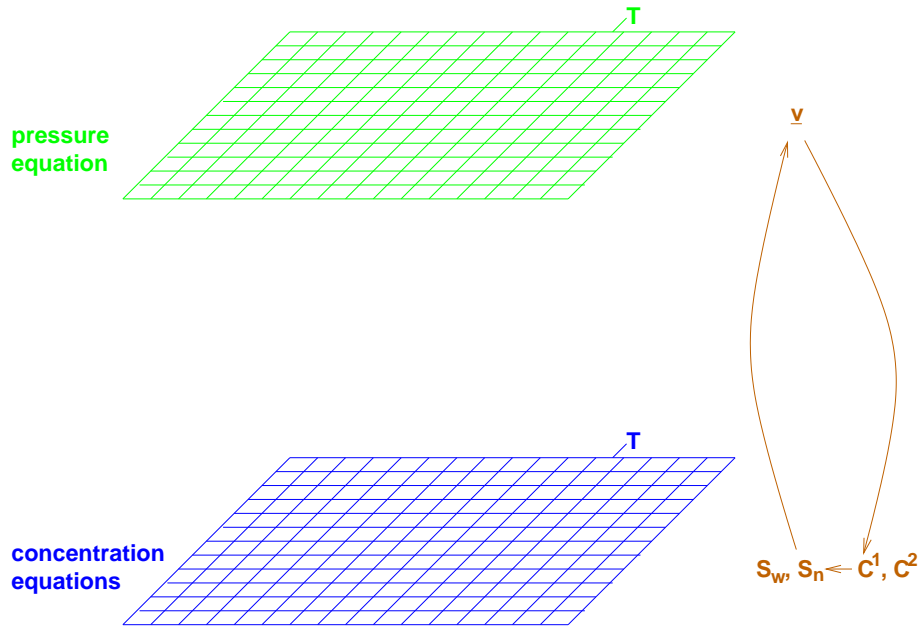


Figure 6.82: Multi-scale structure for the reference test case *DG 3p3c*.

an LNAPL (e.g. xylol) is being dissolved in a surrounding water–gas system with a main flow direction from left to right. Figure 6.83 shows in the upper picture the boundary and initial conditions, whereas in the lower picture, the type of relative permeability–saturation relationships is shown for the different zones. It can be seen, that the three-phase–three-component relationship after Parker et al. is only used in the local domain, i.e. within  $U$ . In the rest of the domain, Van Genuchten relative permeability–saturation functions are chosen taking the parameter  $n = 3.0$ . An overview of the fluid parameters assumed for the comparisnal studies is given in Table 6.22, while vapor pressures, Henry constants and molar weights needed for the three-phase–three-component flash calculation can be taken from Appendix A.

According to Figure 6.83, the domain is again closed at the top and bottom boundary. The pressure boundary conditions are the same as for all of the previous simulation examples, resulting in an average total velocity of  $1.5 \cdot 10^{-10} \frac{m}{s}$  from left to right. The left and right boundary conditions as well as the initial conditions in  $\{T \setminus V\}$  for

phase $\alpha$	$w$	$n$	$g$
$\mu_\alpha \left[ \frac{kg}{ms} \right]$	1.0	1.0	1.0
$\rho_\alpha \left[ \frac{kg}{m^3} \right]$	1000.0	875.8	0.9

Table 6.22: Fluid parameter values for the comparisnal studies to check the module *DG local 3p3c* ( $w$ : water,  $n$ : xylol, and  $g$ : gas).

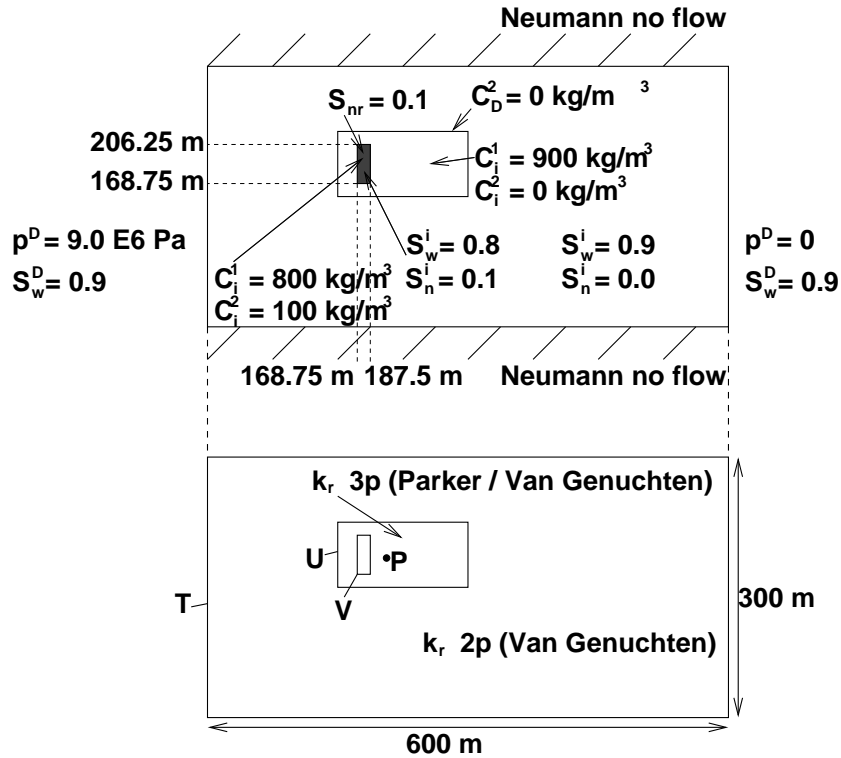


Figure 6.83: Boundary and initial conditions used for the testing of the module *DG local 3p3c*.

the wetting phase saturation are equal to  $S_w = 0.9$ . Within  $V$ , the initial wetting-phase saturation is  $S_w^i = 0.8$ . For the LNAPL phase,  $S_n = 0$  is valid everywhere except in the region  $V$  where the initial saturation is equal to the residual saturation,  $S_n^i = S_{nr} = 0.1$ . Finally, boundary and initial conditions for the total concentrations of water and NAPL,  $C^1$  and  $C^2$  have to be given. Considering the boundary conditions, they are updated as given in Section 5.5.2, where it is assumed that at the boundary of  $U$ , the wetting-phase only consists of water and the gas phase only of air, i.e.  $X_w^1 = 1$ , and  $X_w^2 = X_w^3 = 0$  as well as  $X_g^3 = 1$ , and  $X_g^1 = X_g^2 = 0$ . Furthermore, it is assumed that at  $\partial U$ , no NAPL phase is present,  $C_D^2 = 0$ . Considering the initial conditions,  $C_i^1 = 900 \frac{kg}{m^3}$  and  $C_i^2 = 0 \frac{kg}{m^3}$  are given in  $\{U \setminus V\}$ . Within  $V$ ,  $C_i^1 = 800 \frac{kg}{m^3}$  and  $C_i^2 = 100 \frac{kg}{m^3}$  are taken as initial values.

As for the two-phase-two-component case, results for the module *DG local 3p3c* and its reference module *DG 3p3c* are shown. The linear and nonlinear case are studied in a homogeneous domain as well as for the five test permeability fields. With respect to the mass transfer model, cases B and C introduced in Section 3.4.2 are compared. That means, that either all possible mass transfer types are included except LNAPL–water and water–LNAPL transfer (case B) or that only water–gas and LNAPL–gas mass transfer (case C) are taken into account.

The discretization length is given by  $\Delta x = 9.375$  m for the fine grid (ML 3) and

$\Delta\bar{x} = 18.75$  m for the coarse grid (ML 2). As both saturation and concentration equations are solved time-explicitly, both macro and micro time step are determined according to the CFL condition. In the following simulation results (comparisons of saturation contours, error norms and mole fractions  $x_g^k$  in the gas phase), the state of the system at an intermediate time of 182 d is considered. Note, that the saturation isolines shown are contours of the effective wetting-phase saturation  $S_{we}$ , which has already been defined as

$$S_{we} = \frac{1 - S_g - S_n}{1 - S_{nr}}. \quad (6.310)$$

The reason for that choice is, that in the macro-scale two-phase model, water and gas saturation do not generally sum up to one, but to  $1 - S_{nr}$ . The whole simulation time is 627.17 d. This is the point in time, for which computing times are compared.

Figure 6.84 shows the saturation contours in a homogeneous domain and for the five test permeability fields comparing the module *DG local 3p3c* to *DG 3p3c*, using either mass transfer model B or mass transfer model C. The computing times for all combinations are shown in Table 6.23, whereas the error norms in  $L_1$  and  $L_2$  are compared in Table 6.24.

One can see, that the visual agreement between the two mass transfer models is in all cases very good, for both *DG local 3p3c* and *DG 3p3c*—in fact, one can hardly distinguish any differences. This shows that for the considered setup, it is actually sufficient to consider the very simple mass transfer model C, where only the transfer of LNAPL into the gas phase, and the transfer of water into the gas phase are taken into account.

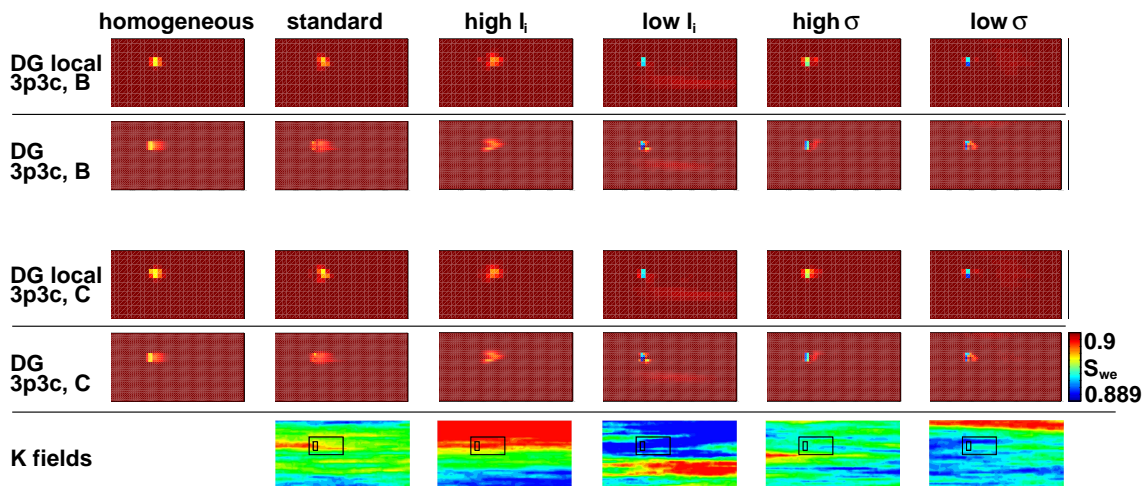


Figure 6.84: Saturation contours in a homogeneous domain and for the heterogeneous test fields for the module *DG local 3p3c* and its reference fine-scale solution *DG 3p3c*. Results for both mass transfer model B and mass transfer model C are shown.

	homogeneous	standard	high $l_i$	low $l_i$	high $\sigma$	low $\sigma$
<i>DG local 3p3c, B</i>	13.579	9.440	11.421	30.632	11.564	15.580
<i>DG 3p3c, B</i>	7.907	8.908	35.469	10.584	9.904	10.375
<i>DG local 3p3c, C</i>	12.555	10.117	12.979	13.436	19.654	10.032
<i>DG 3p3c, C</i>	13.746	15.940	14.568	9.933	11.817	9.350

Table 6.23: System CPU times [s] in the homogeneous and in the five heterogeneous domains with local and global 3p3c processes (mass transfer models B and C).

	homogeneous	standard	high $l_i$	low $l_i$	high $\sigma$	low $\sigma$
<i>DG local 3p3c, B <math>L_1</math></i>	2.64	2.78	3.04	6.13	2.94	5.41
<i>DG local 3p3c, B <math>L_2</math></i>	0.17	0.15	0.14	0.31	0.24	0.28
<i>DG local 3p3c, C <math>L_1</math></i>	1.78	1.91	2.05	5.60	2.34	5.05
<i>DG local 3p3c, C <math>L_2</math></i>	0.17	0.15	0.14	0.31	0.25	0.27

Table 6.24: Error norms  $L_1$  and  $L_2$  for a homogeneous problem and the five heterogeneous domains with local 3p3c processes (mass transfer models B and C). The module *DG 3p3c* with mass transfer model B or C serves as reference module.

Generally, one can also state that considering the saturation contours, in most cases, the agreement between *DG local 3p3c* and *DG 3p3c* is rather good, both for mass transfer model B and C. Although for the permeability field “high  $\sigma$ ” the saturation distribution of *DG local 3p3c* does not seem to visually match the saturation distribution of *DG 3p3c* very well, neither for mass transfer model B, nor for model C, the error norms in  $L_1$  and  $L_2$  prove that the agreement is in fact very good. Actually, all error norms are very small emphasizing the good quality of the test module *DG local 3p3c*.

Considering the CPU times, one can easily see that the result is not consistent and highly dependent on the permeability field under study. For mass transfer model B, the developed algorithm is only in one of the six cases computationally more efficient than the module, where 3p3c processes are solved globally. The reason for that is the same as for the setup with local two-phase–two-component processes: although the module *DG local 3p3c* does only locally solve for 3p3c processes, it necessitates the solution of the upscaled saturation equation as well as various grid transfer operations. If the flash calculation procedure is relatively simple and quick (as is the case for the  $K^\kappa$  flash for isothermal systems, that is used in this work), the module *DG 3p3c* might still be computationally more efficient. Remember, however, that the upscaling technique applied to derive the upscaled saturation equation, was especially adequate for permeability fields with high correlation length—this

was exactly the permeability field where the multi-scale algorithm performed better than the standard module *DG 3p3c*. For mass transfer model C, there are already three out of six permeability fields, for which the module *DG local 3p3c* needed less CPU time than the module *DG 3p3c*.

To compare the two mass transfer models, a closer look is taken at the temporal dependence of the composition of the gas phase, i.e. how water and LNAPL evaporate into the gas phase as a function of time. Figure 6.85 shows the mole fractions  $x_g^1$ ,  $x_g^2$ , and  $x_g^3$  as a function of time at  $(x = 210.9375 \text{ m}, y = 182.8125 \text{ m})$ , which corresponds to a location slightly downstream of the contaminated zone. This point is denoted by P in Figure 6.83. For each of these three mole fractions, mass transfer models B and C are shown and compared to their respective reference solution *DG 3p3c*.

From Figure 6.85, one can see that the dependence of the values of  $x_g^k$  on the permeability field is negligibly small—only for the function  $x_g^3(t)$  a slight difference between the homogeneous domain and the domain with the permeability field “standard” can be detected. Furthermore, the mole fractions of water and LNAPL in the gas phase are for all cases higher for the fine reference module *DG 3p3c* than for *DG local 3p3c*.

Considering the mole fraction of the water component in the gas phase,  $x_g^1$ , the mass transfer models B and C give the same results. Also for the functions  $x_g^2(t)$  and especially for  $x_g^3(t)$ , the difference between the two mass transfer models is very small. However, for the NAPL mole fraction in the gas phase, mass transfer model C gives higher values than model B. Considering the gas mole fractions in the gas phase, it is then, of course, the other way around and model B returns the higher mole fractions  $x_g^3$ .

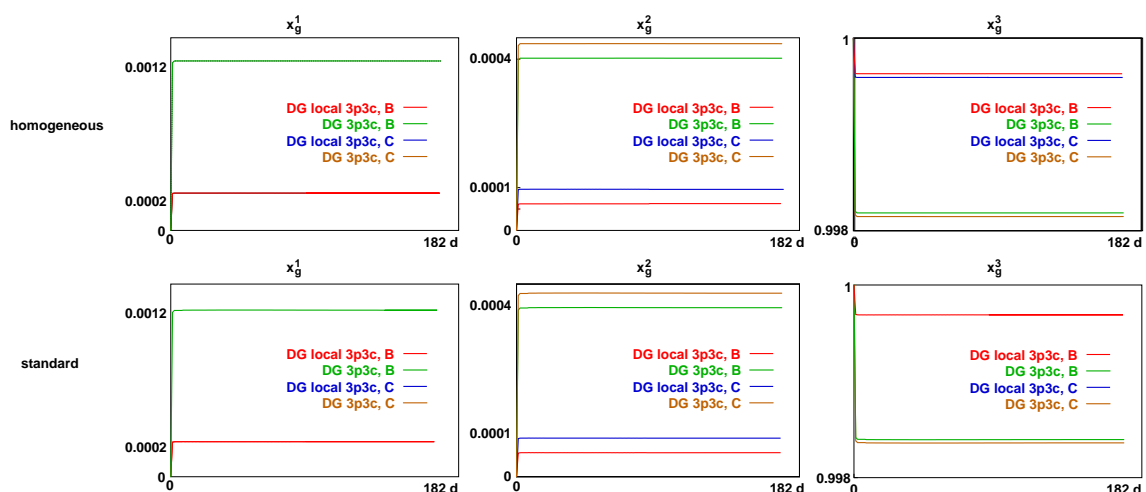


Figure 6.85: Mole fractions  $x_g^k(t)$  as a function of time at location  $(x = 210.9375 \text{ m}, y = 182.8125 \text{ m})$ .

Concludingly, the results investigating the composition of the gas phase are a further indicator, that mass transfer model C gives sufficiently good results for the setup studied in this work.

## 6.5 Summary of the Results

As the results shown so far are numerous and specialized on certain features of the overall algorithm, a summary of the essential findings for the setups with local two-phase–two-component and for the setups with local three-phase–three-component processes is given.

For both setups, an excellent agreement between the results of the algorithm developed in this work and the reference solution was found. This was proven visually by the similarity of the saturation fronts, and mathematically by the error norms in  $L_1$  and  $L_2$ . Thus, it is shown that the multi-scale algorithm gives accurate results, although solving only locally for multi-phase–multi-component processes and although solving for the global saturation distribution on a coarse scale.

Moreover, for the setup with local two-phase–two-component processes, the results still look very good when the center of the plume of high non-wetting phase saturation leaves the local domain where two-phase–two-component processes are modeled. This shows that the implementation of the non-stationary Dirichlet boundary conditions for the total concentration as suggested in this work is reasonable. Considering the setup with local three-phase–three-component processes, only results have been studied where the LNAPL plume is present in residual saturation and is thus immobile—obviously, it will then never leave the local domain.

For the studies including local three-phase–three-component processes, two different mass transfer models have been compared. One of them only considers the transfer of liquid components (water, LNAPL) into the gas phase, while the other additionally takes into account the dissolution of air in the water phase and in the LNAPL phase. The simulation results have shown, that the difference between the models is very small for the considered setup, and that the simpler mass transfer model is a sufficiently accurate choice.

Finally, CPU times of the multi-scale models with local multi-phase–multi-component processes have been compared to their reference which models multi-phase–multi-component processes globally. Contrary to the first predictions, the CPU time for the model accounting only locally for multi-phase–multi-component processes did not always fall below the CPU times of the model taking multi-phase–multi-component processes into account globally. Instead, the outcome is highly

dependent on the permeability field and especially on the complexity of the multi-phase–multi-component model. For more complex mass transfer models, the multi-scale simulations become computationally more efficient compared to the reference solution. For the case of local two-phase–two-component processes it was shown, that for higher levels of coarsening the new multi-scale algorithm becomes computationally more efficient compared to the standard fine-scale solution.

# 7 Final Remarks

In this section, the thesis work is summed up and future research fields evolving from the studies in this work are discussed.

## 7.1 Summary of the Thesis Work

An algorithm for the modeling of processes of different complexity occurring in different parts of a model domain has been developed, implemented, and tested. Specifically, a fine-scale pressure equation is solved in the global domain, whereas multi-phase–multi-component processes are accounted for on a fine scale, but only in a local domain where mass transfer is of non-negligible impact. A coarse-scale saturation distribution is obtained by the solution of an upscaled saturation equation which includes saturations resulting from the concentration equations in the local domain. The coarse-scale saturation distribution influences the fine-scale velocity field and determines the boundary conditions of the local multi-phase–multi-component problem.

Starting from the work of Efendiev et al. [2000] and Efendiev and Durlofsky [2002], who presented an upscaled form of the saturation equation using volume averaging, and a discontinuous Galerkin code developed by Peter Bastian from IWR, Heidelberg, Germany (e.g. Bastian [2003]) which allows to solve a pressure equation and a saturation equation on the fine scale, the following steps were performed in this work:

- **Adaptation of the upscaling approach of Efendiev et al. [2000] and Efendiev and Durlofsky [2002] for a DG discretization and implementation.**

The DG discretization implies a fine-grid pressure solution, an averaging of the *BDM*-projected velocities along coarse-block boundaries and a solution of the coarse-grid saturation equation. The upscaled model was thoroughly tested and compared to other existing coarse-scale models with respect to accuracy and computing time.

- **Development of a multi-scale algorithm accounting locally for multi-phase–multi-component processes.**



- *Implementation of the total concentration equations.*

While for local two-phase–two-component processes only one concentration equation has to be solved, two concentration equations are needed when three-phase–three-component processes are considered.

- *Derivation of mass transfer relations for multi-phase–multi-component systems.* These relations were derived for a two-phase–two-component (air/gas–water) model, and two different mass transfer models were considered for three-phase–three-component (air/gas–water–LNAPL) systems.

- *Implementation of two-phase–two-component and three-phase–three-component flash calculations.*

The three-phase–three-component flash calculations were implemented using two mass transfer models of different complexity. The simpler model takes into account the transition of LNAPL and water components into the gas phase, while the more complex one additionally considers the transfer of the air component into the water and the LNAPL phase.

- *Development of a model for the boundary conditions of the local domain (total concentration equations).*

As the total concentrations depend on saturation, the boundary conditions of the local domain are updated at each macro time step using the saturation given by the solution of the upscaled saturation equation.

- *Development of a model for the coupling of a local-scale multi-phase–multi-component and a macro-scale two-phase model.*

Both concentration and upscaled saturation equations use the velocity field resulting from the fine-scale pressure equation. The saturations resulting from the local fine-scale concentration equations enter the upscaled saturation equation in averaged form. In order to maintain the mass balance locally, source / sink terms are introduced into the upscaled saturation equation as additional coupling terms. The saturations resulting from the upscaled saturation equation influence the velocity field.

- **Investigations on the quality of the multi-scale algorithm.**

To evaluate the quality of the algorithm, it was compared to models involving a global solution for fine-scale total concentrations. The quality criteria were the accuracy of the solution and the computing time. Specifically, the accuracy was checked by comparing the saturation fronts visually and by calculating the error norms.

The results obtained using the newly developed multi-scale algorithm were of an excellent accuracy. This was proven not only visually by the good agreement of saturation fronts, but also mathematically by the error norms in  $L_1$  and  $L_2$ . A gain

in computational speed due to the local instead of global solution of multi-phase–multi-component processes could not always be reached, but the computational efficiency of the multi-scale algorithm outranged the conventional model for higher levels of coarsening. This ambiguity was due to the fact that the transfer operations between the scales also consume computing time and that the multi-phase–multi-component model applied in this work is still relatively simple allowing a fast solution of the respective equations.

## 7.2 Fields of Future Research

The multi-scale algorithm developed in this work is designed to be a general framework and toolbox for incorporating processes of different complexity occurring in different spatial domains and on different spatial and temporal scales. Fields of future research result partly from the assumptions made in this work and aim at obtaining a physically more correct model or at a better model for the upscaled saturation equation, partly they are targeted on a faster solution of the algorithm, on an improvement of the numerical scheme or on a correct treatment of the boundaries of the local domain.

For improving the **physical properties** of the model, it is desirable to revoke the assumptions made in this work step by step. The assumptions were partly justified by physical reasons, partly they were made in order to keep the multi-scale algorithm concise. The most severe simplifications with respect to the physical model were

- the neglect of capillary forces,
- the neglect of gravitational forces,
- the assumption of isothermal conditions,
- the neglect of dissolution of water in the NAPL phase as well as the neglect of dissolution of NAPL in the water phase,
- the assumption of constant phase densities, and
- the assumption of constant phase viscosities.

However, it is not straightforward to revoke these assumptions, as any change of the underlying fine-scale equations will not only necessitate a new derivation of the upscaled saturation equation, but it will also influence (increase) the coupling between the model equations on the different scales. Considering the upscaling of the saturation equation for more complex physical models, it is to question whether

it is possible at all to derive a coarse-scale model in all cases. Therefore, it has to be checked very carefully which of the above assumptions can be withdrawn. A further and probably simpler possibility to include more complex physical processes is, to account for them only locally where their influence is high. This makes sense, for example, for temperature changes or local effects of compressibility of the gas phase.

Also, the flash calculations performed in this work are kept relatively simple as only the pressure dependence of mole and mass fractions is taken into account. The implementation of flash calculations additionally depending on total concentrations would allow a better representation of real-life systems. However, this would in turn necessitate more time consuming Picard or Newton iterations to calculate saturations for a given system state.

When **upscaling** the saturation equation, the fine-scale velocities are averaged along coarse-grid edges. Using this approach, the coarse-scale velocities are continuous across coarse-grid edges which is essential to ensure a mass-conservative solution of the saturation equation. However, the influence of macrodispersion is underestimated, as the variation of fine-scale velocity inside a coarse-grid block is not taken into account. Future research has to be done to develop a velocity-averaging technique accounting for the velocity variation inside a grid-block and still providing a conservative coarse-scale velocity field.

In this work, the pressure equation has (almost) always been solved on the fine scale. However, the **computing time** of the algorithm can be reduced by first calculating a coarse-grid permeability field as described in Section 6.2.2 of this work and then solving the pressure equation on a coarse scale. As for the solution of the total concentration equations fine-scale velocities are needed, they have to be reconstructed within the local domain. This can either be done by a downscaling technique which operates on coarse-grid blocks or by a fine-scale solution of the pressure equation in the local domain including boundary conditions given by the coarse-grid pressure. The accuracy of the thus-obtained multi-scale algorithm has to be thoroughly studied. When solving the pressure equation on the coarse scale, the whole algorithm can be reinterpreted as a downscaling algorithm: the model problem is generally solved on the macro scale. Only in regions where more complex processes occur, one switches to a finer scale.

A further option for saving CPU time lends itself when considering the fact, that a significant change of the system state only occurs in the local domain, whereas outside, the changes are much smaller. Therefore, a possibility of saving computing time is to solve only the concentration equation(s) until a larger change of saturation or pressure gradient occurs inside the local domain. If on the one hand, the change in saturation exceeds a certain threshold value, the saturation equation is solved. If on the other hand, the change in velocity exceeds a threshold, the pressure equation is solved.

A strategy similar to the above-mentioned downscaling strategy consists of the use of a multi-scale **numerical scheme**, i.e. multi-scale finite elements or multi-scale finite volumes. Here, fine-scale properties can be reconstructed from coarse-scale properties using the basis functions. A further possibility for improving the numerical scheme is to stick to a discontinuous Galerkin discretization for saturation and concentration equations, and to replace the discontinuous Galerkin discretization for the pressure equation by a finite volume discretization, for example. This would not only make the *BDM* projection superfluous as finite volume methods return directly conservative velocity fields, but it would also be a simpler and more adequate scheme for the elliptic pressure equation. Finally, it would simplify the upscaling procedure as discontinuous Galerkin schemes include both boundary and volume integrals of the flux term, whereas finite volume methods only need boundary integrals of the flux term.

Although the presented results looked very promising with respect to the **boundary conditions** of the local domain, their adequate choice still represents a delicate issue. In this work, it is presumed that it is known a priori where mass transfer processes have to be accounted for. However, in reality, one cannot always take hold of this information. Moreover, if the components dissolved in other phases reach the boundary of the small domain, the area of the local domain should be enlarged in this direction. This calls for moving mesh strategies where the local domain either moves or is expanded, depending on the locally occurring multi-phase–multi-component processes. Finally, instead of using the saturation directly at the boundary for the calculation of the Dirichlet boundary conditions for the total concentrations, one should actually include an upstream weighting for the saturation.

The newly developed multi-scale algorithm is designed to be a general framework and toolbox for solving processes occurring at different locations and on different spatial and temporal scales in one model domain. Therefore, a wide field of future research comprises the transfer of the multi-scale algorithm to other applications and model equations.

# A Vapor Pressures, Molar Masses, and Henry Constants

The vapor pressures and Henry constants are in the general case dependent on temperature. However, as groundwater systems are considered where the temperature usually does not show much daily or annual variation, a constant temperature of 283.15 K (10°C) is assumed, which is an average middle-European groundwater temperature.

Taking xylol as the LNAPL component, one encounters problems when searching appropriate parameter values, as technical xylol is usually a mixture of p-xylol, m-xylol, and o-xylol. The values taken in this work correspond to a mixture which mainly consists of meta-xylol and which is called “technical xylol”.

The vapor pressure values of water and xylol for different temperatures can be found in various thermodynamic tables. The values taken in this work, are given in Table A.25.

For the temperature dependence of the Henry coefficient  $H_w^3$  of an air–water system, Finsterle [1993] found the relationship

$$H_w^3 = (0.8942 + 1.47 \cdot e^{-0.04394 \cdot (T-273.15)}) \cdot 10^{-10} \quad [1/Pa], \quad (\text{A.311})$$

with  $T$  as the temperature in  $K$ . The Henry coefficient of the air–xylol system is estimated by dividing the solubility of xylol in water at 20°C by its vapor pressure at 10°C which is surely only a first guess.

The parameter values given in Table A.25 correspond to a system with the components water (component 1), xylol (component 2), and air (component 3) as well as the liquid phases water (phase w) and xylol (phase n).

component / phase	vapor pressure $p_{vap}^{\kappa}$ [Pa]	molar mass $M^{\kappa}$ [g/mole]	Henry constant $H_{\alpha}^3$ [1/Pa]
1/w	1228	18.016	1.8415017E-10
2/n	434.97225	106.0	7.8165906E-08
3	-	28.96	-

Table A.25: Vapor pressure of water and xylol, molar masses of water, xylol, and air as well as Henry constants of water–air and LNAPL-air systems used in this work.

## B Evaluations for a $\mathcal{K}_\alpha^\kappa$ Flash for a 3p3c System

When studying the general procedure for a 3p3c flash with different mass transfer models as has been done in Section 3.4.2.2 and Section 3.4.2.3, some of the expressions become quite long. Their evaluation is considered here. Analogous to the proceeding there, mass transfer model B is studied in Section B.1, and mass transfer model C in Section B.2. The definition of the mass transfer models can be taken from Figure 3.37.

### B.1 Evaluations for a 3p3c System—Case B

The evaluation of the mole equilibrium ratios  $K_\alpha^\kappa$ , the calculation of the mole fractions  $x_\alpha^\kappa$  as well as the calculation of the saturations are presented.

#### B.1.1 Derivation of the Mole Equilibrium Ratios $K_w^1$ , $K_w^3$ , $K_n^2$ , and $K_n^3$

The basic equations to derive the mole equilibrium ratios are given by Dalton's law, Raoult's law, and Henry's law. These relationships have been discussed in Section 2.7. In Table B.26, the respective physical laws are given and it is shown for which phases and/or components the respective law is valid. Parameter values for both vapor pressures and Henry constants can be taken from Appendix A. .

eq. number	physical law	equation	valid for
(1)	Dalton's law	$p_g^\kappa = x_g^\kappa \cdot p$	$p = p_w = p_n = p_g$
(2)	Raoult's law	$p_g^\kappa = x_\alpha^\kappa \cdot p_{vap}^\kappa$	$\alpha \in \{w, n\}$
(3)	Henry's law	$x_\alpha^\kappa = H_\alpha^\kappa \cdot p_g^\kappa$	$\alpha = w, n$

Table B.26: Physical laws for the evaluation of the 3p3c mole equilibrium ratios.

**Mole equilibrium ratio  $K_w^1$** 

Applying equation (1) for component 1 and resolving for  $x_g^1$  yields

$$x_g^1 = \frac{p_g^1}{p}. \quad (\text{B.312})$$

Applying (2) to component 1 and resolving for  $x_w^1$  gives

$$x_w^1 = \frac{p_g^1}{p_{vap}^1}. \quad (\text{B.313})$$

Thus,  $K_w^1$  can finally be evaluated to

$$K_w^1 = \frac{x_g^1}{x_w^1} = \frac{\frac{p_g^1}{p}}{\frac{p_g^1}{p_{vap}^1}} = \frac{p_{vap}^1}{p}. \quad (\text{B.314})$$

**Mole equilibrium ratio  $K_w^3$** 

Applying equation (1) for component 3 and resolving for  $x_g^3$  yields

$$x_g^3 = \frac{p_g^3}{p}, \quad (\text{B.315})$$

Using (3) for component 3 and phase w and resolving for  $p_g^3$  gives

$$p_g^3 = \frac{x_w^3}{H_w^3}. \quad (\text{B.316})$$

Inserting this expression for  $p_g^3$  in Equation (B.315) results in

$$x_g^3 = \frac{\frac{x_w^3}{H_w^3}}{p}. \quad (\text{B.317})$$

This equation can finally be rearranged to give an expression for  $K_w^3$ ,

$$K_w^3 = \frac{x_g^3}{x_w^3} = \frac{1}{pH_w^3}. \quad (\text{B.318})$$

**Mole equilibrium ratio  $K_n^2$** 

Applying equation (1) for component 2 and resolving for  $x_g^2$  yields

$$x_g^2 = \frac{p_g^2}{p}. \quad (\text{B.319})$$



Applying (2) to component 2 and resolving for  $x_n^2$  gives

$$x_n^2 = \frac{p_g^2}{p_{vap}^2}. \quad (\text{B.320})$$

Thus,  $K_n^2$  can finally be evaluated to

$$K_n^2 = \frac{x_g^2}{x_n^2} = \frac{\frac{p_g^2}{p}}{\frac{p_g^2}{p_{vap}^2}} = \frac{p_{vap}^2}{p}. \quad (\text{B.321})$$

### Mole equilibrium ratio $K_n^3$

Applying equation (1) for component 3 and resolving for  $x_g^3$  yields

$$x_g^3 = \frac{p_g^3}{p}, \quad (\text{B.322})$$

Using (3) for component 3 and phase n and resolving for  $p_g^3$  gives

$$p_g^3 = \frac{x_n^3}{H_n^3}. \quad (\text{B.323})$$

Inserting this expression for  $p_g^3$  in Equation (B.322) results in

$$x_g^3 = \frac{\frac{x_n^3}{H_n^3}}{p}. \quad (\text{B.324})$$

This equation can finally be rearranged to give an expression for  $K_n^3$ ,

$$K_n^3 = \frac{x_g^3}{x_n^3} = \frac{1}{pH_n^3}. \quad (\text{B.325})$$

## B.1.2 Evaluation of the Mole Fractions $x_\alpha^k$

For model B, only four of the nine mole fractions have to be derived from the mole equilibrium ratios, the other five are directly intellegible and determined by very simple algebraic relations. The mole fractions result from the equation system of the

seven Equations (3.114) through (3.120) and are the following

$$x_w^1 = -\frac{-K_n^3 + K_n^2 K_n^3 - K_n^2 K_w^3 + K_n^3 K_w^3}{K_n^3 K_w^1 + K_n^2 K_w^3 - K_n^3 K_w^3}, \quad (\text{B.326})$$

$$x_n^2 = -\frac{-K_w^3 - K_n^3 K_w^1 + K_n^3 K_w^3 + K_w^1 K_w^3}{K_n^3 K_w^1 + K_n^2 K_w^3 - K_n^3 K_w^3}, \quad (\text{B.327})$$

$$x_g^1 = -\frac{-K_n^3 K_w^1 + K_n^2 K_n^3 K_w^1 - K_n^2 K_w^1 K_w^3 + K_n^3 K_w^1 K_w^3}{K_n^3 K_w^1 + K_n^2 K_w^3 - K_n^3 K_w^3}, \quad (\text{B.328})$$

$$x_g^2 = -\frac{-K_n^2 K_w^3 - K_n^2 K_n^3 K_w^1 + K_n^2 K_n^3 K_w^3 + K_n^2 K_w^1 K_w^3}{K_n^3 K_w^1 + K_n^2 K_w^3 - K_n^3 K_w^3}. \quad (\text{B.329})$$

The five remaining mole fractions are given by

$$x_w^2 = 0, \quad (\text{B.330})$$

$$x_w^3 = 1 - x_w^1, \quad (\text{B.331})$$

$$x_n^1 = 0, \quad (\text{B.332})$$

$$x_n^3 = 1 - x_n^2, \quad (\text{B.333})$$

$$x_g^3 = 1 - x_g^1 - x_g^2. \quad (\text{B.334})$$

### B.1.3 Evaluation of the Saturations $S_n$ and $S_g$

The evaluations of the saturations can be done having calculated the mass fractions  $X_\alpha^\kappa$  from the mole fractions  $x_\alpha^\kappa$ . A solution of the equation system consisting of Equations (3.122) through (3.124) for  $S_n$  and  $S_g$  is presented. This equation system consists of three equations, where the mass fractions  $X_\alpha^\kappa$  are already known, as they are evaluated beforehand in step 3 of the flash solution procedure of Table 3.2. In this notation,  $S_n$  and  $S_g$  can be written in a relatively simple way as

$$S_n = \frac{C^2/\phi X_g^1 \rho_g - C^1/\phi X_g^2 \rho_g - C^2/\phi X_w^1 \rho_w + X_g^2 X_w^1 \rho_g \rho_w}{X_g^1 X_n^2 \rho_g \rho_n + X_g^2 X_w^1 \rho_g \rho_w - X_n^2 X_w^1 \rho_n \rho_w} \quad (\text{B.335})$$

$$S_g = \frac{C^1/\phi X_n^2 \rho_n + C^2/\phi X_w^1 \rho_w - X_n^2 X_w^1 \rho_n \rho_w}{X_g^1 X_n^2 \rho_g \rho_n + X_g^2 X_w^1 \rho_g \rho_w - X_n^2 X_w^1 \rho_n \rho_w}. \quad (\text{B.336})$$

The missing water saturation is then simply  $S_w = 1 - S_n - S_g$ .

## B.2 Evaluations for a 3p3c System—Case C

For a 3p3c system with mass transfer of water and LNAPL components into the gas phase only, the three phase saturations can be easily calculated from a  $2 \times 2$  linear

system of equations. This equation system can be derived from the definition of the total concentrations  $C^1$  and  $C^2$ ,

$$C^1/\phi = \rho_w S_w + \rho_g S_g X_g^1 \quad (\text{B.337})$$

$$C^2/\phi = \rho_n S_n + \rho_g S_g X_g^2, \quad (\text{B.338})$$

where it is accounted for the equalities  $X_w^1 = X_n^2 = 1$  and  $X_w^2 = X_w^3 = X_n^1 = X_n^3 = 0$ .

Inserting  $S_w = 1 - S_n - S_g$ , the  $2 \times 2$  linear equation system for the unknowns  $S_n$  and  $S_g$  can be obtained

$$C^1/\phi - \rho_w = -\rho_w S_n + (\rho_g X_g^1 - \rho_w) S_g \quad (\text{B.339})$$

$$C^2/\phi = \rho_n S_n + \rho_g X_g^2 S_g. \quad (\text{B.340})$$

Resolving Equation (B.340) for  $S_n$  yields

$$S_n = \frac{C^2/\phi - \rho_g X_g^2 S_g}{\rho_n}, \quad (\text{B.341})$$

which is inserted into Equation (B.339) to obtain

$$S_g = \frac{C^1/\phi \rho_n - \rho_w \rho_n + \rho_w C^2/\phi}{\rho_w \rho_g X_g^2 + \rho_g \rho_n X_g^1 - \rho_w \rho_n}. \quad (\text{B.342})$$

## C Parameters for $P_2$ Basis Functions for DG Schemes

	0	1	2
0	1	0	0
1	0	0	0
2	0	0	0

Table C.27: Parameters  $c_{ab}$  for  $P_2$  basis functions for DG schemes of degree 0 (rows: index a, columns: index b).

	0	1	2
0	-1.7320508	0	0
1	3.4641016	0	0
2	0	0	0

Table C.28: A: parameters  $c_{ab}$  for  $P_2$  basis functions for DG schemes of degree 1 (rows: index a, columns: index b).

	0	1	2
0	-1.7320508	3.4641016	0
1	0	0	0
2	0	0	0

Table C.29: B: parameters  $c_{ab}$  for  $P_2$  basis functions for DG schemes of degree 1 (rows: index a, columns: index b).

	0	1	2
0	2.2360680	0	0
1	-13.416408	0	0
2	13.416408	0	0

Table C.30: A: parameters  $c_{ab}$  for  $P_2$  basis functions for DG schemes of degree 2 (rows: index a, columns: index b).

	0	1	2
0	3	6	0
1	6	12	0
2	0	0	0

Table C.31: B: parameters  $c_{ab}$  for  $P_2$  basis functions for DG schemes of degree 2 (rows: index a, columns: index b).

	0	1	2
0	2.2360680	-13.416408	13.416408
1	0	0	0
2	0	0	0

Table C.32: C: parameters  $c_{ab}$  for  $P_2$  basis functions for DG schemes of degree 2 (rows: index a, columns: index b).



# Bibliography

- G. Arfken. Gram-Schmidt Orthogonalization. *Mathematical Methods for Physicists*, pages 516–520, 1985.
- J. L. Auriault. Upscaling Heterogeneous Media by Asymptotic Expansions. *Journal of Engineering Mechanics*, 128(8):817–822, 2002.
- K. Aziz and A. Settari. *Petroleum Reservoir Simulation*. Elsevier Applied Science, 1979.
- P. Bastian. Numerical Computation of Multiphase Flows in Porous Media. Habilitationsschrift vorgelegt an der Technischen Fakultät der Christian–Albrechts–Universität Kiel, 1999.
- P. Bastian. Higher Order Discontinuous Galerkin Methods for Flow and Transport in Porous Media. In E. Bänsch, editor, *Challenges in Scientific Computing – CISC 2002*, number 35 in LNCSE, 2003.
- P. Bastian, K. Birken, K. Johannsen, S. Lang, K. Eckstein, N. Neuss, H. Rentz-Reichert, and C. Wieners. UG - A Flexible Software Toolbox for Solving Partial Differential Equations. *Computing and Visualization in Science*, 1(1), S. 27-40, 1997.
- P. Bastian and B. Rivière. Superconvergence and  $H(\text{div})$ -projection for discontinuous Galerkin methods. *Int. J. Numer. Meth. Fluids*, 42(10):1043–1057, 2003.
- C. E. Baumann and J. T. Oden. A discontinuous Galerkin–finite element method for convection-diffusion problems. *Comput. Methods Appl. Mech. Engrg*, 175:311–341, 1999.
- J. Bear. *Dynamics of Fluids in Porous Media*. Elsevier, New York, 1972.
- P. Binning and M. A. Celia. Practical implementation of the fractional flow approach to multi-phase flow simulation. *Advances in Water Resources*, 22(5):461–478, 1999.
- F. Brezzi, J. Douglas, and L. D. Marini. *Recent results on mixed finite element methods for second order elliptic problems*. Optimization Software Publications, 1986.

- F. Brezzi and M. Fortin. *Mixed and Hybrid Finite Element Methods*. Springer Verlag, New York, 1991.
- P. I. Brooker. Two dimensional simulation by turning bands. *Mathematical Geology*, 17:81–91, 1985.
- A. N. Brooks and A. T. Corey. *Hydraulic Properties of Porous Media*. Colorado State University, 1964.
- S. E. Buckley and M. C. Leverett. Mechanism of Fluid Displacements in Sands. *Transactions of the AIME*, 146:107–116, 1942.
- G. Chavent and J. Jaffré. *Mathematical models and finite elements for reservoir simulation*. North Holland, Amsterdam, 1986.
- Y. Chen, L. J. Durlofsky, M. Gerritsen, and X.H. Wen. A coupled local-global upscaling approach for simulating flow in highly heterogeneous formations. *Advances in Water Resources*, 26:1041–1060, 2003.
- Z. Chen and R. E. Ewing. Fully Discrete Finite Element Analysis of Multiphase Flow in Groundwater Hydrology. *SIAM Journal of Numerical Analysis*, 34(6):2228–2253, 1997.
- Z. Chen and T. Y. Hou. A mixed multiscale finite element method for elliptic problems with oscillating coefficients. *Mathematics of Computation*, 72(242):541–576, 2002.
- H. Class. *Theorie und numerische Modellierung nichtisothermer Mehrphasenprozesse in NAPL-kontaminierten porösen Medien*. Mitteilungsheft, Institut für Wasserbau, Universität Stuttgart, 2001. 3-933761-08-5.
- B. Cockburn, S. Hou, and C.-W. Shu. TVB Runge-Kutta local projection discontinuous Galerkin finite element method for conservation laws IV: The multidimensional case. *Journal of Mathematical Computation*, 54:545–581, 1990.
- B. Cockburn and C.-W. Shu. TVB Runge-Kutta local projection discontinuous Galerkin finite element method for conservation laws II: General framework. *Journal of Mathematical Computation*, 52(186):411–435, 1989.
- B. Cockburn and C.-W. Shu. The Runge-Kutta Discontinuous Galerkin Method for Conservation laws V: Multidimensional Systems. *Journal of Computational Physics*, 141:199–224, 1998.
- C. Cordes and W. Kinzelbach. Continuous Groundwater Velocity Fields and Path Lines in Linear, Bilinear and Trilinear Finite Elements. *Water Resources Research*, 28(11):2903–2911, 1992.



- R. Courant, K. Friedrichs, and H. Lewy. Über die partiellen Differenzgleichungen der mathematischen Physik. *Mathematische Annalen*, 100:32–74, 1928.
- G. Dagan. *Flow and Transport in Porous Formations*. Springer, 1989.
- S. Didierjean, D. Maillet, and C. Moyne. Analytical solutions of one-dimensional macrodispersion in stratified porous media by the quadrupole method: convergence to an equivalent homogeneous porous medium. *Advances in Water Resources*, 27:657–667, 2004.
- L. J. Durlofsky. Numerical Calculation of Equivalent Grid Block Permeability Tensors for Heterogeneous Porous Media. *Water Resources Research*, 27(5):699–708, 1991.
- L. J. Durlofsky. Use of higher moments for the description of upscaled, process independent relative permeabilities. *SPE Journal*, 2:474–484, 1997.
- L. J. Durlofsky. Coarse scale models of two phase flow in heterogeneous reservoirs: volume averaged equations and their relationship to existing upscaling techniques. *Computational Geosciences*, 2:73–92, 1998.
- W. E and B. Engquist. Multiscale modeling and computation . *Notices of the AMS*, 50(9):1062–1070, 2003.
- W. E, B. Engquist, and Z. Huang. Heterogeneous multiscale method: A general methodology for multiscale modeling . *Physical Review*, 67, 2003.
- Y. Efendiev and L. J. Durlofsky. Numerical modeling of subgrid heterogeneity in two phase flow simulations. *Water Resources Research*, 38(8), 2002.
- Y. Efendiev, L. J. Durlofsky, and S. H. Lee. Modeling of subgrid effects in coarse-scale simulations of transport in heterogeneous porous media. *Water Resources Research*, 36(8):2031 – 2041, 2000.
- M. Emmert. *Numerische Modellierung nichtisothermer Gas-Wasser Systeme in porösen Medien*. PhD thesis, Institute of Hydraulic Engineering, University of Stuttgart, 1996.
- R. W. Falta. Modeling sub-grid-block-scale dense nonaqueous phase liquid (DNAPL) pool dissolution using a dual-domain approach. *Water Resources Research*, 39(12), 2003.
- R. W. Falta, K. Pruess, I. Javandel, and P. A. Witherspoon. Numerical Modeling of Steam Injection for the Removal of Nonaqueous Phase Liquids From the Subsurface. 1. Numerical Formulation. *Water Resources Research*, 28(2):433–449, 1992a.

- R.W. Falta, K. Pruess, I. Javandel, and P.A. Witherspoon. Numerical Modeling of Steam Injection for the Removal of Nonaqueous Phase Liquids From the Subsurface. 2. Code Validation and Application. *Water Resources Research*, 28(2):451–465, 1992b.
- C. L. Farmer. Upscaling: a review. *International Journal of Numerical Methods in Fluids*, 40:223 – 238, 2002.
- S. Finsterle. Inverse Modellierung zur Bestimmung hydrogeologischer Parameter eines Zweiphasensystems. Technical report, Versuchsanstalt für Wasserbau, Hydrologie und Glaziologie der Eidgenössischen Technischen Hochschule Zürich, 1993.
- P.A. Forsyth. Three dimensional modeling of steam flush for DNAPL site remediation. Technical report, Dep. of Computer Science, University of Waterloo, 1993. CS-93-56.
- D. D. Fussel and J. L. Yanosik. An Iterative Technique for Compositional Reservoir Models. *SPE Journal*, 1978.
- Geckinli-Yavuz. *Discrete Fourier Transformation and its Applications to Power Spectra Estimation*. Elsevier, 1983.
- L Gelhar. *Stochastic Subsurface Hydrology*. Prentice Hall, 1993.
- H. Hægland. Streamline Tracing on Irregular Grids. Master's Thesis, Department of Mathematics, University of Bergen, 2003.
- S. M. Hassanizadeh and W. G. Gray. General Conservation Equations for Multi-Phase Systems: 2. Mass, Momenta, Energy, and Entropy Equations. *Advances in Water Resources*, 2:191–203, 1979.
- S. M. Hassanizadeh and W. G. Gray. General Conservation Equations for Multi-Phase Systems: 3. Constitutive Theory for Porous Media Flow. *Advances in Water Resources*, 3:25–40, 1980.
- S. M. Hassanizadeh and W. G. Gray. Mechanics and Thermodynamics of Multi-phase Flow in Porous Media Including Interphase Boundaries. *Advances in Water Resources*, 13(4):169–186, 1990.
- S. M. Hassanizadeh and W. G. Gray. Thermodynamic Basis of Capillary Pressure in Porous Media. *Water Resources Research*, 29(10):3389 – 3405, 1993a.
- S. M. Hassanizadeh and W. G. Gray. Toward an improved description of the physics of two-phase flow. *Advances in Water Resources*, 16(1):53–67, 1993b.

- S. M. Hassanizadeh and W. G. Gray. Recent advances in theories of two-phase flow in porous media. In J. P. du Plessis, editor, *Fluid Transport in Porous Media*, pages 105–160. Computational Mechanics Publications, Southampton, 1997.
- R. Helmig. *Theorie und Numerik der Mehrphasenströmungen in geklüftet-porösen Medien*. PhD thesis, Bericht Nr. 34, Institut für Strömungsmechanik und Elektronisches Rechnen im Bauwesen, Universität Hannover, 1993.
- R. Helmig. *Multiphase Flow and Transport Processes in the Subsurface*. Springer, 1997.
- U. Hiester, T. Theurer, A. Winkler, A. Färber, and H.-P. Koschitzky. THERIS: Sanierung der ungesättigten Bodenzone mittels fester Wärmequellen. In V. Schrenk, K. Batera, B. Barczewski, K. Weber, and H.-P. Koschitzky, editors, *Symposium Ressource Fläche und VEGAS - Statuskolloquium 2003*, number 124, pages 173–183, Universität Stuttgart, 10 2003. Institut für Wasserbau. 3-933761-27-1.
- T. Hou and X. H. Wu. A multiscale finite element method for elliptic problems in composite materials and porous media. *Journal of Computational Physics*, 134:169–67, 1997.
- R. U. Huber. *Compositional Multiphase Flow and Transport in Heterogeneous Porous Media*. PhD thesis, Heft 102, Institut für Wasserbau, Universität Stuttgart, 1999.
- P. Jenny, S. H. Lee, and H. Tchelepi. Multi-scale finite-volume method for elliptic problems in subsurface flow simulations. *Journal of Computational Physics*, 187: 47–67, 2003.
- Journel and Huijbregts. *Mining Geostatistics*. Academic Press, 1978.
- R. Juanes and K.-A. Lie. A front-tracking method for efficient simulation of miscible gas injection processes. In *Proceedings of the SPE Reservoir Simulation Symposium, The Woodlands, Texas, January-February 2005*, 2005. SPE 93298.
- R. Juanes, K.-A. Lie, and V. Kippe. A front-tracking method for hyperbolic three-phase models. In *Proceedings of the European Conference on the Mathematics of Oil Recovery, Cannes, France, August-September 2004*, 2004.
- F. Kalaydjian. A Macroscopic Description of Multiphase Flow in Porous Media Involving Spacetime Evolution of Fluid/Fluid Interface. *Transport in Porous Media*, 2:537 – 552, 1987.
- S. E. Koch. A Survey of Nested Grid Techniques and Their Potential for Use Within the MASS Weather Prediction Model. *NASA Technical Memorandum 87808*, 1987.
- J. Kool and J. Parker. Development and evaluation of closed-form expressions for hysteretic soil hydraulic properties. *Water Resources Research*, 23(1):105–114, 1987.

- P. Langlo and M. S. Espedal. Macrodispersion for two-phase, immiscible flow in porous media. *Adv. Water Resour.*, 17:297–316, 1994.
- R. J. Lenhard, J. H. Dane, J.C. Parker, and J. J. Kaluarachchi. Measurement and Simulation of One-Dimensional Transient Three-Phase Flow for Monotonic Liquid Drainage. *Water Resources Research*, 24:853–863, 1988.
- R. J. Lenhard, T. G. Johnson, and J. C. Parker. Experimental observations of nonaqueous-phase liquid subsurface movement. *Journal of Contaminant Hydrology*, 24:79–101, 1993.
- R. J. Lenhard and J. C. Parker. Experimental Validation of the Theory of Extending Two-Phase Saturation-Pressure Relation to Three-Phase Systems for Monotonic Drainage Paths. *Water Resources Research*, 24(3):373–380, 1988.
- C. Lüdecke and D. Lüdecke. *Thermodynamik*. Springer, Berlin, 2000.
- B. T. Mallison, M. G. Gerritson, and S. F. Matringe. Improved Mappings for Streamline-Based Simulation. In *SPE/DOE Fourteenth Symposium on Improved Oil Recovery held in Tulsa, Oklahoma, U.S.A.*, 2004. SPE 89352.
- S. Manthey, M. S. Hassanizadeh, and R. Helmig. Macro-scale dynamic effects in homogeneous and heterogeneous porous media. *Transport in Porous Media*, 58: 121–145, 2005.
- S. F. Matringe. *Accurate Streamline Tracing and Coverage*. PhD thesis, Department of Petroleum Engineering, University of Stanford, 2004.
- C. T. Miller, G. Christakos, P. T. Imhoff, J. F. McBride, J. A. Pedit, and J. A. Trangenstein. Multiphase flow and transport modeling in heterogeneous porous media: challenges and approaches. *Adv. Water Resour.*, 21(2):77–120, 1998.
- Y. Mualem. A new model for predicting the hydraulic conductivity of unsaturated porous media. *Water Resources Research*, 12:513–522, 1976.
- J. T. Oden, I. Babuška, and C. E. Baumann. A discontinuous *hp* finite element method for diffusion problems. *Journal of Computational Physics*, 146:491–519, 1998.
- J. C. Parker and R. J. Lenhard. A Model for Constitutive Relations Governing Multiphase Flow in Porous Media. *Water Resources Research*, 23(12):2187–2196, 1987.
- J. C. Parker, R. J. Lenhard, and T. Kuppusami. A Parametric Model for Constitutive Properties Governing Multiphase Flow in Porous Media. *Water Resources Research*, 23(4):618–624, 1987.
- D. W. Peaceman. *Fundamentals of Numerical Reservoir Engineering*. Elsevier Applied Science, 1977.

- D. W. Pollock. Semi-Analytical Computation of Path Lines for Finite Difference Models. *Ground Water*, 26(6):743–750, 1988.
- J. M. Prausnitz, R. N. Lichtenthaler, and E. G. Azevedo. *Molecular Thermodynamics of Fluid-Phase Equilibria*. Prentice-Hall, 1967.
- M Prévost. The Streamline Method for Unstructured Grids. Master’s Thesis, Stanford University, 2000.
- M. Prévost. *Streamline Tracing on Curvilinear Structured and Unstructured Grids*. PhD thesis, Department of Petroleum Engineering, University of Stanford, 2003.
- K. Pruess. A Fickian diffusion model for the spreading of liquid plumes infiltrating porous media. *Transport in Porous Media*, 24:1–33, 1996.
- W. H. Reed and T. R. Hill. Triangular Mesh Methods for the Neutron Transport Equation. Technical Report LA-UR-73-479, Los Alamos Scientific Laboratory Report, 1973.
- V. Reichenberger, H. Jakobs, P. Bastian, R. Helmig, and J. Niessner. Complex Gas-Water Processes in Discrete Fracture-Matrix Systems. Upscaling, Mass-Conservative Discretization and Efficient Multilevel Solution and Efficient Multilevel Solution. *Mitteilungsheft, Institut für Wasserbau, Universität Stuttgart*, 2004. 3-9337 61-33-6.
- P. Renard and G. de Marsily. Calculating effective permeability: a review. *Advances in Water Resources*, 20:253 – 278, 1997.
- Y. Rubin, A. Bellin, and A. E. Lawrence. On the use of block-effective macrodispersion for numerical simulations of transport in heterogeneous formations. *Water Resources Research*, 39(9), 2003.
- Y. Rubin, A. Sun, R. Maxwell, and A. Bellin. The concept of block-effective macrodispersivity and a unified approach for grid-scale- and plume-scale dependent transport. *J. Fluid Mech.*, 395:161 –180, 1999.
- C.-W. Shu and S. Osher. Efficient implementation of essentially non-oscillatory shock capturing schemes. *Journal of Computational Physics*, 77:439–471, 1988.
- F. Stauffer. Time dependence of the relations between capillary pressure, water content and conductivity during drainage of porous media. In *On scale effects in porous media*, Thessaloniki, Greece, 1978. IAHR.
- F. Stauffer and Th. Dracos. Local infiltration into layered soil and response of the watertable; experiment and simulation. In *Frontiers in Hydrology*, pages 228–242, Littleton, Colorado, 1984. Water Resources Publications.

- H. L. Stone. Probability model for estimating three-phase relative permeability. *Trans. SPE of AIME*, 249:214–218, 1970.
- H. L. Stone. Estimation of three-phase relative permeability and residual oil data. *Journal Can. Petro. Technol.*, 12(4):53–61, 1973.
- M. T. Van Genuchten. A Closed-Form Equation for Predicting the Hydraulic Conductivity of Unsaturated Soils. *American Journal of Soil Science*, 44:892–898, 1980.
- H. Wen, X and J. J. Gómez-Hernández. Upscaling hydraulic conductivities in heterogeneous porous media: an overview. *Journal of Hydrology*, 183, 1996.
- M.F. Wheeler, T. Arbogast, S. Bryant, J. Eaton, Q. Lu, M. Peszynska, and I. Yotov. A parallel multiblock/multidomain approach to reservoir simulation. In *Fifteenth SPE Symposium on Reservoir Simulation, Houston, Texas*, pages 51–62. Society of Petroleum Engineers, 1999. SPE 51884.
- I. Yotov. Advanced techniques and algorithms for reservoir simulation IV. Multiblock solvers and preconditioners. In J. Chadam, A. Cunningham, R. E. Ewing, and M. F. Ortaleva, P. Wheeler, editors, *IMA Volumes in Mathematics and its Applications, Volume 131: Resource Recovery, Confinement, and Remediation of Environmental Hazards*. Springer, 2002.
- L. C. Young and R. E. Stephenson. A General Compositional Approach for Reservoir Simulation. *SPE Journal*, 1983.

# Index

- BDM* projection, 72, 78, 90, 99, 103, 112, 118, 121, 122, 132, 140, 148, 152
- UG, 11
- 2p2c, *see* two-phase–two-component processes
- 3p3c, *see* three-phase–three-component processes
  
- accumulation term, 50
- activity, 57
- advection, 33, 62
  - linear, 66
  - nonlinear, 66
- advection equation, 35
- advective flux, 43
- advective term, 50, 75
- angle deformation, 25
- asymptotic expansion, 11
- average of a function, 70
  
- balance equation, 42, 44, 45
- basis function, 69, 160
- Baumann–Oden method, 72
- biodegradation, 33
- boundary condition, 64, 84, 113, 123, 133, 141, 150, 152
  - Dirichlet, 71, 74, 100
  - instationary, 134
  - Neumann, 71, 74
- Brezzi-Douglas-Marini projection, *see* *BDM* projection
- Brooks-Corey
  - capillary pressure function, 29, 35
  - relative permeability function, 31, 35
- Brownian motion, 34
- Buckley-Leverett problem, 85
  - linear, 86–92
  - nonlinear, 86, 92–97
  
- capillarity, 15, 62
- capillary force, 52
- capillary term, 35
- capillary tube, 28
- CFL condition, 64, 67, 84, 98, 134, 143
- closure relation, 47
- coarsening level, 109, 119, 123, 133, 137
- component, 1, 2, 24, 39, 82
- computing time, 14, 107, 112, 134, 151
- concentration, 33
  - total, 33, 42, 51, 105
- concentration equation, 51, 64, 75, 84, 85, 98, 100, 102, 104, 132, 134, 140, 148
  - DG, 75
- constitutive relationship, 15
- contamination, 1, 5, 12, 56, 141
- control volume, 42, 44
- correlation
  - two-point, 89
- correlation length, 86, 109
- Courant number, 67
- Courant-Friedrichs-Lewy condition, *see* CFL condition

covariance, 38, 89  
 CPU time, 124, 134, 144, 146, 149, 151  
 dense non-aqueous phase liquid, *see*  
     DNAPL  
 density, 1, 13, 15, 24, 42, 82, 150  
 DG 2p2c, 132, 133  
 DG 3p3c, 139, 145  
 DG coarse I, 108, 117, 119, 123  
 DG coarse II, 108, 117, 120–121, 123  
 DG fine, 107, 111–117, 119, 123  
 DG fine  $\bar{v}$ , 109, 117, 122–123  
 DG local 2p2c, 107, 132–139  
 DG local 3p3c, 107, 139–146  
 DG upscaled, 107, 108, 117–130  
 diffusion, 33, 45  
     capillary, 19, 34, 35, 62  
     Fickian, 10  
     local-scale, 82  
     molecular, 34  
     numerical, 11, 34, 35, 62, 68, 76, 78,  
         111, 113, 120  
 diffusive / dispersive term, 75, 76  
 diffusive term, 50  
 dipolar moment, 15  
 discontinuity, 16, 23  
     material, 16  
 discretization, 11, 13, 62  
     discontinuous Galerkin, 11, 13, 62–  
         76, 86, 148  
     finite differences, 80  
     finite volume, 86, 152  
     space, 68–81  
     time, 64–67  
 dispersion, 18, 33, 34, 45  
     hydrodynamic, 45  
     longitudinal, 10, 37  
     transversal, 38  
 dissolution, 1, 5, 141, 150  
 DNAPL, 7, 10, 20  
 downscaling, 97, 151  
 downstream, 2, 35  
 elliptic problem, 62, 63, 69, 97, 152  
 equilibrium  
     chemical, 40  
 equilibrium state, 39  
 error norm, 149  
      $L_1$ , 107, 108, 119, 124, 134, 144, 146  
      $L_2$ , 107, 108, 119, 124, 134, 144, 146  
     definition, 119  
 evaporation, 1, 59  
 explicit scheme, 67  
 exterior skeleton, 70, 71, 74  
 flash  
      $K^k$ , 51  
     equilibrium ratio, 51  
     three-phase–three-component, 56–  
         61, 102, 155–159  
     two-phase–two-component, 52  
 flash calculation, 13, 42, 51–61, 85, 101,  
     105, 132, 137, 140, 141, 149, 151  
 fluid  
     non-wetting, V, 27  
     wetting, V, 27  
 fluid property, 15  
 flux term, 43  
 force  
     capillary, 13, 34, 82, 150  
     gravitational, 82, 150  
 formulation  
     fractional flow, 46, 48, 51, 63, 83, 84  
     fully coupled, 46, 63  
 fractional flow function, 49, 93  
 front tracking, 80–81  
 fugacity, 40, 51  
 function  
     capillary pressure–saturation, 29,  
         47  
     linear relative permeability, 78, 87,  
         107  
     nonlinear relative permeability,  
         107  
     relative permeability–saturation,



- Gauss theorem, 43
- governing equation, 13, 42, 47, 64, 83
- Gram-Schmidt orthonormalization, 69
- gravity, 7, 13, 44, 49, 77, 83
- grid, 35, 62
  - coarse, 84, 85
  - fine, 84, 85
  - unstructured, 11
- grid refinement, 111
- Henry constant, 153, 155
- heterogeneity, 1, 2, 5, 10, 16, 17
  - block, 7, 20
  - intrinsic, 7, 12
- heterogeneous system, 10, 83
- homogeneous medium, 5
- homogenization, 11
- hyperbolic problem, 62, 63, 76, 98, 117, 122
  - linear, 87
  - nonlinear, 92
- hysteresis, 30
- ideal gas, 40
- ideal solution, 40
- IMPES scheme, 46
- inhomogeneity, *see* heterogeneity
- initial condition, 81, 113, 123, 133, 141
- intensive variable, 16
- interface
  - fluid—solid, 36
  - material, 7, 16
  - phase, 5, 7, 15, 16, 23
- interfacial tension, 15
- interior skeleton, 71, 74
- interpolation
  - bilinear, 90
  - linear, 35, 79, 90
- isothermal system, 13, 40, 52, 83, 150, 153
- jump of a function, 70
- kinetics, 39
- Kronecker delta, 51
- Laplace equation, 28
- law
  - Dalton's, 40, 53, 55, 58, 61, 155
  - Darcy's, 16, 49, 77, 90, 121
  - extended Darcy's, 44, 46, 47
  - Fickian, 34, 35
  - Henry's, 19, 40, 53, 55, 58, 155
  - Raoult's, 19, 40, 52, 55, 58, 155
- light non-aqueous phase liquid, *see* LNAPL
- LNAPL, 1, 5, 12, 52, 56, 141, 146
- log-permeability, 38, 89, 109
- macrodispersion, 10, 18, 34, 37, 39, 73, 76, 80, 86, 89, 91, 117, 120
- mapping of saturations, 11, 78
- mass balance, 42, 44–47
- mass conservation, 65, 90, 99, 101, 103, 112, 118, 121, 122, 132, 140, 151, 152
- mass equilibrium ratio, 54, 55
- mass exchange term, 43
- mass fraction, 32, 51
- mass transfer, 1, 5, 6, 13, 15, 19, 39, 52, 57, 98, 148, 159
- mass transfer model
  - A, 56, 57
  - B, 56, 57, 142, 145, 149, 155
  - C, 56, 59, 142, 145, 149, 155, 158
- MAXLEVEL, 113, 115
- mesh, 35
- minmod function, 66
  - corrected, 66
  - standard, 66
- mobility
  - phase, 49
  - total, 49, 78, 99, 103, 118
- molar mass, 153
- mole equilibrium ratio, 52, 55, 58, 155–157

mole fraction, 33, 157  
 molecular weight, 55  
 molecule, 5, 15  
 momentum balance, 44  
 multi-phase flow, 9, 42  
 multi-phase system, 37  
 multi-phase–multi-component process, 42  
 multi-scale finite elements, 9, 97, 152  
 multi-scale finite volumes, 9, 97, 152  
  
 NAPL, 83  
 Navier-Stokes equation, 15  
 Newton iteration, 151  
 Newton–Raphson iteration, 51  
 Newtonian fluid, 25  
 NIPG method, 72  
 no-slip condition, 36  
 nonlinear parameter, 66  
 nonsymmetric interior penalty Galerkin method, *see* NIPG method  
 nonuniform coarsening, 10  
 nonuniform velocity distribution, 18, 36  
 numerical scheme, 35  
  
 ODE, 64, 65  
 ordinary differential equation, *see* ODE  
 oscillation, 65  
  
 parabolic problem, 47, 62, 98  
 partial differential equation, *see* PDE  
 PDE, 48, 62, 67  
 penalty term, 63  
 periodicity, 11  
 permeability, 11  
     absolute, 18, 36, 109, 121  
     relative, 18, 37  
 phase, 1, 23, 39, 82  
     incoherent, 29  
     non-wetting, 2  
     wetting, 1  
 physical model, 13  
 Picard iteration, 151  
 plume of contaminant, 33  
 Pollock’s method, 78, 80  
 polynomial function, 69  
 pooling, 20  
 pore, 36  
 porosity, 15, 42, 82  
 porous medium, 1, 2  
 pressure  
     capillary, 16, 20, 26–30, 35, 47, 77  
         static, 30  
     dynamic capillary, 30  
     entry, 28  
     global, 49, 64  
     partial, 40, 53, 59  
     phase, 46  
     total, 40  
     vapor, 40, 52, 153, 155  
 pressure equation, 10, 46, 50, 51, 63, 68, 77, 84, 85, 97, 102, 107, 111, 118, 122, 132, 140, 148, 151, 152  
     DG, 68  
     upscaled, 120  
 primary variable, 46, 47  
  
 range  
     asymptotic, 34, 37  
     ergodic, 38  
     preasymptotic, 10, 34, 38, 86  
 Rankine-Hugoniot wave speed, 81  
 rarefaction wave, 81  
 reaction, 15, 33  
 relationship  
     capillary pressure–saturation, 29, 47  
     constitutive, 35  
     relative permeability–saturation, 31  
 relative permeability  
     pseudo, 10

representative elementary volume, 15, 16, 27  
 REV, *see* representative elementary volume  
 Riemann fan, 81  
 Riemann problem, 80  
 Runge-Kutta scheme, 11, 13, 63–67  
  
 saturation, 15, 27, 42, 43, 46, 51  
   residual, 29, 87, 146  
 saturation equation, 10, 46, 50, 63, 64, 68, 73, 77, 80, 84, 98, 107, 112, 121–123, 134, 151  
   averaged, 88, 93  
   DG, 73  
   fluctuating, 88, 93  
   linear, 76, 87–92  
   nonlinear, 92–97  
   upscaled, 68, 73, 76, 80, 84–86, 98, 101, 106, 107, 117–130, 148, 150  
 scale  
   coarse, 5, 16, 18, 98  
   fine, 17, 97  
   local, 15, 16, 19, 36, 37, 42, 82, 83, 85  
   macro, 16, 17, 36, 37, 42, 82, 85  
   micro, 15, 17, 19, 36  
   molecular, 15, 17  
 scale separation, 11, 37  
 secondary unknown, 46  
 shear stress, 25  
 shock, 35, 80  
 simset, 109  
 sink  
   external, 13  
 sink / source  
   external, 77, 82  
 slope limiter, 65  
 smearing, 36  
 soil matrix, 13, 17, 82  
 solubility, 57  
 solvent, 41  
  
 sorption, 33  
 source  
   external, 13  
 source / sink term, 18, 43, 50, 73, 75, 98, 106  
 spreading, 20  
 stability, 67  
 standard deviation, 89  
 steep front, 36  
 storage term, 42  
 streamline length, 63, 76, 80, 90, 91  
 streamline method, 63, 68  
 streamline simulation, 11, 77, 108, 111, 113  
 streamline tracing, 68, 76, 78  
 subgrid term, 10, 84, 96  
  
 technical xylol, 153  
 test function, 69  
 three-phase–three-component processes, 1, 5, 14, 102–107, 110, 139–146  
 time discretization  
   explicit, 63, 65, 84, 98, 134  
   implicit, 63, 65  
 time of flight, 78, 80  
   coordinate, 77  
 time step  
   local, 84  
   macro, 98, 100, 105, 134, 143  
   micro, 98, 100, 104, 134, 143  
 time stepping, 64  
   local, 84  
 time–space ray, 80  
 tortuosity, 18  
 total variation bounded, *see* TVB  
 total variation diminishing, *see* TVD  
 trapping, 20  
 triangulation, 69  
 turning-band algorithm, 109  
 TVB, 66  
 TVD, 65

two-phase problem, 84  
two-phase–two-component processes,  
5, 14, 98–102, 107, 110, 132–139,  
146

unit mobility case, 94  
unsaturated zone, 1, 5, 12, 56, 83  
upscaling, 7, 10, 42, 63, 80, 86–97, 150,  
151  
    local–global, 11  
upscaling level, *see* coarsening level  
upstream, 35

Van Genuchten  
    capillary pressure function, 29  
    relative permeability function, 31,  
    141

variance, 38, 109  
variogram, 38  
velocity  
    Darcy, 43, 72  
    phase, 44, 49, 50, 85  
    total, 49, 64, 68, 85, 87, 103, 118  
viscosity, 13, 15, 25, 82, 87, 150  
    dynamic, 25  
volume averaging, 10, 42, 86–97, 148

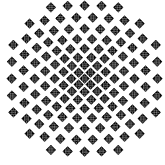
wettability, 46  
wetting angle,  $V$ , 27

# Lebenslauf

**Name, Vorname:** Niessner, Jennifer  
**Anschrift:** Kleiner Ostring 101  
70374 Stuttgart  
**Geburtsort:** Stuttgart  
**Geburtsdatum:** 5. Januar 1979  
**Familienstand:** ledig  
**Nationalität:** deutsch

## Universitäre Ausbildung:

- 1998-2003 Studium der Umweltschutztechnik an der Universität Stuttgart**  
*Abschluss:* Dipl.-Ing. (mit Auszeichnung)  
*Stipendium:* Studienstiftung des deutschen Volkes
- 2000-2003 Studium des internationalen Studiengangs „Water Resources Engineering and Management an der Universität Stuttgart“**  
*Abschluss:* M.Sc. (mit Auszeichnung)
- 2003 Diplomarbeit und Master's Thesis am Institut National de Recherche en Informatique et en Automatique/ Paris, Frankreich  
*Titel:* Influence of the Interface Condition and Exact Linearization in the Newton Iterations for Two-Phase Flow in Heterogeneous Porous Media, dafür
- 2004 Preis der Freunde der Universität Stuttgart
- 2003-2006 Doktorandin am Institut für Wasserbau an der Universität Stuttgart**  
*Dissertationsthema:* Multi-Scale Modeling of Multi-Phase–Multi-Component Processes in Heterogeneous Porous Media  
*Doktorandenprogramm:* ENWAT (Environment Water)  
*Lehrassistentz:* Model Concept and Simulation Methods for Single and Multi-Phase Flow
- 2004-2005 *Stipendium:* Landesgraduiertenförderung Baden Württemberg
- 2005 zweimonatiger Forschungsaufenthalt bei Prof. Espedal und Prof. Dahle an der Universität Bergen, Norwegen
- 2006 *Projektarbeit:* Wissenschaftliche Mitarbeiterin SFB 404 Mehrfeldprobleme in der Kontinuumsmechanik, Teilprojekt A3, Mehrphasenprozesse in porösen Medien



## Institut für Wasserbau Universität Stuttgart

Pfaffenwaldring 61  
70569 Stuttgart (Vaihingen)  
Telefon (0711) 685 - 64717/64741/64752/64679  
Telefax (0711) 685 - 67020 o. 64746 o. 64681  
E-Mail: [iws@iws.uni-stuttgart.de](mailto:iws@iws.uni-stuttgart.de)  
<http://www.iws.uni-stuttgart.de>

### Direktoren

Prof. Dr. rer. nat. Dr.-Ing. András Bárdossy  
Prof. Dr.-Ing. Rainer Helmig  
Prof. Dr.-Ing. Silke Wieprecht

### Vorstand (Stand 31.01.2006)

Prof. Dr. rer. nat. Dr.-Ing. A. Bárdossy  
Prof. Dr.-Ing. R. Helmig  
Prof. Dr.-Ing. S. Wieprecht  
Prof. Dr.-Ing. habil. B. Westrich  
Jürgen Braun, PhD  
Dr.-Ing. H. Class  
Dr.-Ing. A. Färber  
Dr.-Ing. H.-P. Koschitzky  
PD Dr.-Ing. W. Marx

### Emeriti

Prof. Dr.-Ing. Dr.-Ing. E.h. Jürgen Giesecke  
Prof. Dr.h.c. Dr.-Ing. E.h. Helmut Kobus, Ph.D.

### Lehrstuhl für Wasserbau und Wassermengenwirtschaft

Leiter: Prof. Dr.-Ing. Silke Wieprecht  
Stellv.: PD Dr.-Ing. Walter Marx, AOR

### Lehrstuhl für Hydrologie und Geohydrologie

Leiter: Prof. Dr. rer. nat. Dr.-Ing. András Bárdossy  
Stellv.: Dr.-Ing. Arne Färber

### Lehrstuhl für Hydromechanik und Hydrosystemmodellierung

Leiter: Prof. Dr.-Ing. Rainer Helmig  
Stellv.: Dr.-Ing. Holger Class, AOR

**VEGAS**, Versuchseinrichtung zur Grundwasser-  
und Altlastensanierung

Leitung: Jürgen Braun, PhD  
Dr.-Ing. Hans-Peter Koschitzky, AD

### Versuchsanstalt

Leiter: apl. Prof. Dr.-Ing. Bernhard Westrich

## Verzeichnis der Mitteilungshefte

- 1 Röhnisch, Arthur: *Die Bemühungen um eine Wasserbauliche Versuchsanstalt an der Technischen Hochschule Stuttgart,*  
und  
Fattah Abouleid, Abdel: *Beitrag zur Berechnung einer in lockeren Sand gerammten, zweifach verankerten Spundwand,* 1963
- 2 Marotz, Günter: *Beitrag zur Frage der Standfestigkeit von dichten Asphaltbelägen im Großwasserbau,* 1964
- 3 Gurr, Siegfried: *Beitrag zur Berechnung zusammengesetzter ebener Flächentragwerke unter besonderer Berücksichtigung ebener Stauwände, mit Hilfe von Randwert- und Lastwertmatrizen,* 1965
- 4 Plica, Peter: *Ein Beitrag zur Anwendung von Schalenkonstruktionen im Stahlwasserbau,*  
und Petrikat, Kurt: *Möglichkeiten und Grenzen des wasserbaulichen Versuchswesens,* 1966

- 5 Plate, Erich: *Beitrag zur Bestimmung der Windgeschwindigkeitsverteilung in der durch eine Wand gestörten bodennahen Luftschicht, und*  
Röhnisch, Arthur; Marotz, Günter: *Neue Baustoffe und Bauausführungen für den Schutz der Böschungen und der Sohle von Kanälen, Flüssen und Häfen; Gestehungskosten und jeweilige Vorteile, sowie Unny, T.E.: Schwingungsuntersuchungen am Kegelstrahlschieber, 1967*
- 6 Seiler, Erich: *Die Ermittlung des Anlagenwertes der bundeseigenen Binnenschiffahrtsstraßen und Talsperren und des Anteils der Binnenschiffahrt an diesem Wert, 1967*
- 7 *Sonderheft anlässlich des 65. Geburtstages von Prof. Arthur Röhnisch mit Beiträgen von*  
Benk, Dieter; Breitling, J.; Gurr, Siegfried; Haberhauer, Robert; Honekamp, Hermann; Kuz, Klaus Dieter; Marotz, Günter; Mayer-Vorfelder, Hans-Jörg; Miller, Rudolf; Plate, Erich J.; Radomski, Helge; Schwarz, Helmut; Vollmer, Ernst; Wildenhahn, Eberhard; 1967
- 8 Jumikis, Alfred: *Beitrag zur experimentellen Untersuchung des Wassernachschubs in einem gefrierenden Boden und die Beurteilung der Ergebnisse, 1968*
- 9 Marotz, Günter: *Technische Grundlagen einer Wasserspeicherung im natürlichen Untergrund, 1968*
- 10 Radomski, Helge: *Untersuchungen über den Einfluß der Querschnittsform wellenförmiger Spundwände auf die statischen und rammtechnischen Eigenschaften, 1968*
- 11 Schwarz, Helmut: *Die Grenztragfähigkeit des Baugrundes bei Einwirkung vertikal gezogener Ankerplatten als zweidimensionales Bruchproblem, 1969*
- 12 Erbel, Klaus: *Ein Beitrag zur Untersuchung der Metamorphose von Mittelgebirgsschneedecken unter besonderer Berücksichtigung eines Verfahrens zur Bestimmung der thermischen Schneequalität, 1969*
- 13 Westhaus, Karl-Heinz: *Der Strukturwandel in der Binnenschiffahrt und sein Einfluß auf den Ausbau der Binnenschiffskanäle, 1969*
- 14 Mayer-Vorfelder, Hans-Jörg: *Ein Beitrag zur Berechnung des Erdwiderstandes unter Ansatz der logarithmischen Spirale als Gleitflächenfunktion, 1970*
- 15 Schulz, Manfred: *Berechnung des räumlichen Erddruckes auf die Wandung kreiszylindrischer Körper, 1970*
- 16 Mobasseri, Manoutschehr: *Die Rippenstützmauer. Konstruktion und Grenzen ihrer Standsicherheit, 1970*
- 17 Benk, Dieter: *Ein Beitrag zum Betrieb und zur Bemessung von Hochwasserrückhaltebecken, 1970*

- 18 Gál, Attila: *Bestimmung der mitschwingenden Wassermasse bei überströmten Fischbauchklappen mit kreiszylindrischem Staublech*, 1971, vergriffen
- 19 Kuz, Klaus Dieter: *Ein Beitrag zur Frage des Einsetzens von Kavitationserscheinungen in einer Düsenströmung bei Berücksichtigung der im Wasser gelösten Gase*, 1971, vergriffen
- 20 Schaak, Hartmut: *Verteilleitungen von Wasserkraftanlagen*, 1971
- 21 *Sonderheft zur Eröffnung der neuen Versuchsanstalt des Instituts für Wasserbau der Universität Stuttgart mit Beiträgen von*  
Brombach, Hansjörg; Dirksen, Wolfram; Gál, Attila; Gerlach, Reinhard; Giesecke, Jürgen; Holthoff, Franz-Josef; Kuz, Klaus Dieter; Marotz, Günter; Minor, Hans-Erwin; Petrikat, Kurt; Röhnisch, Arthur; Rueff, Helge; Schwarz, Helmut; Vollmer, Ernst; Wildenhahn, Eberhard; 1972
- 22 Wang, Chung-su: *Ein Beitrag zur Berechnung der Schwingungen an Kegelstrahlschiebern*, 1972
- 23 Mayer-Vorfelder, Hans-Jörg: *Erdwiderstandsbeiwerte nach dem Ohde-Variationsverfahren*, 1972
- 24 Minor, Hans-Erwin: *Beitrag zur Bestimmung der Schwingungsanfachungsfunktionen überströmter Stauklappen*, 1972, vergriffen
- 25 Brombach, Hansjörg: *Untersuchung strömungsmechanischer Elemente (Fluidik) und die Möglichkeit der Anwendung von Wirbelkammerelementen im Wasserbau*, 1972, vergriffen
- 26 Wildenhahn, Eberhard: *Beitrag zur Berechnung von Horizontalfilterbrunnen*, 1972
- 27 Steinlein, Helmut: *Die Eliminierung der Schwebstoffe aus Flußwasser zum Zweck der unterirdischen Wasserspeicherung, gezeigt am Beispiel der Iller*, 1972
- 28 Holthoff, Franz Josef: *Die Überwindung großer Hubhöhen in der Binnenschifffahrt durch Schwimmerhebewerke*, 1973
- 29 Röder, Karl: *Einwirkungen aus Baugrundbewegungen auf trog- und kastenförmige Konstruktionen des Wasser- und Tunnelbaues*, 1973
- 30 Kretschmer, Heinz: *Die Bemessung von Bogenstaumauern in Abhängigkeit von der Talform*, 1973
- 31 Honekamp, Hermann: *Beitrag zur Berechnung der Montage von Unterwasserpipelines*, 1973
- 32 Giesecke, Jürgen: *Die Wirbelkammertriode als neuartiges Steuerorgan im Wasserbau, und Brombach, Hansjörg: Entwicklung, Bauformen, Wirkungsweise und Steuereigenschaften von Wirbelkammerverstärkern*, 1974



- 33 Rueff, Helge: *Untersuchung der schwingungserregenden Kräfte an zwei hintereinander angeordneten Tiefschützen unter besonderer Berücksichtigung von Kavitation*, 1974
- 34 Röhnisch, Arthur: *Einpreßversuche mit Zementmörtel für Spannbeton - Vergleich der Ergebnisse von Modellversuchen mit Ausführungen in Hüllwellrohren*, 1975
- 35 *Sonderheft anlässlich des 65. Geburtstages von Prof. Dr.-Ing. Kurt Petrikat mit Beiträgen von:* Brombach, Hansjörg; Erbel, Klaus; Flinspach, Dieter; Fischer jr., Richard; Gál, Attila; Gerlach, Reinhard; Giesecke, Jürgen; Haberhauer, Robert; Hafner Edzard; Hausenblas, Bernhard; Horlacher, Hans-Burkhard; Hutarew, Andreas; Knoll, Manfred; Krummet, Ralph; Marotz, Günter; Merkle, Theodor; Miller, Christoph; Minor, Hans-Erwin; Neumayer, Hans; Rao, Syamala; Rath, Paul; Rueff, Helge; Ruppert, Jürgen; Schwarz, Wolfgang; Topal-Gökceli, Mehmet; Vollmer, Ernst; Wang, Chung-su; Weber, Hans-Georg; 1975
- 36 Berger, Jochum: *Beitrag zur Berechnung des Spannungszustandes in rotationssymmetrisch belasteten Kugelschalen veränderlicher Wandstärke unter Gas- und Flüssigkeitsdruck durch Integration schwach singulärer Differentialgleichungen*, 1975
- 37 Dirksen, Wolfram: *Berechnung instationärer Abflußvorgänge in gestauten Gerinnen mittels Differenzenverfahren und die Anwendung auf Hochwasserrückhaltebecken*, 1976
- 38 Horlacher, Hans-Burkhard: *Berechnung instationärer Temperatur- und Wärmespannungsfelder in langen mehrschichtigen Hohlzylindern*, 1976
- 39 Hafner, Edzard: *Untersuchung der hydrodynamischen Kräfte auf Baukörper im Tiefwasserbereich des Meeres*, 1977, ISBN 3-921694-39-6
- 40 Ruppert, Jürgen: *Über den Axialwirbelkammerverstärker für den Einsatz im Wasserbau*, 1977, ISBN 3-921694-40-X
- 41 Hutarew, Andreas: *Beitrag zur Beeinflußbarkeit des Sauerstoffgehalts in Fließgewässern an Abstürzen und Wehren*, 1977, ISBN 3-921694-41-8, vergriffen
- 42 Miller, Christoph: *Ein Beitrag zur Bestimmung der schwingungserregenden Kräfte an unterströmten Wehren*, 1977, ISBN 3-921694-42-6
- 43 Schwarz, Wolfgang: *Druckstoßberechnung unter Berücksichtigung der Radial- und Längsverschiebungen der Rohrwandung*, 1978, ISBN 3-921694-43-4
- 44 Kinzelbach, Wolfgang: *Numerische Untersuchungen über den optimalen Einsatz variabler Kühlsysteme einer Kraftwerkskette am Beispiel Oberrhein*, 1978, ISBN 3-921694-44-2
- 45 Barczewski, Baldur: *Neue Meßmethoden für Wasser-Luftgemische und deren Anwendung auf zweiphasige Auftriebsstrahlen*, 1979, ISBN 3-921694-45-0

- 46 Neumayer, Hans: *Untersuchung der Strömungsvorgänge in radialen Wirbelkammerverstärkern*, 1979, ISBN 3-921694-46-9
- 47 Elalfy, Youssef-Elhassan: *Untersuchung der Strömungsvorgänge in Wirbelkammerdiolen und -drosseln*, 1979, ISBN 3-921694-47-7
- 48 Brombach, Hansjörg: *Automatisierung der Bewirtschaftung von Wasserspeichern*, 1981, ISBN 3-921694-48-5
- 49 Geldner, Peter: *Deterministische und stochastische Methoden zur Bestimmung der Selbstdichtung von Gewässern*, 1981, ISBN 3-921694-49-3, vergriffen
- 50 Mehlhorn, Hans: *Temperaturveränderungen im Grundwasser durch Brauchwassereinleitungen*, 1982, ISBN 3-921694-50-7, vergriffen
- 51 Hafner, Edzard: *Rohrleitungen und Behälter im Meer*, 1983, ISBN 3-921694-51-5
- 52 Rinnert, Bernd: *Hydrodynamische Dispersion in porösen Medien: Einfluß von Dichteunterschieden auf die Vertikalvermischung in horizontaler Strömung*, 1983, ISBN 3-921694-52-3, vergriffen
- 53 Lindner, Wulf: *Steuerung von Grundwasserentnahmen unter Einhaltung ökologischer Kriterien*, 1983, ISBN 3-921694-53-1, vergriffen
- 54 Herr, Michael; Herzer, Jörg; Kinzelbach, Wolfgang; Kobus, Helmut; Rinnert, Bernd: *Methoden zur rechnerischen Erfassung und hydraulischen Sanierung von Grundwasserkontaminationen*, 1983, ISBN 3-921694-54-X
- 55 Schmitt, Paul: *Wege zur Automatisierung der Niederschlagsermittlung*, 1984, ISBN 3-921694-55-8, vergriffen
- 56 Müller, Peter: *Transport und selektive Sedimentation von Schwebstoffen bei gestau tem Abfluß*, 1985, ISBN 3-921694-56-6
- 57 El-Qawasmeh, Fuad: *Möglichkeiten und Grenzen der Tropfbewässerung unter besonderer Berücksichtigung der Verstopfungsanfälligkeit der Tropfelemente*, 1985, ISBN 3-921694-57-4, vergriffen
- 58 Kirchenbaur, Klaus: *Mikroprozessorgesteuerte Erfassung instationärer Druckfelder am Beispiel seegangbelasteter Baukörper*, 1985, ISBN 3-921694-58-2
- 59 Kobus, Helmut (Hrsg.): *Modellierung des großräumigen Wärme- und Schadstofftransports im Grundwasser*, Tätigkeitsbericht 1984/85 (DFG-Forschergruppe an den Universitäten Hohenheim, Karlsruhe und Stuttgart), 1985, ISBN 3-921694-59-0, vergriffen
- 60 Spitz, Karlheinz: *Dispersion in porösen Medien: Einfluß von Inhomogenitäten und Dichteunterschieden*, 1985, ISBN 3-921694-60-4, vergriffen

- 61 Kobus, Helmut: *An Introduction to Air-Water Flows in Hydraulics*, 1985, ISBN 3-921694-61-2
- 62 Kaleris, Vassilios: *Erfassung des Austausches von Oberflächen- und Grundwasser in horizontalebenen Grundwassermodellen*, 1986, ISBN 3-921694-62-0
- 63 Herr, Michael: *Grundlagen der hydraulischen Sanierung verunreinigter Porengrundwasserleiter*, 1987, ISBN 3-921694-63-9
- 64 Marx, Walter: *Berechnung von Temperatur und Spannung in Massenbeton infolge Hydratation*, 1987, ISBN 3-921694-64-7
- 65 Koschitzky, Hans-Peter: *Dimensionierungskonzept für Sohlbelüfter in Schußrinnen zur Vermeidung von Kavitationsschäden*, 1987, ISBN 3-921694-65-5
- 66 Kobus, Helmut (Hrsg.): *Modellierung des großräumigen Wärme- und Schadstofftransports im Grundwasser*, Tätigkeitsbericht 1986/87 (DFG-Forschergruppe an den Universitäten Hohenheim, Karlsruhe und Stuttgart) 1987, ISBN 3-921694-66-3
- 67 Söll, Thomas: *Berechnungsverfahren zur Abschätzung anthropogener Temperaturanomalien im Grundwasser*, 1988, ISBN 3-921694-67-1
- 68 Dittrich, Andreas; Westrich, Bernd: *Bodenseeufererosion, Bestandsaufnahme und Bewertung*, 1988, ISBN 3-921694-68-X, vergriffen
- 69 Huwe, Bernd; van der Ploeg, Rienk R.: *Modelle zur Simulation des Stickstoffhaushaltes von Standorten mit unterschiedlicher landwirtschaftlicher Nutzung*, 1988, ISBN 3-921694-69-8, vergriffen
- 70 Stephan, Karl: *Integration elliptischer Funktionen*, 1988, ISBN 3-921694-70-1
- 71 Kobus, Helmut; Zilliox, Lothaire (Hrsg.): *Nitratbelastung des Grundwassers, Auswirkungen der Landwirtschaft auf die Grundwasser- und Rohwasserbeschaffenheit und Maßnahmen zum Schutz des Grundwassers*. Vorträge des deutsch-französischen Kolloquiums am 6. Oktober 1988, Universitäten Stuttgart und Louis Pasteur Strasbourg (Vorträge in deutsch oder französisch, Kurzfassungen zweisprachig), 1988, ISBN 3-921694-71-X
- 72 Soyeaux, Renald: *Unterströmung von Stauanlagen auf klüftigem Untergrund unter Berücksichtigung laminarer und turbulenter Fließzustände*, 1991, ISBN 3-921694-72-8
- 73 Kohane, Roberto: *Berechnungsmethoden für Hochwasserabfluß in Fließgewässern mit überströmten Vorländern*, 1991, ISBN 3-921694-73-6
- 74 Hassinger, Reinhard: *Beitrag zur Hydraulik und Bemessung von Blocksteinrampen in flexibler Bauweise*, 1991, ISBN 3-921694-74-4, vergriffen
- 75 Schäfer, Gerhard: *Einfluß von Schichtenstrukturen und lokalen Einlagerungen auf die Längsdispersion in Porengrundwasserleitern*, 1991, ISBN 3-921694-75-2

- 76 Giesecke, Jürgen: *Vorträge, Wasserwirtschaft in stark besiedelten Regionen; Umweltforschung mit Schwerpunkt Wasserwirtschaft*, 1991, ISBN 3-921694-76-0
- 77 Huwe, Bernd: *Deterministische und stochastische Ansätze zur Modellierung des Stickstoffhaushalts landwirtschaftlich genutzter Flächen auf unterschiedlichem Skalenniveau*, 1992, ISBN 3-921694-77-9, vergriffen
- 78 Rommel, Michael: *Verwendung von Kluftdaten zur realitätsnahen Generierung von Kluftnetzen mit anschließender laminar-turbulenter Strömungsberechnung*, 1993, ISBN 3-92 1694-78-7
- 79 Marschall, Paul: *Die Ermittlung lokaler Stofffrachten im Grundwasser mit Hilfe von Einbohrloch-Meßverfahren*, 1993, ISBN 3-921694-79-5, vergriffen
- 80 Ptak, Thomas: *Stofftransport in heterogenen Porenaquiferen: Felduntersuchungen und stochastische Modellierung*, 1993, ISBN 3-921694-80-9, vergriffen
- 81 Haakh, Frieder: *Transientes Strömungsverhalten in Wirbelkammern*, 1993, ISBN 3-921694-81-7
- 82 Kobus, Helmut; Cirpka, Olaf; Barczewski, Baldur; Koschitzky, Hans-Peter: *Versucheinrichtung zur Grundwasser und Altlastensanierung VEGAS, Konzeption und Programmrahmen*, 1993, ISBN 3-921694-82-5
- 83 Zang, Weidong: *Optimaler Echtzeit-Betrieb eines Speichers mit aktueller Abflußregenerierung*, 1994, ISBN 3-921694-83-3, vergriffen
- 84 Franke, Hans-Jörg: *Stochastische Modellierung eines flächenhaften Stoffeintrages und Transports in Grundwasser am Beispiel der Pflanzenschutzmittelproblematik*, 1995, ISBN 3-921694-84-1
- 85 Lang, Ulrich: *Simulation regionaler Strömungs- und Transportvorgänge in Karstaquiferen mit Hilfe des Doppelkontinuum-Ansatzes: Methodenentwicklung und Parameteridentifikation*, 1995, ISBN 3-921694-85-X, vergriffen
- 86 Helmig, Rainer: *Einführung in die Numerischen Methoden der Hydromechanik*, 1996, ISBN 3-921694-86-8, vergriffen
- 87 Cirpka, Olaf: *CONTRACT: A Numerical Tool for Contaminant Transport and Chemical Transformations - Theory and Program Documentation -*, 1996, ISBN 3-921694-87-6
- 88 Haberlandt, Uwe: *Stochastische Synthese und Regionalisierung des Niederschlages für Schmutzfrachtberechnungen*, 1996, ISBN 3-921694-88-4
- 89 Croisé, Jean: *Extraktion von flüchtigen Chemikalien aus natürlichen Lockergesteinen mittels erzwungener Luftströmung*, 1996, ISBN 3-921694-89-2, vergriffen

- 90 Jorde, Klaus: *Ökologisch begründete, dynamische Mindestwasserregelungen bei Ausleitungskraftwerken*, 1997, ISBN 3-921694-90-6, vergriffen
- 91 Helmig, Rainer: *Gekoppelte Strömungs- und Transportprozesse im Untergrund - Ein Beitrag zur Hydrosystemmodellierung*-, 1998, ISBN 3-921694-91-4
- 92 Emmert, Martin: *Numerische Modellierung nichtisothermer Gas-Wasser Systeme in porösen Medien*, 1997, ISBN 3-921694-92-2
- 93 Kern, Ulrich: *Transport von Schweb- und Schadstoffen in staugeregelten Fließgewässern am Beispiel des Neckars*, 1997, ISBN 3-921694-93-0, vergriffen
- 94 Förster, Georg: *Druckstoßdämpfung durch große Luftblasen in Hochpunkten von Rohrleitungen* 1997, ISBN 3-921694-94-9
- 95 Cirpka, Olaf: *Numerische Methoden zur Simulation des reaktiven Mehrkomponententransports im Grundwasser*, 1997, ISBN 3-921694-95-7, vergriffen
- 96 Färber, Arne: *Wärmetransport in der ungesättigten Bodenzone: Entwicklung einer thermischen In-situ-Sanierungstechnologie*, 1997, ISBN 3-921694-96-5
- 97 Betz, Christoph: *Wasserdampfdestillation von Schadstoffen im porösen Medium: Entwicklung einer thermischen In-situ-Sanierungstechnologie*, 1998, ISBN 3-921694-97-3
- 98 Xu, Yichun: *Numerical Modeling of Suspended Sediment Transport in Rivers*, 1998, ISBN 3-921694-98-1, vergriffen
- 99 Wüst, Wolfgang: *Geochemische Untersuchungen zur Sanierung CKW-kontaminierter Aquifere mit Fe(0)-Reaktionswänden*, 2000, ISBN 3-933761-02-2
- 100 Sheta, Hussam: *Simulation von Mehrphasenvorgängen in porösen Medien unter Einbeziehung von Hysterese-Effekten*, 2000, ISBN 3-933761-03-4
- 101 Ayros, Edwin: *Regionalisierung extremer Abflüsse auf der Grundlage statistischer Verfahren*, 2000, ISBN 3-933761-04-2, vergriffen
- 102 Huber, Ralf: *Compositional Multiphase Flow and Transport in Heterogeneous Porous Media*, 2000, ISBN 3-933761-05-0
- 103 Braun, Christopherus: *Ein Upscaling-Verfahren für Mehrphasenströmungen in porösen Medien*, 2000, ISBN 3-933761-06-9
- 104 Hofmann, Bernd: *Entwicklung eines rechnergestützten Managementsystems zur Beurteilung von Grundwasserschadensfällen*, 2000, ISBN 3-933761-07-7
- 105 Class, Holger: *Theorie und numerische Modellierung nichtisothermer Mehrphasenprozesse in NAPL-kontaminierten porösen Medien*, 2001, ISBN 3-933761-08-5

- 106 Schmidt, Reinhard: *Wasserdampf- und Heißluftinjektion zur thermischen Sanierung kontaminierter Standorte*, 2001, ISBN 3-933761-09-3
- 107 Reinhold Josef.: *Schadstoffextraktion mit hydraulischen Sanierungsverfahren unter Anwendung von grenzflächenaktiven Stoffen*, 2001, ISBN 3-933761-10-7
- 108 Schneider, Matthias: *Habitat- und Abflussmodellierung für Fließgewässer mit unscharfen Berechnungsansätzen*, 2001, ISBN 3-933761-11-5
- 109 Rathgeb, Andreas: *Hydrodynamische Bemessungsgrundlagen für Lockerdeckwerke an überströmbaren Erddämmen*, 2001, ISBN 3-933761-12-3
- 110 Lang, Stefan: *Parallele numerische Simulation instationärer Probleme mit adaptiven Methoden auf unstrukturierten Gittern*, 2001, ISBN 3-933761-13-1
- 111 Appt, Jochen; Stumpp Simone: *Die Bodensee-Messkampagne 2001, IWS/CWR Lake Constance Measurement Program 2001*, 2002, ISBN 3-933761-14-X
- 112 Heimerl, Stephan: *Systematische Beurteilung von Wasserkraftprojekten*, 2002, ISBN 3-933761-15-8
- 113 Iqbal, Amin: *On the Management and Salinity Control of Drip Irrigation*, 2002, ISBN 3-933761-16-6
- 114 Silberhorn-Hemminger, Annette: *Modellierung von Kluftaquifersystemen: Geostatistische Analyse und deterministisch-stochastische Kluftgenerierung*, 2002, ISBN 3-933761-17-4
- 115 Winkler, Angela: *Prozesse des Wärme- und Stofftransports bei der In-situ-Sanierung mit festen Wärmequellen*, 2003, ISBN 3-933761-18-2
- 116 Marx, Walter: *Wasserkraft, Bewässerung, Umwelt - Planungs- und Bewertungsschwerpunkte der Wasserbewirtschaftung*, 2003, ISBN 3-933761-19-0
- 117 Hinkelmann, Reinhard: *Efficient Numerical Methods and Information-Processing Techniques in Environment Water*, 2003, ISBN 3-933761-20-4
- 118 Samaniego-Eguiguren, Luis Eduardo: *Hydrological Consequences of Land Use / Land Cover and Climatic Changes in Mesoscale Catchments*, 2003, ISBN 3-933761-21-2
- 119 Neunhäuserer, Lina: *Diskretisierungsansätze zur Modellierung von Strömungs- und Transportprozessen in geklüftet-porösen Medien*, 2003, ISBN 3-933761-22-0
- 120 Paul, Maren: *Simulation of Two-Phase Flow in Heterogeneous Poros Media with Adaptive Methods*, 2003, ISBN 3-933761-23-9
- 121 Ehret, Uwe: *Rainfall and Flood Nowcasting in Small Catchments using Weather Radar*, 2003, ISBN 3-933761-24-7

- 122 Haag, Ingo: *Der Sauerstoffhaushalt staugeregelter Flüsse am Beispiel des Neckars - Analysen, Experimente, Simulationen* -, 2003, ISBN 3-933761-25-5
- 123 Appt, Jochen: *Analysis of Basin-Scale Internal Waves in Upper Lake Constance*, 2003, ISBN 3-933761-26-3
- 124 Hrsg.: Schrenk, Volker; Batereau, Katrin; Barczewski, Baldur; Weber, Karolin und Koschitzky, Hans-Peter: *Symposium Ressource Fläche und VEGAS - Statuskolloquium 2003, 30. September und 1. Oktober 2003*, 2003, ISBN 3-933761-27-1
- 125 Omar Khalil Ouda: *Optimisation of Agricultural Water Use: A Decision Support System for the Gaza Strip*, 2003, ISBN 3-933761-28-0
- 126 Batereau, Katrin: *Sensorbasierte Bodenluftmessung zur Vor-Ort-Erkundung von Schadensherden im Untergrund*, 2004, ISBN 3-933761-29-8
- 127 Witt, Oliver: *Erosionsstabilität von Gewässersedimenten mit Auswirkung auf den Stofftransport bei Hochwasser am Beispiel ausgewählter Stauhaltungen des Oberrheins*, 2004, ISBN 3-933761-30-1
- 128 Jakobs, Hartmut: *Simulation nicht-isothermer Gas-Wasser-Prozesse in komplexen Kluft-Matrix-Systemen*, 2004, ISBN 3-933761-31-X
- 129 Li, Chen-Chien: *Deterministisch-stochastisches Berechnungskonzept zur Beurteilung der Auswirkungen erosiver Hochwasserereignisse in Flusstauhaltungen*, 2004, ISBN 3-933761-32-8
- 130 Reichenberger, Volker; Helmig, Rainer; Jakobs, Hartmut; Bastian, Peter; Niessner, Jennifer: *Complex Gas-Water Processes in Discrete Fracture-Matrix Systems: Upscaling, Mass-Conservative Discretization and Efficient Multilevel Solution*, 2004, ISBN 3-933761-33-6
- 131 Hrsg.: Barczewski, Baldur; Koschitzky, Hans-Peter; Weber, Karolin; Wege, Ralf: *VEGAS - Statuskolloquium 2004*, Tagungsband zur Veranstaltung am 05. Oktober 2004 an der Universität Stuttgart, Campus Stuttgart-Vaihingen, 2004, ISBN 3-933761-34-4
- 132 Asie, Kemal Jabir: *Finite Volume Models for Multiphase Multicomponent Flow through Porous Media*. 2005, ISBN 3-933761-35-2
- 133 Jacoub, George: *Development of a 2-D Numerical Module for Particulate Contaminant Transport in Flood Retention Reservoirs and Impounded Rivers*, 2004, ISBN 3-933761-36-0
- 134 Nowak, Wolfgang: *Geostatistical Methods for the Identification of Flow and Transport Parameters in the Subsurface*, 2005, ISBN 3-933761-37-9
- 135 Süß, Mia: *Analysis of the influence of structures and boundaries on flow and transport processes in fractured porous media*, 2005, ISBN 3-933761-38-7

- 136 Jose, Surabhin Chackiath: *Experimental Investigations on Longitudinal Dispersive Mixing in Heterogeneous Aquifers*, 2005, ISBN: 3-933761-39-5
- 137 Filiz, Fulya: *Linking Large-Scale Meteorological Conditions to Floods in Mesoscale Catchments*, 2005, ISBN 3-933761-40-9
- 138 Qin, Minghao: *Wirklichkeitsnahe und recheneffiziente Ermittlung von Temperatur und Spannungen bei großen RCC-Staumauern*, 2005, ISBN 3-933761-41-7
- 139 Kobayashi, Kenichiro: *Optimization Methods for Multiphase Systems in the Subsurface - Application to Methane Migration in Coal Mining Areas*, 2005, ISBN 3-933761-42-5
- 140 Rahman, Md. Arifur: *Experimental Investigations on Transverse Dispersive Mixing in Heterogeneous Porous Media*, 2005, ISBN 3-933761-43-3
- 141 Schrenk, Volker: *Ökobilanzen zur Bewertung von Altlastensanierungsmaßnahmen*, 2005, ISBN 3-933761-44-1
- 142 Hundecha, Hirpa Yeshewatesfa: *Regionalization of Parameters of a Conceptual Rainfall-Runoff Model*, 2005, ISBN: 3-933761-45-X
- 143 Wege, Ralf: *Untersuchungs- und Überwachungsmethoden für die Beurteilung natürlicher Selbstreinigungsprozesse im Grundwasser*, 2005, ISBN 3-933761-46-8
- 144 Breiting, Thomas: *Techniken und Methoden der Hydroinformatik - Modellierung von komplexen Hydrosystemen im Untergrund*, 2006, 3-933761-47-6
- 145 Hrsg.: Braun, Jürgen; Koschitzky, Hans-Peter; Müller, Martin: *Ressource Untergrund: 10 Jahre VEGAS: Forschung und Technologieentwicklung zum Schutz von Grundwasser und Boden*, Tagungsband zur Veranstaltung am 28. und 29. September 2005 an der Universität Stuttgart, Campus Stuttgart-Vaihingen, 2005, ISBN 3-933761-48-4
- 146 Rojanschi, Vlad: *Abflusskonzentration in mesoskaligen Einzugsgebieten unter Berücksichtigung des Sickerraumes*, 2006, ISBN 3-933761-49-2
- 147 Winkler, Nina Simone: *Optimierung der Steuerung von Hochwasserrückhaltebeckensystemen*, 2006, ISBN 3-933761-50-6
- 148 Wolf, Jens: *Räumlich differenzierte Modellierung der Grundwasserströmung alluvialer Aquifere für mesoskalige Einzugsgebiete*, 2006, ISBN: 3-933761-51-4
- 149 Kohler, Beate: *Externe Effekte der Laufwasserkraftnutzung*, 2006, ISBN: 3-933761-52-2
- 150 Hrsg.: Braun, Jürgen; Koschitzky, Hans-Peter; Stuhmann, Matthias: *VEGAS-Statuskolloquium 2006*, Tagungsband zur Veranstaltung am 28. September 2006 an der Universität Stuttgart, Campus Stuttgart-Vaihingen,, 2006, ISBN: 3-933761-53-0



151 Niessner, Jennifer: *Multi-Scale Modeling of Multi-Phase - Multi-Component Processes in Heterogenous Porous Media*, 2006, ISBN: 3-933761-54-9

Die Mitteilungshefte ab dem Jahr 2005 stehen auch als pdf-Datei über die Homepage des Instituts: [www.iws.uni-stuttgart.de](http://www.iws.uni-stuttgart.de) zur Verfügung.